NANO-BIO HYBRID SENSORS FOR CHEMICAL DETECTION AND DISEASE DIAGNOSTICS

Nicholas J. Kybert

A DISSERTATION

in

Physics and Astronomy

Presented to the Faculties of the University of Pennsylvania

in

Partial Fulfillment of the Requirements for the

Degree of Doctor of Philosophy

2015

Supervisor of Dissertation

_____

A. T. Charlie Johnson, Professor, Department of Physics and Astronomy

Graduate Group Chairperson

_____

Marija Drndic, Professor, Department of Physics and Astronomy

Dissertation Committee

Cherie Kagan, Stephen J. Angello Professor, Department of Electrical and Systems Engineering

Mark Trodden, Fay R. and Eugene L. Langberg Professor, Department of Physics and Astronomy

Arjun Yodh, James M. Skinner Professor of Science, Department of Physics and Astronomy

George Preti, Monell Chemial Senses Center & Adjunct Professor, Department of Dermatology, School of Medicine

NANO-BIO HYBRID ELECTRONIC SENSORS FOR CHEMICAL DETECTION AND DISEASE DIAGNOSTICS

This work is dedicated to my loving, caring wife Ani and our two amazing girls, Mia and Kate. Thank you for everything you bring to my life and for making any struggles in lab melt away when I walk through the door.

ACKNOWLEDGMENTS

I would like to thank the following people for their contributions towards me completing this thesis:

Above everyone else, I owe a tremendous amount to my thesis advisor, Prof. Charlie Johnson for his guidance and support. Charlie first accepted me into his lab as a naïve undergraduate through the Penn REU program and without that start in research I may not have pursued graduate school at all. I also owe my start in research to Drew McGhie, who runs the REU program and accepted me to Penn. When I returned as a graduate student, Charlie's mentorship provided direction and focus for my work while allowing me freedom to run my experiments. His long leash allowed me to make mistakes and spin my wheels in my early days in graduate school – an experience that helped me more deeply understand the science and generate my own lists of do's and don'ts and helped me greatly later on once the experiments began to click and the results came in. I also learned a great deal from Charlie about effectively communicating with other researchers and presenting my work most effectively, skills that will stick with me moving forward.

I am also hugely indebted to the graduate students and post-docs that preceded me. Brett Goldsmith, Zhengtang Luo and Ye Lu were my first mentors and laid the groundwork for a lot of our work. Ganghee Han was our growth wizard, whose knowledge and intuition for all things CVD will never cease to amaze me. Mitchell Lerner educated me on nanotubes and surface chemistry and his insight helped me immensely through the early years of my PhD. He also shepherded me through graduate school and is one of my most trusted friends and advisors in both lab and life.

Graduate students Carl Naylor and Pedro Ducos joined the lab after me and provided fresh energy and enthusiasm. Watching them go from fresh-faced novices to spearheading the next generation of experiments has been great. The lab is in good hands with them. I was very fortunate to be surrounded by smart and friendly people that made coming to lab every day a pleasure. Post docs Madeline Diaz-Serrano, Eric Dattoli, Jinglei Ping and Zhaoli Gao all played their role in this environment, along with graduate students John Qi, Ramya Vishnubotla and Julian Holder. I owe a great deal to undergraduate and junior graduate collaborators Jeremy Yodh, Ruben Waldman, William Zhou and Christopher Kehayias who all helped me at one time or another with vapor sensing experiments. By fabricating samples, taking data and just being there to brainstorming with me, you all added a great amount to this work. In other experiments I have been very fortune to mentor a string of very talented undergraduates, including Gabriela Romero, Yarely Davila Vasquez, Alex Crook, Alex Hunt, Camilla Schneier and Ik Soo Kwan and Masters students Sen Cong, Rajatesh Gudibande, Ji Soo Kang and Ryan Mendoza.

I must also thank our collaborators from other departments that helped push this research forward, including Jeffrey Saven in Chemistry, Renyu Liu in the Medical School and Cindy Otto in the Veterinary School. Our collaborators at the Monell Cheimical Senses Center, George Preti and Katherine Prokop-Prigge, were invaluable due to their expertise in analytical chemistry and olfaction which informed our push towards sensing experiments on biological samples. I also learned a great deal – in and out of the lab – from our international visitors and collaborators, including Sung Ju Hong, Ali Esfandiar, Chun Zhai and Rajesh.

Finally, I'd like to thank my parents, Anne and Martin Kybert. The nurturing and supportive environment I grew up in was a critical ingredient in getting me to where I am today.

ABSTRACT

NANO-BIO HYBRID ELECTRONIC SENSORS FOR CHEMICAL DETECTION AND DISEASE DIAGNOSTICS

Nicholas J. Kybert

A. T. Charlie Johnson

The need to detect low concentrations of chemical or biological targets is ubiquitous in environmental monitoring and biomedical applications. The goal of this work was to address challenges in this arena by combining nanomaterials grown via scalable techniques with chemical receptors optimized for the detection problem at hand. Advances were made in the CVD growth of graphene, carbon nanotubes and molybdenum disulfide. Field effect transistors using these materials as the channel were fabricated using methods designed to avoid contamination of the nanomaterial surfaces. These devices were used to read out electronic signatures of binding events of molecular targets in both vapor and solution phases. Single-stranded DNA functionalized graphene and carbon nanotubes were shown to be versatile receptors for a wide variety of volatile molecular targets, with characteristic responses that depended on the DNA sequence and the identity of the target molecule, observable down to part-per-billion concentrations. This technology was applied to increasingly difficult detection challenges, culminating in a study of blood plasma samples from patients with ovarian cancer. By working with large arrays of devices and studying the devices' responses to pooled plasma samples and plasma samples from 24 individuals, sufficient data was collected to identify statistically robust patterns that allow samples to be classified as coming from individuals who are healthy or have either benign or malignant ovarian tumors. Solution-phase detection experiments focused on the

design of surface linkers and specific receptors for medically relevant molecular targets. A non-covalent linker was used to attach a known glucose receptor to carbon nanotubes and the resulting hybrid was shown to be sensitive to glucose at the low concentrations found in saliva, opening up a potential pathway to glucose monitoring without the need for drawing blood. In separate experiments, molybdenum disulfide transistors were functionalized with a re-engineered variant of a μ-opiod receptor, a cell membrane protein that binds opiods and regulates pain and reward signaling in the body. The resulting devices were shown to bind opiods with affinities that agree with measurements in the native state. This result could enable not only an advanced opiod sensor but moreover could be generalized into a solid-state drug testing platform, allowing the interactions of novel pharmaceuticals and their target proteins to be read out electronically. Such a system could have high throughput due to the quick measurement, scalable device fabrication and high sensitivity of the molybdenum disulfide transistor.

TABLE OF CONTENTS

LIST OF TABLES

LIST OF ILLUSTRATIONS

CHAPTER 1: Overview of the Thesis

The ability to detect low concentrations of chemical or biological targets is a ubiquitous need in environmental monitoring and biomedical applications. However, compared to advances made in other technological realms, progress towards effective bio/chemical sensors has been extremely slow. For example, for detection of vapor traces in air, no technology has been able to match the sensitivity of a canine's sense of smell, hence their routine presence alongside law enforcement personnel in airports, malls and train stations worldwide. Recently, however, hybrid nano-bio devices have garnered significant interest due to their potential to make a large impact in this field. The properties of nanomaterials, defined in this work as materials that have at least one dimension comparable to the unit cell of the material, can be extremely sensitive to changes in their local environment due to their extraordinarily high surface-to-volume ratio, giving devices based on nanomaterials a huge geometric sensitivity advantage compared to their bulk counterparts. Nano-bio hybrid devices couple these materials to biomolecules that are chosen for their affinity for biochemical targets. The biomolecules can be either borrowed directly from nature, such as protein antibodies produced by the body to bind to antigen molecules, or re-engineered to retain their original capability while building in other function.

The overarching goal of the work presented in this doctoral thesis was to develop, characterize and test a new set of nano-bio hybrid sensors based on nanomaterials grown and processed with scalable techniques, in order to push these devices closer to commercialization. Furthermore, significant effort was expended to advance the complexity of the sensing experiments conducted, moving away from testing the limits of the technologies in perfect

conditions and towards the detection of targets in complex backgrounds more representative of real-world challenges. Significant progress was made towards these goals by making advances throughout the development process. On the materials end, the growth of new materials such as molybdenum disulfide and boron nitride was investigated and improved. Also, the fabrication of devices based on more established materials was scaled up by growing material on larger scale (graphene) or taking advantage of commercially available, presorted material (carbon nanotubes). Beyond material growth, new biomolecule linker chemistries were investigated, and target molecules were detected in environments as simple as pure nitrogen and as complex as human blood plasma. While there are remain significant hurdles to clear, I believe the work described in this thesis has advanced nanomaterial-based sensors and moved them closer to commercial and clinical implementation.

Chapter 2 of this thesis introduces the electronic, chemical and structural properties of the nanomaterials used throughout the work, including carbon nanotubes, graphene, boron nitride and molybdenum disulfide. In particular, electronic properties of the materials are introduced that will be important in the understanding of later chapters of this work that focus on material characterization.

Chapter 3 is devoted to the key characterization techniques that are used throughout this work. These include microscopy techniques for visualizing materials and spectroscopy techniques that are invaluable in characterizing material parameters. Furthermore, electronic measurement geometries are introduced that serve not only to characterize the electronic characteristics of the nanomaterials but will also be used to read out the biochemical binding events in later chapters.

Chapter 4 is devoted to advances in materials growth and device fabrication. First, we describe our progress in the fabrication of high yield, reproducible arrays of carbon nanotube field

effect transistors. By moving away from basing devices on individual nanotubes and instead using sparse networks of pre-sorted, highly semiconducting enriched single-wall carbon nanotubes, we can greatly improve the electronic transport properties of the devices while gaining significantly in reproducibility across devices.

Monolayer graphene growth and device fabrication is also described in detail. Growth methods at ambient and low pressure are described and the methods used to transfer graphene off of the copper growth substrate and outlined and compared. Furthermore, a method for fabricating large arrays of devices via photolithography while avoiding graphene surface contamination due to the photoresist residue is outlined. Next, growth of monolayer hexagonal boron nitride is described, followed by a detailed study of graphene-boron nitride heterostructures. This includes both atomically-stitched in-plane crystal lattices, that are only possible due to the almost perfect lattice matching of the two materials, and layered structures, where the large bandgap, similar lattice constant, smooth surface and large optical phonon modes of boron nitride make it an ideal substrate for graphene electronics, leading to enhances electrical properties.

Finally, growth methods for molybdenum disulfide (MoS_2) are introduced. In all cases, sulfur sublimation from a solid source provides the sulfur vapor necessary for growth. First, growth using a large droplet of ammonium heptamolybdate as the molybdenum-containing precursor is described, a technique that yields highly crystalline monolayer flakes of MoS_2 all across a silicon dioxide growth substrate. Then, a technique developed to pattern the molybdenum disulfide growth is described that used lithographically defined, micrometer-sized molybdenum precursor particles as both the growth seed location and growth material feedstock, resulting in highly crystalline monolayer MoS_2 flakes grown only in desired locations.

In chapter 5, the focus shifts towards combining the materials from chapter 4 with single stranded DNA to make vapor sensor arrays. Target vapors range from conceptually simple problems such as the detection of a chemical warfare agent at very low concentrations to complex real-world vapors, such as the volatile compounds that can be evaporated out of human blood plasma samples. We first demonstrate that carbon nanotube-DNA hybrids are able to detect chemical traces in vapor down to part-per-billion concentrations, with responses that depend on the DNA sequence used as the target receptor. The devices are sufficiently sensitive to the target molecule's chemical and physical structure that they are able to distinguish homologous series, isomers and even enantiomers. We show that these devices are sufficiently sensitive to distinguish dilute chemical vapor mixtures, even when the concentration of only one of more than a dozen compounds in the mixture is changed. Finally, we distinguish blood serum samples from women with ovarian cancer from samples from women with benign tumors and samples from healthy women. Statistically robust trends are observed that allow individual samples to be assigned to a class (cancer, benign, control) with a high degree of confidence.

Also in chapter 5, CVD-grown graphene is introduced as a replacement for carbon nanotubes in these devices, with the promise of even greater device-to-device reproducibility, lower electrical noise and faster electrical responses. After demonstrating successful fabrication of large arrays of devices with clean surfaces, the devices are coated with single stranded DNA and it is shown that many of the chemical recognition properties already shown with carbon nanotube based devices translate to graphene. An additional wrinkle is incorporated by send-assembling 100nm polystyrene beads on the graphene that can be used as an etch mask for graphene nanomesh fabrication. Etching the graphene into islands connected by ribbons increases the on/off ratio of the transistor and provides edge states for target binding.

In chapter 6 we discuss two separate experiments to detect biomolecules in solution. In the first, non-covalent attachment of pyrene boronic acid to carbon nanotubes is utilized as a linker for the binding of glucose. The resulting devices are sensitive to glucose in the range 1uM – 100mM, making them a potential platform for glucose detection in saliva, where glucose concentrations are on the micromolar scale. We also discuss the functionalization of MoS2 using a nickel ion linker to connect to the top layer of sulfur atoms and the co-ordinate covalently bind to a histidine-tagged protein. This approach is used to tether a re-engineered human cell membrane protein to the MoS_2 surface. The resulting hybrids are able to detect opioids with affinities that are consistent with previously measured values. Consequently, we envision these devices as not only opioid sensors, but also potentially as a drug testing platform, where the interaction between a drug and a protein target can be measured quickly and inexpensively on a solid-state substrate.

A summary of the experimental results is presented in chapter 7, along with a discussion of prospects for future experiments and the remaining hurdles that stand between these results and commercial or clinical applications.

CHAPTER 2: Introduction to Structural, Physical, Chemical and Electronic Properties of Atomically Thick Nanomaterials

Crystalline nanomaterials are attractive candidates for the electronic readout element in biosensors for a variety of reasons. First, their low-dimensional geometry with extremely high surface-to-volume ratio ensures that these materials have a large interaction with their environment compared to traditional three-dimensional materials. To put it another way, it is much more plausible to read out a nanoscale binding event with a nanometer-sized probe that with a millimeter sized one. Furthermore, their highly ordered atomic structure means that reliable surface chemistries can be developed for attachment of biomolecules. Finally, pristine unfunctionalized nanomaterials have characteristic electronic properties. Changes in these properties can be monitored as evidence of interaction with target biomolecules.

In this chapter, I discuss the structural, physical, chemical and electronic properties of all materials used in this work: graphene, carbon nanotubes, boron nitride and molybdenum disulfide. In each case, an understanding of the atomic arrangement and its resulting implications dictates the material's behavior.

2.1 The Material Properties of Graphene

2.1.1 The Structure of Graphene

Graphene is a two-dimensional allotrope of carbon, a single honeycomb lattice of sp^2 hybridized carbon atoms first isolated in a free-standing state in 2004 [1]. The carbon-carbon bond length, a, is 1.4 angstroms and each carbon atom is bonded to three neighbors with bond angles of 120°. The unit cell of graphene contains two atoms, referred to as the A and B sub-lattices. The basis vectors that allow the unit cell to be tessellated into the complete planar structure can be written in terms of a as

$$a_1 = \left(-\left(a + acos\frac{\pi}{3}\right), a\sin\frac{\pi}{3}\right)$$

$$a_2 = \left(a + a\cos\frac{\pi}{3}, a\sin\frac{\pi}{3}\right).$$

The resulting hexagonal lattice has a lattice constant of 2.46 angstroms. The unit cell of graphene, the two sublattices and two unit vectors are shown in figure 2.1. Sheets of graphene can stacked on top of each-other to form bilayer graphene, few layer graphene and ultimately graphite.

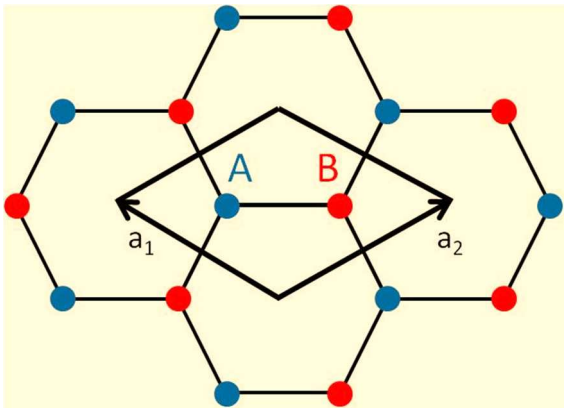

Figure 2.1: Graphene lattice with basis vectors. The two distinct sublattices are differentiated in red and blue.

The interlayer spacing between graphene layers is 3.35 angstroms. The pitch and rotation angle between the layers in bi- and few-layer graphene dictates whether the layers behave

electronically as separate graphene layers or whether they are electronically coupled. The layers are most tightly coupled in bilayer graphene when the layers are Bernal stacked, i.e. when the lattices are not rotated with respect to each other and one corner of the hexagon in the upper lattice is shifted to the center of the hexagon in the lower lattice. This shift corresponds to a vector

$$\overrightarrow{AB} = \left(a + 2a\cos\frac{\pi}{2}, 0\right).$$

This arrangement is also referred to as AB stacked graphene. Multilayer graphene can either be Bernal stacked (ABABAB…) or rhombohedral stacked (ABCABC…) depending on whether the third layer is shifted back onto the A lattice (Bernal) or shifted from the second layer by vector $\overrightarrow{AB}$, onto the C lattice[2]. These structures are shown in figure 2.2.

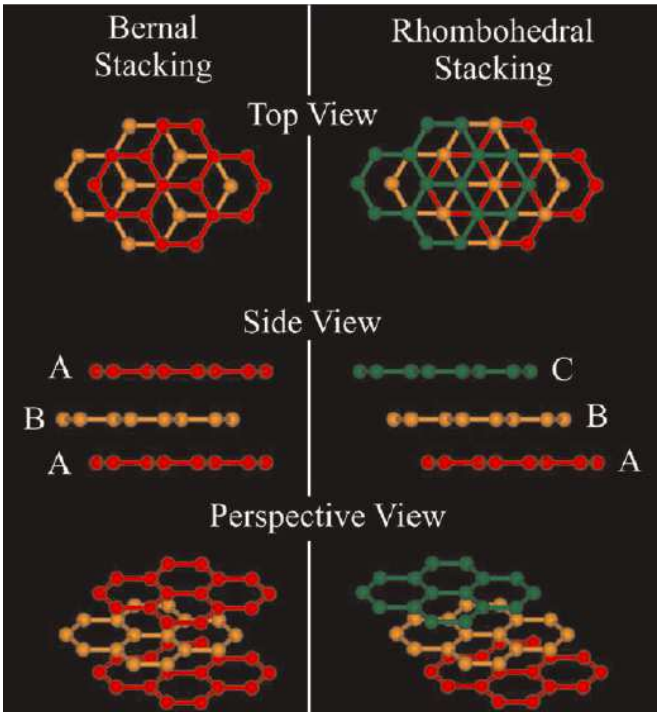

Figure 2.2: Bernal and rhombohedral stacking of graphene layers. Figure modified from [2].

2.1.2 The Electronic Structure of Graphene

Electronically, the band structure of graphene is well-described by a tight-binding model which shows that the valence and conduction bands meet at six points at the corners of the first

momentum space Brillouin zone, called Dirac points [3, 4]. As the density of states vanishes at these points, we refer to graphene as a zero bandgap semiconductor. The dispersion relation relating energy and momentum that emerges from the tight binding calculation is

$$E = \pm\gamma_0\sqrt{1 + 4\cos^2\left(\frac{k_y a}{2}\right) + 4\cos\frac{k_y a}{2}\cos\frac{\sqrt{3}k_x a}{2}}$$

where γ_0 is the nearest-neighbor hopping energy, confirmed by both density functional theory [5] and scanning probe microscopy [6] to be 2.5 eV. Uniquely to graphene, the conduction and valence bands are linear, not parabolic, in the low Energy limit where they meet at the Dirac points. This is reminiscent of the dispersion relation of relativistic particles, including light, and consequently the correct equation for describing the transport of electrons in graphene is not the Fermi equation but the Dirac equation [7]. In this low energy regime, the dispersion relation then simplifies to

$$E = v_F\hbar\left(\sqrt{{k_x}^2 + {k_y}^2}\right)$$

where k_x and k_y are now defined from the Dirac point and v_F is the Fermi velocity which calculations and experiments both show to be ~ 10^6 m/s, a three hundredth of the speed of light [7, 8].

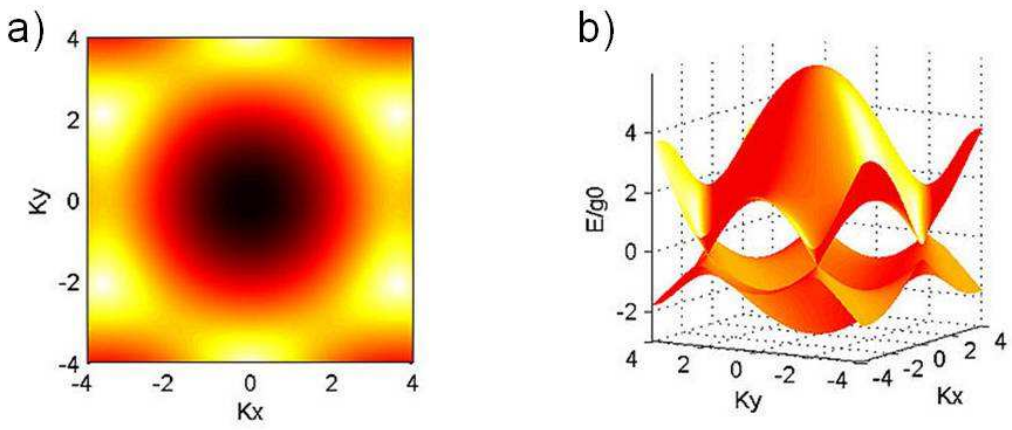

Figure 2.3: The band structure of graphene. a) The valence band, with white being the highest energy and black the lowest. b) The conduction and valence bands meet at the six corners of the Brillouin zone. The dispersion relation about these points is linear.

The quasi-massless nature of the charge carriers in graphene are responsible for the remarkable electron mobility of the material, which at room temperature is higher for graphene that any other material ever measured [9]. The carrier mobility is a measure of how quickly a charge carrier moves through a material when acted upon by an electric field, i.e.

$$v_d = \mu E,$$

where v_d is the drift velocity of the charge carriers, E is the electric field and μ is the mobility. The mobility of routine graphene samples prepared on silicon wafers exceeds 1000 cm^2/Vs, which is still orders of magnitude lower than in suspended low-temperature experiments, where removing the substrate has allowed mobilities as high as 10^6 to be measured [9, 10]. In these experiments, transport though the graphene is ballistic up to micrometer length scales [11, 12] and the dominant scattering mechanism is off defects [7]. In practical devices, typically on silicon wafers, the mobility is limited by scattering off acoustic phonons in both the graphene itself and the substrate [13, 14]. The intrinsic room temperature mobility of graphene is around 200,000 cm^2/Vs, while scattering of electrons in the graphene off acoustic phonons in silicon oxide limits

the mobility of devices on that substrate to a theoretical maximum of 40,000 cm^2/Vs [14]. In practice, typical carrier mobilities measured from field effect geometries are often an order of magnitude lower than this theoretical limit. Electronic characterization of graphene in field effect transistors is further described in chapter 3.4, and used routinely as a tool for evaluating graphene sample quality.

2.1.3 An Introduction to Graphene Surface Chemistry

The chemical reactivity of graphene is also known to depend on the substrate conditions and the number of layers of material [15]. Graphene burns at low temperature, and reactions with oxygen occur below 250 °C. Consequently annealing procedures where the graphene is heated to remove surface contaminants have to be conducted in oxygen-free conditions, typically an argon/hydrogen environment [16].

Reactions between graphene and linker molecules can be either covalent or non-covalent. One widely used technique is to generation of an sp^3 defect and form a carboxylate anchor, from which further linker chemistry steps can be conducted. A typical way to conduct this oxidation is to react the graphene with a diazonium compound, which is a compound with the functional group $R\text{-}N_2^+ X^-$. The nitrogen triple bond will detach, leaving the R functional group tethered to the graphene [15, 17]. A typical diazonium salt used in such a reaction is 4-carboxybenzene diazonium tetrafluoroborate [17]. This technique generates a strong covalent bond for permanent surface modification, but does have the drawback of inducing a defect into the hexagonal graphene lattice, which has a mild to severe impact on the electronic properties of the material (e.g. conductivity, mobility) depending on the density of the defects.

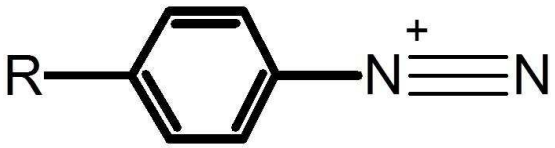

Figure 2.4: The structure of a benzene diazonium cation. The triple bond reacts with the graphene or nanotube, forming an sp^3 defect and anchoring the molecule to the surface. The R functional group can be varied depending on the desired chemical linkage and the final chemical residue that the chemistry is targeting.

Another approach to graphene chemistry is to take advantage of graphene's π-orbitals by using aromatic linkers that can π-π stack with the graphene. This approach has the advantage of non-covalent attachment, which ensures minimal degradation of the graphene electronics. It is a versatile linker approach, as it can be used to attach a desired chemical receptor directly, e.g. single-stranded DNA, via the aromatic rings in the DNA bases [18], or indirectly, such as in the case of pyrene linkers [19]. Pyrene consists of four fused benzene rings, and can be synthesized with a variety of different chemical groups attached to it. For example, pyrene-boronic acid will be used in chapter 6.1 to link to graphitic surfaces via a π-π stacking interaction and then bind glucose from solution, via a previously known boronic acid-glucose reaction. Aside from pyrene, there are other plausible non-covalent linkers, including but not limited to phenol [20] and naphthalene [21].

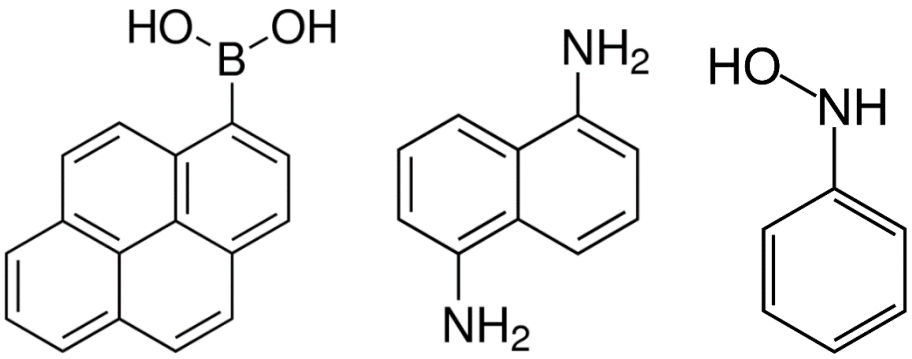

Figure 2.5: Selected non-covalent linkers that combine aromatic rings that π-π stack with graphene (pyrene, naphthalene, benzene) with functional groups (boronic acid, amine, hydroxyl amine).

2.2 Structural, Electronic and Chemistry Differences between Carbon Nanotubes and graphene

Topologically, carbon nanotubes are strips of graphene that have been rolled up and seamlessly stitched together. They are considered one-dimensional materials as the diameter of the tube is typically on the order of 1 nm, while the length of the tube can range from 1 µm to over half a meter in specially grown samples [22], resulting in an aspect ratio of 10^3-10^8. Carbon nanotubes can be 'single-walled carbon nanotubes', meaning a single isolated tube of carbon atoms, or "multi-walled carbon nanotubes', the term given to multiple concentric tubes of carbon. In this work, only single-walled carbon nanotubes will be considered in detail, but many reviews on multi-walled carbon nanotubes are available for the interested reader [23-25].

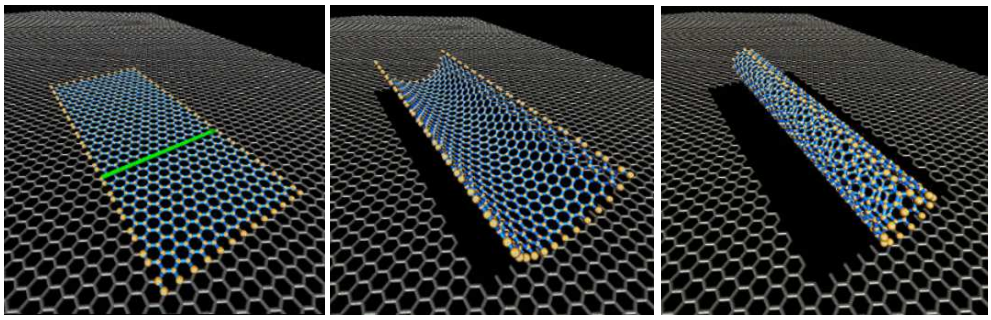

Figure 2.6: Wrapping graphene into a nanotube. The electronic properties of the nanotube depend on the chiral (wrapping) vector, shown in green. Modified from [26].

All properties of a carbon nanotube are determined by the so-called chirality of the nanotube. This refers to the chiral vector (or wrapping vector) that, if the carbon nanotube were 'unzipped', links two points in the graphene lattice that correspond to the same atom in the rolled up carbon nanotube[27]. The length of the chiral vector is therefore equal to the circumference of the carbon nanotube and this vector must be an integer sum of the two graphene basis vectors, ie.

$$C = na_1 + ma_2.$$

The electronic properties of the carbon nanotube vary drastically depending on the chirality. This can be understood starting from the graphene band structure shown in figure 2.3. This was calculated assuming an infinite two-dimensional lattice. When the lattice is shrunk into a nanometer wide strip and rolled up, the electron wave function around the nanotube must be self-consistent. Consequently, the component of the electron's momentum around the nanotube is quantized, i.e.

$$k_{\perp} = \frac{2\pi N}{C}$$

where N is an integer. This can be accounted for in the band structure calculation using a zone folding method [5, 28]. Ultimately, the quantization results in allowed 'slices' of the graphene band structure for carbon nanotubes, with most of the graphene states prohibited for carbon nanotubes. Critically for applications, the full calculation reveals that two thirds of all carbon nanotubes are semiconducting as the allowed $k_{\perp}$ values do not intersect with the Dirac points of the graphene band structure. The other one third of nanotubes have $k_{\perp}$ values that match the corners of the Brillouin zone and are thus metallic. The metallic carbon nanotubes are determined by the selection rule

$$n - m = 3N$$

where N is an integer. The two cases, semiconducting and metallic carbon nanotube band structures, are shown in figure 2.7.

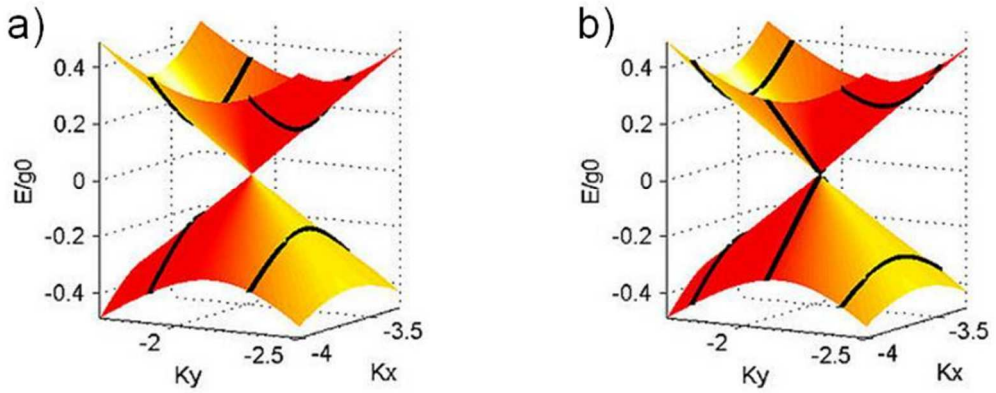

Figure 2.7: The band structure of carbon nanotubes. The allowed states are shown in black, superimposed on the graphene band structure, with the y-direction being around the nanotube. In a), the quantized momentum in y does not pass through a Dirac point in graphene, so the nanotube is semiconducting. In b) the conduction and valence bands touch and the nanotube is metallic.

Technologically, it would be a great advance to be able to grow exclusively either metallic or semiconducting carbon nanotubes directly onto an insulating substrate. For example, the ability to grow exclusively semiconducting carbon nanotubes without metallic content would allow for fabrication of arrays of highly semiconducting devices. However, despite many years of research in this direction, that level of control over the CVD growth process is yet to be achieved. An alternate approach has been adopted of growing all chiralities of carbon nanotubes together, and then suspending the resulting nanotubes in solution and sorting them using techniques such as density centrifugation[29, 30] and polymer [31] and DNA wrapping [32, 33], all of which have the fidelity to select individual chiralities of carbon nanotubes out of the as-grown mixture. This progress has allowed for arrays of devices to be fabricated with predominantly semiconducting or metallic characteristics, as shown later in chapter 4.2.

Surface chemistry conducted on carbon nanotubes is very similar to what was outlined above for graphene. One difference to be noted is that the curvature of the tube induces stress on the carbon-carbon bonds, making the π electrons more reactive for covalent attachment

procedures. In practice, this is typically accounted for by lowering the reaction temperature. This avoids excessive reactions that are particularly troublesome for carbon nanotubes as, being one-dimensional conductors, their conductivity can be completely eliminated by only a small number of defects if they are clustered close to each other on the carbon nanotube. There is also a significant amount of work being conducted to develop chemistries that are selective for particular carbon nanotube chiralities, both as a means of sorting carbon nanotubes as well as to induce chemical functionality [34].

2.3 Material Properties of Hexagonal Boron Nitride

Hexagonal boron nitride has the same lattice structure as graphene, shown in figure 2.1. However, instead of containing exclusively carbon, one of the A and B sublattices is made of nitrogen atoms and the other of boron. Unlike graphene, boron nitride has a large band gap of 5.2 eV [35], a result of the different onsite energies of the boron and nitrogen atoms. The lattice constant of hexagonal boron nitride is 2.5 angstroms [36], approximately 1.7% larger than graphene. In plane, strong covalent boron-nitrogen bonds hold the material together, while weak van der Waals forces are responsible for holding the layers together in multilayer samples.

Boron nitride has emerged as the ideal material for fabrication of graphene heterostructures. Its identical lattice structure and closely matching lattice constant mean that in-plane structures can be formed in which graphene and boron nitride are atomically stitched together [37], as will be described in section 4.8. Boron nitride is relatively inert due to the somewhat ionic in-plane bonding, and should be free of dangling bonds and surface charge traps. Furthermore, the phonon modes in boron nitride have an activation energy two orders of magnitude higher that comparable modes in silicon dioxide[13]. This combination of properties, as well as the atomically smooth nature of the surface make boron nitride the ideal substrate for graphene electronics, a concept that has been heavily explored in exfoliated, micrometer-sized samples[13, 38, 39]. We address the question of whether the same effects can be achieved by scalable methods in section 4.7.

2.4 The Properties of Transition Metal Dichalcogenides such as Molybdenum Disulfide

Layered transition metal dichalcogenides are another set of nanomaterials 'beyond graphene' that have seen increasing interest in recent years. These materials have the chemical formula MX_2, where M is a transition metal such as molybdenum or tungsten and X is a chalcogen such as sulfur or selenium. In the monolayer material, the transition metal is sandwiched between two layers of the chalcogen, and each transition metal atom is bonded to six chalcogen atoms – three in the top layer and three in the lower one. Top and side views of this crystal structure are shown in figure 2.8.

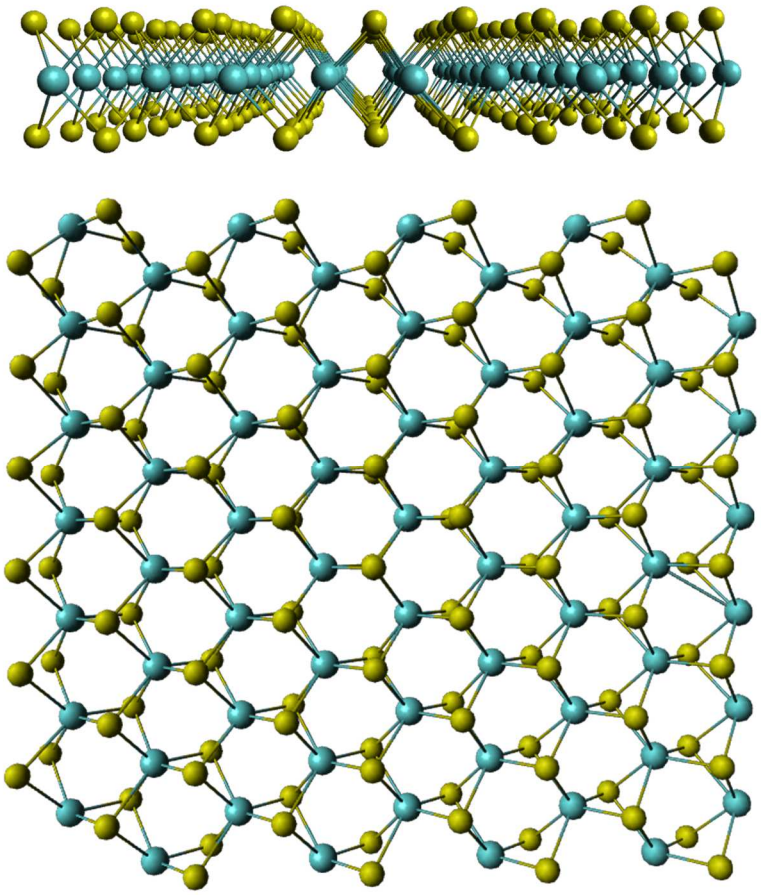

Figure 2.8: Side and top view images of transition metal dichalcogenides structure. The transition metal atoms are drawn in blue and the chalcogen atoms in yellow. From above, the lattice appears hexagonal, but a side view reveals a pair of sulfur atoms sitting on top of each other.

Bulk transition metal dichalcogenides have properties that vary depending on the transition metal and chalcogen chosen, as shown in table 2.1. In this work, we have focused on molybdenum disulfide, MoS_2, in part because it is a true semiconductor with an indirect bandgap of 1.2 eV for the bulk and a direct band gap of 1.8 eV for the monolayer [40]. Consequently, conduction through MoS_2 can be strongly tuned by a gate voltage, with on/off ratios as high as 10^8 reported [40].

Transition metal	Chalcogen	Electrical/Magnetic properties (MX_2)
Ti, Hf, Zr	S, Se, Te	Semiconducting. Diamagnetic
V, Nb, Ta	S, Se, Te	Narrow band metals or semimetals, superconducting
Mo, W	S, Se, Te	S, Se: semiconducting. Te: semimetallic
Tc, Re	S, Se, Te	Small-gap semiconductor
Pd, Pt	S, Se, Te	S, Se: semiconducting. Te: metallic. $PdTe_2$ is

Table 2.1: Transition metal dichalcogenides and their electronic properties. [41]

The chemistry of monolayer MoS_2 surfaces is an emerging field of study will few results to date. Molybdenum disulfide is known to oxidize when heated in the presence of oxygen, to form molybdenum trioxide and sulfur trioxide. Doping MoS_2 monolayers with rhenium or introducing gold adatoms have been shown to increase the local chemical affinity [42]. The top sulfur groups can be reacted with noble metals, which has been used to attach gold nanoparticles. Furthermore, it has previously been shown that nickel ions can be coordinate covalently-bound to the top sulfur layer of molybdenum disulfide nanoparticles [43], a technique which is adapted later in this work as an anchor site for protein attachment.

References

1. Novoselov, K.S., A.K. Geim, S.V. Morozov, D. Jiang, et al., *Electric field effect in atomically thin carbon films.* Science, 2004. **306**(5696): p. 666-9.
2. Warner, J.H., M. Mukai, and A.I. Kirkland, *Atomic structure of ABC rhombohedral stacked trilayer graphene.* ACS Nano, 2012. **6**(6): p. 5680-6.
3. Wallace, P.R., *The Band Theory of Graphite.* Physical Review, 1947. **71**(7): p. 476.
4. Reich, S., J. Maultzsch, C. Thomsen, and P. Ordejón, *Tight-binding description of graphene.* Physical Review B, 2002. **66**(3): p. 035412.
5. Mintmire, J.W. and C.T. White, *Electronic and structural properties of carbon nanotubes.* Carbon, 1995. **33**(7): p. 893-902.
6. Wilder, J.W.G., L.C. Venema, A.G. Rinzler, R.E. Smalley, et al., *Electronic structure of atomically resolved carbon nanotubes.* Nature, 1998. **391**(6662): p. 59-62.
7. Novoselov, K.S., A.K. Geim, S.V. Morozov, D. Jiang, et al., *Two-dimensional gas of massless Dirac fermions in graphene.* Nature, 2005. **438**(7065): p. 197-200.
8. Novoselov, K.S., Z. Jiang, Y. Zhang, S.V. Morozov, et al., *Room-Temperature Quantum Hall Effect in Graphene.* Science, 2007. **315**(5817): p. 1379.
9. Bolotin, K.I., K.J. Sikes, J. Hone, H.L. Stormer, et al., *Temperature-dependent transport in suspended graphene.* Phys Rev Lett, 2008. **101**(9): p. 096802.
10. Kretinin, A.V., Y. Cao, J.S. Tu, G.L. Yu, et al., *Electronic properties of graphene encapsulated with different two-dimensional atomic crystals.* Nano Lett, 2014. **14**(6): p. 3270-6.
11. Du, X., I. Skachko, A. Barker, and E.Y. Andrei, *Approaching ballistic transport in suspended graphene.* Nat Nano, 2008. **3**(8): p. 491-495.
12. Fogler, M.M., F. Guinea, and M.I. Katsnelson, *Pseudomagnetic Fields and Ballistic Transport in a Suspended Graphene Sheet.* Physical Review Letters, 2008. **101**(22): p. 226804.
13. Dean, C.R., A.F. Young, MericI, LeeC, et al., *Boron nitride substrates for high-quality graphene electronics.* Nat Nano, 2010. **5**(10): p. 722-726.
14. Chen, J.-H., C. Jang, S. Xiao, M. Ishigami, et al., *Intrinsic and extrinsic performance limits of graphene devices on SiO2.* Nat Nano, 2008. **3**(4): p. 206-209.
15. Wang, Q.H., Z. Jin, K.K. Kim, A.J. Hilmer, et al., *Understanding and controlling the substrate effect on graphene electron-transfer chemistry via reactivity imprint lithography.* Nat Chem, 2012. **4**(9): p. 724-732.
16. Dan, Y., Y. Lu, N.J. Kybert, Z. Luo, et al., *Intrinsic response of graphene vapor sensors.* Nano Lett, 2009. **9**(4): p. 1472-5.
17. Lerner, M.B., F. Matsunaga, G.H. Han, S.J. Hong, et al., *Scalable production of highly sensitive nanosensors based on graphene functionalized with a designed G protein-coupled receptor.* Nano Lett, 2014. **14**(5): p. 2709-14.
18. Kybert, N., G. Han, M. Lerner, E. Dattoli, et al., *Scalable arrays of chemical vapor sensors based on DNA-decorated graphene.* Nano Research, 2014. **7**(1): p. 95-103.
19. Ghosh, S., X. An, R. Shah, D. Rawat, et al., *Effect of 1- Pyrene Carboxylic-Acid Functionalization of Graphene on Its Capacitive Energy Storage.* The Journal of Physical Chemistry C, 2012. **116**(39): p. 20688-20693.

20. Zhao, X., Y. Li, J. Wang, Z. Ouyang, et al., *Interactive Oxidation–Reduction Reaction for the in Situ Synthesis of Graphene–Phenol Formaldehyde Composites with Enhanced Properties.* ACS Applied Materials & Interfaces, 2014. **6**(6): p. 4254-4263.
21. Park, S.J., O.S. Kwon, S.H. Lee, H.S. Song, et al., *Ultrasensitive flexible graphene based field-effect transistor (FET)-type bioelectronic nose.* Nano Lett, 2012. **12**(10): p. 5082-90.
22. Zhang, R., Y. Zhang, Q. Zhang, H. Xie, et al., *Growth of half-meter long carbon nanotubes based on Schulz-Flory distribution.* ACS Nano, 2013. **7**(7): p. 6156-61.
23. Coleman, J.N., U. Khan, W.J. Blau, and Y.K. Gun'ko, *Small but strong: A review of the mechanical properties of carbon nanotube–polymer composites.* Carbon, 2006. **44**(9): p. 1624-1652.
24. Ajayan, P. and O. Zhou, *Applications of Carbon Nanotubes*, in *Carbon Nanotubes*, M. Dresselhaus, G. Dresselhaus, and P. Avouris, Editors. 2001, Springer Berlin Heidelberg. p. 391-425.
25. Baughman, R.H., A.A. Zakhidov, and W.A. de Heer, *Carbon Nanotubes--the Route Toward Applications.* Science, 2002. **297**(5582): p. 787-792.
26. Johnson, R.R. *Rolling up a Graphene Sheet into a Carbon Nanotube*. 2015 [cited 2015; Available from: http://www.physics.upenn.edu/~robertjo/gallery/.
27. Dresselhaus, M.S., G. Dresselhaus, and P. Avouris, *Carbon nanotubes : synthesis, structure, properties, and applications*. Topics in applied physics. 2001, Berlin ; New York: Springer. xv, 447 p.
28. Mintmire, J.W. and C.T. White, *Universal Density of States for Carbon Nanotubes.* Physical Review Letters, 1998. **81**(12): p. 2506-2509.
29. Arnold, M.S., A.A. Green, J.F. Hulvat, S.I. Stupp, et al., *Sorting carbon nanotubes by electronic structure using density differentiation.* Nat Nano, 2006. **1**(1): p. 60-65.
30. Arnold, M.S., S.I. Stupp, and M.C. Hersam, *Enrichment of Single-Walled Carbon Nanotubes by Diameter in Density Gradients.* Nano Letters, 2005. **5**(4): p. 713-718.
31. Nish, A., J.-Y. Hwang, J. Doig, and R.J. Nicholas, *Highly selective dispersion of single-walled carbon nanotubes using aromatic polymers.* Nat Nano, 2007. **2**(10): p. 640-646.
32. Zheng, M., A. Jagota, E.D. Semke, B.A. Diner, et al., *DNA-assisted dispersion and separation of carbon nanotubes.* Nat Mater, 2003. **2**(5): p. 338-42.
33. Tu, X., S. Manohar, A. Jagota, and M. Zheng, *DNA sequence motifs for structure-specific recognition and separation of carbon nanotubes.* Nature, 2009. **460**(7252): p. 250-3.
34. Hodge, S.A., M.K. Bayazit, K.S. Coleman, and M.S. Shaffer, *Unweaving the rainbow: a review of the relationship between single-walled carbon nanotube molecular structures and their chemical reactivity.* Chem Soc Rev, 2012. **41**(12): p. 4409-29.
35. Hoffman, D.M., G.L. Doll, and P.C. Eklund, *Optical properties of pyrolytic boron nitride in the energy range 0.05\char22{}10 eV.* Physical Review B, 1984. **30**(10): p. 6051-6056.
36. Kobayashi, Y., T. Akasaka, and T. Makimoto, *Hexagonal boron nitride grown by MOVPE.* Journal of Crystal Growth, 2008. **310**(23): p. 5048-5052.
37. Han, G.H., J.A. Rodriguez-Manzo, C.W. Lee, N.J. Kybert, et al., *Continuous growth of hexagonal graphene and boron nitride in-plane heterostructures by atmospheric pressure chemical vapor deposition.* ACS Nano, 2013. **7**(11): p. 10129-38.
38. Gannett, W., W. Regan, K. Watanabe, T. Taniguchi, et al., *Boron nitride substrates for high mobility chemical vapor deposited graphene.* Applied Physics Letters, 2011. **98**(24): p. 242105.

39. Dean, C.R., A.F. Young, P. Cadden-Zimansky, L. Wang, et al., *Multicomponent fractional quantum Hall effect in graphene.* Nat Phys, 2011. **7**(9): p. 693-696.
40. RadisavljevicB, RadenovicA, BrivioJ, GiacomettiV, et al., *Single-layer MoS2 transistors.* Nat Nano, 2011. **6**(3): p. 147-150.
41. Chhowalla, M., H.S. Shin, G. Eda, L.-J. Li, et al., *The chemistry of two-dimensional layered transition metal dichalcogenide nanosheets.* Nat Chem, 2013. **5**(4): p. 263-275.
42. Sreeprasad, T.S., P. Nguyen, N. Kim, and V. Berry, *Controlled, Defect-Guided, Metal-Nanoparticle Incorporation onto MoS2 via Chemical and Microwave Routes: Electrical, Thermal, and Structural Properties.* Nano Letters, 2013. **13**(9): p. 4434-4441.
43. Tahir, M.N., N. Zink, M. Eberhardt, H.A. Therese, et al., *Overcoming the Insolubility of Molybdenum Disulfide Nanoparticles through a High Degree of Sidewall Functionalization Using Polymeric Chelating Ligands.* Angewandte Chemie International Edition, 2006. **45**(29): p. 4809-4815.

CHAPTER 3: Growth and Device Fabrication

Accurate and informative characterization of the properties of a nanomaterials a critical in forming a judgment on the quality of the material. These techniques are also invaluable as a tool for optimizing material growth and processing techniques. All of the techniques presented here are non-destructive, and the techniques are complementary as each probes the material in a different way.

Raman spectroscopy is used to probe low energy vibrational modes of a system and thus provides insight into the bonding of a sample. More direct evidence of the crystal structure can be obtained from transition electron microscopy. Here, the sample is mounted on a thin membrane or suspended off the substrate entirely. Highly accelerated electrons are scattered off the material as they pass through it, resulting in either direct imaging of the material or the formation of the diffraction pattern, depending on the mode used. Atomic Force Microscopy (AFM) uses a sharp, micrometer-sized silicon tip to scan across the sample. The AFM tip is mounted on a cantilever that can be driven at its resonant frequency, allowing the tip to tap across the sample, yielding information about the height and mechanical properties of the sample.

Finally, and most importantly, we can characterize the samples electronically by using them as the channel in field effect transistors. This is especially important as the goal of this work is to fabricate electronic nano-bio sensors. Truly understanding the electronics of the materials and being able to read out the electronics accurately are critical in this endeavor.

3.1 Raman Spectroscopy

Raman spectroscopy is a technique used to probe low-energy vibrational and rotational modes of a system. Laser light is inelastically scattered off the sample and when it interacts with these modes, energy can be transferred from the photons to the sample or vice-versa. As the interactions are quite weak, a notch filter is used to eliminate all the reflected light at the incident wavelength. Any light at shifted wavelengths gives information on the sample. These Raman shifts are reported in wavenumbers, with units of cm^{-1}, given by

$$\Delta w = \left(\frac{1}{\lambda_1} - \frac{1}{\lambda_2}\right) \times 10^7$$

where Δw is the Raman shift in cm^{-1}, λ_1 is the incident wavelength in nanometers and λ_2 is the Raman shifted wavelength in nanometers. As this scattering is dependent on the vibrational modes of specific bonds in the sample, the Raman shift provides a characteristic signature that allows for molecular identification and material characterization.

Several peaks have been identified in graphitic carbon that can be associated with specific bonds[1]. These are called the G band, D band and 2D (or G') band. The G-band resonance is associated with the stretching of an sp^2 hybridized C-C bond and is located at approximately 1582 cm^{-1} [1]. The D band resonance is associated with vibrational modes of sp^3 hybridized carbon and therefore reflects defect density and material edges. It is located at approximately 1350 cm^{-1}. Finally, the 2D band, which is in the range of 2500-2800 cm^{-1} depending on the material, is a second order, two-phonon process related to phonons near the K point in graphene, activated by double resonant processes [1]. This resonance is strongly dependent on any disturbance of the phonon and electronic structures of the material. Consequently, the location, size and shape of the 2D peak is a very sensitive probe for differentiating sp^2 nanocarbons, including distinguishing single, bi and many layer graphene [2, 3]. The raman spectrum of graphene is further influenced

by factors including the doping level of the sample, as has been shown by varying a back gate voltage during spectrum collection [4]. In sum, Raman spectroscopy is a quick, efficient, non-destructive tool for evaluating number and quality of graphene layers and sample doping level.

Metrics that can be used to evaluate the quality of a monolayer graphene sample include the D/G ratio, which should be less than 0.05, and the 2D/G ratio, which should be ~ 2. Furthermore, we can consider the shape and width of the peaks. Small full-width-half-maxima of the peaks indicate higher quality, while the 2D peak should be well fit by a single Lorentzian for monolayer graphene. A superposition of multiple Lorentzians is needed to accurately fit the 2D peak for multilayer graphene [5].

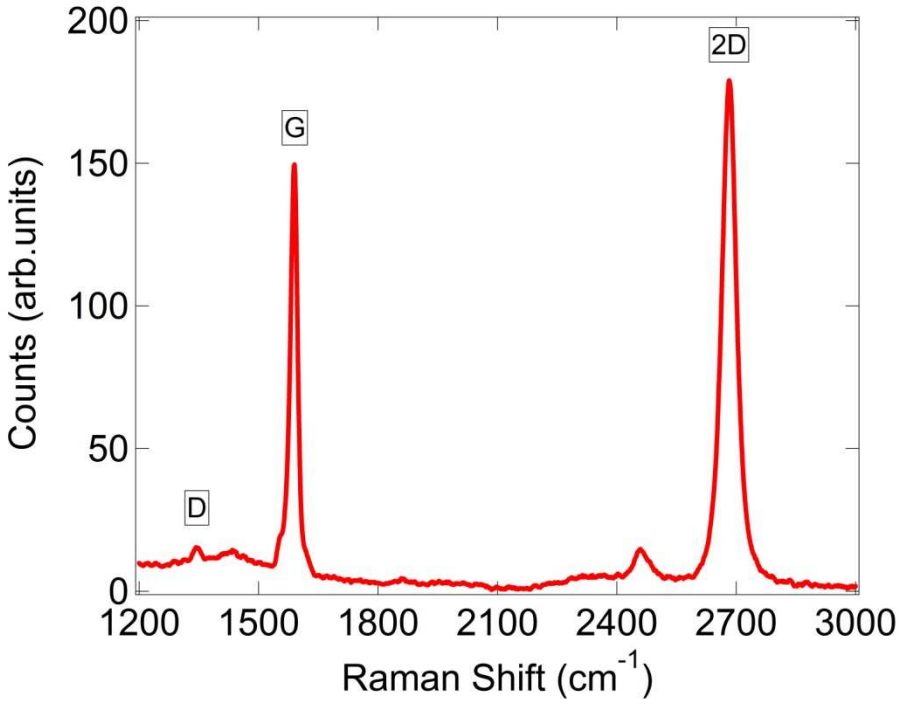

Figure 3.1: A Raman spectrum of graphene. The small D/G ratio is indicative of high quality material.

In carbon nanotubes, there are another set of peaks that provide qualitative and quantitative information on the material. These are the so-called radial breathing modes of the sample, corresponding to radial expansion and contraction of the tube. These are found at Raman

shifts below 500 cm^{-1} and are particularly insightful as the Raman shift depends on diameter, i.e. $w_{RBM} = w_{RBM}(n,m)$ [1]. Another feature of Raman spectra that differs between carbon nanotubes and graphene is the splitting of the G resonance observed in carbon nanotube. This splitting is attributed to the difference in frequency for the sp^2 resonances along the nanotube axis and around the circumference [6]. Most importantly, the higher frequency (G_+) component has a line shape that depends on whether the carbon nanotubes are semiconducting or metallic. For semiconducting nanotubes, the line shape should be fit by a Lorentzian that is approximately the same width as the lower frequency (G_-) resonance, while for metallic nanotubes, the G_- resonance is a very broad Briet-Wigner-Fano line due to photon coupling to the electronic continuum on the nanotube [7].

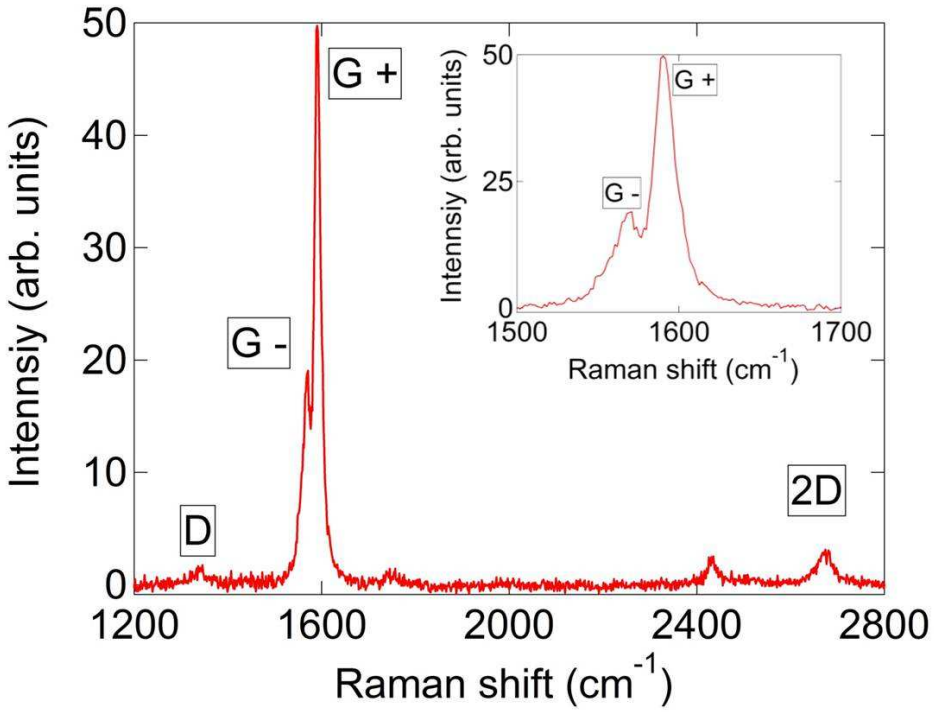

Figure 3.2: A carbon nanotube Raman spectrum. The split G peak and very large G/2D ratio are factors that distinguish this spectrum from graphene. The sharpness of the G_ peak indicates a highly semiconducting enriched nanotube sample.

3.2 Atomic Force Microscopy

There is a need for techniques that can image surfaces and resolve sizes below the diffraction limit of light. Scanning probe techniques fill this void by scanning a micrometer scale probe across the sample and generating an image by monitoring the interaction. In atomic force microscopy (AFM), a mechanical tip with a radius of curvature on the order of ten nanometers is mounted to the end of resonating cantilever [8]. In tapping mode, the cantilever is driven close to its resonant frequency, typically on the order of 100 kHz, and the tip is moved across the surface by a very precise piezoelectric controller. The tip is deflected from its driven oscillation when it interacts with the surface, due to damping by intramolecular forces between atoms in the tip and the sample. These deflections are monitored by reflecting a laser off the top surface of the cantilever and monitoring the laser reflection with a position-sensitive detector, typically a four quadrant photodetector. A feedback loop maintains a constant interaction strength between the tip and surface during a scan by moving the cantilever up and down. The voltage required to do so then gives a measure of surface height. Other parameters of the cantilever oscillation, in particular the phase and amplitude of oscillation, can give information on the properties of the surface including stiffness and stickiness [9, 10].

The lateral resolution of an AFM image is limited by the radius of the tip so 10-100nm is typical. Out of plane, however, the resolution is not tip radius limited and but determined only by the vibrational and electronic noise of the measurement apparatus. Consequently, height resolution down to less than an angstrom is routine. A schematic of AFM operation is shown in figure 3.3.

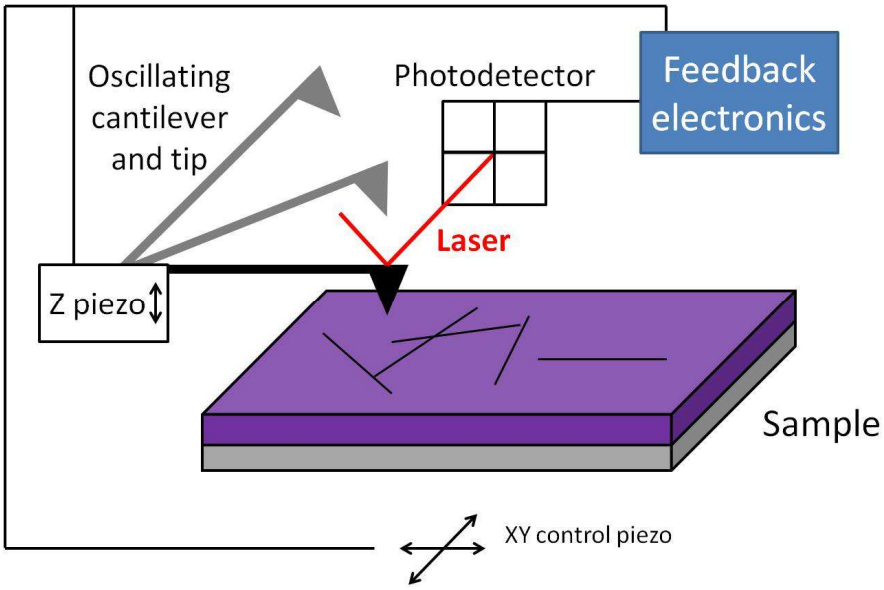

Figure 3.3: Schematic of an AFM.

Given the circumference of carbon nanotubes is on the order of a nanometer and the interlayer spacing in graphene is 0.335 nm, AFM measurements have sufficient resolution to image these materials routinely. In the resulting height images, a color gradient is used to denote height. Figure 3.4 shows a network of carbon nanotubes between two metal electrodes. In this image, the individual carbon nanotubes can easily be resolved. We are also informed that in this particular sample, small bundles of carbon nanotubes are forming (in particular on the right of the image). The image also reveals that the surface is smooth and clean and that the nanotubes are clean as well, as their heights (0.5-1.5 nm) are consistent with what was expected for this material.

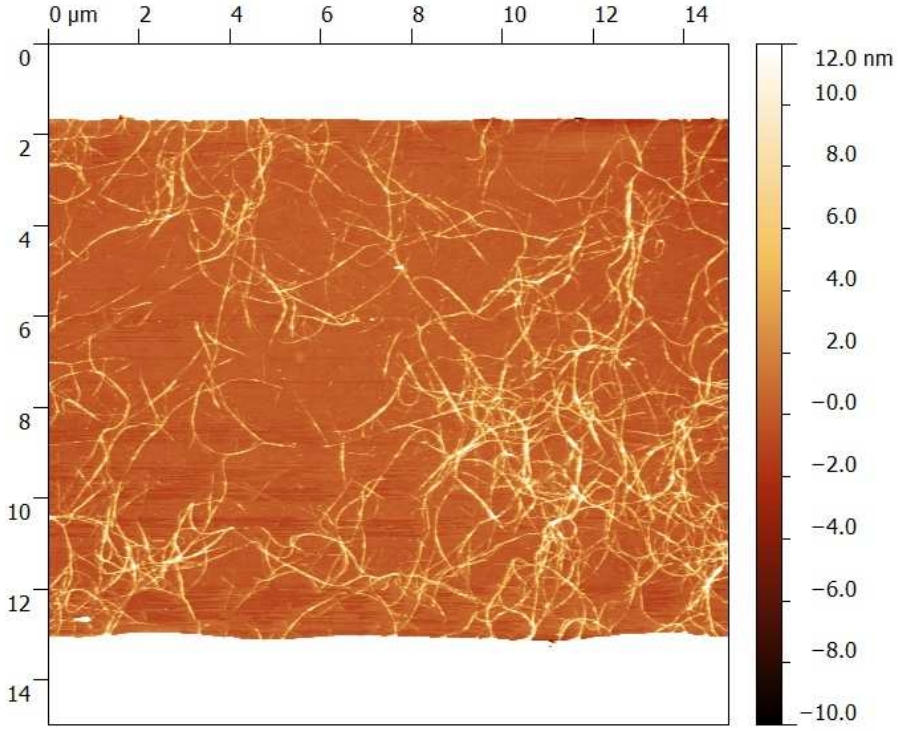

Figure 3.4: AFM image of a dense array of carbon nanotubes. The white regions top and bottom are the metal electrodes. The left side of the image has many single (1-3 µm length) carbon nanotubes, while on the right small bundles are forming that are longer and brighter (i.e. higher).

Figure 3.5 shows another example AFM height image. In this case, the sample is a graphene strip between metal electrodes. Aside from a couple of contaminant particles, the surface looks extremely smooth and the edges very straight. In this image, each horizontal line scan has been set to the same average height. One result of this is that the electrodes do not look while like in figure 3.4. This data processing choice means that while the height of the electrodes cannot be judged from the final image, we in return get information on the electrode surface roughness. Amazingly, AFM is so sensitive that the edge of the graphene strip that is buried under 45 nm of gold can still be imaged.

Due to its unrivaled height sensitivity and ability to image surfaces for contamination, AFM is a ubiquitous tool in nanotechnology and is used heavily throughout the remainder of this work as a premier surface characterization technique.

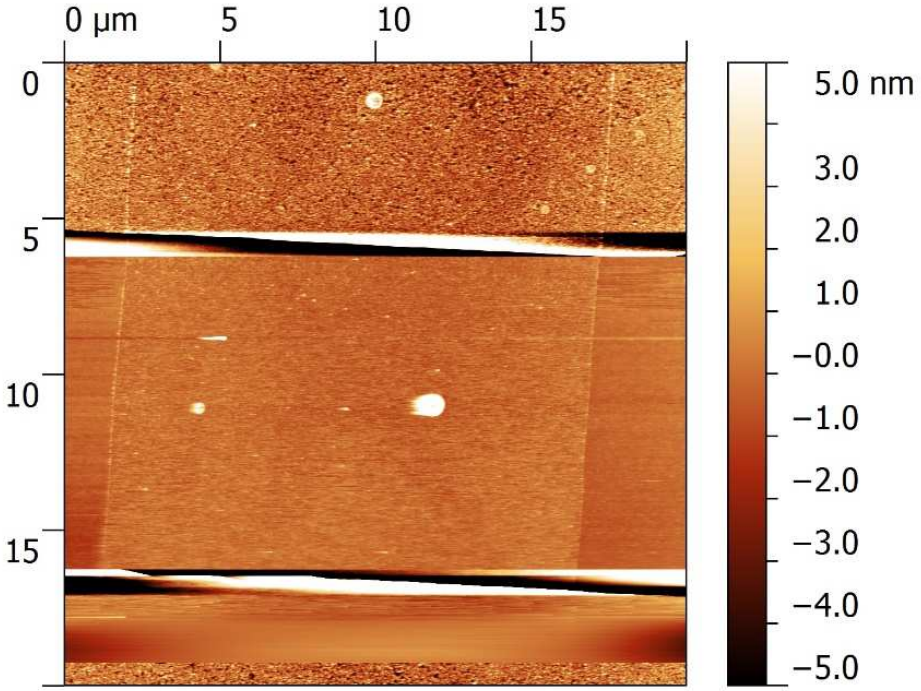

Figure 3.5: AFM image of graphene. The graphene strip runs top to bottom down the middle of the image. In this case, the image has been processed such that the electrodes are artificially lowered, allowing their surface morphology to be imaged. The graphene strip is 0.7 nm high, very flat and has very little surface residue.

3.3 Transition Electron Microscopy

In transition electron microscopy (TEM), electrons are transmitted through a thin sample to characterize the material's structure. Transmitted electrons are captured by a detector and form an image that reflects the interactions of the electrons with the material. The resolution of TEM is much greater than what can be achieved by optical microscopy as the incident electrons are highly accelerated and thus their effective wavelength is small. The wavelength sets a lower limit for the resolution of the TEM and is given by

$$\lambda = \frac{h}{\sqrt{2m_0E\left(1+\frac{E}{2m_0c^2}\right)}}$$

where m_0 is the rest mass of the electron, c is the speed of light, h is Planck's constant and E is the energy of the electron. For an accelerating voltage of 300 keV, this equation yields a wavelength of 2 pm. The electrons used in this imaging are generated by thermionic emission from a filament located in the electron gun. Electromagnetic lenses are used to accelerate and focus the electron beam.

State of the art TEMS are aberration-corrected, meaning that they correct for spherical aberration in the lens system [11]. Spherical aberration refers to variability in the focusing deflection of electrons that are off the central axis of the electron beam. Typically, the further from the central axis the electron is, the more strongly it is bent back towards the central axis. If this is not corrected for, the electrons are focused into a small disk instead of a true point, limiting the resolution of the tool. Aberration-corrected TEMs have demonstrated lateral resolution below an angstrom [12] and are thus able to image samples with atomic resolution.

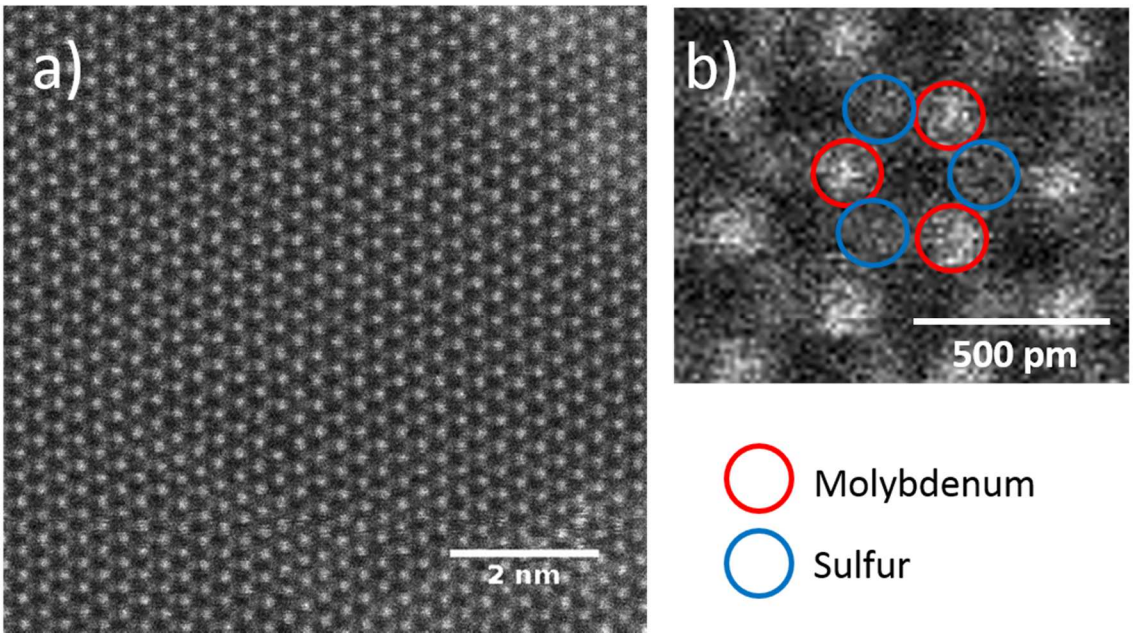

Figure 3.6: TEM image of MoS_2. In this dark field image, bright areas are where the bean has been most scattered. The expected hexagonal structure of the material is verified. Two different levels of brightness, corresponding to the molybdenum (heavy, bright) and sulfur (light, dim) atom sites are observed.

A variety of different imaging modes are possible in TEM, including selected area electron diffraction, energy loss spectroscopy and a variety of direct, real-space imaging techniques. Figure 3.6 shows an example of atomic resolution real space imaging of one of our MoS_2 samples. The hexagonal lattice observed is in agreement with the top-view of the MoS_2 lattice shown schematically in figure 2.8. Around the hexagon, three bright and three dark spots are observed, corresponding to the molybdenum and sulfur sites respectively. Despite two sulfur atoms sitting on top of each other, the molybdenum sites appear much brighter due to the much larger molybdenum atoms scattering more significantly. The hexagonal lattice in figure 3.6a extends across the entire image without any visible defects, indicating highly ordered, crystalline material, at least over the scales imaged.

Imaging samples with atomic resolution using TEM is significantly less straightforward than the other characterization techniques (Raman, AFM) due to the need to suspend the sample

on a support grid and the difficulty in getting time on one of a limited number of high resolution TEM instruments. However, direct imaging of the material is extremely valuable and provides direct evidence to supplement and reinforce the findings of the other techniques.

3.4 Three-terminal Field Effect Transistor Measurements

Ultimately, the most important material properties for the applications discussed in this work are the electric transport characteristics, as they are used as the readout mechanism for biochemical detection. The most common measurement geometry is that of a three terminal field effect transistor (FET), in which the nanomaterial is contacted by two metal electrodes, source and drain, across which a fixed bias voltage is applied. A third terminal is used to apply a gating voltage, typically to the bulk of a highly doped Si/SO_2 wafer on which the nanomaterial is located, which capacitively couples to the nanomaterial channel. This external field alters the Fermi level in the semiconducting nanomaterial channel and thus modulates the source-drain current.

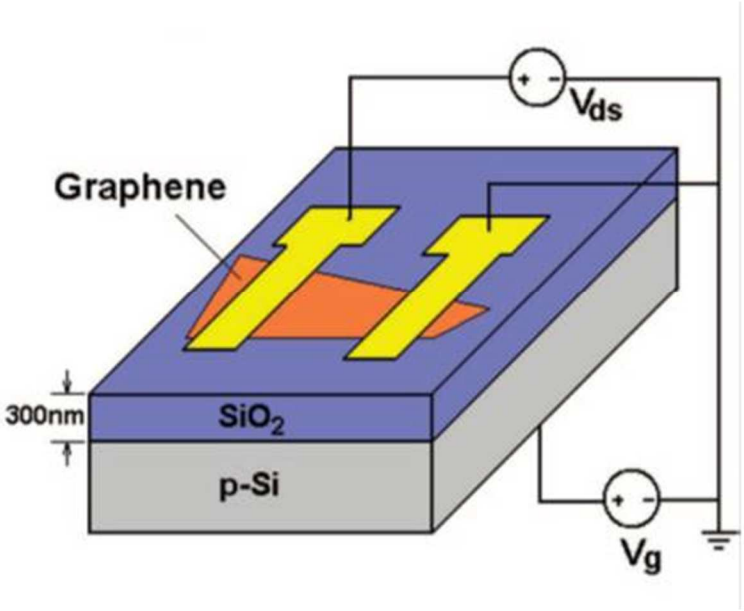

Figure 3.7: Graphene FET schematic

Transistor behavior is generally dependent on the interaction of the channel material with the applied voltages but can also heavily depend on the nanomaterial-metal contact properties. In graphene transistors at room temperature, this contact is typically reasonably Ohmic due to the high carrier concentrations in the graphene. Typical contact resistances are on the order of a

few hundred Ohms and thus the device properties are dominated by the graphene channel itself. Contact effects are more important at low temperatures or when the graphene dimensions are reduced [13]. In these cases, the number of carriers are reduced and Schottky barriers can manifest themselves at the contacts. These conditions are not present in the bulk of this work and are thus not reviewed in detail here.

Carbon nanotube FETs on the other hand can be dominated by Schottky barriers at the contacts. As shown in figure 3.8, the Fermi level of the nanotube must align with the work function of the metal contacts, resulting in bending of the conduction and valence bands at zero gate voltage [14]. This creates barriers of width w, for holes to move from the drain to the nanotube and then from the nanotube to the source. As the gate voltage is made negative, the negative charges on the back gate induce positive charges in the channel, equivalent to decreasing the Fermi energy. As the Fermi energy is fixed at the level of the metal work function, the conduction and valence bands of the nanotube are shifted further upwards. This thins the barriers for hole conduction, w, at the metal-nanotube interface. Consequently, the thermionic emission current over the Schottky barrier and the tunneling current through the barrier are both increased. As the gate voltage is made more positive, the Schottky barrier become larger and hole conduction is decreased. Eventually, electrons are induced in the nanotube channel due to increase in the Fermi energy. At very large positive gate voltages, the bands are bent in the opposite directions and electron conduction from the source to the channel to the drain becomes preferred. Similar contact effects are also observed in MoS_2 transistors. The large band gap means that Schottky barriers very similar to those discussed here for carbon nanotubes dominate conduction in MoS_2 devices.

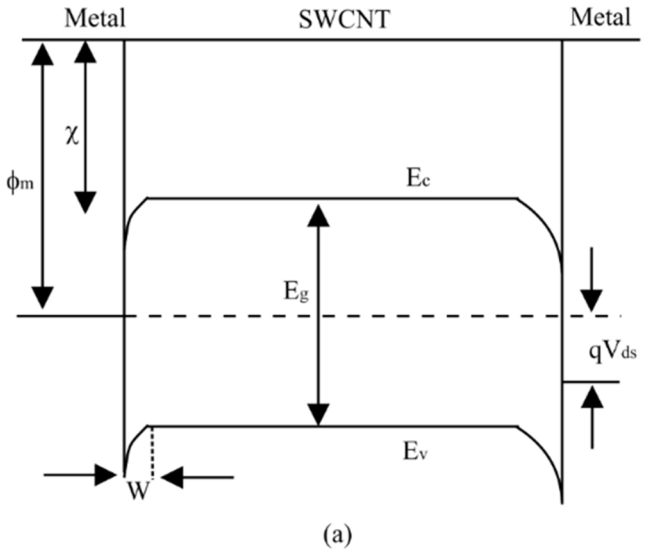

Figure 3.8: Band structure of a CNT Field Effect transistor. From [14]

In carbon nanotube devices, the height of the Schottky barriers for electrons and holes are greatly affected by the metal work function. By choosing a high (low) work function metal, primarily p-type (n-type) transistors can be fabricated. Low work function metals that have been shown to be effective in fabrication of n-type devices include scandium (3.5 eV) and erbium (3.0 eV). However, these low work function metals generally suffer from oxidation that causes transistor degradation and low device yield. More stable options are readily available for large work function metals, including gold (work function symbol = 5.1 eV), palladium (5.12 eV) and platinum (5.65 eV), all of which are stable in air and do not suffer from significant oxidation [14]. Typically, these metals and are combined with thin adhesion layers of oxidizing metals such as chromium and titanium to prevent delamination from the SiO_2 surface of the wafer. Throughout this work, Cr/Au and Ti/Pd contacts are used for optimal p-type devices unless otherwise stated.

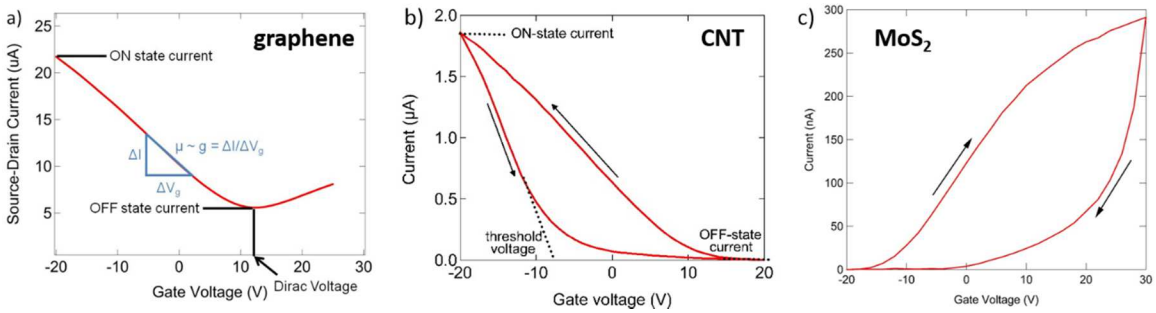

Figure 3.9: Current vs. back gate for graphene, nanotubes and MoS_2. As labelled, parameters of interest that can be extracted include the on/off state currents, the threshold/Dirac voltage and the transconductance, g, which is a critical parameter and allows the field effect carrier mobility.

Typical current vs back gate voltage (I-V_g) curves for graphene, carbon nanotube and MoS_2 transistors on 300nm SiO_2/Si wafer are shown in figure 3.8. Many parameters of interest can be extracted from these I(Vg) curves that provide information on the sample quality. For graphene, these include the Dirac voltage and hole and electron carrier mobilities. As explained in section 2.1.2, un-doped graphene should have the minimum number of carriers when no gate is applied as the density of states tends to zero at the Fermi energy. The density of states increases linearly as the Fermi level is moved away from zero by applying a back gate. Consequently, the quality of graphene transistors can be judged based on a) the shift of the Dirac point away from V_g = 0 V and b) the transistor transconductance, i.e. the slope of the curve given by $\frac{dI_{SD}}{dV_g}$. The transconductance is important for multiple reasons. Technologically, a high transconductance device requires only a small voltage to switch from the off state to the on state. Furthermore, the transconductance is also related to the carrier mobility by the equation

$$\mu_{FE} = \frac{L}{W}\frac{g}{C\,V_{DS}},$$

where L is the channel length, W is the channel width, g is the transconductance and C is the gate capacitance [15]. The FE subscript on μ_{FE} refers to the fact that this mobility is the so-called 'field effect mobility' and reflects not just the intrinsic properties of the channel material but also

the impact of any Schottky barriers or other contact resistance sources. Consequently, while the field effect mobility is often calculated and quoted for the mobility of the channel material, it typically underestimates the true intrinsic carrier mobility. The gate capacitance can be calculated by assuming a parallel-plate geometry for a two-dimensional channel material (i.e. graphene, MoS_2), i.e.

$$C = \frac{\varepsilon_r \varepsilon_0}{d}$$

where d is the dielectric thickness.

The understanding of CVD graphene growth and scalable processing methods (see sections 4.3 - 4.5) have progressed to the point that the mobility of CVD samples is comparable to exfoliated graphene samples. Consequently, field effect hole mobilities of at least 1000 cm^2/Vs are required for graphene devices to be considered of high quality. Electron mobilities are often somewhat suppressed compared to hole mobilities in devices on silicon dioxide. This is due to substrate interactions and atmospheric adsorbates that preferentially scatter electrons. Nevertheless, high quality devices have close-to-symmetric hole and electron conduction and a dramatic decrease in electron mobility is indicative of higher defect density or surface contamination. Regarding the Dirac point, unfunctionalized graphene FETs on silicon dioxide show a shift of the Dirac point to positive voltages, again due to substrate interactions and atmospheric adsorbates. Finally, we note that all devices measured in ambient show hysteresis in the $I(V_g)$, with the back-sweep curve shifted towards more positive gate voltages. This is a consequence of charge traps in the silicon oxide layer that fill during the back gate sweep, resulting in a different electrostatic environment on the return sweep [16]. A Dirac point in the range 0-30V is generally required for high quality devices. In summary, the electronic hallmarks of high quality graphene

FETs are strong hole and electron conduction, high electron and hole mobilities and a low Dirac voltages.

For carbon nanotube transistors with Cr/Au contacts, exclusively p-type conduction is observed on silicon dioxide. We can define a turn-off voltage for the transistor by drawing a tangent to the $I(V_g)$ curve at the point of greatest transconductance and extrapolating the tangent to the voltage axis. The turn-off voltage is the voltage at which the tangent crosses the gate voltage axis. Clean, defect-free semiconducting carbon nanotubes generally have turn-off voltages close to $V_g = 0$ V. Another important metric for semiconducting carbon nanotube FETs is the on/off ratio, i.e. the ratio between the maximum and minimum currents measured during a gate sweep. Individual devices can show on/off ratios as high as 10^5, but for the sparse arrays of many nanotubes used in this work, on/off ratios in the range 10^2-10^3 are more typical.

As with graphene, we can define the field effect mobility for a carbon nanotube FET by

$$\mu_{FE} = \frac{L}{W}\frac{g}{C\,V_{DS}}$$

with the only difference being the model used for the gate capacitance. For a carbon nanotube, the appropriate model is that of a conducting cylinder and a charged plate, which is given by

$C = \frac{2\pi\varepsilon_r\varepsilon_0}{\cosh\left(\frac{2h}{d}\right)}$ [17].

For individual carbon nanotubes, the field effect mobility measured is strongly channel length dependent due to the large resistance of the Schottky barriers at the contacts. For extremely long (300 μm) CVD grown carbon nanotube FETs, carrier transport is diffusive, the channel resistance dominates the transport characteristics and mobilities over 50,000 cm^2/Vs have been reported [18]. As channel lengths are shortened and devices become more contact dominated, field effect mobilities drop accordingly.

In practice, it is non-trivial to measure the mobility of devices in which the channel is made up of many carbon nanotubes as each device would have to be imaged with AFM/SEM in order to calculate the number of conducting pathways. Consequently, the metrics used to define the highest quality starting transistors in the carbon nanotube experiments presented in this work are a) resistance in the range 10-1000 kΩ, b) on/off ratio greater than 100 and c) turn-off voltage close to V_g = 0 V.

MoS_2 FETs can be characterized by the same parameters – mobility, on/off ratio and turn on voltage. As a true semiconductor with a significant bandgap, the carrier concentrations in MoS_2 are much lower than in graphene, leading to much lower conductance and lower mobility. Devices based on CVD grown material show n-type behavior with mobilities in the range 0.1-30 [19, 20]. On/off ratios as high as 10^8 have been reported [20]. The MoS_2 $I(V_g)$ shown in figure 3.8 is from a device in which interdigitated fingers are used as source and drain electrodes that are spanned by multiple CVD-grown MoS_2 flakes (for details on the growth and device fabrication, see chapter 4.9). As with graphene and carbon nanotubes, hysteresis in the $I(V_g)$ is observed and attributed to the silicon dioxide charge traps.

In bio-sensing experiments using these FETs, characteristic shifts in the parameters of the $I(V_g)$ will be used as sensing parameters. These can be Dirac point/turn-on voltage shifts, mobility changes, on-state current changes or even hysteresis changes. None of these parameters is more 'valid' than any other, but considering the type of observed shift can help to elucidate the sensing mechanism [21, 22] and understand the biochemical interactions occurring on the sensor surface. This will be done throughout the vapor (chapter 5) and solution-based (chapter 6) sensing experiments later in this work.

References

1. Dresselhaus, M.S., A. Jorio, M. Hofmann, G. Dresselhaus, et al., *Perspectives on Carbon Nanotubes and Graphene Raman Spectroscopy.* Nano Letters, 2010. **10**(3): p. 751-758.
2. Ferrari, A.C., J.C. Meyer, V. Scardaci, C. Casiraghi, et al., *Raman Spectrum of Graphene and Graphene Layers.* Physical Review Letters, 2006. **97**(18): p. 187401.
3. Malard, L.M., M.A. Pimenta, G. Dresselhaus, and M.S. Dresselhaus, *Raman spectroscopy in graphene.* Physics Reports, 2009. **473**(5–6): p. 51-87.
4. Ferrari, A.C., *Raman spectroscopy of graphene and graphite: Disorder, electron–phonon coupling, doping and nonadiabatic effects.* Solid State Communications, 2007. **143**(1–2): p. 47-57.
5. Frank, O., M. Mohr, J. Maultzsch, C. Thomsen, et al., *Raman 2D-Band Splitting in Graphene: Theory and Experiment.* ACS Nano, 2011. **5**(3): p. 2231-2239.
6. Dresselhaus, M.S., G. Dresselhaus, A. Jorio, A.G. Souza Filho, et al., *Raman spectroscopy on isolated single wall carbon nanotubes.* Carbon, 2002. **40**(12): p. 2043-2061.
7. Brown, S.D.M., A. Jorio, P. Corio, M.S. Dresselhaus, et al., *Origin of the Breit-Wigner-Fano lineshape of the tangential \textit{G} -band feature of metallic carbon nanotubes.* Physical Review B, 2001. **63**(15): p. 155414.
8. Binnig, G., C.F. Quate, and C. Gerber, *Atomic Force Microscope.* Physical Review Letters, 1986. **56**(9): p. 930-933.
9. Meyer, E., *Atomic force microscopy.* Progress in Surface Science, 1992. **41**(1): p. 3-49.
10. Cubillas, P. and M.W. Anderson, *Atomic Force Microscopy*, in *Multi Length-Scale Characterisation*. 2014, John Wiley & Sons, Ltd. p. 121-193.
11. Haider, M., H. Rose, S. Uhlemann, E. Schwan, et al., *A spherical-aberration-corrected 200 kV transmission electron microscope.* Ultramicroscopy, 1998. **75**(1): p. 53-60.
12. Rose, H.H., *Historical aspects of aberration correction.* Journal of Electron Microscopy, 2009. **58**(3): p. 77-85.
13. Li, X., X. Wang, L. Zhang, S. Lee, et al., *Chemically Derived, Ultrasmooth Graphene Nanoribbon Semiconductors.* Science, 2008. **319**(5867): p. 1229-1232.
14. Liu, W., C. Hierold, and M. Haluska, *Electrical contacts to individual SWCNTs: A review.* Beilstein J Nanotechnol, 2014. **5**: p. 2202-15.
15. Schwierz, F., *Graphene transistors.* Nat Nano, 2010. **5**(7): p. 487-496.
16. Ishigami, M., J.H. Chen, W.G. Cullen, M.S. Fuhrer, et al., *Atomic Structure of Graphene on SiO2.* Nano Letters, 2007. **7**(6): p. 1643-1648.
17. Biercuk, M., S. Ilani, C. Marcus, and P. McEuen, *Electrical Transport in Single-Wall Carbon Nanotubes*, in *Carbon Nanotubes*, A. Jorio, G. Dresselhaus, and M. Dresselhaus, Editors. 2008, Springer Berlin Heidelberg. p. 455-493.
18. Dürkop, T., S.A. Getty, E. Cobas, and M.S. Fuhrer, *Extraordinary Mobility in Semiconducting Carbon Nanotubes.* Nano Letters, 2004. **4**(1): p. 35-39.
19. George, A.S., Z. Mutlu, R. Ionescu, R.J. Wu, et al., *Wafer Scale Synthesis and High Resolution Structural Characterization of Atomically Thin MoS2 Layers.* Advanced Functional Materials, 2014. **24**(47): p. 7461-7466.
20. Wu, W., D. De, S.-C. Chang, Y. Wang, et al., *High mobility and high on/off ratio field-effect transistors based on chemical vapor deposited single-crystal MoS2 grains.* Applied Physics Letters, 2013. **102**(14): p. 142106.

21. Lerner, M.B., J.M. Resczenski, A. Amin, R.R. Johnson, et al., *Toward Quantifying the Electrostatic Transduction Mechanism in Carbon Nanotube Molecular Sensors.* Journal of the American Chemical Society, 2012. **134**(35): p. 14318-14321.
22. Heller, I., A.M. Janssens, J. Männik, E.D. Minot, et al., *Identifying the Mechanism of Biosensing with Carbon Nanotube Transistors.* Nano Letters, 2008. **8**(2): p. 591-595.

CHAPTER 4: Growth and Device Fabrication

High quality nanomaterials, grown via scalable techniques, are critical to advancing nano-bio hybrid technologies beyond one-off devices. In this chapter, we discuss the growth methods used to synthesize large area graphene, carbon nanotube, molybdenum disulfide (MoS_2) and boron nitride samples. Beyond supplying material for applications, we are interested in understanding and controlling the growth processes to understand the relevant growth parameters and how they affect the quality of the material that is grown. To this end, we also perform fundamental studies of the synthesis processes and the resulting materials.

In section 4.1, we outline the growth recipe used to grow single-wall carbon nanotubes by CVD and in section 4.2 we outline the procedures used to deposit nanotubes from solution, using commercially sourced semiconducting-enriched nanotube solutions. Section 4.3 gives an overview of CVD graphene growth at low pressure and sections 4.5 and 4.5 outline the procedures developed for transferring the graphene off the growth substrate and patterning it via photolithography while avoiding direct contact of the photoresists and the graphene surface.

Section 4.6 explains the growth method used for CVD boron nitride, which is used in section 4.7 as a substrate material for graphene electronics with markedly improved performance. In section 4.8, we demonstrate growth of boron nitride directly around a just-grown hexagonal graphene flake, resulting in atomically-stitched graphene-boron nitride in-plane heterostructures with crystallographically terminated edges. In section 4.9, we discuss the CVD synthesis of triangular crystals of monolayer MoS_2 using solid sulfur and dried droplets of ammonium heptamolybdate as precursors. We wrap up the growth section of this thesis with section 4.10 in which we discuss a technique for growing MoS_2 in desired locations by patterning

the growth substrate with beads of molybdenum precursor material that act as both the molybdenum feedstock and a seed location for crystal growth.

4.1 Carbon Nanotube Growth

Carbon nanotubes can be grown using a variety of methods including arc discharge, laser ablation and chemical vapor deposition. The arc discharge method, used by Sumio Ijima in 1991 that brought carbon nanotubes widespread international attention [1], involves application of a large arc voltage between two graphite electrodes in an inert gas environment. The cathode is pure graphite, while the anode includes a metal catalyst such as iron or cobalt that is responsible for preferential growth of single all carbon nanotubes over fullerenes or other carbon structures. In laser ablation growth of carbon nanotubes, a high-power laser is used to vaporize material from a graphite target at high temperature inside a growth reactor [2]. As with arc discharge, metal catalyst particles are included to promote synthesis of single wall nanotubes.

Arc discharge is a comparatively simple process, but the yield of carbon nanotubes is typically only 30% by weight. Laser ablation, on the other hand, can be optimized to yield up to 90% long single wall carbon nanotubes with a very tight diameter distribution (1.0-1.6 nm). However, it is comparatively costly and complex.

Chemical vapor deposition (CVD) has become the most widely used technique for carbon nanotube growth. It is a scalable technique that produces a high yield of nanotube material and, importantly, the carbon nanotubes can be grown directly on an oxidized silicon substrate, which is very convenient for device fabrication. In CVD, metal ion particles are deposited onto a wafer which is heated in a tube furnace in a methane/hydrogen/argon environment. Typical growth occurs at 900 °C, where the methane breaks down and the carbon is absorbed by the metal nanoparticles. Carbon is continuously absorbed and ejected from the nanoparticle and the ejected carbon precipitates into a carbon nanotube with a diameter approximately equal to the

diameter of the nanoparticle. If the process is well-controlled, the resulting carbon nanotubes are almost exclusively single-walled and have low defect densities [3].

The recipe used for CVD growth of carbon nanotubes in the Johnson group is given in detail in Appendix A.

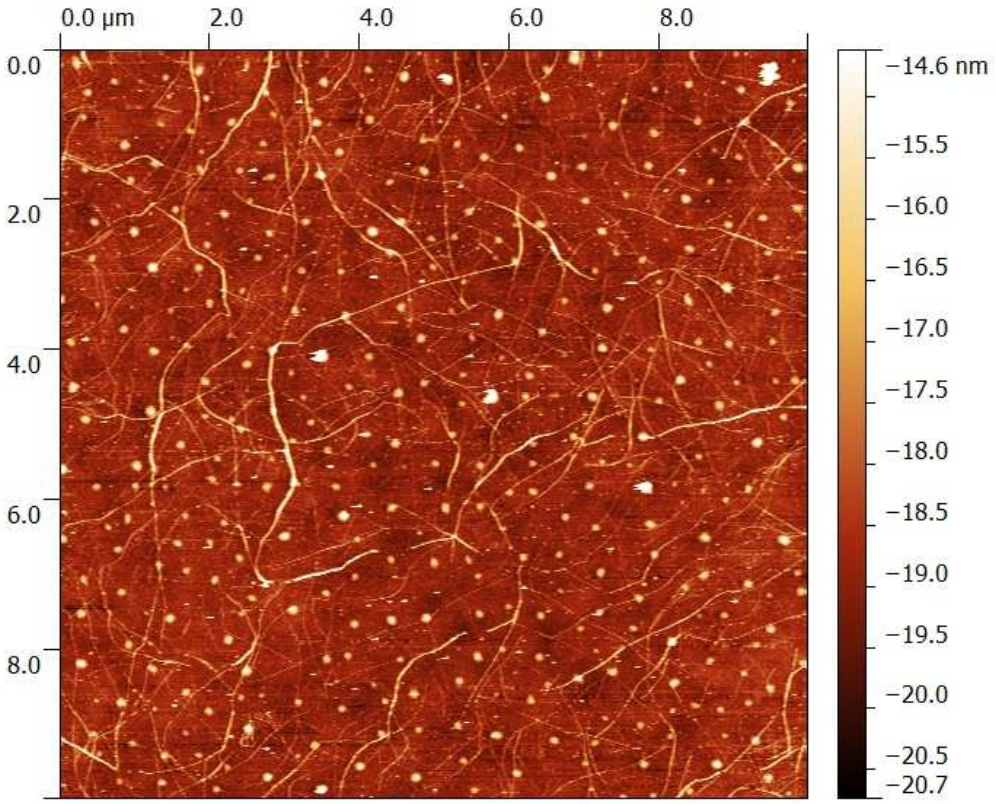

Figure 4.1: A network of CVD nanotubes. Catalyst particles are uniformly spread across the wafer and result in dense growth. Nanotube density can be reduced by reducing catalyst concentration.

Fig. 4.1 shows an AFM image of carbon nanotubes we grew by CVD. In this case, the catalyst concentration was 10mg/L resulting in a network of a carbon nanotubes. As is typical for growth using the above recipe, individual nanotubes are a few microns long. Many of the nanotubes are approximately 1 nm in diameter. As the growth is performed at high catalyst density, a significant number of catalyst particles are visible on the substrate. These should not

significantly affect the device quality. This material is then processed into devices using a bilayer photolithography process [4].

The significant downside of these devices is that, as explained in chapter 2.2, one third of the nanotubes grown in a process such as the one just described are metallic. Consequently, networks such as the one shown in fig. 4.1 typically contain a non-negligible fraction of metallic nanotubes that cannot be turned off in the final FET device and thus the on/off ratio of the device suffers. As the catalyst density is lowered, fewer devices will show metallic behavior but an increasing number will be disconnected completely. Consequently, the yield of devices that show semiconducting behavior is limited to $\sim$ 20%.

4.2 Semi-conducting Enriched Carbon Nanotube FETs

Sufficient control over the growth process to grow only semiconducting chiralities is a goal that has yet to be accomplished. As a result, the carbon nanotube devices used for the chem/biosensing experiments in chapters 5 and 6 are not fabricated using nanotubes grown directly onto the wafer by CVD. Instead, those devices take advantage of advances in the sorting of CVD grown carbon nanotubes [5]. Specifically, the devices are fabricated using a carbon nanotube suspension from NanoIntegris Inc. These carbon nanotubes have been grown in large quantity by CVD, harvested from their growth substrate, suspended in solution. Being hollow tubes of varying diameters, the carbon nanotube mixture can then be separated by density gradient ultracentrifugation, in which the solution is spun in a centrifuge at 200,000 rpm for several days. The solution separates into bands by nanotube diameter and selecting particular bands yields solution that is highly enriched with particular nanotube chiralities [5]. The result is a highly semiconducting enriched (typically 98%) nanotube solution that consists of only carbon nanotubes in water soluble surfactants, as shown in fig. 4.2.

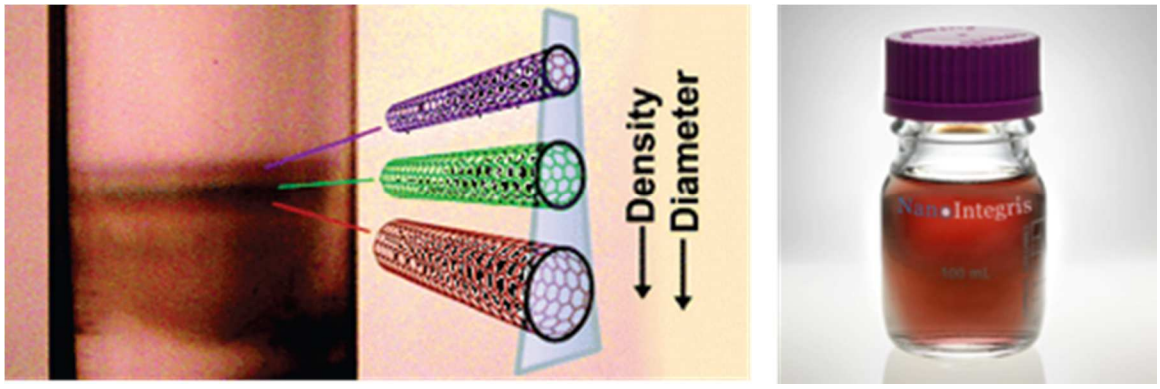

Figure 4.2: Density gradient ultracentrifugtion is used to separate as-grown CVD carbon nanotubes, allowing production of highly semiconducting-enriched carbon nanotube solutions. These are commercially available from suppliers including NanoIntegris Inc.

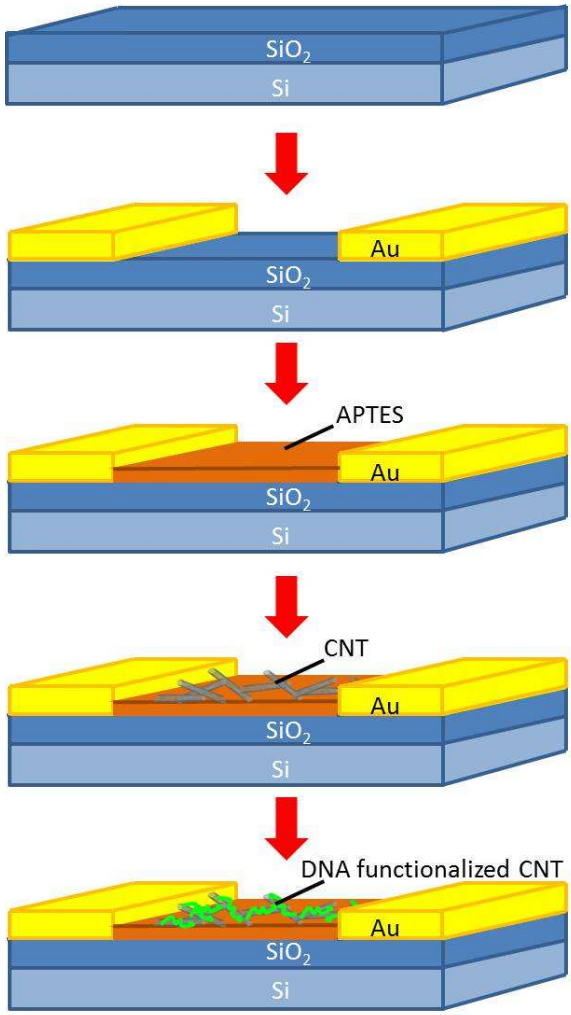

Figure 4.3: Schematic of carbon nanotube deposition from solution. The adhesion layer can be either a self-assembled monolayer such as APTES (3-aminopropyltriethoxysilane) or a hydrophobic dielectric such as Al_2O_3.

Figure 4.3 shows a schematic of how the carbon nanotubes are then deposited from solution on to prefabricated electrodes. The electrodes are pre-patterned using standard photolithography, metal evaporation and lift-off techniques, after which the surface oxide is treated with (3-Aminopropyl)triethoxysilane (APTES). APTES is a silane that binds to the surface oxide and increases the adhesion of carbon nanotubes by leaving amine groups on the substrate. This can be done using wet chemistry techniques, but in this work APTES is condensed from vapor inside an ALD chamber, which was found to be more reproducible. Deposition in an ALD chamber

is also a natural fit as APTES is routinely used as a precursor in the growth of silicon oxide via ALD. The carbon nanotube solution is then pipetted onto the chip surface and kept in a humid environment for 20 minutes to prevent any evaporation while the nanotubes adhere to the surface.

Rather than picking the chips up and moving them to a solvent bath, the crystalizing dish in which the chips are sitting is flooded with approximately 100 mL of isopropanol, which dilutes the concentration of the carbon nanotube solution and washes off the majority of the unbound nanotubes. This was found to be a more uniform and reproducible technique that moving the chips into a solvent bath, which was found to be prone to surface tension effects that resulted in bands of nanotubes and regions of sparse coverage. Indeed, this surface tension effect has been used by other researchers to deliberately induce dense bands of aligned nanotubes. After gently agitating the flooded isopropanol bath for 15 minutes, the chips were moved into a pure isopropanol bath for 5 minutes and finally to a DI water bath for 5 minutes that washed the surfactants off the bound nanotubes, leaving pristine, highly semiconducting-enriched nanotubes uniformly distributed across the surface, linking the prefabricated metal electrodes. A hot plate bake at 170 °C for an hour, which improves the nanotube-metal contacts, rounds out the fabrication procedure. One alternative to the method presented here is to replace the APTES layer with a 15nm thick layer of Al_2O_3, which is deposited before the metal electrodes. Both surfaces bind carbon nanotubes sufficiently well to make devices. Al_2O_3 is used in the later experiments presented in this thesis as the transistor properties (transconductance, on-off ratio) are improved. The typical nanotube density used in the experiments in this thesis is shown via AFM in figure 4.4.

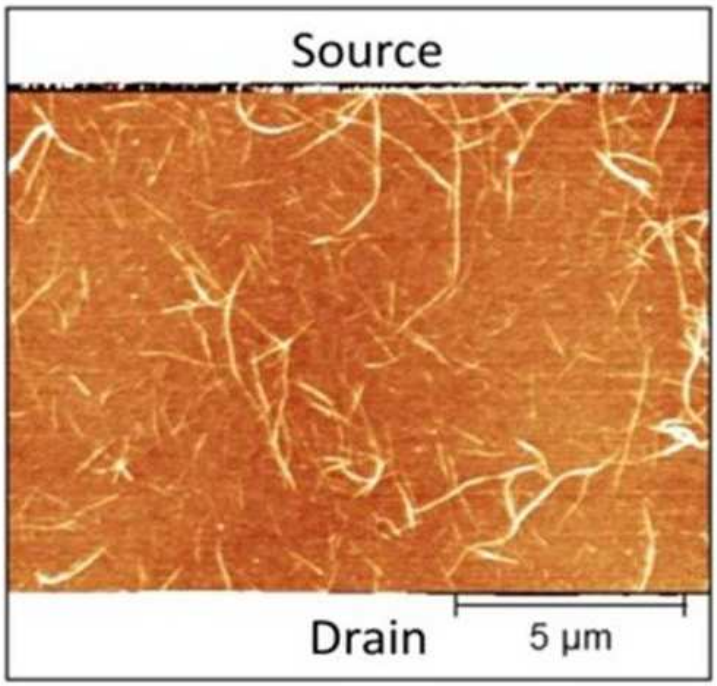

Figure 4.4: AFM taken between source and drain electrodes after nanotube deposition. Nanotubes are 0.5-1.5 nm in diameter.

The mechanism by which these layers bind carbon nanotubes is still open to debate. For APTES, proposed mechanisms include that the lone pair electrons on the nitrogen atom could noncovalently bind to the nanotube sidewall and donate electron density, which would produce significant physisorption binding energies [6, 7]. Another plausible interaction is a charged interaction between positive charges in the amine groups (NH_3) and charged groups on the carbon nanotube, such as carboxyl defects at the ends of the nanotube [8]. As for Al_2O_3, the hydrophobic nature of the surface may be sufficient to drive the carbon nanotubes out of solution and onto the surface. This is reinforced by the fact that carbon nanotubes do not adhere at all to bare silicon dioxide, a hydrophilic surface.

4.3 CVD Graphene Growth

Single and few-layer graphene was first isolated by Andre Geim and collaborators using a manual exfoliation technique [9], where adhesive tape was used to separate layers in graphite and transfer them to an insulating substrate such as silicon oxide. An optical interference effect means that even though the material is atomically thick, micrometer scale monolayer regions can be found using an optical microscope and contacted using electron beam lithography. The resulting devices demonstrated the promise of graphene for a variety of electronic applications, including gigahertz transistors [10], solar cells [11] and vapor sensors [12].

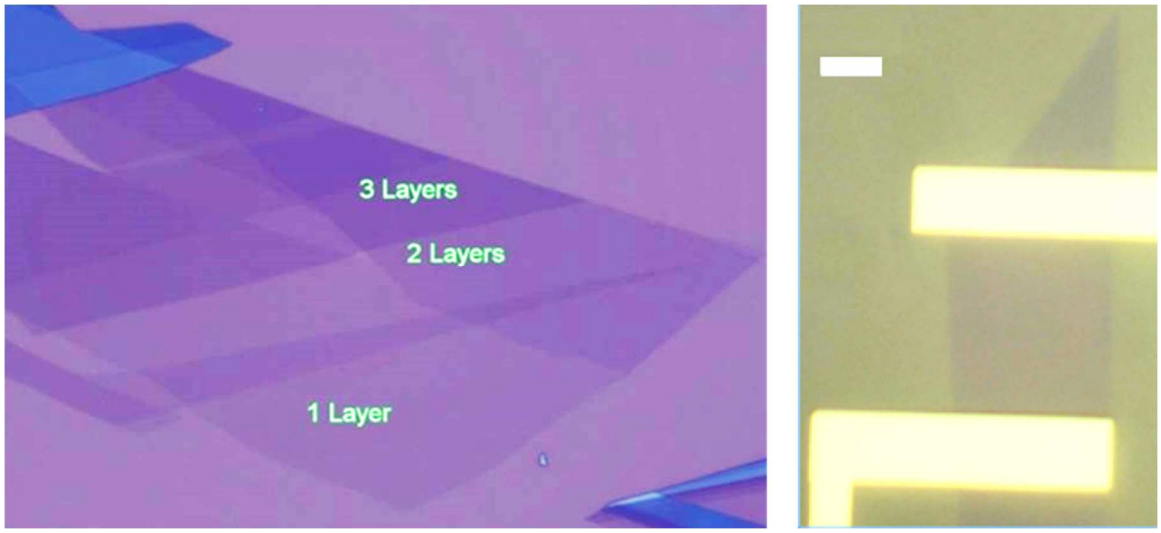

Figure 4.5: Exfoliated graphene. Color contrast can be used to distinguish monolayer, bilayer and trilayer regions. Devices can be made from micrometer-scale single layer flakes using electron beam lithography. Scale bar is 1 µm.

While exfoliated samples provide the highest quality material and are well suited for investigating fundamental physical phenomena, scalable graphene synthesis is critical for technological development. The development of CVD growth of monolayer graphene on copper foil [13] provided the breakthrough necessary to make that transition. In this process, copper foil is loaded into a tube furnace and heated to approximately 1020 °C. The growth can be done at ambient pressure in inert gas or at low pressure (typically ~ 1 Torr). In both cases, methane gas is

used as the carbon feedstock. Methane adsorbs onto the copper surface, the hydrogen atoms dissociate and form H_2 gas molecules that leave the reaction chamber. The reactive carbon radicals diffuse across the copper surface and form polycyclic hydrocarbon structures, i.e. nanoscale graphene islands, whose reactive edges serve as nucleation sites for further graphene growth [14]. As the solubility of carbon in copper is extremely low, the carbon remains on the foil surface and does not diffuse into the bulk. Hydrogen gas is also flowed into the chamber and the ratio of hydrogen and methane flows is one of the main factors in determining the graphene growth rate. The hydrogen is necessary in order to etch away carbon atoms that are not sp^2 bonded and are thus preferentially etched. Other factors that impact the growth include temperature, copper grain size, copper surface roughness and surface contamination. This is because graphene nucleates preferentially at defect sites including copper grain boundaries, adatoms, or surface contaminants. Indeed, deliberate placement of surface contaminants can be used to pattern graphene growth [15]. As the copper foil plays a catalytic role in the graphene growth, the growth is self-terminating upon complete coverage of the foil and > 95% monolayer coverage of the foil is routinely achieved. Multilayer graphene growth can be achieved using nickel foil as the high temperature solubility is larger. As the foil cools, the carbon precipitates out, forming multiple layers of graphene [16, 17].

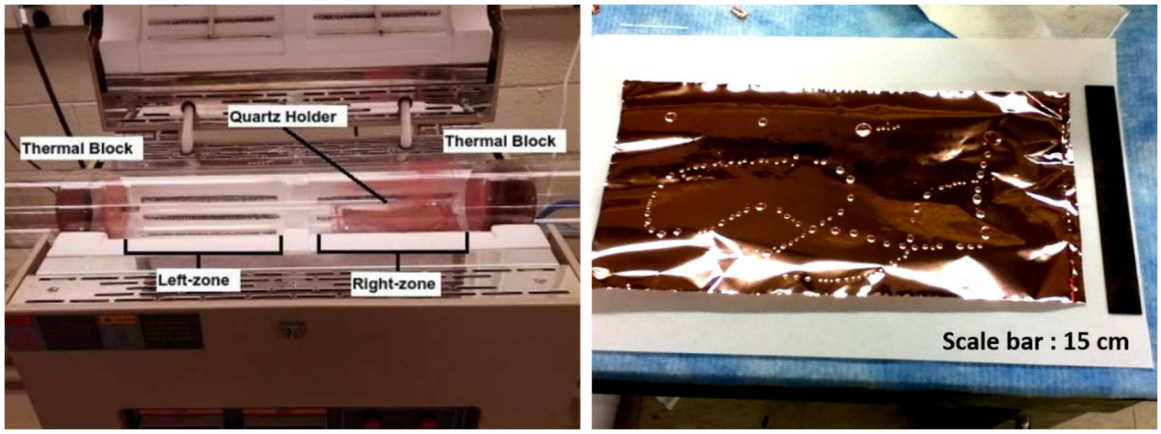

Figure 4.6: Graphene growth furnace with foil of a quartz holder, between thermal bocks. The foil becomes hydrophobic after growth due to the graphene layer on top.

The graphene samples used in this work were grown at low pressure in a 4" clamshell-type furnace. The furnace is on rails that allow the heating element to be slid left and right with respect to the quartz tube. The most critical growth parameters are the pressure (~ 1 Torr), gas flows (80 sccm H_2, 40 sccm CH_4), temperature (1020 °C), duration of growth (60 minutes). The copper foil growth substrate is cleaned thoroughly and pre-annealed at 1020 °C for 40 minutes in just H_2 to increase the copper grain size. After growth, the furnace was cracked open about 1" and slid to the left, exposing the quartz tube and rapidly cooling the sample. The full recipe used for graphene growth is detailed in Appendix B.

4.4 Electrochemical 'Bubble' Transfer Technique

After growth, graphene must be transferred off the copper foil growth substrate and onto an insulating substrate, typically a silicon wafer. In early research on CVD graphene, a polymer layer was typically spun on top of the graphene/foil, after which the sample was floated in a bath of iron chloride, a copper etchant, to dissolve the copper from the back side. After the copper was all etched, the graphene would remain stuck to the polymer support. The sample could then be transferred to a water bath for cleaning and finally scooped onto a target substrate. After drying out the polymer/graphene film, the polymer could then be removed using solvents, leaving the graphene adhered to the new substrate. The downsides of this method include that the etch rate of copper is quite slow and that the final graphene film is decorated with a significant number of iron particles from the etchant.

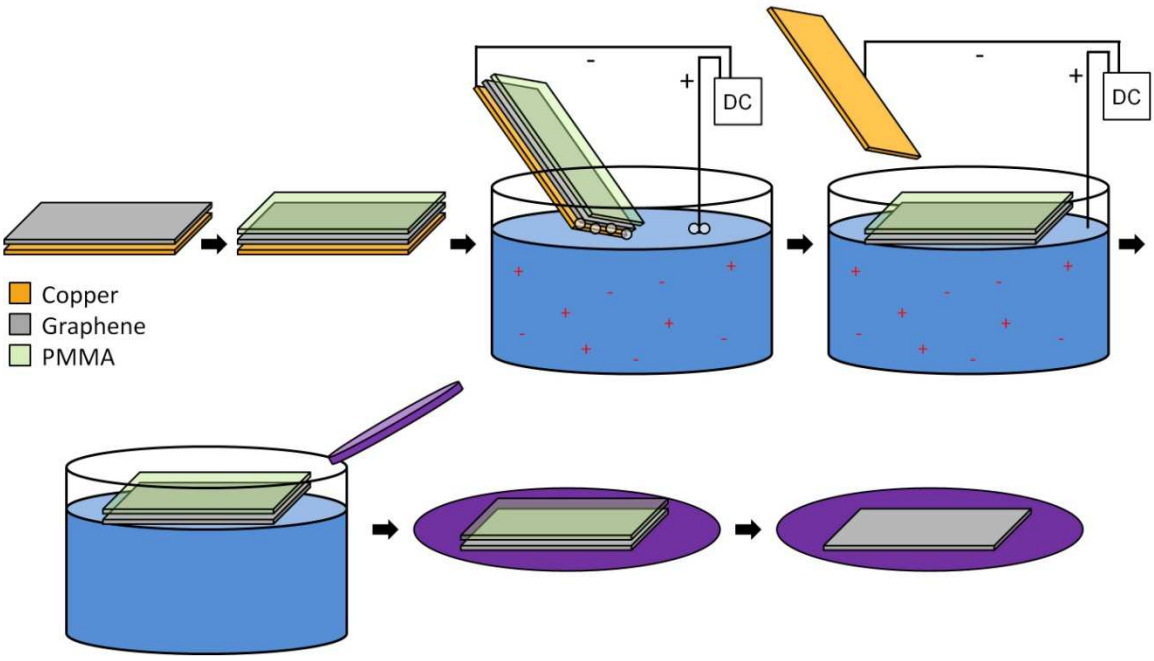

Figure 4.7: Electrochemical graphene transfer technique. Hydrogen bubbles mechanically push the graphene and its PMMA support away from the copper foil, releasing it to float on the bath.

As a consequence of these drawbacks, an electrochemical transfer technique is used instead, shown schematically in figure 4.7. As with the iron chloride etch technique, a PMMA polymer support is spin coated onto the copper foil. A DC voltage (20V) is then applied between the polymer/graphene/copper sandwich and a counter electrode. The counter electrode is placed into a 0.1 M sodium hydroxide solution, and the polymer/graphene/copper sandwich is then slowly slid into the solution. Na^+, H^+ and OH^- ions then conduct through the solution and form O_2 and H_2 bubbles at the metal electrodes, i.e. the counter electrode and the exposed edge of the copper foil. The bubbles on the copper mechanically separate the PMMA layer from the copper foil. As the adhesion of the graphene to the PMMA is larger than the adhesion to the copper, the graphene is displaced from the foil and floats on the underside of the PMMA film in the sodium hydroxide bath. As the polymer/graphene/copper sandwich is slid further into the bath, more of the PMMA/graphene is released from the foil until finally the entire PMMA/graphene film is floating on the bath and the copper foil can be pulled out.

A rigid support, typically a polyethylene terephthalate sheet, is used to lift the floating PMMA/graphene structure out of the sodium hydroxide bath and then release it into a water bath to wash off ionic residues. After moving through a series of water baths, the sample is scooped onto the target substrate, typically a Si/SiO_2 wafer and blown dry with nitrogen. A baking step (e.g. 100 °C for 2 minutes) is typically used to increase the adhesion to the surface. Finally, the PMMA layer is dissolved by gently spraying at it with acetone for 2 minutes, and the surface is rinsed with acetone before blowing dry with nitrogen. Polymer residue can be removed by soaking in acetone for 12 hours or by annealing at 200 °C in Ar/H_2. The final sample consists of a clean, high quality monolayer graphene film on 300nm of dielectric, ready for patterning and device fabrication.

4.5 Clean Photolithographic Processing of Graphene

Photolithography would be an ideal processing technique for patterning graphene devices due to its scalability and established industrial presence. However, photoresist patterning on graphene has been shown to leave behind residues that contaminate the graphene surface [18, 19]. Although effective methods based on annealing have been identified to remove residues associated with electron-beam lithography [12, 20-22], most photoresists are based on novolac resins, whose high aromatic content is expected to give them much higher affinity for the graphene surface. This is problematic since a pristine surface is critical to applications where functionalization chemistries are to be carried out on the graphene to target its chemical interactions. Further, surface contamination reduces the carrier mobility of the graphene and provides unintended, uncontrolled doping [18]. This has driven interest in non-lithographic fabrication of graphene device arrays based on patterned growth [23] and dielectrophoretic assembly of graphene flakes [24, 25]. Lithographic processes have incorporated novel cleaning methods, including modified-RCA procedures [26] and even cleaning by contact-mode Atomic Force Microscopy [27]. However, these methods either require fine control of volatile chemical reactions to produce high quality graphene devices or lacked scalability.

Our approach to overcoming the issues is to modify standard photolithography to prevent contact of the photoresists with the graphene. To this end, a 20 nm layer of gold was deposited to protect the graphene from subsequent processing. A first round of bi-layer (PMGI/S1813) photolithography [4] was used to define the channel region, exposing the surrounding gold and graphene. The exposed gold was removed by wet etching (1:9 Gold etchant TFA (iodine/potassium iodide complex): deionized water) and the now-exposed graphene was removed using oxygen plasma (300 mTorr, 50W, 1 min). After liftoff of the resist on top of the

channel, a second round of photolithography was used to contact the channel region with Ti/Pd contacts. Finally, gold on top of the channel was removed by wet etching with TFA as described above, leaving pristine graphene with Au/Ti/Pd contacts, connected to large Ti/Pd features. This method ensured that the graphene channel was free of photoresist residue contamination. Any gold etchant or PMMA residue on the graphene was removed by first annealing at atmospheric pressure at 200 °C for 1 hour in an Ar/H2 environment and then soaking the sample in acetone for 5 hours.

4.6 Boron Nitride Growth

Similar to graphene, single layer boron nitride is grown on copper foil. Unlike graphene growth, boron nitride is grown at atmospheric pressure and uses a solid precursor, ammonia borane. Ammonia borane powder is pressed into cylindrical pellets weighing approximately 5 mg. In a 1" furnace, copper foil is annealed in Ar/H_2, after which the ammonia borane precursor is moved closer to the furnace inside the quartz tube using a magnetic holder, as shown in figure 4.8. The ammonia borane sublimates and nucleation of monolayer boron nitride domains on the copper foil occurs. Growth proceeds for a few minutes, after which the precursor is moved away from the furnace to halt sublimation. The quartz tube is slid to the side to rapidly cool the copper foil, which is now covered in a monolayer of hexagonal boron nitride. The detailed growth recipe for the material used in this work is given in Appendix C.

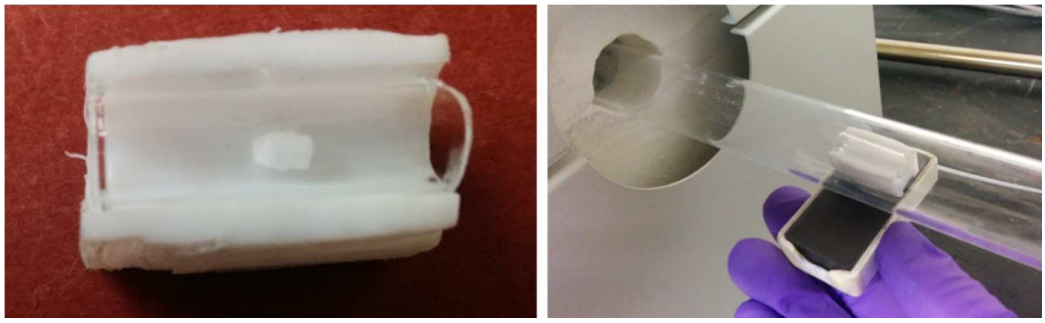

Figure 4.8: A solid boron nitride precursor, ammonia borane, is placed into a custom made Teflon holder with metallic bottom plate, to allow it to be maneuvered inside the quartz tube during the growth using a magnet.

The resulting boron nitride monolayer can be transferred off of the copper foil and onto a silicon wafer using the electrochemical 'bubbling' transfer technique described in detail in chapter 4.4. The optical contrast of a monolayer of boron nitride is much weaker than that of graphene. Figure 4.9a shows a uniform, monolayer boron nitride sample, fabricated using the process just described. As described in section 2.3, boron nitride is an ideal substrate material for graphene electronics. However, in order to completely screen the underlying substrate, multiple

boron nitride sheets are required. One approach is to grow thicker boron nitride films by replacing the copper growth surface with nickel, which yields thin films 5-50 nm in thickness [28]. Another approach is to stack high quality monolayers of boron nitride to build up a substrate with an exactly controlled number of layers. The result is shown in figure 4.9b and the process used to fabricate this sample and incorporate it as a graphene substrate are explored in detail in section 4.7.

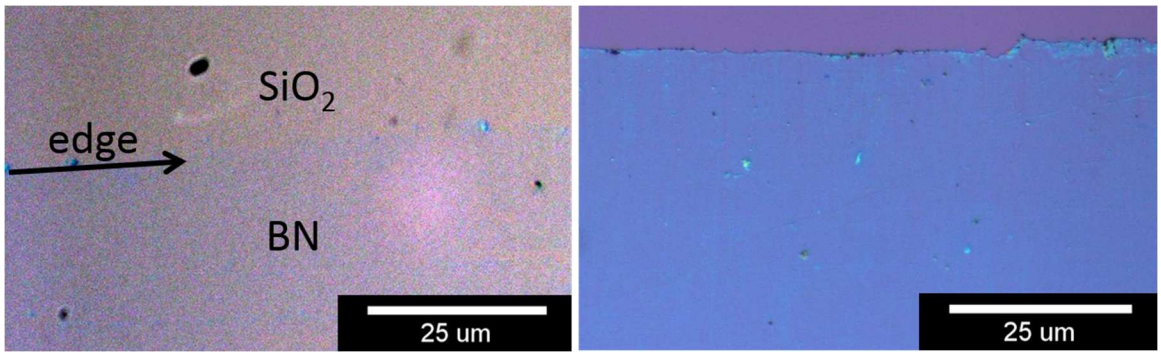

Figure 4.9: Mono- and five-layer boron nitride films. The five layer film is made by successive stacking of individual monolayers, as described in section 4.7.

4.7 Stacked CVD Boron Nitride as a Substrate for CVD Graphene Electronics

The results presented in this section have also appeared in the publication "Electronic Transport in Heterostructures of Chemical Vapor Deposited Graphene and Hexagonal Boron Nitride", Z. J. Qi, S. J. Hong, J. A. Rodriguez-Manzo, N. J. Kybert, R. Gudibande, M. Drndic, Y. W. Park, A. T. C. Johnson, *Small*, 2014, doi: 10.1002/smll.201402543

Graphene is a candidate material for an array of nanoelectronic applications, due to its favorable physical properties, including superior carrier mobility[29, 30][1,2] and thermal conductivity [31, 32], high current breakdown density [33, 34], and compatibility with integrated circuit (IC) fabrication [35, 36]. Progress in wafer-scale growth of highly crystalline graphene films provides a potential route towards commercialization of high-quality graphene-based electronics [37, 38]. However, carrier transport in graphene is often significantly degraded by surface charge traps and impurities [39-41], roughness due to the substrate [42] or intrinsic graphene rippling [43], and charged vibrational modes [44] associated with commonly used SiO2 substrates. Extrinsic carrier scattering by substrate phonons limits graphene's room temperature mobility to ca. 40,000 cm^2/Vs, significantly reduced compared to the intrinsic mobility in excess of 200,000 cm^2/Vs that is expected due to acoustic phonon scattering alone [45]. The constraining effects of SiO2 drive interest in substrate engineering, specifically the introduction of hexagonal boron nitride (hBN) dielectrics to improve graphene performance. Due to its robust, planar, and predominantly covalent bonding, hBN is expected to be atomically smooth, free of dangling bonds and charge traps, and chemically inert, with a bandgap of 5.97 eV and a slight $\sim$1.7% lattice mismatch to graphene [46]. Dean et al. used exfoliated films for the first demonstration of significant enhancement of graphene-hBN heterostructures, reporting carrier mobilities of 60,000

cm^2/Vs – three times larger than similar devices on SiO_2 [47]. Chemical vapor deposited (CVD) graphene has also been characterized on exfoliated hBN layers, with room temperature mobilities in excess of 14,000 cm^2/Vs [48, 49]. However, exfoliation is not a scalable process, so there remains a need to introduce a platform that allows for substrate engineering at the wafer-scale.

Recently, CVD growth of hBN has been demonstrated [50-52] providing a route towards scalable, large-area fabrication of graphene-hBN heterostructure devices. In this work, we provide a systematic study to inform practical design considerations for hBN integration and report record low- and high-field transport in CVD-grown graphene-hBN heterostructure devices. A novel methodology was used to minimize the presence of contaminants in between layers of the graphene-hBN stack, allowing for continuous sheets of CVD-grown monolayer hBN to be consecutively stacked beneath CVD-grown monolayer graphene in intimate contact. The crystallographic orientation between the 2D materials is also controllable, allowing for well-defined stacking orientation and material thickness, advancing beyond previous methods [51, 52]. High-vacuum current-annealing was utilized to lower the contact resistivity and vaporize surface contaminants from the fabrication process of CVD graphene-hBN heterostructures, resulting in hole and electron mobility values in excess of 8,000 cm^2/Vs, more than twice that of previous reports [51, 52]. Finally, improved high-temperature (power dissipation) and high-bias (breakdown current density) performance were observed in graphene-hBN heterostructures and attributed to the effect of the 200 times greater thermal conductivity of five-layer hBN as compared to a SiO2 substrate [53] and the higher energy optical phonon modes [47].

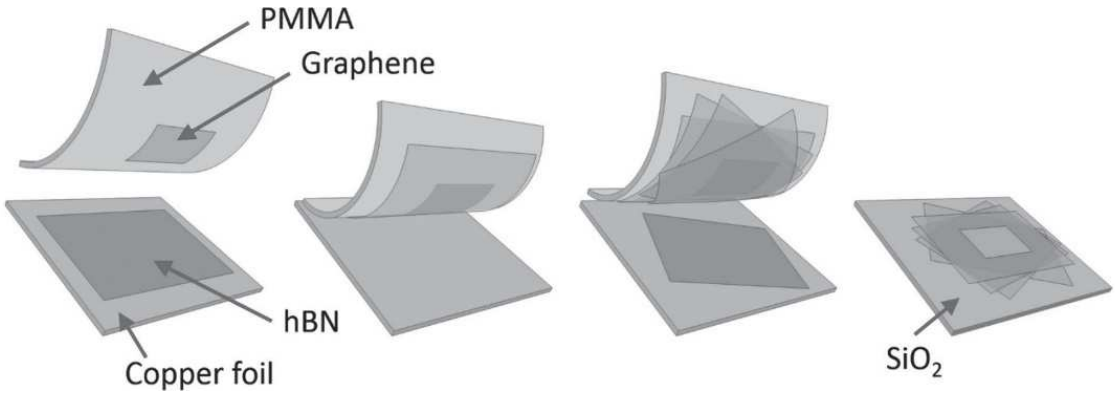

Figure 4.10: Schematic of the low-contamination process for graphene-hBN stacking and transfer.

Fig. 4.10 is a schematic of the fabrication process, which is based on transferring and stacking of monolayer materials using a single PMMA resist scaffold to minimize contamination, similar to a recent report [54]. Device fabrication began with separating monolayer graphene from its copper growth substrate using a PMMA layer for mechanical support. Metal nanoparticle contamination introduced during etching of the growth substrate was avoided by utilizing the bubbling transfer method described in section 4.4. The PMMA-graphene stack was subsequently cleaned in multiple deionized water baths and transferred directly onto a sample of monolayer hBN grown by CVD on a catalytic copper substrate, with the goal of preventing the introduction of unwanted contaminants (e.g., resist residue) between the graphene and hBN. This process was repeated until the graphene was supported by five hBN layers. We note that this transfer process allows for layer-by-layer control of the heterostructure thickness and could be utilized to define twist angles between crystalline 2D materials by orienting known edge structures (crystallographic orientation) of single flakes with micromanipulators under an optical microscope [47] (i.e. zig-zag edged hexagonal graphene [55], Sulfur-terminated MoS2 [56] and others), advancing beyond previous methods [54]. A final transfer to a SiO2/Si substrate and removal of the PMMA scaffold using acetone left the desired graphene-hBN heterostructure for patterning

into device structures. Electron beam lithography (EBL) was used to pattern 1-µm wide electrodes in the transfer length method (TLM) configuration [57] with channel separations ranging from 500 nm to 6 µm. A 3 µm-wide graphene ribbon was defined via a second round of EBL followed by oxygen plasma etching (see Figure S1 in the Supplementary Information). Fabrication of graphene devices on SiO2 for TLM measurements followed the same lithographic process flow.

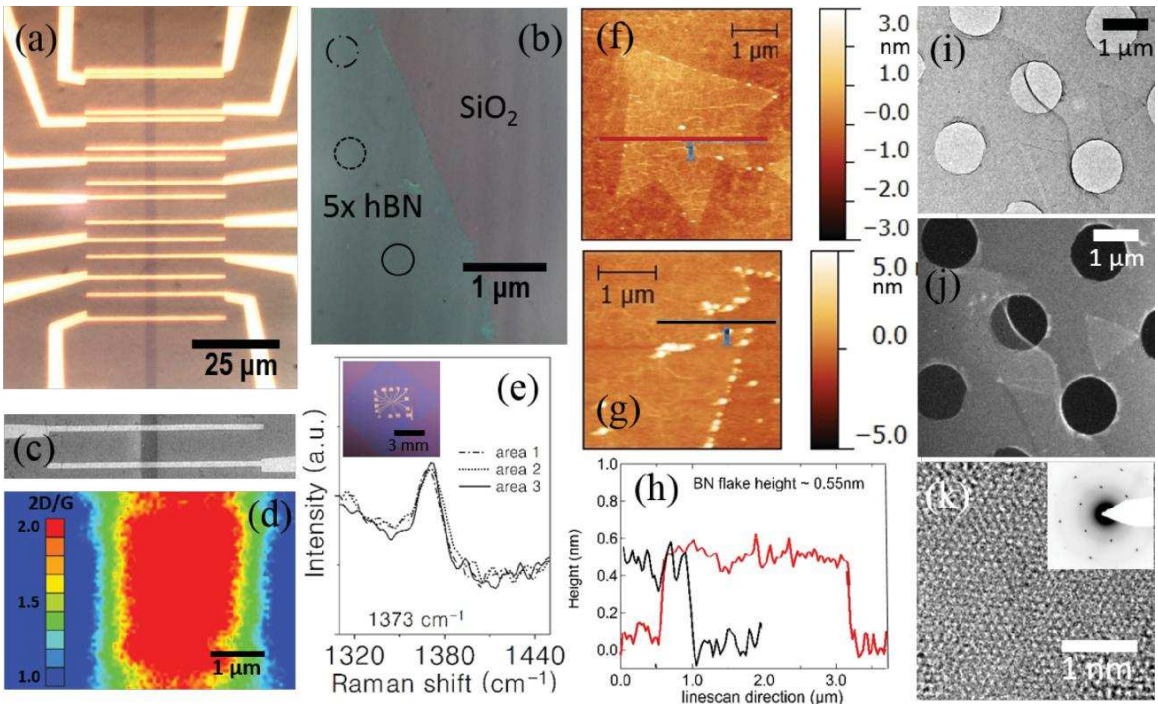

Figure 4.11: Characterization of CVD graphene/hBN and fabricated devices. (a) Optical micrograph of a 3-µm wide graphene ribbon contacted in the TLM configuration. (b) Optical micrograph of five-layer CVD hBN on SiO_2, with no graphene layer. Raman spectra from the three circled regions are presented in panel (e). (c) SEM image of a 3-µm graphene ribbon contacted by source and drain electrodes. (d) Raman map (2D/G ratio) of the channel region of a graphene ribbon. (e) Three Raman spectra of five-layer CVD hBN taken from the three areas circled in panel (b). All spectra show the peak centered near 1373 cm^{-1}, which is characteristic of monolayer hBN. Inset: Optical micrograph of patterned CVD graphene devices supported by a five-layer CVD hBN stack (appears darker as compared to SiO_2). (f) AFM image of a CVD hBN flake on SiO_2. (g) AFM edge morphology of a CVD hBN large-are sheet on SiO_2. (h) Corresponding height profile as extracted from line scans in (f) and (g). The observed step height of approximately 0.5 nm confirms that the sample is a monolayer. (i) Bright-field TEM image of CVD hBN showing a very clean surface. (j) Dark-field TEM image of (i) shows single crystal domains with size ca. 1 µm. (k) High resolution TEM image showing atomically pristine monolayer hBN. Inset: Electron diffraction showing six-fold intensity peaks in monolayer hBN.

Microscopic characterization of finished devices is presented in fig. 11. Figure 4.11a is an optical micrograph of a 3-μm wide graphene ribbon on an oxidized silicon substrate, contacted in the TLM configuration. SEM micrographs indicated that the dimensions of the TLM channels were consistent with the design pattern (fig. 4.11c). Raman maps of device channels on SiO2 were consistent with expectations for high-quality monolayer graphene, with 2D/G ratios consistently ∼2 (fig. 4.11d) [58-60]. An optical micrograph of a five-layer hBN stack (without graphene) on a 300 nm SiO2 substrate is shown in fig. 4.11b. A design based on five layers of hBN was specifically chosen to effectively screen graphene carriers from dangling bonds associated with the oxide and to provide an atomically smooth surface (roughness <100pm) [47]. Furthermore, a stack of five layers of BN has been shown to provide sufficient insulation from oxide charge traps (> 1 GΩ) [61]. Fig. 4.11e shows corresponding Raman spectra from three distinct regions highlighted by circles in fig. 4.11b. The peak at 1373 cm^{-1} is representative of hBN and demonstrates uniform coverage of the hBN across the transferred area, consistent with our past report [50]. Atomic force microscopy (AFM) analysis of CVD-grown hBN flakes (fig. 4.11f) and sheets (fig. 4.11g) transferred on SiO2 shows clean, monolayer hBN with triangular domains ∼1 μm in size, low surface roughness, and a layer thickness of ∼0.5 nm (fig. 4.11h). Interestingly, fig. 4.11g provides evidence that contaminant material is attracted to the edge of hBN monolayer sheets. We further characterized the hBN with aberration-corrected transmission electron microscopy (AC-TEM). For TEM analysis, hBN samples were transferred onto an amorphous carbon grid with 1-μm holes (fig. 4.11i). Consistent crystal orientation was observed across the suspended regions. Figure 4.11j shows the dark-field (DF) TEM image of fig. 4.11i, taken with one diffraction beam fixed at an atomic plane spacing of 0.12 nm. Crystallographic continuity is observed for domains ∼1 μm, consistent with AFM findings. A high resolution TEM image of the hBN surface (fig. 4.11j) shows a

pristine surface morphology, as expected from a low-contamination (bubble) transfer process. A single six-fold diffraction pattern is observed (inset fig. 4.11k), consistent with AFM height measurements showing that the samples are monolayers (fig. 4.11h). All the data are consistent with a very clean transfer process of high quality monolayer hBN with crystal domains ∼1 µm in size. We therefore expect intimate contact between stacked 2D materials attracted by Van der Waals forces [62]. An optical image of the final graphene-hBN device stack contacted in the TLM con-figuration is presented in the inset of fig. 4.11e.

Current-annealing was performed on a set of devices under high vacuum (10^{-6} Torr) with a slow voltage ramp (∼5 mV/s) to 3 – 4 V in order to use Joule heating to vaporize contaminants from the lithography process and to improve the contact resistance [63]. Figure 4.12a shows typical I-V characteristics for the current-annealing process where the device was held at 3, 3.5, and 4 V to anneal the graphene at progressively higher temperatures. From the TLM measurements, it was found that this current annealing process caused the device resistance to decrease from ∼3.3 kΩ to ∼1.3 kΩ (inset Fig. 4.12a) while the contact resistivity decreased from ∼1.2 kΩ-µm to ∼0.8 kΩ-µm (Fig. 4.12b; see Figure S2 in Supplementary Information). The measured contact resistivity of ∼0.75 kΩ-µm for annealed devices on hBN was approximately the same as that found for annealed devices on SiO2 (Fig. 4.12b), suggesting that the use of hBN as a substrate does not strongly affect the quality of the graphene-Cr/Au contact.

To inform development of future design rules for graphene-hBN device integration for both low- and high- field applications, we provide comparisons between various device configurations. A systematic study of high-field transport in SiO2 and hBN-supported graphene devices is shown in Fig 4.12. References to hBN-supported devices indicate current-annealed, monolayer graphene on five-layer CVD hBN measured at a pressure of 10^{-6} Torr. Graphene

devices on SiO2 were probed in ambient air, under high vacuum (10^{-6} Torr), and after current-annealing. These devices were systematically biased to electrical breakdown once their contact resistance had been extracted, and the measurements were compared with those performed on hBN-supported samples. We find that breakdown characteristics, which reflect high-field performance, depend on vacuum conditions, substrate type, annealing, and channel length. Figure 4.12c shows a consistent increase in maximum sustained current for 500 nm channel length devices when measured in ambient air, in high vacuum (10^{-6} Torr), post-annealing (10^{-6} Torr), and on a hBN substrate, respectively. These successive improvements are attributed to several factors and will be discussed in the following section. We also observed that devices with shorter channel lengths showed larger breakdown currents (Fig 4.12d) and higher maximum current densities (Fig 4.12e), but sustained less power as compared to longer channels (Fig 4.12f). This is consistent with the expectation that longer channel lengths provide better heat dissipation via a larger graphene-substrate contact area, while shorter channels have fewer total surface impurities limiting carrier scattering, allowing greater sustained current. From the data in Fig 4.12, we find that annealed, hBN-supported graphene devices under high vacuum exhibited superior high-field performance, with current densities of ∼109 A/cm2 (3 mA/μm), three orders of magnitude greater than state-of-the-art copper interconnects [64] and an order of magnitude increase in sustained power as compared to similar devices under ambient. Performance disparities due to varying vacuum conditions, current-annealing, and substrate engineering are discussed in detail below.

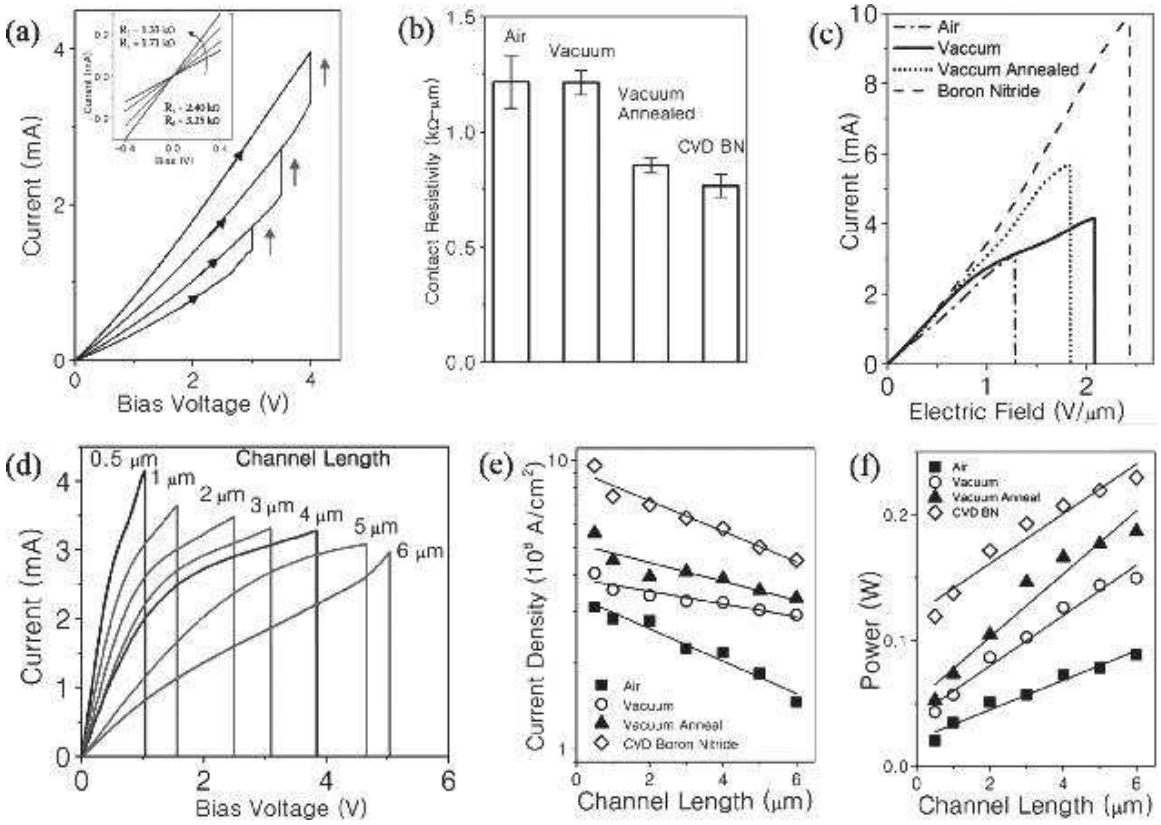

Figure 4.12: Current-annealing and breakdown characteristics of devices in the TLM configuration. (a) Current-voltage traces of consecutive high vacuum current-annealing runs on the same graphene device. Bias is held at 3.0 V, 3.5 V, and 4.0 V for 30 min. (b) Contact resistivity extracted from TLM measurements showing a ~30% decrease after current annealing. (c) Comparison of device breakdown at high-fields for devices with a channel length of 500 nm. (d) Typical breakdown characteristics of graphene ribbons of varying channel length. (e) Maximum current density of devices before breakdown. (f) Sustained power before device breakdown.

Samples tested under ambient conditions were found to fail earlier (i.e, lower electric field, lower current density, and lower power) than devices measured in vacuum, which is attributed to oxidation at the elevated temperature caused by Joule heating (Fig 4.12c-f) [65]. Oxidation is suppressed for devices under high vacuum, and they sustained twice as much power before electrical breakdown as compared to devices in air (Fig 4.12f). We attribute device failure primarily to defect formation and growth at contamination and scattering sites. This is supported by the fact that annealed devices consistently showed better high-field performance and greater

current/power before electrical breakdown (Fig 4.12c and Fig 4.12e), suggesting that adsorbed surface impurities [66] (e.g. water [9], oxygen [67] and PMMA [22], which are known to be removed by Joule heating, act as nuclei for defect formation and accumulation that lead to device breakdown. Furthermore, improved crystallinity resulting from current-annealing is known to enhance transport [63, 68, 69]. It has been suggested that breakdown of the SiO_2 may account for device failure [70]; however, greater sustained power was observed in annealed devices (Fig 4.12f), suggesting oxide breakdown is not the limiting factor under these test conditions. Device failure in annealed samples can be ascribed to self-heating effects that originate from the increasing electrical stress at high bias [71]. Finally, we observed that hBN-supported devices showed superior high-field performance, sustaining greater current densities and power to that of similar devices on SiO_2 (Fig 4.12e and Fig 4.12f). The performance gains are accredited to hBN's greater thermal conductivity and surface optical phonon modes as compared to SiO_2. A thermal conductivity of 250 W/mK at 300 K was measured for five-layer hBN, over 200 times greater than that of SiO_2 [53]while larger optical phonon modes in hBN allow for greater energy absorption at high fields [48]. These properties pro-vide exceptional heat dissipation for the graphene channel, suppressing premature breakdown and contributing to a maximum current density of $\sim 10^9$ A/cm^2 (Fig 4.12e) and sustained power over 200 mW (Fig 4.12f) in a 500 nm channel, the highest measured for CVD graphene-hBN heterostructures. Electrical breakdown in hBN-supported devices is attributed to excessive Joule heating, which could potentially be mitigated by using an hBN-graphene-hBN stack to allow for greater thermal dissipation. The results thus far provide rational design considerations and potential tradeoffs for future graphene nanoelectronic device fabrication. In brief, record high-field performance was achieved in stacked CVD graphene-hBN

heterostructures by utilizing a high vacuum environment, a current annealing process, and an atomically smooth and high thermal conductivity substrate.

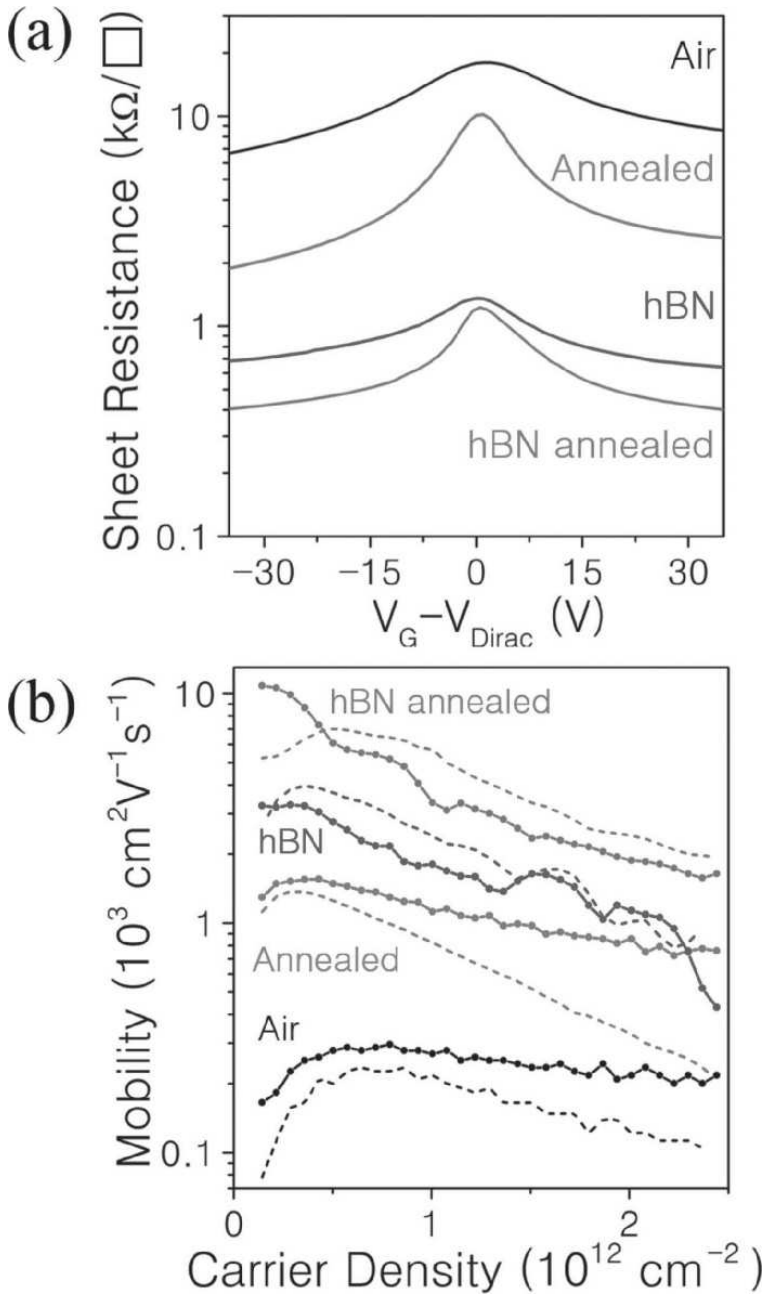

Figure 4.13: Sheet resistance and mobility. (a) Sheet resistance as a function of gate voltage for graphene devices before/after high-vacuum current-annealing on a SiO2/five-layer CVD hBN substrate. (b) Hole (solid) and electron (dotted line) mobility as a function of carrier density. Labeling nomenclature is consistent with (a).

Low-field transport data shown in fig. 4.13 allow for a comparison of graphene sheet resistivity and mobility in four distinct systems: as-prepared and annealed devices on SiO2 and five-layer CVD hBN. As-prepared devices on SiO2 were measured in air while annealed and hBN-

supported devices were measured under high vacuum (10−6 Torr). At large carrier density (V_g = V_{Dirac} + 35 V), as-prepared devices in air exhibited a sheet resistance of ∼7 kΩ/η, which was reduced to ∼2 kΩ/η by high-vacuum annealing, consistent with the high-temperature vaporization of surface contaminants by Joule heating (fig 4.13a). Devices supported on hBN showed even lower sheet resistance of ∼0.7 kΩ/η and ∼0.4 kΩ/η after annealing (fig 4.13a), ascribed to their relative isolation from SiO2 phonon interactions and dangling bonds/ charge traps. The reduction in sheet resistance for the various systems is mirrored in an increase in the measured mobility (fig. 4.13b). At a density of 5 x 10^{11} cm^{-2}, the hole and electron carrier mobility is less than 300 $cm^{2/}$Vs for devices on SiO2 under ambient conditions, but increases over an order of magnitude for annealed devices on five-layer hBN (fig. 4.13b). We report record high hole and electron mobility for CVD hBN-graphene heterostructures, found to exceed 10,000 and 8,000 cm^2/Vs, respectively (fig. 4.13b). Additional information on the derivation of the field-effect mobility using the back-gate configuration is provided in the supporting information [72]. For each type of sample, the mobility reaches a maximum at an intermediate carrier density, as noted in an earlier study [45]. The mobility is suppressed at low carrier density by impurity scattering and at high density due to the increased effect of acoustic phonon scattering.

To summarize, we investigated the transport of CVD graphene on five-layer CVD hBN as a way to explore capabilities to scale high quality graphene devices via substrate engineering. A novel transfer method was utilized to provide low-contamination layer-by-layer stacking to fabricate CVD graphene-hBN heterostructures. Devices were fabricated in the TLM configuration, and high-field transport revealed consistent performance improvements from devices in ambient air, to a high vacuum environment, after current annealing, and finally on hBN substrates. At high-bias, the hBN substrate aided significantly in device cooling, resulting in very high maximum

current densities (~109 A/cm2) and sustained power (> 200 mW). At low-bias the smooth surface and low density of charge traps associated with the hBN substrate allowed observation of hole and electron carrier mobilities in excess of 8,000 cm^2/Vs, the highest measured for CVD graphene-hBN heterostructures, and a sheet resistance of 400 Ω/ η . The resulting work provides a pathway towards a scalable method for improving graphene transport properties via substrate engineering applicable in both high- and low-field applications.

Experimental Section

Synthesis: Graphene monolayers were synthesized on 100-µm thick Cu foil (Alfa Aesar, 42189) in a 1 in. tube furnace (Lindberg blue M, TF55035) at atmospheric pressure. The furnace was first heated to 1057 °C for 35 min in a stream of 500 sccm of Ar (99.999%) and 50 sccm of H2 (99.999%). After annealing of the Cu foil, H_2 gas flow was reduced to 25 sccm and diluted CH_4 (GTS-WELCO, 1.05% balanced by Ar) was introduced at 2 sccm. Graphene was grown for 100 min before the methane was stopped and the furnace allowed to cool. Hexagonal boron nitride monolayers synthesis followed identical starting procedures as graphene growth however an ammonia borane source (Sigma-Aldrich, 682098) was introduced into the 1 in. tube furnace. The source was placed 15 cm away from the edge of the furnace. After annealing the Cu foil at 1057 °C for 35 min under 500 sccm of Ar and 50 sccm of H_2, the source was moved 7 cm towards the Cu foil, and growth was conducted with a reduced H_2 flow rate of 20 sccm. After 15 min, the system was cooled to 1030 °C before the ammonia borane source was relocated to its original position. The furnace was rapidly cooled to room temperature in a flow of 1000 sccm of Ar and 10 sccm of H_2.

Fabrication of graphene-hBN heterostructures: A sacrificial layer (MicroChem Corp., 950 PMMA C4) was spin coated on copper foil containing monolayer graphene and gently dried under nitrogen for 30 min. The graphene was then released from the copper foil using the bubbling transfer method described in section 4.4 and transported from the ionic solution using a polyethylene therepthalate (PET) substrate to three consecutive deionized water baths. The PMMA-graphene sample was then scooped onto the surface of a hBN-copper foil sample synthesized as outlined above. The PMMA-graphene-hBN-Cu foil stack was allowed dry for 40 min at an incline. Repeated identical bubbling transfer steps were used to allow additional hBN layers to be stacked beneath the original structure. After the final bubbling transfer of the desired PMMA-graphene-multilayer-hBN stack, the heterostructure was scooped onto a SiO2/Si substrate and allowed to dry at an incline for 30 min. The wafer was coated with PMMA to allow the original scaffolding layer to soften and then dried for 20 min. The PMMA was removed with gentle acetone rinsing for 10 min and submerged in an acetone bath for 7 min. The chip was rinsed with Isopropanol for 3 min and dried with compressed N2 gas.

Fabrication of devices: Positive tone electron beam resist (MicroChem Corp., 950 PMMA C4) was spin-coated onto the graphene-hBN chip and baked at 170 °C for 1 min. Ebeam lithography was used to pattern a TLM structure in the resist and a 3 nm Cr/40 nm Au metallization layer was deposited using a home built thermal evaporator followed by liftoff. Using the same resist, a second round of ebeam lithography was used to define a 3-µm wide etch mask that was patterned above the TLM electrodes (see Figure S2 in Supplementary Information). The chip was etched in O2 plasma for 30 seconds at 40 W (Technics PE II-A) to isolate a graphene ribbon that spanned the TLM electrodes (Figure 2a); the bulk of the silicon substrate was used as the backgate

electrode. A final liftoff completed device fabrication. Identical steps were used to fabricate graphene devices on SiO2.

Sample Characterization: Scanning electron micrographs (FEI Strata DB235) were taken with 5 kV beam voltage. For Raman spectroscopy and mapping, an excitation laser of 532 nm wavelength was used. Atomic force micrographs (Asylum MFP-3D) of hBN on SiO_2/Si (300 nm oxide) were taken with tapping mode. Transmission electron microscopy, electron diffraction, and high resolution imaging were carried out in a JEOL 2010, a JEOL 2010F, and a FEI Titan operating at 200, 200, and 300 kV, respectively. Graphene devices were electrically probed using a Lakeshore probe station that allowed for high vacuum (10^{-6} Torr) measurements. A National Instruments 6221 DAQ card was used to sources the bias voltage and a preamplifier was used to read the current. A Keithley 5417A multimeter was used to supply the gate voltage. A custom Labview program is used to set/sweep the bias and gate voltages in addition to electrical measurements.

Acknowledgements

This work was supported by SRC contract # 2011-IN-2229, which is associated with the NSF AIR Program ENG-1312202. Z. J. Q. acknowledges support from the IBM Ph.D. Fellowship and the NSF IGERT program (Grant DGE02–21664). Z. J. Q. and R. G. acknowledge support from the University of Pennsylvania GAPSA-Provost Fellowship for Interdisciplinary Innovation. J.A.R.M. and M.D. were supported by NIH grant R21HG006313. Y.W.P. and S.J.H. acknowledge support from the Leading Foreign Research Institute Recruitment Program (0409–20100156) of NRF and the FPRD of BK21 through the MEST, Korea. Electron Microscopy was carried out in part at the Center for Functional Nanomaterials, Brookhaven National Laboratory, which is sup-ported by the U.S. Department of Energy, Office of Basic Energy Sciences, under Contract No. DE-AC02–98CH10886.

Additional support was provided by the Nano/Bio Interface Center and the use of its facilities through National Science Foundation NSEC DMR 08–32802. The Raman mapping system utilized for this work was supported by the NSF Major Research Instrumentation Grant DMR-0923245.

4.8 In-plane Graphene-Boron Nitride Heterostructures

The results presented in this section have also appeared in the publication "Continuous Growth of Hexagonal Graphene and Boron Nitride In-Plane Heterostructures by Atmospheric Pressure Chemical Vapor Deposition", G. H. Han, J. A. Rodríguez-Manzo, C-W Lee, N. J. Kybert, M. B. Lerner, Z. J. Qi, E. N. Dattoli, A. M. Rappe, M. Drndic and A. T. C. Johnson, *ACS Nano*, 2013, 7 (11), pp 10129–10138

Abstract

In-plane growth of graphene-boron nitride monolayer heterostructures enables the formation of electrically patterned, geometrically continuous layers of single-atom thickness. Although there have been reports as to the stitch between graphene and boron nitride, the structure have been fabricated only by low pressure chemical vapor deposition which cannot provide certain edge direction due to their irregular shapes. Here we report the templated growth of single crystalline hexagonal boron nitride nano-hoops directly from the oriented edge of hexagonal single crystal graphene through an atmospheric pressure chemical vapor deposition process, as well as physical property measurements that provided valuable information for the design of in-plane hybrid devices and circuits. The hexagonal boron nitride monolayer ribbons were observed to grow from the edge of graphene template and to inherit its crystallographic orientation. Stability of boron and nitrogen termination from graphene would be discussed through density functional theory calculation due to the observation of tearing at the interface of graphene and boron nitride for the first time.

Introduction

Graphene (Gr) has been intensively studied as a next-generation electronic material because of its extremely high carrier mobility at room temperature [9, 29, 45], among other performance advantages. Boron nitride (BN) has attracted attention as a two-dimensional, large bandgap dielectric that is chemically and structurally compatible with Gr. This prompted the idea of integrated heterostructures, such as vertical stacking of Gr/BN layers [47, 61, 73] and, more recently, templated growth of one material from the other. In-plane hybrid structures have been generated by lithographical re-growth of BN around patterned Gr [74] and re-growth of Gr around patterned BN [75]. In these approaches, the patterning step has the potential to induce unwanted structural and chemical disorder in the resulting hybrid monolayer. To avoid this complication, direct (uninterrupted) growth of in-plane heterostructures has also been investigated, such as few-nm scale domains ("patches") of hexagonal BN in a Gr matrix [76] and graphene-boron nitride monolayer heterostructures (Gr-BN) grown on Ru [77] and Cu [60] by low pressure chemical vapor deposition (LPCVD). These methods avoided the presence of chemical contaminants but did not provide control over the interface structure, as discussed in the next paragraph. Finally, there is significant theoretical interest in lateral Gr-BN hybrids, which may enable energy band modulation for future digital electronics [78-80].

Many Gr-enabled device concepts derive functionality from the atomic-scale geometry of the Gr edge [81-84]. The edge structure of chemical vapor deposition (CVD) - grown Gr is determined by the total chamber pressure and the partial pressure of CH_4 feedstock gas and typical LPCVD growth of Gr leads to dendritic structures with irregular edges [85]. In contrast, our experiments were based on atmospheric pressure chemical vapor deposition (APCVD), which has been shown to promote the formation of crystallographically-aligned straight Gr edges [86-89].

We found that precise control of the furnace conditions enabled continuous growth of regular BN ribbons (BNR) from the crystallographically-aligned edge of Gr hexagons, where the crystallographic orientation of the BNR was determined by that of Gr seed structure. The most critical factor in the growth of oriented Gr-BN heterostructures was the use of near-identical, optimized growth conditions for Gr and BN. We found that the growth time could be used to control the width of the BNRs templated by the Gr hexagonal flakes. Isolated BNRs were obtained by annealing the Gr-BN structure in air at high temperature [90] (500 ^{o}C, 3 h) to remove the Gr region. We also demonstrated that the Gr-BN interface could be tuned from abrupt to graded by controlling the duration of a pre-annealing period of the BN source. Finally, as a proof-of-concept application, an in-plane side-gated transistor was fabricated based on a Gr channel and side-gate, separated by a BN gate dielectric region, all sharing the same crystallographic orientation. This work paves the way for experiments exploring the properties of BN nanoribbons (BNNR) with well-defined edge structure and known chemical termination [90].

Results

Growth of graphene-boron nitride (Gr-BN) in-plane heterostructures

For ease of handling and to ensure reproducibility of the growth process, a controlled mass (ca. 4 mg) of ammonia borane (AB) powder was compressed into a cylindrical pellet and used as the BN growth feedstock (See Fig. S1 in the Supplementary Information).As mentioned, we used APCVD rather than LPCVD to get hexagonal Gr with straight edges; further, we found this method could also be used for controlled growth of triangular BN structures growth *via* APCVD which has not previously been reported.

The AB pellet was placed in a home-built container that was mounted inside the tube furnace and could be moved using a handheld magnet located outside the growth chamber

(Supplementary Information, Fig. S2). To prepare for Gr-BN growth, the AB pellet was placed in the holder and positioned in the quartz tube far from the heated furnace region so it remained below the sublimation point of AB ($\sim$ 40 ^{o}C) even when the furnace temperature was higher than 1000 ^{o}C. Gr was then grown at the temperature range of 1000-1060 ^{o}C using CH_4, H_2 and Ar process gases, as detailed in the method section. Under these conditions, Gr grew in regular hexagonal structure. After 10-20 min of Gr growth, the AB source was moved to a position closer to the furnace for 2 min 'pre-annealing' period. During this time, the flow of 1 % CH_4 feedstock was maintained in order to avoid hydrogen etching of the hexagonal Gr template while the AB temperature rose to a steady state value of 60-70 ^{o}C, which induced sublimation [91]. It was found that 2 min pre-anneal led to Gr-BN structures with a sharp/straight interface. In contrast, a longer pre-anneal led to the growth of a graded Gr-BN interface due to co-injection of CH_4 and AB feedstock. After the pre-anneal, the CH_4 gas flow was stopped, and there was a BN growth phase which lasted 2-10 min. The sample was then rapidly cooled by sliding the furnace downstream while the flow of Ar and H_2 were kept at 10 and 1000 sccm, respectively, and the AB source holder was moved back to the cold zone to prevent sublimation of AB source during cooling process.

Shape of Gr-BN flakes

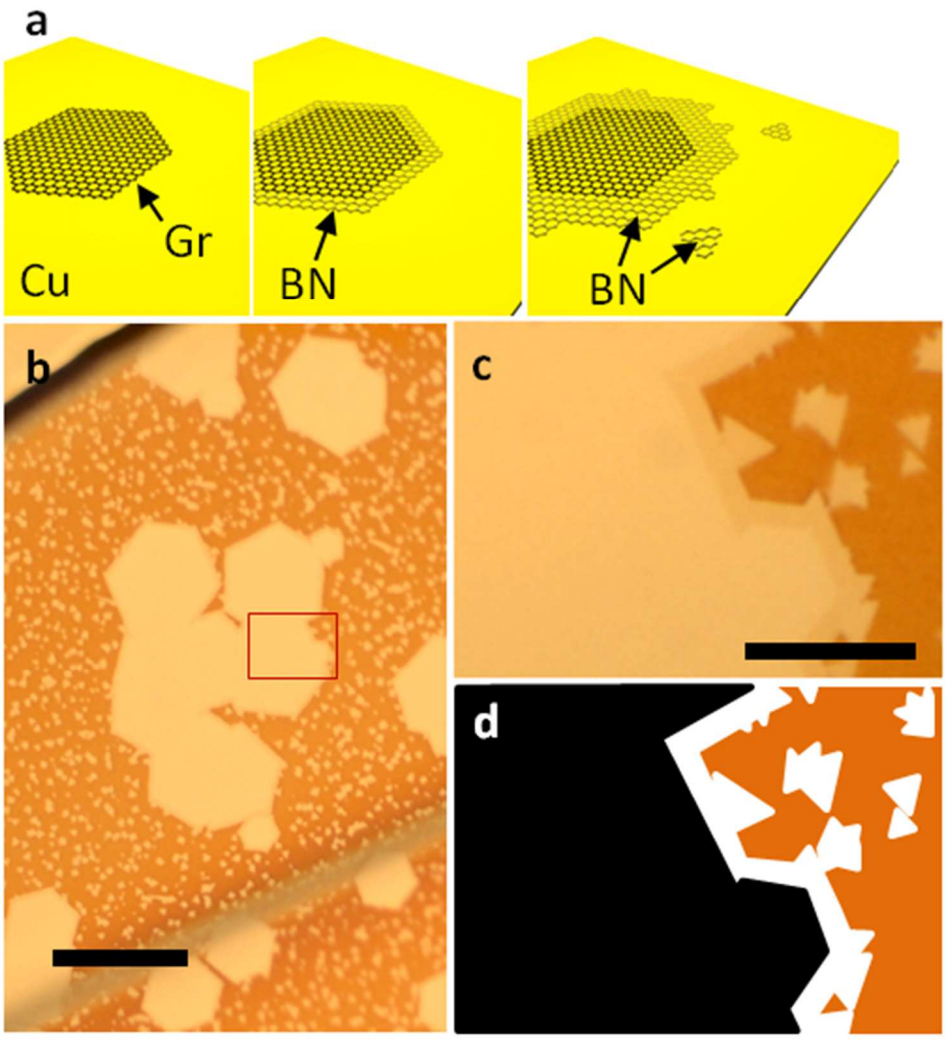

Figure 4.14: Schematic and optical micrographs of continuous growth of graphene-boron nitride (Gr-BN) heterostructures. Gr growth starts from seeds on the Cu foil (a) and hexagonal-BN grows continuously from the graphene template (left to right). b, c Low (b) and high (c) magnification image (of region marked with red solid line in (b)) for Gr-BN heterostructure on the Cu growth substrate that has been oxidized by hot plate baking (180 °C, 30 sec). In (c), the Gr flake and GN stripe and flakes show differing optical contrast. (d) False colour black, white and brown regions indicate Gr, BN, and bare Cu regions in (c), respectively. Scale bar in (b) is 50 μm, and the scale bar in (c) is 10 μm .

Figure 4.14a is a schematic of the growth progression for Gr-BN hybrid monolayers, as inferred from the result of multiple growth runs (see Supplementary Information, Fig. S3 and inset

in fig 4.20). During the Gr growth period, regular hexagonal structures nucleated and grew (left, Fig. 4.14a), and their shape was preserved during the pre-anneal period. For the first few minutes, BN grew exclusively as nanoribbons aligned along the edges of the Gr hexagons (middle, Fig. 4.14a), while isolated triangular flakes of BN nucleated and grew on the exposed Cu growth substrate at later times (right, fig. 4.14a). We concluded that the edges of the Gr hexagons are more reactive for BN growth compared to bare Cu foil. Figure 4.14b is an optical micrograph that shows Gr-BN hybrid structures and triangular BN flakes on Cu foil. To create the optical contrast, the Cu substrate was oxidized for 30-60sec on a hotplate at 180 ^{o}C after the growth. The morphology of the BNRs along the edge of the Gr hexagon is clearly seen at higher magnification (Fig. 4.14c,d; Fig. 4.14d is the false color image in fig. 4.14c).

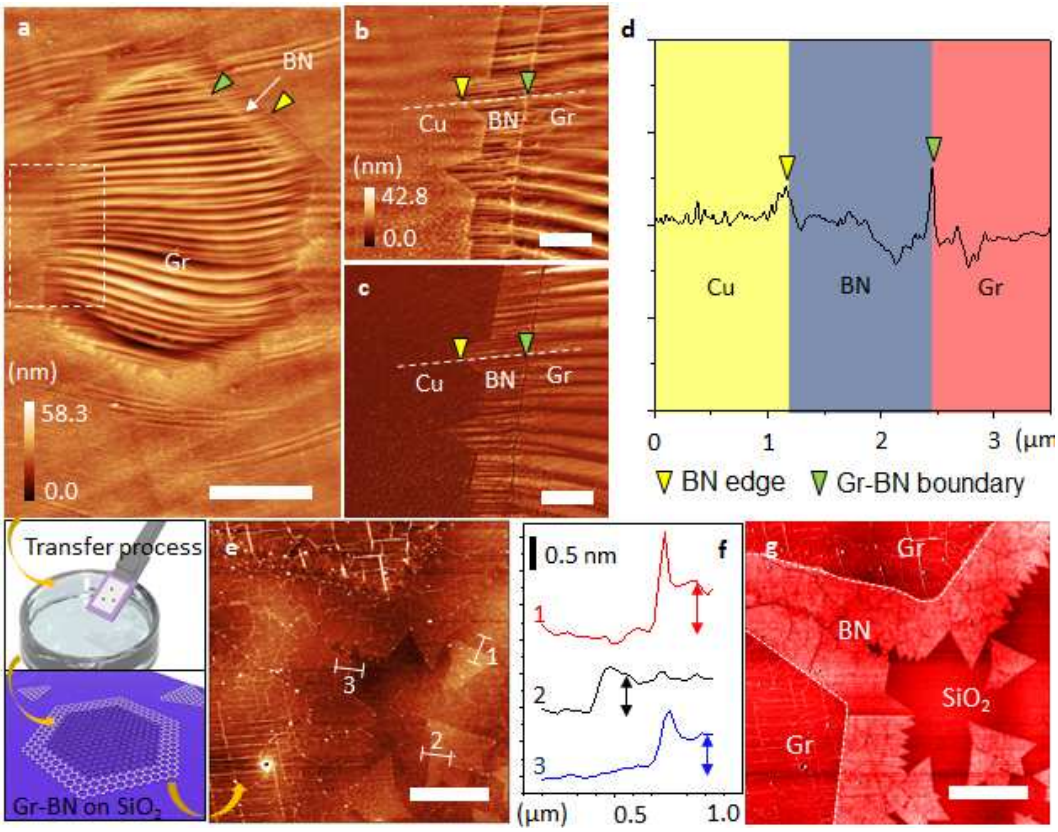

Figure 4.15: Atomic force microscopy (AFM) analysis of Gr-BN heterostructures on Cu growth substrate and after transfer to a silicon dioxide surface (a-d) AFM images and line scans of Gr-BN heterostructure on Cu and (e-g) after

transfer onto an oxidized silicon wafer. In (a-d), topographical AFM images were taken after baking at 180 °C for 1 min. Yellow and green triangles indicate the BN edge and Gr-BN boundary, respectively. (a) low-magnification image of Gr-BN flake (b) higher magnification topographic and (c) phase image from the dashed rectangle in Fig (a). (d) Height profiles of bare Cu-BN-Gr. (e) Topographical image of Gr-BN on SiO_2 (300 nm oxide)/Si wafer, and (f) height profiles (1-3) in fig (e). (g) Phase-mode image shows the Gr-BN boundary clearly. Scale bar in (a), (e) and (g) is 4 μm. Scale bar in (b), (c) is 1 μm.

Figure 4.15a is a topographical image of the sample taken by atomic force microscopy (AFM) after Cu oxidation. Oxidation led to volume expansion of the Cu foil, so the oxidized Cu surface was observed to be slightly higher than the edge of BN (Fig. 4.15a-d, yellow and green triangles indicate the transition from BN to oxidized Cu and the Gr-BN interface, respectively.). These images provided strong evidence that BNRs grew directly from Gr edge atoms, and not by stitching of seeds that grew on the Cu foil. First, as noted previously, BNR formation occurred during the first 3 min of growth, while BN triangle flakes grew at later times from seeds on the Cu foil. This time lag suggested distinctly different growth mechanism for the two structures. Second, the observation of very straight Gr-BN interfaces (Fig. 4.15b-c) provided strong support for the picture of direct growth of BN from the hexagonal Gr template.

To determine the height and establish the monolayer nature of Gr-BN heterostructures, we transferred the sample to Si/SiO_2 wafers by the bubbling transfer technique [92]. The height profile of the Gr-BN (Fig. 4.15e) shows that the structure is ~0.5 nm in height, consistent with a single atomic layer, and that there is no significant height difference between the Gr and BN regions. However, the materials are clearly distinguishable in the phase image, consistent with earlier observations [74]. In fig. 4.15a-c, periodic bumps observed which caused from cooling process for Gr and BN due to reconstruction behavior.

Discussions

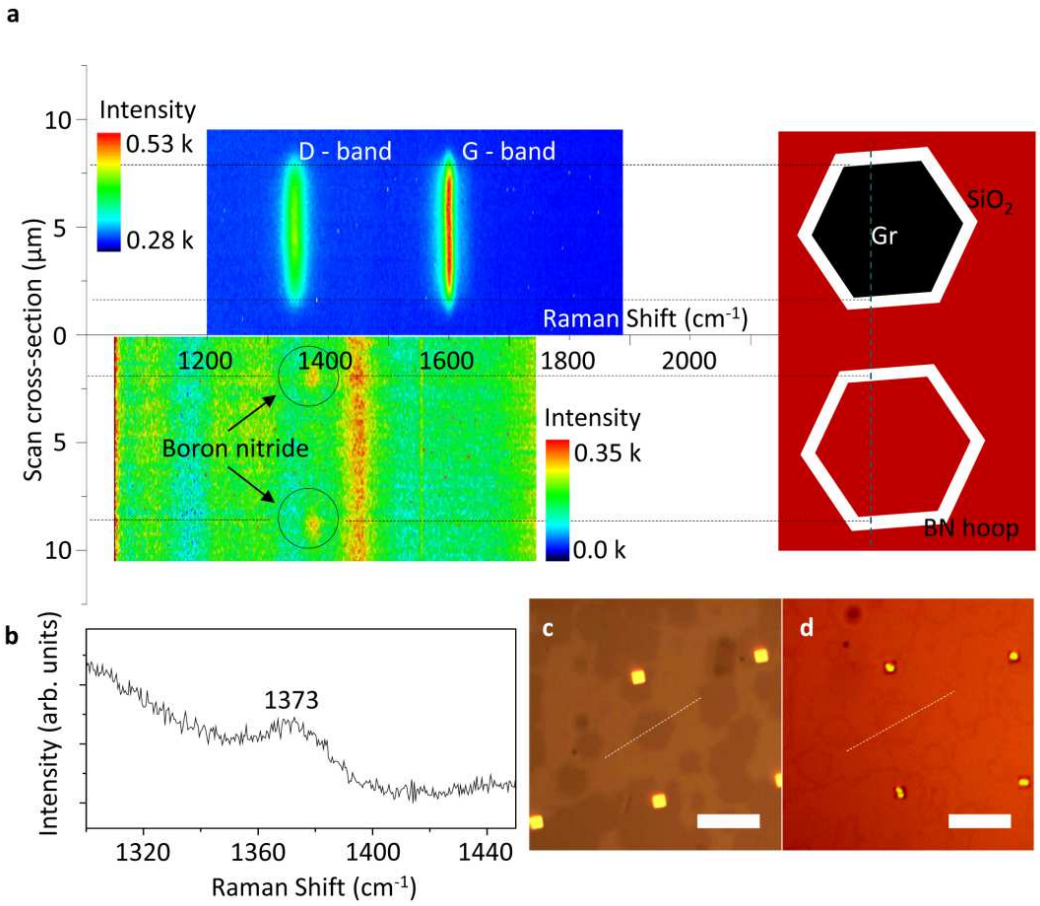

Figure 4.16: 1D Raman maps of Gr-BN and BN structures (a) 1d Raman spectrum map across Gr-BN (top) and BN ribbons (BNR, bottom) after graphene removal by heat treatment (500 °C, 3 h) in air. (b) Raman spectrum of the BNR showing the characteristic peak of BN centered near 1373 cm^{-1}. c, d Optical micrographs before (c) and after (d) the heat treatment used to remove graphene. Contrast and gamma values of (d) were modified to enhance the visibility of the BN nanoribbons on the substrate.

Raman spectroscopy may be used to identify both Gr and BN, although the BN signal is weak compared to that of Gr [93]. This technique provided additional evidence for the presence of both Gr and BN in hybrid structures that had been transferred onto oxidized silicon substrates. Because of the proximity of the strong D peak (1360 cm^{-1}) of Gr to the much weaker characteristic peak of BN (1373 cm^{-1}), it was not possible to collect signals from both materials simultaneously.

Instead, we first collected a Raman line map that established the presence of the Gr hexagon (Fig. 4.16a, top). The sample was then oxidized at 500 ^{o}C in air for 3 h to remove the Gr (supplementary information, Fig. S4), and a second Raman map, taken along the same line, showed that BNRs remained in the regions that were along the two opposite sides of the Gr hexagon (Raman peaks near 1370 cm^{-1} indicated by circles in Fig. 4.16a, bottom). In the Raman map collected after the Gr was removed, higher laser power was required, and only two regions (highlighted in black dashed circles) showed evidence of the peak at 1370 cm^{-1}. Fig. 4.16b shows the corresponding Raman spectrum collected in one of the circled regions. The full spectrum of the Gr and BN hoop is provided in the supplementary information (Fig. S5). Fig. 4.16c,d show the optical images for before and after heating as shown in Fig. 4.16a (top) and 4.16a (bottom), respectively.

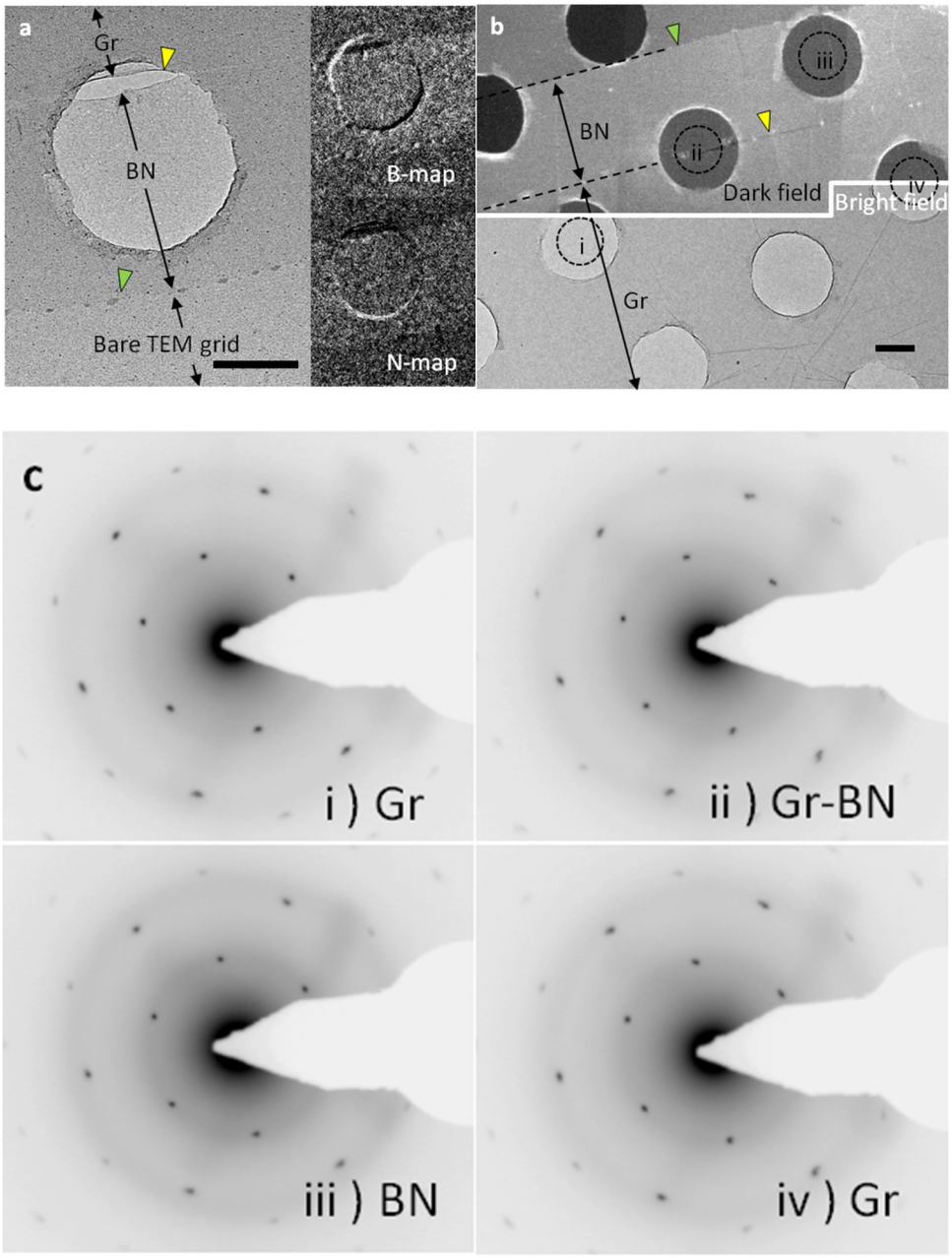

Figure 4.17: Transmission electron microscopy (TEM) and electron diffraction (ED) analysis (a) TEM image of a region containing both a Gr-BN boundary (yellow arrow) and a BN ribbon with its termination (green arrow). Scale bar is 400 nm. Inset: Energy filtered images for B and N, proving that BN is present only in the ribbon region. (b) Composite dark-field (top)/bright-field (bottom)-TEM image and ED data confirming that the Gr and BN regions have the same crystallographic orientation (see text). (c) ED patterns were taken from the areas labeled as i, ii, iii and iv in Fig(b) (each DP was taken from a 0.6 um diameter area).

We further characterized Gr-BN heterostructures by electron energy loss spectroscopy (EELS) in transmission electron microscopy (TEM). For TEM analysis, Gr-BN samples were transferred onto amorphous carbon TEM grids with 1 μm holes (Fig. 4.17a). Energy-filtered images (Fig. 4.17a, inset) show conclusively the presence of B and N only in the region identified as the BNR. The presence of B and N at such regions was confirmed by EELS (see Supplementary Information, Fig. S6a), where the spectrum showed the K-edge peaks for B and N (188 and 400 eV, respectively); a weak carbon peak was also observed at 283 eV due to the carbon deposition during transfer, as observed by others [52, 91, 94].

Electron diffraction (ED) analysis of Gr hexagonal flakes, covering areas of 16 μm^2 (Supplementary Information, Fig S6b), showed that the majority had a single crystal orientation with zigzag edges [59, 88, 89]. Strikingly, the crystal orientation of the BNR consistently matched that of the Gr template from which they grew. This is shown in Fig. 4.17b, where a dark-field (DF) TEM taken with only one diffracted beam fixed at an angle (corresponding to an atomic plane spacing of 0.12 nm) highlights the continuity of the crystal orientation across the interface of the Gr-BN structure. Figure 4c shows ED patterns taken from the areas labelled as i (Gr), ii (BN), iii (Gr-BN) and iv (Gr) in the Fig. 4.17b. The crystallographic orientations were identical to within 2 degree. Larger angle deviations (~ 5 degree) of Gr-BN were also observed near torn or folded region, usually at their interface.

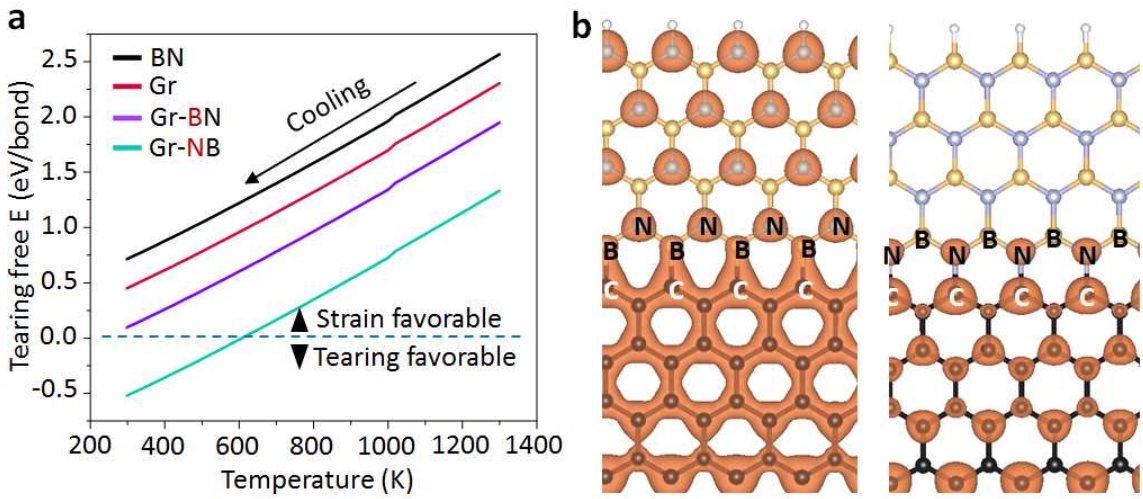

Figure 4.18: DFT calculations of Gr-BN and related structures (a) Calculated dependence of tearing energy versus temperature with p(H_2)=0.01 atm. Black, red, purple and light blue curves indicate tearing energies of BN, Gr, B-terminated Gr-BN and N-terminated Gr-BN, respectively. (b) Real-space charge density of Gr-BN. N-terminated Gr-BN (right) is predicted to be weaker than B-terminated Gr-BN (left) due to the presence of filled anti-bonding interfacial states.

Tearing between Gr and BN, meanwhile, has been frequently observed on our TEM samples. Although theoretical predictions of favorable electronic properties encourage the creation of Gr-BN hybrid structures such as half metallicity [95] and bandgap modulation [83-85, 95], structural stability of these proposed hybrids must first be demonstrated in order to access these electrical properties. For example, tearing at the Gr-BN interface is an important issue that has not been thoroughly investigated, either experimentally or theoretically. Strikingly, we observed frequent tearing at the Gr-BN interface, even in the absence of post-synthesis treatment or handling (e.g., sample baking or transfer process; see Supplementary Information, Fig. S7). From this, we concluded that the Gr-BN interface was vulnerable to fracture by thermal stress associated with the cooling process by calculating tearing free energy (Fig. 4.18a). To support this conjecture, we investigated the thermodynamics of Gr-BN interfaces from first principles to analyze the relevant energetics. Specifically, density functional theory (DFT) total energy

calculations of Gr, BN, and hybrids were performed and compared. Since Gr hexagonal flakes are known to have a zigzag edge structure [87-89, 92], we considered two interface structures, one terminated by boron and the other by nitrogen (Fig. 4.18b). To incorporate the influence of hydrogen gas at high temperature, we used first-principles thermodynamics: the tearing free energy was defined as

$$G_{\text{tearing}} = G_{\text{BN}} + G_{\text{GR}} - (G_{\text{GR-BN}} + \frac{1}{2} n_{\text{H}} \mu_{\text{H}_2})$$

where n_{H} is the number of H atoms that saturate dangling bonds after tearing and μ_{H2} is the chemical potential of H_2 at temperature *T* and pressure *P*. The temperature range used was typical of the post-synthesis cooling process (see the Methods section for further details of the calculation). The Gr-BN interfaces for both B and N terminations were found to be less stable than lines of bonds within either Gr or BN. Furthermore, the B termination was calculated to be more stable than the N termination. The computed first-principles thermodynamics predicted that the N-terminated Gr-BN interface is less stable than separated, hydrogenated Gr and BN for $T < 600$ K.

The instability of the N-terminated interface can be explained as a result of hybridization and charge transfer. Because of the electronic configurations of B and N, the bonding character of BN is relatively ionic, with electron transfer from N to B, while that of Gr is completely covalent. For the B-terminated Gr-BN interface, carbon at the edge of Gr is predicted to donate electrons to B, filling π-bonding states (left of Fig. 4.18b). In contrast, the N-terminated structure requires charge transfer from N to C, which results in the occupation of anti-bonding states (right of Fig. 4.18b and inset) and weaker interfacial bonding. These contrasting bonding motifs explain the difference in net tearing free-energy for the two terminations, and led to the conclusion that the N-terminated interface would be vulnerable to spontaneous separation during cooling.

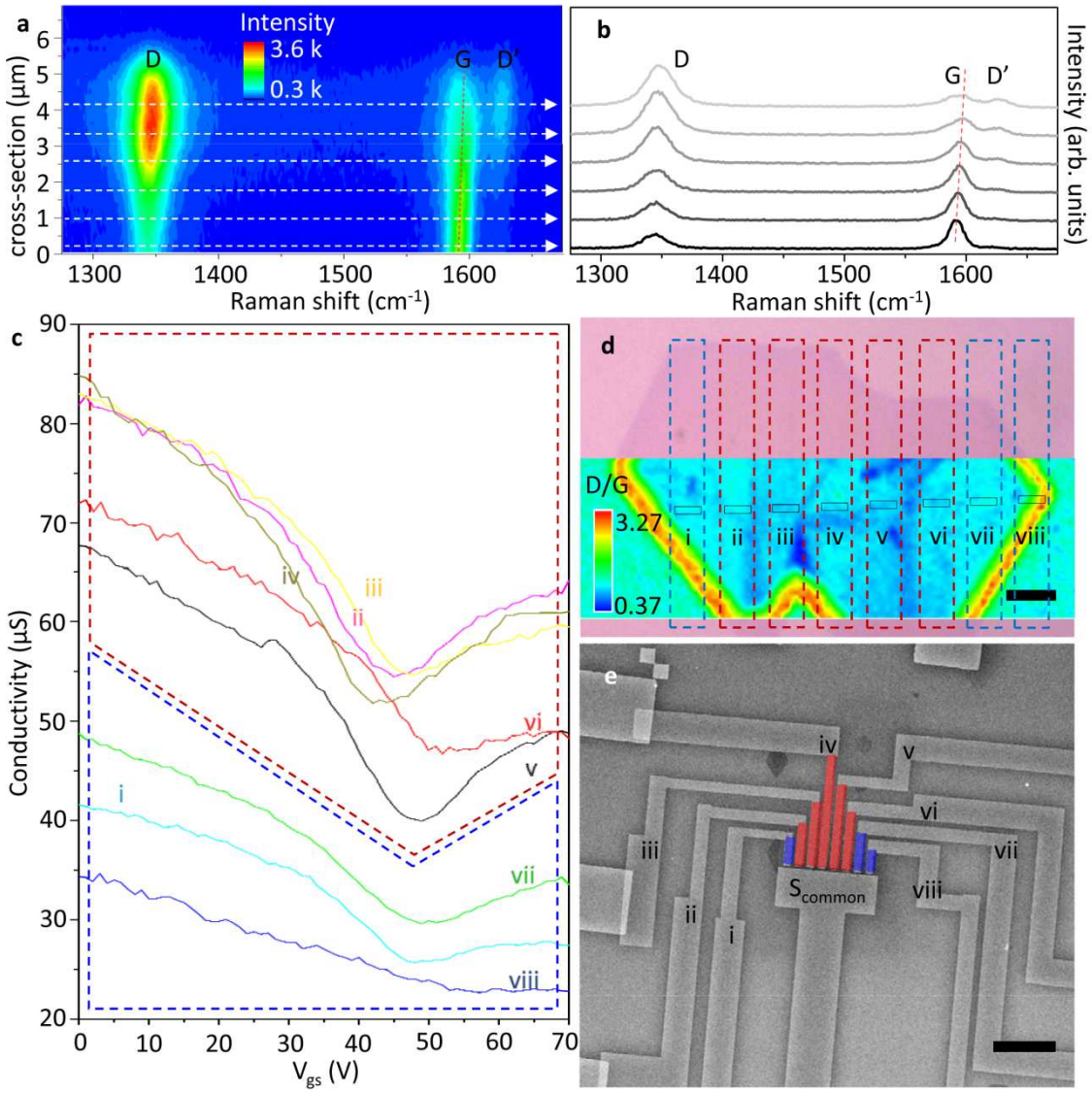

Figure 4.19: Influence of ammonia borane (AB) pre-annealing time on Gr-BN growth a, b (a) 1-D Raman map from a Gr-BN sample grown using a 6 min pre-anneal of the AB source. (b) Raman spectra from the six locations indicated by white dashed lines in (a). c-e I-V_g measurements were taken from edge (blue dashed line, i, vii, viii) and middle (red dashed line, ii - vi) of the Gr-BN flake (c) I-V_g data from the selected area in Fig (d). (d) Optical image and 2-D Raman mapping (D/G) for the device. Solid boxes are the device channels. Scale bar, 4 μm. (e) Scanning electron microscopy (SEM) image of the device. Source was fabricated as a common electrode. Scale bar, 20 μm.

We found that extending the duration of the pre-annealing period of the AB source material enabled the generation of a graded Gr-BN interface. This was demonstrated in an experiment where Gr-BN heterostructures were grown with 0, 2, 4 and 6 min of AB pre-annealing

time. It was found that 2 min was the optimal pre-annealing time of the AB source for generation of a sharp Gr-BN interface. For 0 and 2 min of preheating, the Raman signal of Gr was uniform over the whole flake (in Fig. 4.17a, top), which was interpreted to imply that there was no significant etching of the Gr template by hydrogen gas, and that no B or N impurity atoms were incorporated into the bulk of the Gr flake. In contrast, for samples subject to a longer pre-annealing period, the intensity of the D- and D'-bands (indicative of disorder) increased progressively near the Gr-BN interface, while the G-band intensity associated with C-C bonding decreased (Fig. 4.19a, b). This was attributed to incorporation of boron and/or nitrogen impurity atoms in the Gr region, similar to what has been reported for *h*-BNC film growth. To support this interpretation, a multi-electrode, back-gated device was fabricated to enable electrical measurements of specified regions within the Gr flake. It was observed that the conductivity and carrier mobility decreased progressively for regions nearer to the Gr-BN interface, consistent with the formation of a graded interface where the carbon component decreased monotonically towards the Gr-BN interface (Fig. 4.19c).

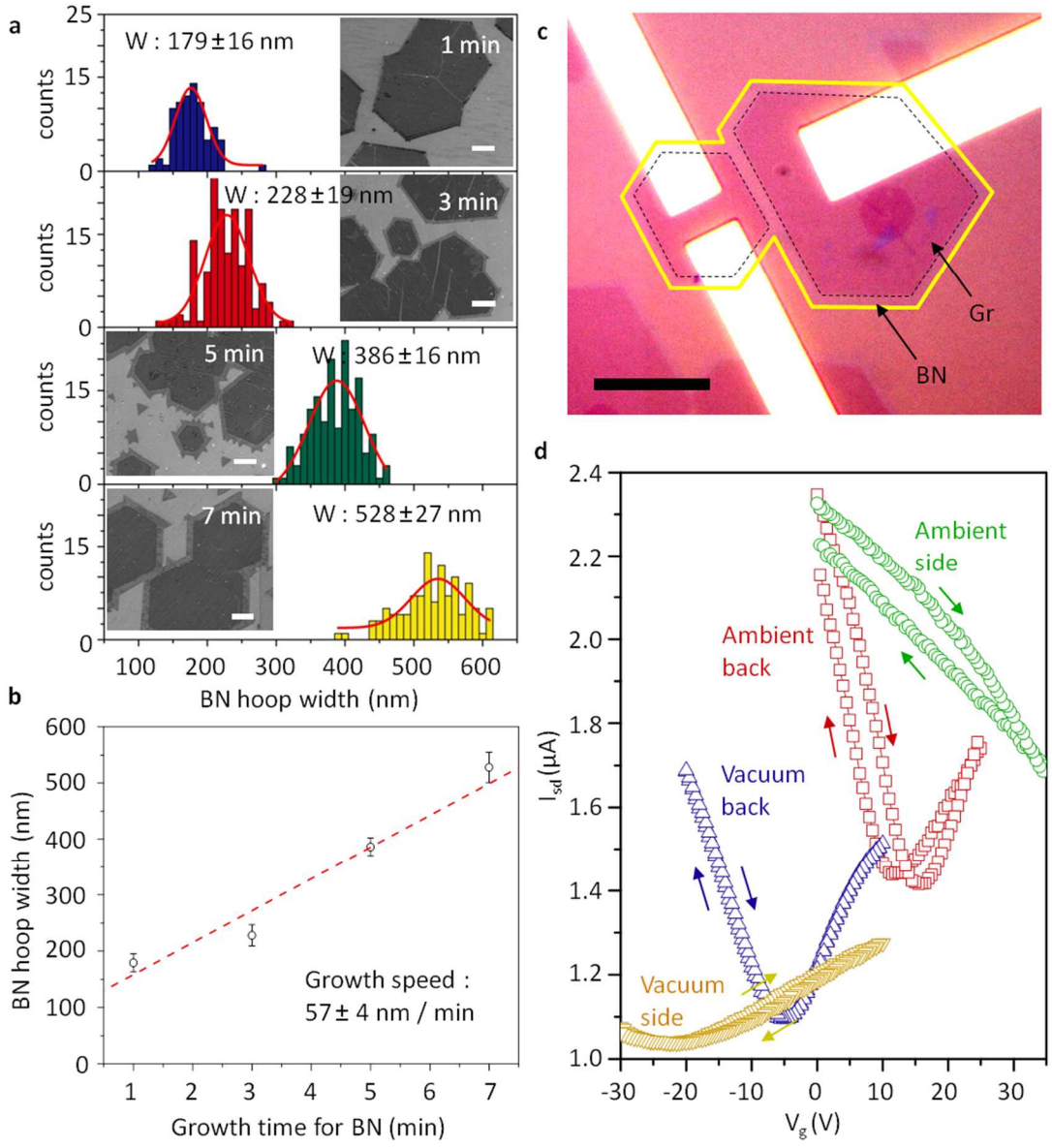

Figure 4.20: Width control of boron nitride hoop around graphene flake BN width around graphene controlled by growth time. (a) For 1-6 (top-bottom) min growth time, 6 min was used for pre-annealing. (b) Extracted growth rate is 57±4 nm/min. (C) Boron nitride is between graphene flakes. Scale bar is 10 um. (d) I-V characteristics for the device in (c).

Unzipping of boron nitride nanotubes (BNNT)[96-98] by Ar^+-ion bombardment is a well-established approach to obtain BNNR for BN electronics. Based on the results presented in Fig. 4.16, it is clear that an alternative approach is the use of single-crystal Gr as a sacrificial template

for BNNR growth. This motivated a demonstration of methods to control the BNR width and in this way to enable bottom-up BNNR synthesis. To this end, we first reduced the BN growth temperature to reduce the BN growth rate to 1000 °C. We determined that at this temperature, the optimum pre-annealing period of the AB source was increased to 6 min, compared to 2 min for a growth temperature of 1030 °C. Gr-BN heterostructures were grown using BN growth times of 1-7 min (see Fig. 4.20a), and the corresponding widths of the BNRs were 179 ± 16, 228 ± 19, 386 ± 16 and 528 ± 27 nm, respectively, for a growth rate of 57 ± 4 nm/min (Fig. 4.20b). For very short growth times of less than 1 min, we expect that BNNR of a few tens of nm in width could be obtained.

Introducing BN for fabrication of in-plane heterostructures with Gr is beneficial for the realization of "2D electronics" [74, 75]. As a proof-of-concept, we fabricated three-terminal, side gated devices [99-101] on oxidized silicon substrates, where BN served as the gate insulator. To accomplish this, Gr-BN flakes were transferred onto 300 nm of SiO_2/Si wafer, and we identified two Gr flakes that were crystallographically aligned and where the region between flakes was filled by BN (Fig. 4.20c). One flake was contacted by two electrodes that served as a source and drain, while the other flake was contacted by a third electrode to serve as a side-gate. In Fig. 4.20c, black dashed and yellow solid lines indicate the boundaries between Gr-BN and BN-bare SiO_2, respectively. The I_{ds}-V_g characteristics of the device were measured using the global back gate and the side gate in ambient and vacuum (1×10^{-6} torr) conditions (Fig. 4.20d). The red (square) curve in Fig. 4.20d is typical for a back-gated Gr device that is p-doped by atmospheric impurities. The effect of the Side gate (green circle) is comparable to that of the back gate after accounting for the micrometer spacing between the Gr flake and the neighboring gate Gr flake. We then measured the I-V_g characteristics of the same device in vacuum. With the back gate (blue triangle),

the device had a slightly negative charge neutral point (-5 V) which can be caused by electrode doping [102]. For both ambient and vacuum measurements, back gate effect is about 5 times greater than the side gate effect in terms of transconductance extraction from the plot in Fig. 4.20d. Interestingly, the side gate sweep in vacuum (yellow inverted triangle) became more left shifted (-20 V). It is reasonable to have a more negative charge neutral point because the side gate is less effective in this device because the width of the BN gate insulator between Gr hexagons is ~1 um, which is >3 times greater than the thickness of the SiO_2 back gate dielectric.

In conclusion, Gr-BN heterostructure monolayers have been grown *via* APCVD, which is advantageous for obtaining well-defined edge structures. We also elucidate the role of preheating the BN source material, which was essential to avoid both unwanted etching of Gr and co-deposition of Gr and BN. Electron diffraction showed that the BNR shared the crystallographic orientation of the Gr flake that served as its growth template, providing further evidence of continuous, direct growth of BN from the Gr. Through control of the growth parameters, specifically the pre-heating time of the AB source, both sharp and graded Gr-BN interfaces can be produced. We also studied tearing at the Gr-BN interface, which can be induced by strain during the cooling process, through DFT calculations and N termination is weaker than B termination due to the presence of anti-bonding state occupation although both B and N termination is energetically possible. Finally, our approach may open up a route for BNNR growth and pave the way for 2D Gr-BN hybrid electronics.

Methods

Graphene-boron nitride heterostructure growth

Graphene-boron nitride (Gr-BN) lateral heterostructure monolayers were synthesized by introducing diluted CH_4 (GTS-WELCO, 1.05 %, balanced by Ar) and ammonia borane (AB) source

(Sigma-Aldrich, 682098) into a 1" tube furnace. The AB source was prepared according to the procedure in Supplementary Information Fig. S1. A 100 μm thick Cu foil (Alfa Aesar, 42189), either polished [103] or unpolished [14], was loaded into the tube furnace (Lindberg blue M, TF55035) and heated to 1057 ^{o}C for 25 min in a flow of 500 sccm of Ar (99.999 %) and 50 sccm of H_2 (99.999 %). After 5 min annealing, the system was cooled to 1030 ^{o}C (1000 ^{o}C for fig. 4.20a,b to reduce growth rate) for 5 min to grow hexagonal Gr flakes. The process gas flows were 500 sccm of Ar, 30-35 sccm H_2 and 2 sccm of diluted (1.02 % in Ar) CH_4. Gr was grown for 8-20 min to obtain flakes with the desired average size, and then the AB source was moved closer to the furnace (7.5 cm from the furnace end) (Supplementary Information Fig. S2c). The AB source was pre-annealed for 2 min (6 min for flake in Fig 6) to induce sublimation, while H_2 and CH_4 gas flows were continued to prevent etching of Gr. After the pre-annealing step, H_2 gas flow was reduced to 20 sccm, the CH_4 gas flow was stopped, and sublimed material from the AB pellet was used to grow BNR "hoops" around the Gr templates for 1 to 7 min. When the BN growth finished, the furnace was physically shifted downstream, thus moving the sample outside of the heating zone. The gas flow of Ar and H_2 was maintained so the sample cooled rapidly to room temperature.

AFM, TEM and RAMAN characterization

The AFM (Asylum, MFP-3D) images of Gr-BN heterostructures on Cu foil and SiO_2/Si (300 nm oxide) were taken under ambient condition in tapping mode. For TEM analysis, the sample was carefully transferred to a holey (1 μm hole) carbon grid (Electron Microscopy Sciences, c-flat) by bubbling transfer method[25] with poly(methyl-methacrylate) (*PMMA)* (Microchem, 950 K). Transmission electron microscopy, electron diffraction and electron energy loss spectroscopy (EELS) were carried out in a JEOL 2010, a JEOL 2010F and a FEI Titan operating at 200, 200 and 300 kV, respectively. EEL spectra and energy filtered TEM images were acquired with a GIF

camera. In particular, filtered images were taken with 30 eV energy windows centered at 188 and 401 eV, for B and N, respectively. For Raman spectroscopy (NT-MDT), the Gr-BN flake was transferred onto 80 nm oxide and mapped with 532 nm wavelength excitation laser. Scanning electron microscopy images were taken with 5 kV operation bias.

DFT calculation

DFT calculations were performed using Quantum ESPRESSO [104] with generalized gradient approximation (GGA-PBE) [105] for exchange-correlation functionals. Norm-conserving nonlocal pseudopotentials within Rappe-Rabe-Kaxiras-Joannopoulos (RRKJ)[106, 107] scheme were adopted to generate plane-wave pseudopotentials of B, C, N, and H atoms. The plane-wave was expanded with a kinetic energy cutoff of 50 Ry. Convergence thresholds for self-consistency and ionic relaxation were set as 1×10^{-6} Ry and 1×10^{-3} Ry/Bohr respectively. 3×1×1 K-points Monkhorst-Pack [108] meshes were used for supercell consisting of 32 hexagons with four zigzag chains (eight atoms per each chain). Tearing free energy is calculated with an assumption that tearing is achieved with zigzag terminations for pristine BN and GR, and their hybrid. The model sheets are separated by a vacuum region of 10 Å, and their edges are saturated by hydrogen atoms.

4.9 CVD Growth of monolayer MoS_2 crystals

Monolayer transition metal dichalcogenides such as molybdenum disulfide are of fundamental and technological interest due to the robust direct band gap. Synthesis of MoS_2 via annealing of ammonium tetrathiomolybdate [109], which contains both molybdenum and sulfur, and direct sulfiding of a molybdenum film [110] have been reported, while more recent reports have detailed CVD techniques that yield highly crystalline flakes with micrometer grain sizes using separate sulfur and molybdenum precursor vapors [111, 112] . One aspect of the growth of molybdenum disulfide that differs strongly from that of graphene and boron nitride is that the material can be grown directly onto an insulating substrate (Si/SiO_2 wafer). Typically, solid sulfur is sublimated to provide a sulfur vapor source which is reacted with a molybdenum precursor such as molybdenum trioxide at growth temperatures of approximately 800 °C. This general setup is shown in figure 4.21.

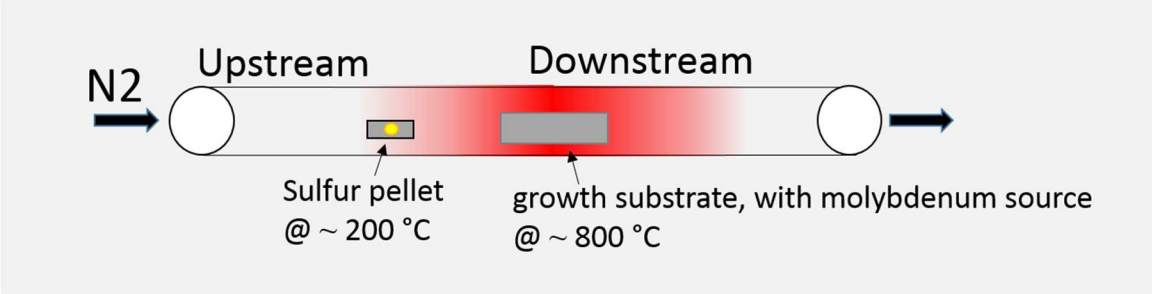

Figure 4.21: Schematic of the furnace setup used for MoS_2 growth. The sulfur pellet is located just outside the furnace, while the growth substrate with the molybdenum feedstock is in the middle of the furnace. The growth temperature is approximately 800 °C.

In this work, we use two different growth approaches. In the first, microliter droplets of saturated ammonium heptamolybdate (AHM) solution are dried on the corners of the growth substrate. During growth, this molybdenum feedstock diffuses across the growth substrate, reacts with the sulfur vapor and nucleates growth of crystalline, monolayer MoS_2 flakes. Before applying

the AHM and performing the growth, the SiO_2 surface is treated with a diffusion promoter, sodium cholate. A 1% sodium cholate solution in water is spin cast onto the substrate, which promotes monolayer growth by increasing the surface adhesive energy relative to the adatom cohesive energy [113].

Optical images of the sample after growth are shown in fig. 4.22. The growth substrate is covered in triangular monolayer flakes. While present all across the growth substrate, their density is typically slightly higher in the corners, closest to the AHM feedstock. Some multilayer regions and monolayers with adlayers can be found near the AHM source.

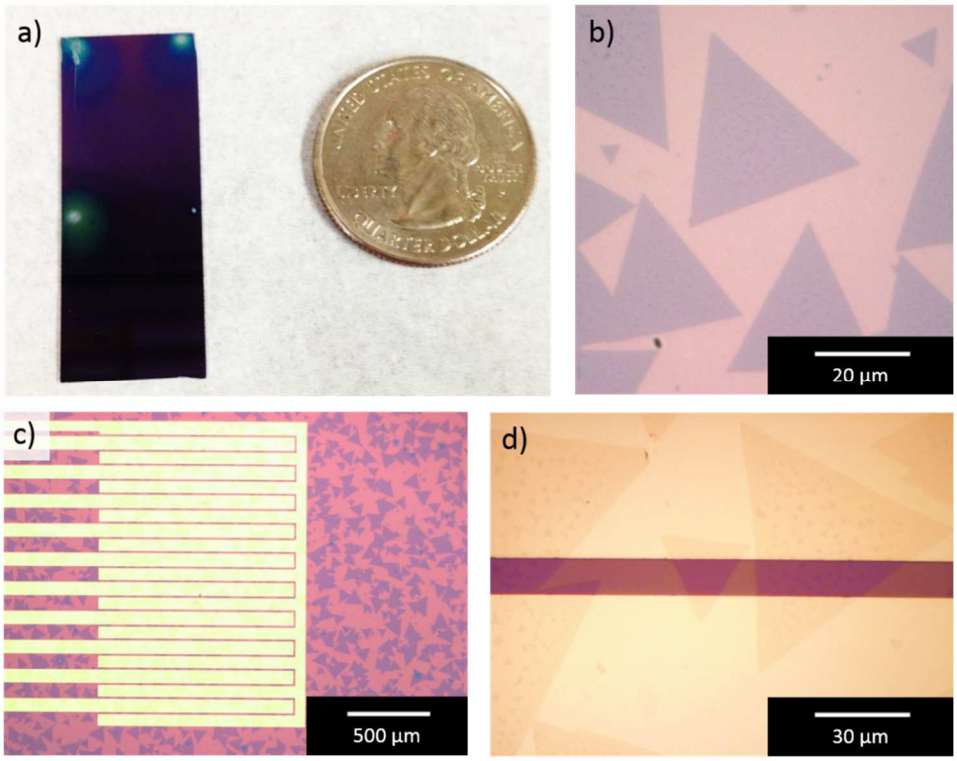

Figure 4.22: Optical images of typical samples after growth using global AHM precursor. Triangular flakes are scattered across the entire growth substrate and easily span the 10 µm once transferred onto prefabricated electrodes.

In order to fabricate arrays of devices while minimizing the need for lithography and etching steps that can contaminate and degrade the samples, we transferred the randomly grown

MoS_2 onto prefabricated electrodes by releasing the samples from the growth substrate onto a polymer support [110]. This was accomplished by spinning a layer of PMMA onto the sample and floating it on a bath of 0.1 M KOH, which released the PMMA and MoS_2 flakes from the SiO_2 substrate by slowly etching the very top SiO_2 atoms. The floating PMMA layer was then transferred into successive water baths in order to wash off residual KOH and finally scooped onto a target substrate that had prefabricated arrays of metal contacts, defined using photolithography, as shown in fig 4.22, panels c and d.

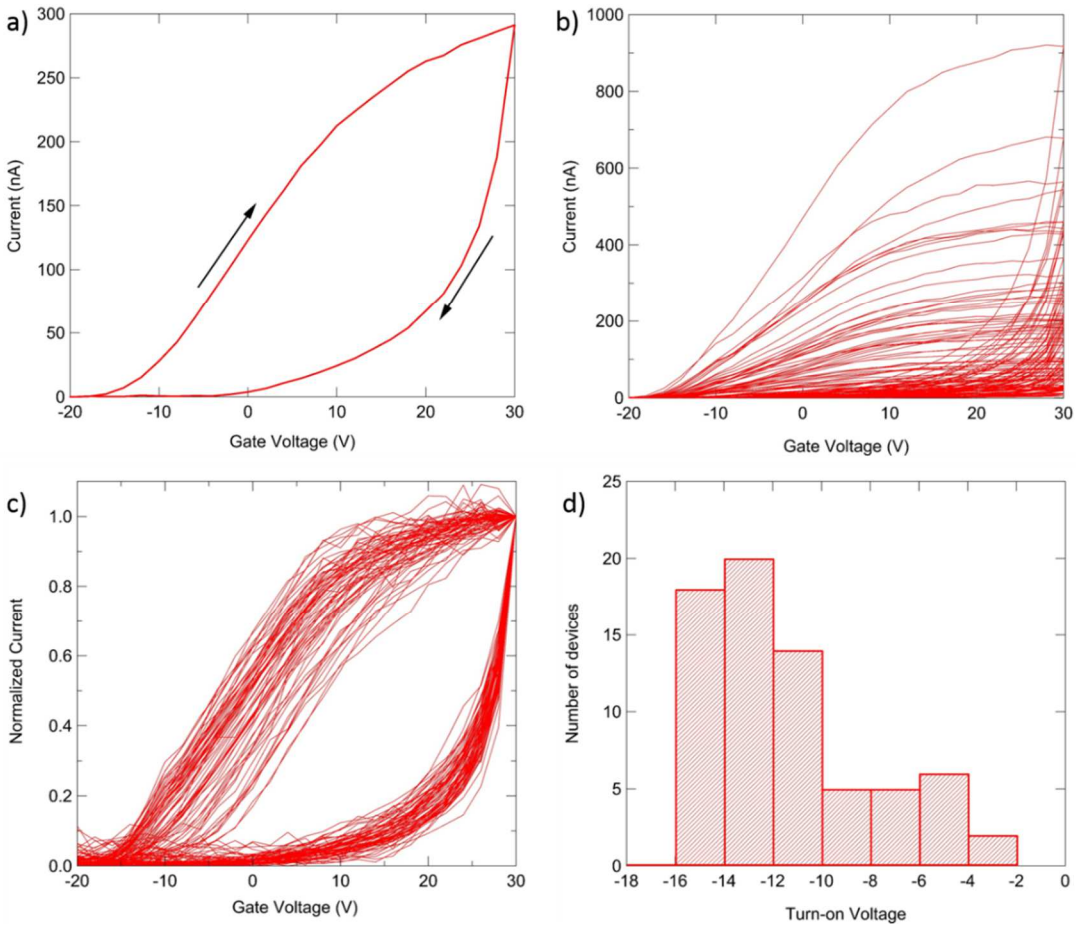

Figure 4.23: Electrical characteristics of the MoS2 devices. a) Devices turn on around -10 V and show hysteresis on the return sweep. 70 devices all exhibit similar shape of the transistor curve (c) with significant spread in on-state current (b). A histogram of turn-on voltages shows that most devices turn on in a reasonably tight window of -16 V to -10 V (d).

The electrode design used individual source fingers, interdigitated with a common drain. The separation between the fingers was 10 µm and each pair of contacts had an effective device area of 10 µm x 2 mm, which ensured that many MoS_2 flakes would be spanning the electrodes and the yield of functional devices would be high. One hundred devices on a single chip were arranged into ten clusters of ten devices that could later be biochemically functionalized by cluster. One such cluster is shown in fig 4.22c. Fig 4.23b shows $I(V_g)$ curves for 70 devices from seven clusters on a single chip. The yield is over 95 % and the devices demonstrate very similar curves with different on-state currents. The spread in on-state currents primarily reflects the variability in the number of MoS_2 flakes spanning the electrodes. This is shown clearly in fig XXc, where the curves are normalized by the on-state current. A histogram of threshold voltages shows a tight distribution, with roughly ¾ of devices having a turn-on voltage in the range -16 to -10 V. These devices are used in protein functionalization experiments described in detail in section 6.2. A further refined growth method, where the molybdenum precursor is patterned locally in order to grow material only at specific, desired locations is detailed in section 4.10.

4.10 Seeded Growth of Highly Crystalline Molybdenum Disulfide Monolayers at Controlled Locations

The results presented in this section have also appeared in the publication "Seeded Growth of Highly Crystalline Molybdenum Disulfide Monolayers at Controlled Locations", G. H. Han, N. J. Kybert, C. H. Naylor, B. S. Lee, J. Ping, J. H. Park, J. Kang, S. Y. Lee, Y. H. Lee, R. Agarwal and A. T. C. Johnson, *Nature Communications*, 2015, 6 (6128) doi:10.1038/ncomms7128

Abstract

Monolayer transition metal dichalcogenides are a materials set with atomic structure complementary to graphene but diverse properties, including direct energy band gaps that make them intriguing candidates for future optoelectronic devices. Various approaches were demonstrated for growth on insulating substrates of the representative material molybdenum disulphide (MoS_2), but to date growth of isolated crystalline flakes has been only at random locations. Here we introduce a method where patterned seeds of molybdenum source material are used to grow isolated flakes of MoS_2 at predetermined locations with micrometer-scale resolution. MoS_2 flakes are predominantly of monolayer thickness and high material quality, as confirmed by atomic force microscopy, transmission electron microscopy, and Raman and photoluminescence spectroscopy. Since the monolayer flakes are isolated and in predetermined locations, fabrication of transistor structures requires only a single lithographic step. Device measurements showed a carrier mobility and on/off ratio that exceeded 10 $cm^2V^{-1}s^{-1}$ and 10^6, respectively. The growth technique provides a path for in-depth physical analysis of monolayer MoS_2 as well as fabrication of integrated circuits of MoS_2-based devices.

The presence of an intrinsic direct energy bandgap in molybdenum disulphide (MoS_2) monolayers makes this two-dimensional material of both fundamental and technological interest [114-122]. Several synthetic methods have been reported, including sulphiding of Mo thin film[123], and annealing of ammonium tetrathiomolybdate (ATM), which has both Mo and S components[124]. One promising technique is the growth of MoS_2 flakes by chemical vapour deposition (CVD) of molybdenum trioxide (MoO_3) and solid sulfur, which can yield highly crystalline, predominantly monolayer material[125-129]. However, this method typically leads to growth of MoS_2 flakes in uncontrolled locations on the substrate, which limits its utility for many applications. Control over the position of MoS_2 flakes on oxidized silicon has been reported through the use of stamping[130] and masking[131] techniques, but neither of these allowed for the creation of large (10s of μm) monolayer domains at predetermined locations with micrometer-scale resolution. Substrate patterning has been used to control nucleation and growth of crystalline flakes of two-dimensional topological insulator materials on mica[132], but it unclear whether this approach can be generalized to MoS_2 on oxidized silicon. Seeding techniques that allow growth at defined locations are well established for graphene[133, 134], and equivalent approaches for MoS_2 synthesis are highly desirable.

Here we report the use of lithographically patterned islands of MoO_3 or ammonium heptamolybdate (AHM) as seed material for the growth of crystalline MoS_2 monolayers at pre-defined locations on oxidized silicon substrates. MoS_2 grown by this approach shows many favourable characteristics, e.g., high crystallinity; excellent optical properties, including a direct band gap, as indicated by photoluminescence and reflection measurements; and carrier mobility ca. 10 $cm^2V^{-1}s^{-1}$. Because the method enables control over the location of discrete MoS_2 flakes, integration into device structures is straightforward using optical lithography, with no need for an

etch step. Although some applications may require further studies to achieve control over the precise shape and size of the MoS_2 flakes, the methodology presented here opens a path towards scalable production of high quality devices and circuits based on MoS_2 and other transition metal dichalcogenides.

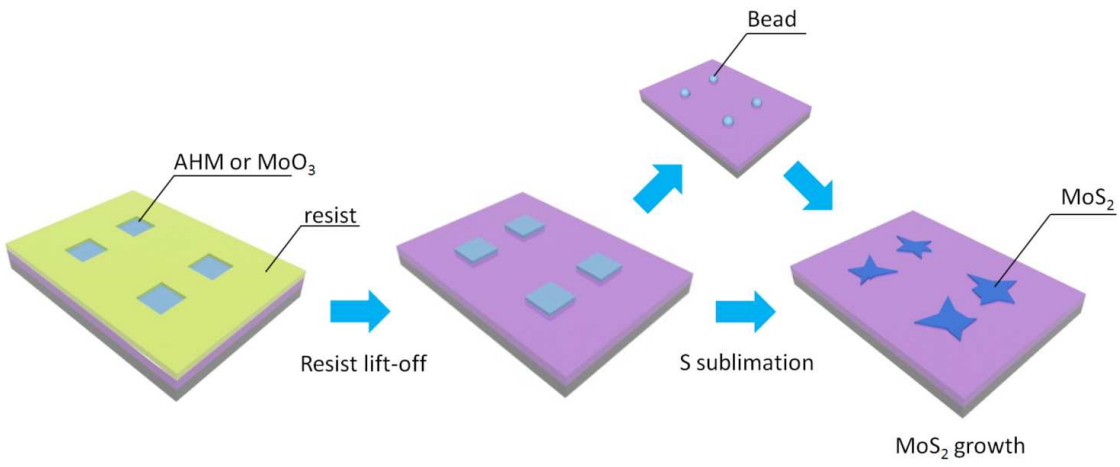

Figure 4.24: Schematic of the growth process for molybdenum disulphide using patterned molybdenum sources. An array of square wells is patterned in a conventional lithographic resist. The wells are filled by spin-coating with ammonium heptamolybdate ($(NH_4)_6Mo_7O_{24}\cdot 4H_2O$, AHM) solution or thermal evaporation of molybdenum trioxide (MoO_3). The resist is removed in a lift-off process. Water droplets are condensed onto the AMH or MoO_3 by reducing the sample temperature to below the dew point using a Peltier cooler. The AMH or MoO_3 is solubilized and forms spherical beads upon drying. MoS_2 flakes are then synthesized by sublimation of solid S in a nitrogen environment in a tube furnace.

Results

Growth process. Figure 4.24 is a schematic of the MoS_2 growth process (see the Methods section and Supplementary Fig. S1 for details). The process begins with patterning of an array of square windows, typically 5 - 10 µm on a side, by e-beam or optical lithography. Next, molybdenum-containing seed material is deposited into the windows, either by thermal evaporation of MoO_3 or by spin-casting of a saturated solution of AHM in water. The AHM solution collects in the square wells but there is almost no deposition of AHM on the resist layer, which is not wet by the solution.

Spin coating of AHM has advantages of speed, simplicity, and requiring no equipment beyond a standard spin coater. The resist and unwanted molybdenum source material are removed in a standard lift-off step.

At this point, the molybdenum-containing seed particle has a shape that depends upon the relative humidity and other details of the deposition process. To improve the uniformity of the seed shape and subsequent MoS_2 growth, an aggregation step is performed (see Supplementary Figs. S2 and S3) where the sample temperature is reduced to below the dew point using a Peltier cooler. Due to the hygroscopic nature of MoO_3 and AHM, water collects on the surface of the seed, which is transformed into a spherical-cap shape. This reduces the surface area of the seed particles and makes them more uniform, leading to more efficient and reproducible MoS_2 growth. This step ensures that the seed particle is sufficiently thick to not be consumed by evaporation during the heat-up phase of the growth process. This step is essential when AHM is used as the moblydenum source, since it is quite thin when initially deposited (~ 50 nm, see Supplementary Fig. S2). In contrast, the aggregation step improves the growth reproducibility but is not required when evaporation is used to deposit a MoO_3 seed of thickness approximately 150 nm or greater. The aggregation step is followed by an annealing step at 300 °C in a nitrogen atmosphere, which converts AHM to MoO_3 [135, 136].

The next step in the process is chemical treatment of the SiO_2 surface, which has been shown to facilitate growth of MoS_2. For example, it was reported that MoS_2 growth was promoted when the SiO_2 surface was coated with materials that contain carbon ring structures that persist at the MoS_2 growth temperature, e.g., perylene-3,4,9,10-tetracarboxylicdianhydride, perylene-3,4,9,10-tetracarboxylic acid tetrapotassium salt[125], or reduced graphene oxide[125, 128].

These materials promote monolayer growth by increasing the surface adhesive energy relative to the adatom cohesive energy[129]. We achieved excellent results by first preparing the surface with an oxygen plasma treatment and then spin-casting onto the substrate an aqueous solution of 0.1 – 1 % sodium cholate (SC), which contains multiple carbon ring structures.

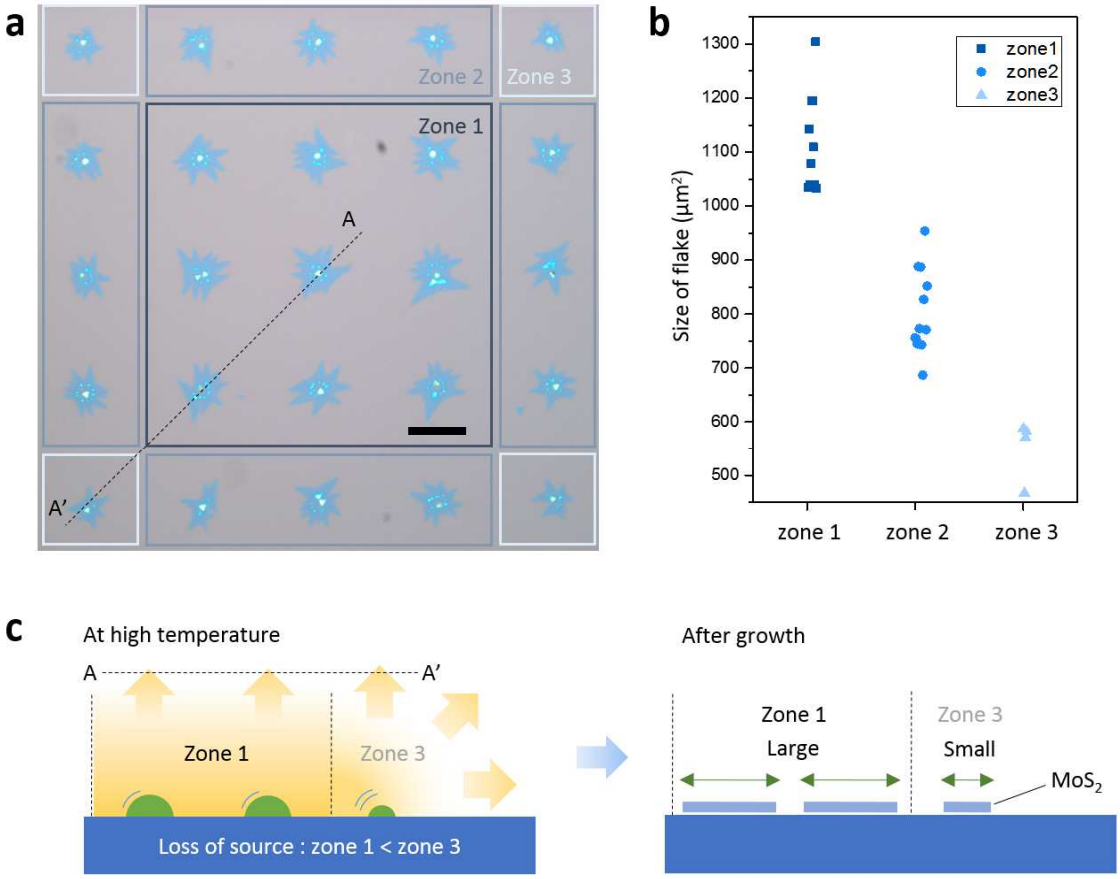

Figure 4.25: Growth of molybdenum disulphide (MoS_2) (a) 5 x 5 array of flakes of monolayer MoS_2 grown by chemical vapour deposition. Scale bar is 50µm. Different growth zones, with different average size of the flakes (see panel (b)), are indicated by outlining: dark blue (zone 1), blue (zone 2) and light blue (zone 3). (b) Areas of individual flakes for Zone 1, 2 and 3 in panel (a). Large (500 – 1300 µm²) flakes of crystalline, monolayer MoS_2 (with small multilayer regions) were grown from the seed particles. The size of the flakes is largest in zone 1 and smallest in zone 3. (c) Schematic illustrating the proposed mechanism underlying the observation that the growth process results in larger MoS_2 flakes in the interior of the array and smaller flakes towards the edges.

For MoS_2 growth, the sample was placed in the middle of the furnace, and 20 - 50 mg of solid sulfur was placed at the upstream end. The entire growth process, including temperature ramp, growth, and cooling, was conducted under a nitrogen flow of 700 sccm. The use of patterned molybdenum source material resulted in the growth of an array of triangular/spike shaped flakes of monolayer MoS_2 (Figs. 4.25a, 4.26a-b,d). The flakes were comprised of multiple crystalline domains of MoS_2, as analysed below (see Fig. 4.27). The majority of the flake region consisted of monolayer MoS_2, with small regions of multi-layer MoS_2 and/or residual seed material observed at the center of the flake (Fig. 4.26d). It was found that multilayer regions could be minimized by using a thinner growth seed. The structure is consistent with a model where growth is initiated at multiple points on the MoO_3 seed to produce MoS_2 crystallites that eventually merge into a larger, faceted structure. Although the sizes and locations of the flakes were primarily determined by the array of the growth seeds, it was consistently observed that flakes that grew at the edge of the array were markedly smaller than those that grew in the middle. This is presumed to reflect diffusion of source material as the furnace temperature was increased that led to shrinkage of seed particles on the edge of the array. Particles in the center of the array are more replenished than those at the edges due to the larger number of neighboring particles. Once sulfur sublimation and transport into the furnace occurs, the larger source particles at the center of the array grow larger MoS_2 flakes than the smaller source particles at the edges. In some experiments, small, triangular, presumably single-crystal MoS_2 flakes were observed to grow in the regions between the MoO_3 seeds (data not shown). This occurred during growths that were at higher temperature compared to the samples shown in Figs 4.25a and 4.26a, and where sulfur was introduced at a later time. Presumably these conditions allowed for

evaporation of Mo from the growth seed, which then reacted with the injected sulfur to form MoS_2 crystallites in regions between the seeds.

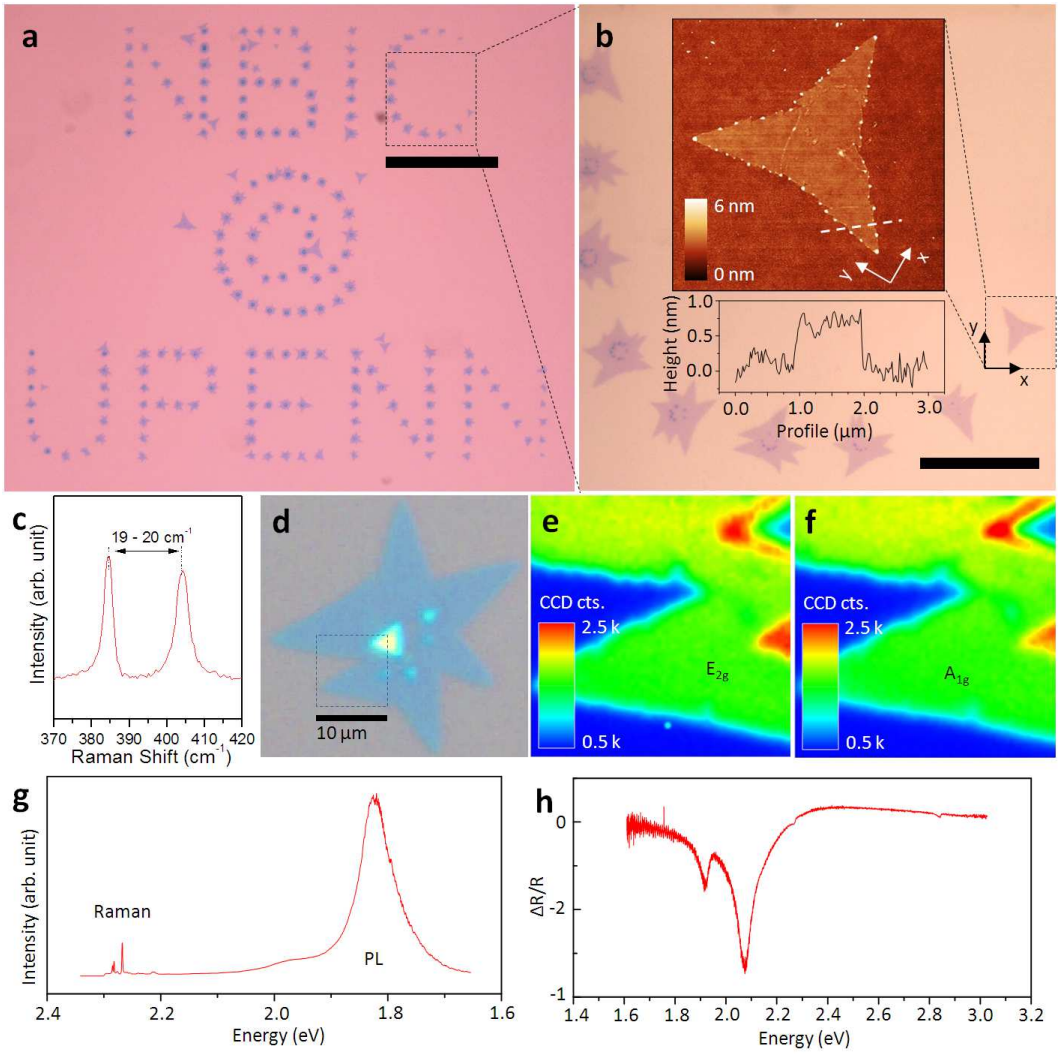

Figure 4.26: AFM and optical analysis of MoS_2 flakes (a) Optical micrograph of MoS_2 flakes grown at locations that form NBIC @ UPENN. Scale bar is 100 μm. (b) Selected area (dashed square in panel (a)) at higher magnification. Scale bar is 20 μm. Inset: AFM image of selected MoS_2 flake (dashed square). Scan image is 10 x 10 μm². (c) Raman signal from the flake shows the E_{2g} and A_{1g} peaks with a spacing (19 cm^{-1}) characteristic of monolayer MoS_2. (d) Optical image of MoS2 flake from the array in fig 2a. Scale bar is 10 μm. (e-f) 2D Raman maps taken from the flake shown in (d, dashed line) for the E_{2g} mode (panel (e)) and A_{1g} mode (panel (f)). Scan images are 10 x 10 μm². (g) Photoluminescence (PL) spectrum for the flake shows strong emission associated with the A and B excition. at 1.83 eV and 1.97 eV, respectively. Strong PL is characteristic of monolayer $MoS_2$and is absent in multilayer films. (h) Differential reflectance spectrum showing the A and B exciton features.

Structural and optical property measurements. To demonstrate the versatility of the growth technique, we synthesized a set of monolayer MoS_2 flakes to spell out the acronym for the Nano-Bio Interface Center at the University of Pennsylvania, 'NBIC@UPENN' (Fig. 4.26a). The center-to-center spacing between adjacent seeds was ca. 15 μm. Atomic force microscopy (AFM) was used to confirm that the height of a typical flake was 0.7 nm (Fig. 4.26b, inset; additional line scan data is provided in Supplementary Fig S4), as expected for monolayer MoS2[125, 127, 137-139]. The Raman spectrum of the monolayer region of the flakes (Fig. 4.26c) showed the expected peak spacing of 19 cm^{-1} between the E_{2g} and A_{1g} modes. Raman mapping (Fig. 4.26e-f) was used to confirm that the Raman spectrum was uniform over the monolayer region as well as distinct from the spectra associated with multilayer regions and the substrate[138-140]. (Maps of Raman peak positions are also shown in Supplementary Fig, S5). We performed photoluminescence (PL) and reflection measurements to confirm that the existence of a direct band gap, which is known to be characteristic of monolayer MoS_2[141-144]. Peak features associated with the A (1.83 eV in PL and 1.91 eV in reflection measurement) and B (1.97 eV in PL and 2.07 eV in reflection measurement) excitons were also observed (Figs. 4.26f-g), confirming that the MoS_2 grown by the seeded CVD process shows the same characteristics as monolayer material fabricated by mechanical exfoliation[145].

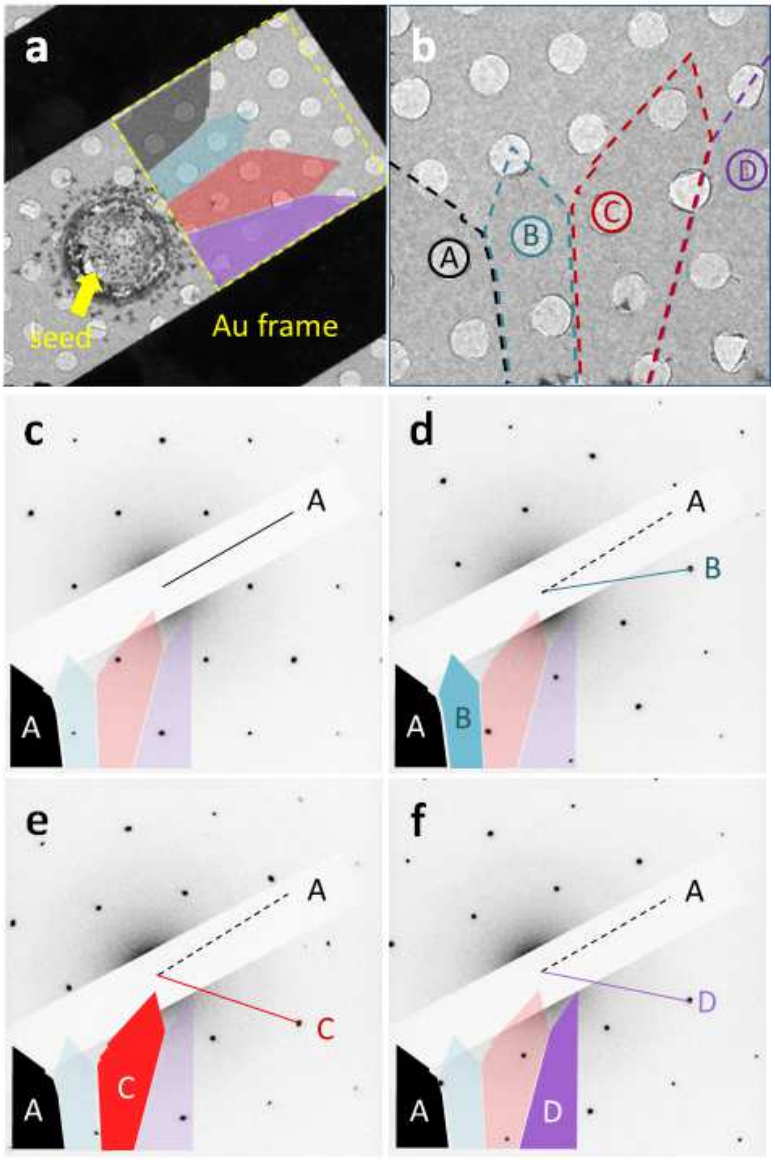

Figure 4.27: Transmission electron micrographs and electron diffraction data (a) Monolayer MoS_2 regions are coloured grey, light blue, red, and purple (top-bottom) according to their crystallographic orientation. The black regions are parts of a gold frame used to prevent tearing during the transfer process (see main text and Supplementary Fig. S6). Triangular shaped multilayer MoS_2 flakes were formed in the seed region, indicated by the yellow arrow. The 1 μm holes in the TEM grid serve as the scale bar. (b) Bright field (BF) image from the square region outlined by a dashed white line in panel (a). (c-f) Electron diffraction data from the regions labelled A-D in panel (b).

Sample crystallinity was further characterized with bright-field imaging and selected-area electron diffraction (SAED) measurements conducted in the transmission electron

microscope (TEM). A gold grid was first patterned onto a MoS_2 flake to prevent tearing of the flake when it was transferred onto a TEM grid covered by a carbon membrane with 1-um diameter holes (Fig. 4.27a and Supplementary Fig. S6). To minimize damage to the sample, imaging and SAED were conducted using an accelerating voltage of 80 kV. The TEM bright-field images are shown in Figs. 4.27a-b. Triangular shaped multi-layer MoS_2 flakes were observed very close to the seed particle, possibly due to limited diffusion of the source during the growth time. Further from the seed, flower-petal-like monolayer MoS_2 regions were observed (dashed square in Fig. 4.27a and Fig 4.27b; see Supplementary Fig. S7 for the raw image used to create Fig. 4.27b and an atomic resolution image of a monolayer MoS_2 flake). The crystalline structure of the MoS_2 was investigated by SAED. Using the intensities of the first and/or second order diffraction spots[146, 147], the flower-petal-like structures were identified as monolayer MoS_2 (see Supplementary Fig. S8). Individual single-crystal MoS_2 domains, labelled (a)-(d) in Fig. 4.27b, were distinguished by the orientations of the diffraction spots in SAED (Fig 4.27c-f). The data indicate that each domain is well crystallized and their orientations are uncorrelated.

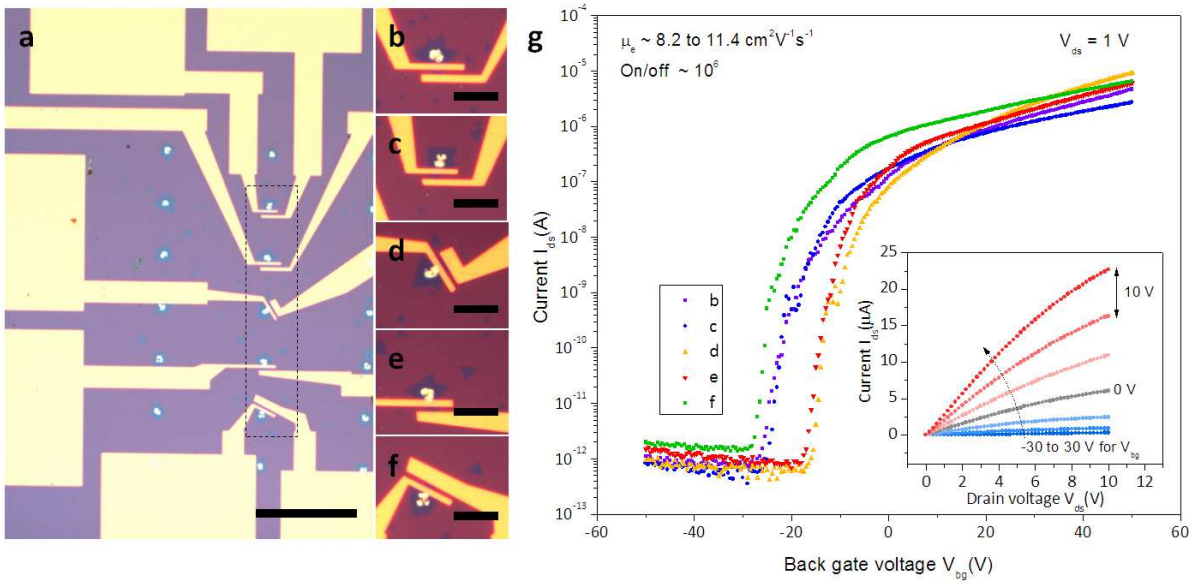

Figure 4.28: Device fabrication and I-V measurement (a) Optical micrograph of devices that were fabricated from MoS_2 grown by the patterned seed technique. Scale bar is 100 µm. (b-f) Higher magnification images of the rectangular region indicated in panel (a). Scale bar is 20 µm. (g) I-V_g characteristics for the devices in panels (b-f). Inset: I_{ds}-V_{ds} characteristics at several back gate voltages.

Fabrication and measurement of electronic devices. An etch step is typically used to define individual devices from a continuous layer of material, which creates the risk of degrading a two-dimensional material as well as added processing cost. In contrast, the patterned growth approach to monolayer MoS_2 outlined here has the advantage of enabling direct fabrication of multiple devices (Figs. 4.28a) and (4.28b-5f), without the need for etching. To demonstrate process compatibility with conventional manufacturing, an array of MoO_3 growth seeds was patterned by e-beam lithography, and MoS_2 monolayer flakes were synthesized as described above. Since the MoS_2 flakes were grown at known, pre-patterned locations, it would be straightforward to align an electrode pattern to the MoS_2 flakes, with no need for a separate etch step. After fabrication of the electrodes, the sample was annealed at 150 °C at 10^{-5} Torr for 1h. Figure 4.28g shows the I-V_g characteristics for a set of devices prepared using this approach,

measured at a pressure of 40 mTorr. Device mobilities were between 8.2 and 11.4 $cm^2V^{-1}s^{-1}$ and the on/off ratios were in excess 10^6 comparable to earlier best reports for exfoliated MoS_2 monolayers [126, 127, 145, 146].

Discussion

In summary, we have developed a novel patterned growth method for flakes of highly crystalline monolayer MoS_2, where molybdenum-containing growth seeds (AHM or MoO_3) are defined using conventional lithographic methods. This technique should be generalizable to the growth of any layered transition metal dichalcogenide (LTMD), and it creates a pathway to controllably tailor the size and position of the material. Control of growth parameters enables synthesis of high quality, crystalline, monolayer MoS_2 with electrical and optical properties comparable to exfoliated material. The process enables straightforward fabrication of integrated circuits without the need for a separate etch step. The work represents an important advance towards scalable production of high quality LTMD-based devices and circuits.

Methods

Preparation of patterned molybdenum sources. 5 x 5 arrays of 5-µm square windows were prepared by electron-beam or photolithography. 7 x 7 arrays of 3-µm square patterns also prepared and growth was also carried out. (see the Supplementary Fig. S9). Molybdenum-containing source material was then deposited by either spin coating (1000 rpm for 30 sec, followed by 3000 rpm for 10 sec) with a saturated solution of ammonium heptamolybdate (AHM, product number A674, Fisher Scientific) in deionized water or thermal evaporation of 150-nm thick molybdenum trioxide (MoO_3, product number 203815, Sigma-Aldrich). The resist was removed using acetone followed by isopropyl alcohol, and the sample was then blown dry with

compressed nitrogen gas. An aggregation step was then performed to obtain regular beads of the source material. While monitoring the sample under an optical microscope, the substrate was cooled until the hygroscopic AHM or MoO_3absorbed water, forming droplets at the seed locations. As the temperature was increased back to room temperature, the water evaporated, leaving behind rounded, uniform, beads of AHM or MoO_3 as shown in Supplementary Fig. S2. Samples were then annealed at 300 °C for 20 min in a flow of 500 sccm of nitrogen gas (99.999% purity). To promote MoS_2 growth, the sample was treated with oxygen plasma (65W, 300 mTorr, 2 min) and then spin-coated(3000 rpm, 1 min) with a surfactant solution (0.1 – 1 % solution of sodium cholate in deionized water).

Growth process Samples with patterned growth seeds were placed into a 1-inch CVD furnace with a 25-mg solid sulfur source (part number 213292, Sigma-Aldrich) at the upstream end. The furnace temperature was increased to 750 ^{o}C at a ramp rate of 70 ^{o}C/min under a nitrogen (99.999%) flow of 700 sccm. The temperature was held constant for 20 min during the MoS_2 growth phase, and the system was then rapidly cooled to room temperature. It was noted that the sulfur source started to melt when the temperature in the middle of the furnace was ca. 650 ^{o}C.

Device fabrication and current-voltage measurements After growth of monolayer MoS_2 flakes from patterned growth seeds, electron beam lithography was used to define an electrode pattern that was aligned to the growth sites. The electrode metallization consisted of 1 nm Cr and 30 nm Au deposited by e-beam evaporation. After metallization, devices were annealed for 60 min at 150 °C at a pressure of 10^{-5} Torr. Current-voltage measurements were conducted at room temperature under a vacuum of 40 mTorr.

Acknowledgment

This work was supported by the National Science Foundation Accelerating Innovation in Research program AIR ENG-1312202 and the Nano/Bio Interface Center NSF NSEC DMR08-32802. B.L., J.H.P., and R.A. were supported by the National Institutes of Health through the NIH Director's New Innovator Award Program, 1-DP2-7251-01 and the U.S. Army Research Office under Grant No. W911NF-11-1-0024. The authors acknowledge use of facilities associated with the Nano/Bio Interface Center (Raman spectroscopy, AFM) and the Nanoscale Characterization Facility (TEM) at the University of Pennsylvania. The aberration-corrected TEM image presented in Supplementary Fig. S6 was obtained by Zhengqing John Qi and Julio A. Rodríguez-Manzo (Drndic group, University of Pennsylvania), using an aberration-corrected transmission electron microscope at the Center for Functional Nanomaterials, Brookhaven National Laboratory.

References

1. Iijima, S., *Helical microtubules of graphitic carbon.* Nature, 1991. **354**(6348): p. 56-58.
2. Thess, A., et al., *Crystalline Ropes of Metallic Carbon Nanotubes.* Science, 1996. **273**(5274): p. 483-487.
3. Fan, Y., B.R. Goldsmith, and P.G. Collins, *Identifying and counting point defects in carbon nanotubes.* Nat Mater, 2005. **4**(12): p. 906-911.
4. Khamis, S.M., R.A. Jones, and A.T.C. Johnson, *Optimized photolithographic fabrication process for carbon nanotube devices.* AIP Advances, 2011. **1**(2): p. 022106.
5. Arnold, M.S., et al., *Sorting carbon nanotubes by electronic structure using density differentiation.* Nat Nano, 2006. **1**(1): p. 60-65.
6. Lu, J., et al., *Why semiconducting single-walled carbon nanotubes are separated from their metallic counterparts.* Small, 2007. **3**(9): p. 1566-76.
7. Basiuk, E.V., et al., *Interaction of Oxidized Single-Walled Carbon Nanotubes with Vaporous Aliphatic Amines.* The Journal of Physical Chemistry B, 2002. **106**(7): p. 1588-1597.
8. Opatkiewicz, J.P., M.C. LeMieux, and Z. Bao, *Influence of Electrostatic Interactions on Spin-Assembled Single-Walled Carbon Nanotube Networks on Amine-Functionalized Surfaces.* ACS Nano, 2010. **4**(2): p. 1167-1177.
9. Novoselov, K.S., et al., *Electric Field Effect in Atomically Thin Carbon Films.* Science, 2004. **306**(5696): p. 666-669.
10. Lin, Y.-M., et al., *Operation of Graphene Transistors at Gigahertz Frequencies.* Nano Letters, 2009. **9**(1): p. 422-426.
11. Wang, X., L. Zhi, and K. Müllen, *Transparent, Conductive Graphene Electrodes for Dye-Sensitized Solar Cells.* Nano Letters, 2008. **8**(1): p. 323-327.
12. Lu, Y., et al., *DNA-decorated graphene chemical sensors.* Applied Physics Letters, 2010. **97**(8): p. 083107.
13. Li, X., et al., *Large-Area Synthesis of High-Quality and Uniform Graphene Films on Copper Foils.* Science, 2009. **324**(5932): p. 1312-1314.
14. Luo, Z., et al., *Effect of Substrate Roughness and Feedstock Concentration on Growth of Wafer-Scale Graphene at Atmospheric Pressure.* Chemistry of Materials, 2011. **23**(6): p. 1441-1447.
15. Gan, L. and Z. Luo, *Turning off Hydrogen To Realize Seeded Growth of Subcentimeter Single-Crystal Graphene Grains on Copper.* ACS Nano, 2013. **7**(10): p. 9480-9488.
16. Kim, K.S., et al., *Large-scale pattern growth of graphene films for stretchable transparent electrodes.* Nature, 2009. **457**(7230): p. 706-710.
17. Li, X., et al., *Evolution of Graphene Growth on Ni and Cu by Carbon Isotope Labeling.* Nano Letters, 2009. **9**(12): p. 4268-4272.
18. Pirkle, A., et al., *The effect of chemical residues on the physical and electrical properties of chemical vapor deposited graphene transferred to SiO2.* Applied Physics Letters, 2011. **99**(12): p. 122108.
19. Kumar, S., et al., *Reliable processing of graphene using metal etchmasks.* Nanoscale Research Letters, 2011. **6**(1): p. 390.
20. Ishigami, M., et al., *Atomic Structure of Graphene on SiO2.* Nano Letters, 2007. **7**(6): p. 1643-1648.

21. Ohno, Y., K. Maehashi, and K. Matsumoto, *Label-Free Biosensors Based on Aptamer-Modified Graphene Field-Effect Transistors.* Journal of the American Chemical Society, 2010. **132**(51): p. 18012-18013.
22. Dan, Y., et al., *Intrinsic Response of Graphene Vapor Sensors.* Nano Letters, 2009. **9**(4): p. 1472-1475.
23. Safron, N.S., et al., *Barrier-Guided Growth of Micro- and Nano-Structured Graphene.* Advanced Materials, 2012. **24**(8): p. 1041-1045.
24. Burg, B.R. and D. Poulikakos, *Large-scale integration of single-walled carbon nanotubes and graphene into sensors and devices using dielectrophoresis: A review.* Journal of Materials Research, 2011. **26**(13): p. 1561-1571.
25. Pengfei, L., et al., *High-Yield Fabrication of Graphene Chemiresistors With Dielectrophoresis.* Nanotechnology, IEEE Transactions on, 2012. **11**(4): p. 751-759.
26. Liang, X., et al., *Toward Clean and Crackless Transfer of Graphene.* ACS Nano, 2011. **5**(11): p. 9144-9153.
27. Goossens, A.M., et al., *Mechanical cleaning of graphene.* Applied Physics Letters, 2012. **100**(7): p. 073110.
28. Shi, Y., et al., *Synthesis of Few-Layer Hexagonal Boron Nitride Thin Film by Chemical Vapor Deposition.* Nano Letters, 2010. **10**(10): p. 4134-4139.
29. Bolotin, K.I., et al., *Ultrahigh electron mobility in suspended graphene.* Solid State Communications, 2008. **146**(9–10): p. 351-355.
30. Bolotin, K.I., et al., *Temperature-Dependent Transport in Suspended Graphene.* Physical Review Letters, 2008. **101**(9): p. 096802.
31. Balandin, A.A., et al., *Superior Thermal Conductivity of Single-Layer Graphene.* Nano Letters, 2008. **8**(3): p. 902-907.
32. Balandin, A.A., *Thermal properties of graphene and nanostructured carbon materials.* Nat Mater, 2011. **10**(8): p. 569-581.
33. Behnam, A., et al., *Transport in Nanoribbon Interconnects Obtained from Graphene Grown by Chemical Vapor Deposition.* Nano Letters, 2012. **12**(9): p. 4424-4430.
34. Qi, Z.J., et al., *Correlating Atomic Structure and Transport in Suspended Graphene Nanoribbons.* Nano Letters, 2014. **14**(8): p. 4238-4244.
35. Liu, G., et al., *Epitaxial graphene nanoribbon array fabrication using BCP-assisted nanolithography.* ACS nano, 2012. **6**(8): p. 6786-6792.
36. Lin, Y.-M., et al., *Wafer-scale graphene integrated circuit.* Science, 2011. **332**(6035): p. 1294-1297.
37. Hao, Y., et al., *The Role of Surface Oxygen in the Growth of Large Single-Crystal Graphene on Copper.* Science, 2013. **342**(6159): p. 720-723.
38. Lee, J.-H., et al., *Wafer-scale growth of single-crystal monolayer graphene on reusable hydrogen-terminated germanium.* Science, 2014. **344**(6181): p. 286-289.
39. Hwang, E.H., S. Adam, and S.D. Sarma, *Carrier Transport in Two-Dimensional Graphene Layers.* Physical Review Letters, 2007. **98**(18): p. 186806.
40. Ando, T., *Screening Effect and Impurity Scattering in Monolayer Graphene.* Journal of the Physical Society of Japan, 2006. **75**(7): p. 074716.
41. Nomura, K. and A.H. MacDonald, *Quantum Transport of Massless Dirac Fermions.* Physical Review Letters, 2007. **98**(7): p. 076602.
42. Ishigami, M., et al., *Atomic structure of graphene on SiO2.* Nano letters, 2007. **7**(6): p. 1643-1648.

43. Katsnelson, M. and A. Geim, *Electron scattering on microscopic corrugations in graphene.* Philosophical Transactions of the Royal Society A: Mathematical, Physical and Engineering Sciences, 2008. **366**(1863): p. 195-204.
44. Fratini, S. and F. Guinea, *Substrate-limited electron dynamics in graphene.* Physical Review B, 2008. **77**(19): p. 195415.
45. Chen, J.-H., et al., *Intrinsic and extrinsic performance limits of graphene devices on SiO2.* Nat Nano, 2008. **3**(4): p. 206-209.
46. Bresnehan, M.S., et al., *Integration of hexagonal boron nitride with quasi-freestanding epitaxial graphene: toward wafer-scale, high-performance devices.* ACS nano, 2012. **6**(6): p. 5234-5241.
47. Dean, C.R., et al., *Boron nitride substrates for high-quality graphene electronics.* Nat Nano, 2010. **5**(10): p. 722-726.
48. Gannett, W., et al., *Boron nitride substrates for high mobility chemical vapor deposited graphene.* Applied Physics Letters, 2011. **98**(24): p. 242105.
49. Jain, N., et al., *Graphene interconnects fully encapsulated in layered insulator hexagonal boron nitride.* Nanotechnology, 2013. **24**(35): p. 355202.
50. Han, G.H., et al., *Continuous growth of hexagonal graphene and boron nitride in-plane heterostructures by atmospheric pressure chemical vapor deposition.* ACS nano, 2013. **7**(11): p. 10129-10138.
51. Wang, M., et al., *A Platform for Large-Scale Graphene Electronics – CVD Growth of Single-Layer Graphene on CVD-Grown Hexagonal Boron Nitride.* Advanced Materials, 2013. **25**(19): p. 2746-2752.
52. Lee, K.H., et al., *Large-Scale Synthesis of High-Quality Hexagonal Boron Nitride Nanosheets for Large-Area Graphene Electronics.* Nano Letters, 2012. **12**(2): p. 714-718.
53. Jo, I., et al., *Thermal conductivity and phonon transport in suspended few-layer hexagonal boron nitride.* Nano letters, 2013. **13**(2): p. 550-554.
54. Iqbal, M.W., et al., *Superior characteristics of graphene field effect transistor enclosed by chemical-vapor-deposition-grown hexagonal boron nitride.* Journal of Materials Chemistry C, 2014. **2**(37): p. 7776-7784.
55. Luo, Z., et al., *Growth mechanism of hexagonal-shape graphene flakes with zigzag edges.* Acs Nano, 2011. **5**(11): p. 9154-9160.
56. Lauritsen, J.V., et al., *Size-dependent structure of MoS2 nanocrystals.* Nature nanotechnology, 2007. **2**(1): p. 53-58.
57. Xia, F., et al., *The origins and limits of metal-graphene junction resistance.* Nature nanotechnology, 2011. **6**(3): p. 179-184.
58. Sun, Z., et al., *Growth of graphene from solid carbon sources.* Nature, 2010. **468**(7323): p. 549-552.
59. Luo, Z., et al., *Effect of substrate roughness and feedstock concentration on growth of wafer-scale graphene at atmospheric pressure.* Chemistry of Materials, 2011. **23**(6): p. 1441-1447.
60. Gao, Y., et al., *Toward Single-Layer Uniform Hexagonal Boron Nitride–Graphene Patchworks with Zigzag Linking Edges.* Nano Letters, 2013. **13**(7): p. 3439-3443.
61. Britnell, L., et al., *Electron Tunneling through Ultrathin Boron Nitride Crystalline Barriers.* Nano Letters, 2012. **12**(3): p. 1707-1710.
62. Wang, L., et al., *One-Dimensional Electrical Contact to a Two-Dimensional Material.* Science, 2013. **342**(6158): p. 614-617.

63. Lu, Y., et al., *In Situ Electronic Characterization of Graphene Nanoconstrictions Fabricated in a Transmission Electron Microscope.* Nano Letters, 2011. **11**(12): p. 5184-5188.
64. Amit, C., *Interconnects for nanoscale MOSFET technology: a review.* Journal of Semiconductors, 2013. **34**(6): p. 066001.
65. Liao, A.D., et al., *Thermally Limited Current Carrying Ability of Graphene Nanoribbons.* Physical Review Letters, 2011. **106**(25): p. 256801.
66. Moser, J., A. Barreiro, and A. Bachtold, *Current-induced cleaning of graphene.* Applied Physics Letters, 2007. **91**(16): p. 163513.
67. Liu, L., et al., *Graphene Oxidation: Thickness-Dependent Etching and Strong Chemical Doping.* Nano Letters, 2008. **8**(7): p. 1965-1970.
68. Westenfelder, B., et al., *Transformations of carbon adsorbates on graphene substrates under extreme heat.* Nano letters, 2011. **11**(12): p. 5123-5127.
69. Barreiro, A., et al., *Graphene at High Bias: Cracking, Layer by Layer Sublimation, and Fusing.* Nano Letters, 2012. **12**(4): p. 1873-1878.
70. Liao, A., et al., *Thermal dissipation and variability in electrical breakdown of carbon nanotube devices.* Physical Review B, 2010. **82**(20): p. 205406.
71. Murali, R., et al., *Breakdown current density of graphene nanoribbons.* Applied Physics Letters, 2009. **94**: p. 243114.
72. Liao, L., et al., *High-κ oxide nanoribbons as gate dielectrics for high mobility top-gated graphene transistors.* Proceedings of the National Academy of Sciences, 2010. **107**(15): p. 6711-6715.
73. Quhe, R., et al., *Tunable and sizable band gap of single-layer graphene sandwiched between hexagonal boron nitride.* NPG Asia Mater, 2012. **4**: p. e6.
74. Levendorf, M.P., et al., *Graphene and boron nitride lateral heterostructures for atomically thin circuitry.* Nature, 2012. **488**(7413): p. 627-632.
75. Liu, Z., et al., *In-plane heterostructures of graphene and hexagonal boron nitride with controlled domain sizes.* Nat Nano, 2013. **8**(2): p. 119-124.
76. Ci, L., et al., *Atomic layers of hybridized boron nitride and graphene domains.* Nat Mater, 2010. **9**(5): p. 430-435.
77. Sutter, P., et al., *Interface Formation in Monolayer Graphene-Boron Nitride Heterostructures.* Nano Letters, 2012. **12**(9): p. 4869-4874.
78. Kim, S.M., et al., *Synthesis of Patched or Stacked Graphene and hBN Flakes: A Route to Hybrid Structure Discovery.* Nano Letters, 2013. **13**(3): p. 933-941.
79. Fujita, M., et al., *Peculiar Localized State at Zigzag Graphite Edge.* Journal of the Physical Society of Japan, 1996. **65**(7): p. 1920-1923.
80. Nakada, K., et al., *Edge state in graphene ribbons: Nanometer size effect and edge shape dependence.* Physical Review B, 1996. **54**(24): p. 17954-17961.
81. Ritter, K.A. and J.W. Lyding, *The influence of edge structure on the electronic properties of graphene quantum dots and nanoribbons.* Nat Mater, 2009. **8**(3): p. 235-242.
82. Liu, Y., A. Dobrinsky, and B.I. Yakobson, *Graphene Edge from Armchair to Zigzag: The Origins of Nanotube Chirality?* Physical Review Letters, 2010. **105**(23): p. 235502.
83. Zhang, A., et al., *Band gap engineering in graphene and hexagonal BN antidot lattices: A first principles study.* Applied Physics Letters, 2011. **98**(2): p. 023105.
84. Fiori, G., et al., *Lateral Graphene–hBCN Heterostructures as a Platform for Fully Two-Dimensional Transistors.* ACS Nano, 2012. **6**(3): p. 2642-2648.

85. Fan, X., et al., *Band gap opening of graphene by doping small boron nitride domains.* Nanoscale, 2012. **4**(6): p. 2157-2165.
86. Li, X., et al., *Large-Area Graphene Single Crystals Grown by Low-Pressure Chemical Vapor Deposition of Methane on Copper.* Journal of the American Chemical Society, 2011. **133**(9): p. 2816-2819.
87. Luo, Z., et al., *Growth Mechanism of Hexagonal-Shape Graphene Flakes with Zigzag Edges.* ACS Nano, 2011. **5**(11): p. 9154-9160.
88. Vlassiouk, I., et al., *Role of Hydrogen in Chemical Vapor Deposition Growth of Large Single-Crystal Graphene.* ACS Nano, 2011. **5**(7): p. 6069-6076.
89. Wu, B., et al., *Equiangular Hexagon-Shape-Controlled Synthesis of Graphene on Copper Surface.* Advanced Materials, 2011. **23**(31): p. 3522-3525.
90. Garcia, A.G.F., et al., *Effective Cleaning of Hexagonal Boron Nitride for Graphene Devices.* Nano Letters, 2012. **12**(9): p. 4449-4454.
91. Kim, K.K., et al., *Synthesis of Monolayer Hexagonal Boron Nitride on Cu Foil Using Chemical Vapor Deposition.* Nano Letters, 2012. **12**(1): p. 161-166.
92. Gao, L., et al., *Repeated growth and bubbling transfer of graphene with millimetre-size single-crystal grains using platinum.* Nat Commun, 2012. **3**: p. 699.
93. Gorbachev, R.V., et al., *Hunting for Monolayer Boron Nitride: Optical and Raman Signatures.* Small, 2011. **7**(4): p. 465-468.
94. Song, L., et al., *Large Scale Growth and Characterization of Atomic Hexagonal Boron Nitride Layers.* Nano Letters, 2010. **10**(8): p. 3209-3215.
95. Liu, Y., et al., *Half-Metallicity in Hybrid Graphene/Boron Nitride Nanoribbons with Dihydrogenated Edges.* The Journal of Physical Chemistry C, 2011. **115**(19): p. 9442-9450.
96. Zeng, H., et al., *"White Graphenes": Boron Nitride Nanoribbons via Boron Nitride Nanotube Unwrapping.* Nano Letters, 2010. **10**(12): p. 5049-5055.
97. Erickson, K.J., et al., *Longitudinal Splitting of Boron Nitride Nanotubes for the Facile Synthesis of High Quality Boron Nitride Nanoribbons.* Nano Letters, 2011. **11**(8): p. 3221-3226.
98. Li, L., et al., *High-Quality Boron Nitride Nanoribbons: Unzipping during Nanotube Synthesis.* Angewandte Chemie, 2013. **125**(15): p. 4306-4310.
99. Molitor, F., et al., *Local gating of a graphene Hall bar by graphene side gates.* Physical Review B, 2007. **76**(24): p. 245426.
100. Tian, J.F., et al., *Ambipolar graphene field effect transistors by local metal side gates.* Applied Physics Letters, 2010. **96**(26): p. 263110.
101. Hähnlein, B., et al., *Side-gate graphene field-effect transistors with high transconductance.* Applied Physics Letters, 2012. **101**(9): p. 093504.
102. Ryo, N., S. Tatsuya, and T. Katsumi, *Determination of Carrier Type Doped from Metal Contacts to Graphene by Channel-Length-Dependent Shift of Charge Neutrality Points.* Applied Physics Express, 2011. **4**(3): p. 035101.
103. Han, G.H., et al., *Influence of Copper Morphology in Forming Nucleation Seeds for Graphene Growth.* Nano Letters, 2011. **11**(10): p. 4144-4148.
104. Paolo, G., et al., *QUANTUM ESPRESSO: a modular and open-source software project for quantum simulations of materials.* Journal of Physics: Condensed Matter, 2009. **21**(39): p. 395502.

105. Perdew, J.P., K. Burke, and M. Ernzerhof, *Generalized Gradient Approximation Made Simple.* Physical Review Letters, 1996. **77**(18): p. 3865-3868.
106. Rappe, A.M., et al., *Optimized pseudopotentials.* Physical Review B, 1990. **41**(2): p. 1227-1230.
107. Ramer, N.J. and A.M. Rappe, *Designed nonlocal pseudopotentials for enhanced transferability.* Physical Review B, 1999. **59**(19): p. 12471-12478.
108. Monkhorst, H.J. and J.D. Pack, *Special points for Brillouin-zone integrations.* Physical Review B, 1976. **13**(12): p. 5188-5192.
109. Liu, K.-K., et al., *Growth of Large-Area and Highly Crystalline MoS2 Thin Layers on Insulating Substrates.* Nano Letters, 2012. **12**(3): p. 1538-1544.
110. Zhan, Y., et al., *Large-Area Vapor-Phase Growth and Characterization of MoS2 Atomic Layers on a SiO2 Substrate.* Small, 2012. **8**(7): p. 966-971.
111. van der Zande, A.M., et al., *Grains and grain boundaries in highly crystalline monolayer molybdenum disulphide.* Nat Mater, 2013. **12**(6): p. 554-561.
112. Najmaei, S., et al., *Vapour phase growth and grain boundary structure of molybdenum disulphide atomic layers.* Nat Mater, 2013. **12**(8): p. 754-759.
113. Ling, X., et al., *Role of the Seeding Promoter in MoS2 Growth by Chemical Vapor Deposition.* Nano Letters, 2014. **14**(2): p. 464-472.
114. Radisavljevic, B., M.B. Whitwick, and A. Kis, *Integrated circuits and logic operations based on single-layer MoS2.* ACS Nano, 2011. **5**(12): p. 9934-8.
115. Jariwala, D., et al., *Gate-tunable carbon nanotube-MoS2 heterojunction p-n diode.* Proc Natl Acad Sci U S A, 2013. **110**(45): p. 18076-80.
116. Zhang, W., et al., *High-gain phototransistors based on a CVD MoS(2) monolayer.* Adv Mater, 2013. **25**(25): p. 3456-61.
117. Bao, W.Z., et al., *High mobility ambipolar MoS2 field-effect transistors: Substrate and dielectric effects.* Applied Physics Letters, 2013. **102**: p. 042104.
118. Jariwala, D., et al., *Emerging device applications for semiconducting two-dimensional transition metal dichalcogenides.* ACS Nano, 2014. **8**(2): p. 1102-20.
119. Yu, W.J., et al., *Highly efficient gate-tunable photocurrent generation in vertical heterostructures of layered materials.* Nat Nanotechnol, 2013. **8**(12): p. 952-8.
120. Yu, W.J., et al., *Vertically stacked multi-heterostructures of layered materials for logic transistors and complementary inverters.* Nat Mater, 2013. **12**(3): p. 246-52.
121. Chang, H.Y., et al., *High-performance, highly bendable MoS2 transistors with high-k dielectrics for flexible low-power systems.* ACS Nano, 2013. **7**(6): p. 5446-52.
122. Salvatore, G.A., et al., *Fabrication and transfer of flexible few-layers MoS2 thin film transistors to any arbitrary substrate.* ACS Nano, 2013. **7**(10): p. 8809-15.
123. Zhan, Y., et al., *Large-area vapor-phase growth and characterization of MoS(2) atomic layers on a SiO(2) substrate.* Small, 2012. **8**(7): p. 966-71.
124. Liu, K.K., et al., *Growth of large-area and highly crystalline MoS2 thin layers on insulating substrates.* Nano Lett, 2012. **12**(3): p. 1538-44.
125. Lee, Y.H., et al., *Synthesis of large-area MoS2 atomic layers with chemical vapor deposition.* Adv Mater, 2012. **24**(17): p. 2320-5.
126. van der Zande, A.M., et al., *Grains and grain boundaries in highly crystalline monolayer molybdenum disulphide.* Nat Mater, 2013. **12**(6): p. 554-61.
127. Najmaei, S., et al., *Vapour phase growth and grain boundary structure of molybdenum disulphide atomic layers.* Nat Mater, 2013. **12**(8): p. 754-9.

128. Lee, Y.H., et al., *Synthesis and transfer of single-layer transition metal disulfides on diverse surfaces.* Nano Lett, 2013. **13**(4): p. 1852-7.
129. Ling, X., et al., *Role of the seeding promoter in MoS2 growth by chemical vapor deposition.* Nano Lett, 2014. **14**(2): p. 464-72.
130. Nam, H., et al., *MoS_2 Transistors Fabricated via Plasma-Assisted Nanoprinting of Few-Layer MoS_2 Flakes into Large-Area Arrays.* ACS Nano, 2013. **7**: p. 5870-5881.
131. Park, W., et al., *Photoelectron Spectroscopic Imaging and Device Applications of Large-Area Patternable Single-Layer MoS_2 Synthesized by Chemical Vapor Deposition.* ACS Nano, 2014. **8**: p. 4961-4968.
132. Li, H., et al., *Controlled synthesis of topological insulator nanoplate arrays on mica.* Journal of the American Chemical Society, 2012. **134**: p. 6132-6135.
133. Yu, Q., et al., *Control and characterization of individual grains and grain boundaries in graphene grown by chemical vapour deposition.* Nat Mater, 2011. **10**(6): p. 443-449.
134. Wu, W., et al., *Growth of Single Crystal Graphene Arrays by Locally Controlling Nucleation on Polycrystalline Cu Using Chemical Vapor Deposition.* Advanced Materials, 2011. **23**(42): p. 4898-4903.
135. Hanafi, Z.M., M.A. Khilla, and A.M. H., *The thermal decomposition of ammonium heptamolybdate.* Thermochimica Acta, 1981. **45**: p. 221-232.
136. Wienold, J., R.E. Jentoft, and T. Ressler, *Structural investigation of the thermal decomposition of ammonium heptamolybdate by in situ XAFS and XRD.* European Journal of Inorganic Chemistry, 2003(6): p. 1058-1071.
137. Radisavljevic, B., et al., *Single-layer MoS2 transistors.* Nat Nanotechnol, 2011. **6**(3): p. 147-50.
138. Lee, C., et al., *Anomalous lattice vibrations of single- and few-layer MoS2.* ACS Nano, 2010. **4**(5): p. 2695-700.
139. Li, H., et al., *From Bulk to Monolayer MoS2: Evolution of Raman Scattering.* Advanced Functional Materials, 2012. **22**(7): p. 1385-1390.
140. Gong, C., et al., *Metal Contacts on Physical Vapor Deposited Monolayer MoS2.* ACS Nano, 2013. **7**(12): p. 11350-11357.
141. Mak, K.F., et al., *Atomically thin MoS(2): a new direct-gap semiconductor.* Phys Rev Lett, 2010. **105**(13): p. 136805.
142. Sundaram, R.S., et al., *Electroluminescence in single layer MoS2.* Nano Lett, 2013. **13**(4): p. 1416-21.
143. Splendiani, A., et al., *Emerging photoluminescence in monolayer MoS2.* Nano Lett, 2010. **10**(4): p. 1271-5.
144. Shi, H., et al., *Exciton dynamics in suspended monolayer and few-layer MoS(2) 2D crystals.* ACS Nano, 2013. **7**(2): p. 1072-80.
145. He, K., et al., *Experimental demonstration of continuous electronic structure tuning via strain in atomically thin MoS2.* Nano Lett, 2013. **13**(6): p. 2931-6.
146. Brivio, J., D.T.L. Alexander, and A. Kis, *Ripples and layers in ultrathin MoS2 membranes.* Nano Letters, 2011. **11**: p. 5148-5153.
147. Ping, J. and M.S. Fuhrer, *Layer number and stacking sequence imaging by transmission electron microscopy.* Nano Letters, 2012. **12**: p. 4635-4641.

CHAPTER 5: Carbon Nanotube-DNA and Graphene-DNA Vapor Sensors: From Explosives to Ovarian Cancer

This chapter focuses on the development of vapor sensors using carbon nanotube and graphene field effect transistors (FETs) as the electronic readout element and single stranded DNA as the molecular receptor. In this sensor scheme, we leverage the reduced dimensionality of the nanomaterial to create a sensor where every atom is exposed to the environment, resulting in a huge geometric sensitivity advantage over traditional and thin film materials. We find that coating the nanomaterial in a self-assembled DNA monolayer dramatically increases the affinity of the surface for a wide variety of target analytes and, more importantly, the exact sequence used in these experiments directly impacts the sensitivity of the resulting sensor to a series of vapor targets. The result is a prototype 'electronic-nose' technology, where we generate large arrays of tens or hundreds of sensors functionalized with different DNA sequences allowing patterns of responses for a wide range of volatile biochemical targets to be generated. Electronic signatures are seen down to part-per-billion concentrations of single chemicals and can be collected in seconds. Furthermore, the electronic properties of the sensor return to their baseline characteristics after simply flushing the sensor chamber with clean air, allowing the sensors to be reused many times over.

In section 5.1, I discuss the automated, custom vapor sensing test bed that has been created for these experiments, which allows volatiles from synthetic chemicals and human-derived samples such as blood plasma to be sampled by up to one hundred individual sensors in a few seconds. Section 5.2 demonstrates the range of capabilities of DNA-functionalized carbon

nanotube FETs. We demonstrate high yield fabrication of arrays of FETs based on solution-processed, highly semiconducting enriched nanotubes. These devices are shown to be sensitive to stock chemicals down to part-per-billion concentrations. They are also able to distinguish isomers and enantiomers as well as detecting the introduction of traces of volatile compounds in a background of a known olfactory inhibitor. Finally, chemical mixtures are examined and their differentiation is demonstrated. This motivates the work of section 5.3, which describes a detailed study of synthetic human sweat. We demonstrate the ability to differentiate controlled, subtle changes in the sweat composition, well below the differences found between individuals' samples.

Section 5.4 pushes this work further, as we demonstrate use of this technology to classify blood plasma samples according to disease state. The samples are from three classes of individuals; women with ovarian cancer, women with benign ovarian growths and healthy age-matched controls. We first show that pooled plasma samples, where plasma from ten individuals is combined, induce characteristic responses for the sensors that depend on the DNA sequence used and hint at tangible differences between the patient classes. We then move on to measuring volatiles from the headspaces of 25 individual patient samples and show that a clear pattern emerges allowing groups of individuals to be differentiated. We are hopeful that further work on a large number of patient samples will verify these differences, which would open up a pathway to detection of ovarian cancer – a disease for which there are currently no diagnostic tests and mortality rates are unacceptably high.

In section 5.5 we transition from carbon nanotubes to graphene which, as a two-dimensional layer, offers promise of even greater compatibility with standard industrial fabrication techniques while retaining the all-surface advantage of carbon nanotubes. We

demonstrate a photolithographic device fabrication process, which allows large arrays of graphene FETs to be fabricated without contaminating the graphene surface with photoresists by incorporating a gold buffer layer that subsequently doubles are the immediate contact material for the device. When functionalized with DNA, these devices show many of the same advantages as carbon nanotube sensors, with even faster readout times. We demonstrate differentiation of a sequence of homologous carboxylic acids and pinene isomers and also clarify the sensing mechanism by comparing the responses of chemicals whose structure differs only in the substitution of a methyl group for a hydroxyl group.

In section 5.6, we explore a method for further increasing device sensitivity by switching from a continuous graphene device channel to a graphene nanomesh. The nanomesh is created by self-assembling a lattice of polystyrene spheres on the graphene and using them as an etch mask. The resulting graphene mesh devices were shown to be capable of detecting different classes of volatile compounds, including carboxylic acids, aldehydes, organophosphates, and explosives and the devices had larger vapor responses than standard graphene FETs, suggesting the presence of more binding sites for molecules at oxidized edges and lattice defects.

5.1 A custom setup for vapor delivery and electrical readout

In order to conduct experiments on detection of volatile compounds at low concentrations, a dual vapor delivery and electronic measurement setup was constructed and computer-controlled using Labview/Microsoft Visual Studio software. Analyte vapors were delivered into a home-built 6 cm x 2.5 cm x 1 cm chamber using a system of mass flow controllers (MKS 1179) with an intermediary controller (MKS 247D). For chemicals of sufficient volume (≥ 10 mL), bubblers (Ace Glass) with o-ring fittings for ¼" Teflon tubing were used. Clean, dry air from a compressed air cylinder (Praxair UN1002) was flowed through a bubbler containing analyte liquid to create a stream of saturated vapor, with flow rates in the range of 1 – 500 standard cubic centimeters per minute (sccm). This stream was diluted with clean air to obtain vapor at a desired concentration. In many experiments, air was also flowed through a bubbler containing water to create a stream of saturated water vapor (typically 500 sccm). The total flow rate was usually held fixed throughout an experiment. Standard total flow rates were in the range 1000 - 1500 sccm. For small volume samples, in particular blood plasma that were in the range of 250 – 500 µL, 2-neck round-bottom flasks were used. These could be heated in a water/oil bath and individually stirred with millimeter sized stir bars to induce evaporation of the volatile content. The input and output lines of these samples were heated in order to minimize condensation of the volatiles onto the tubing. Check valves were placed into the lines in order to prevent unwanted mixing of samples and, in the case of the blood plasma, to build up volatiles. Once a flow was turned on through the mass flow controller, the check valve cracked open and the vapor from the sample was carried into the sensor chamber.

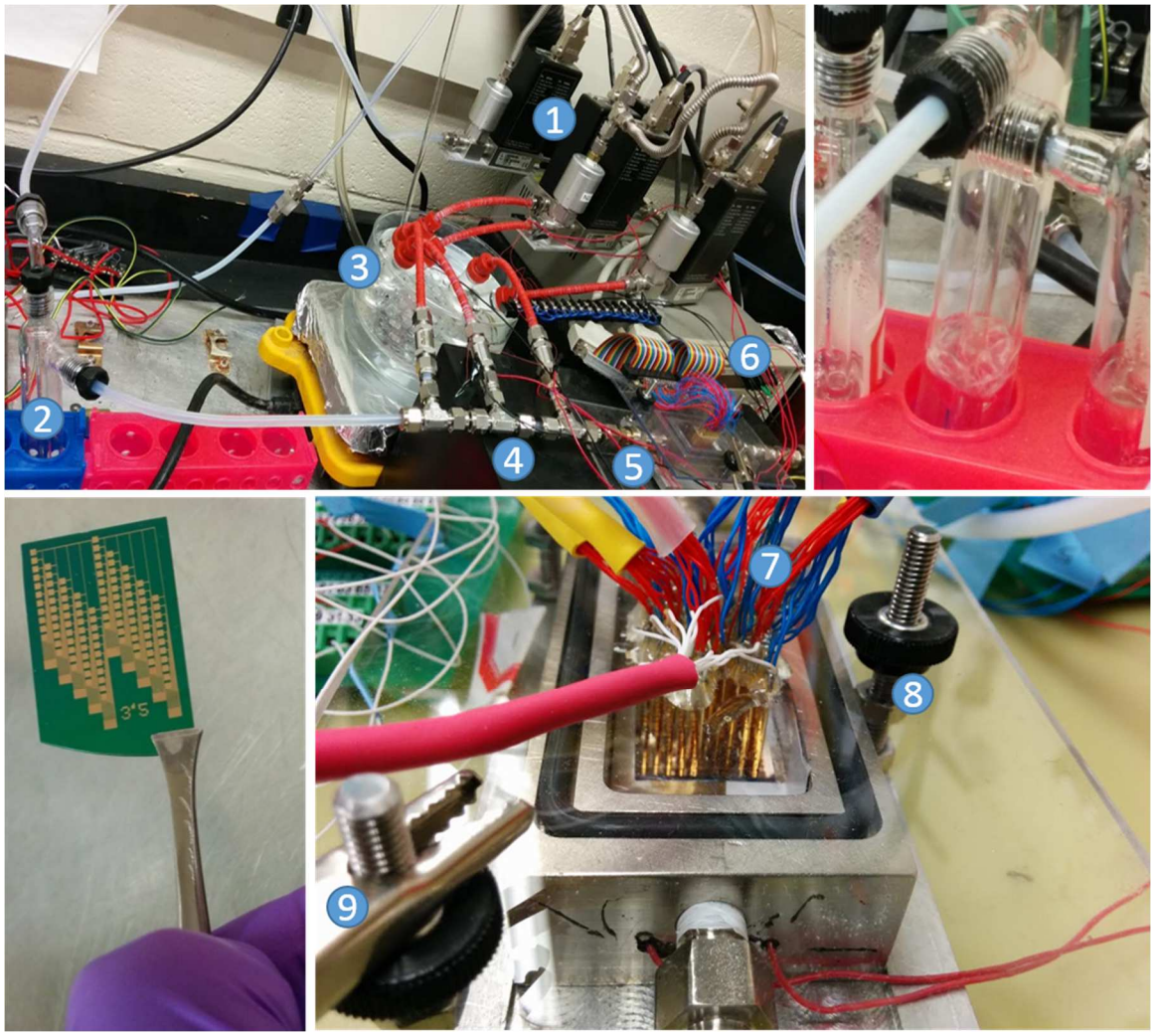

Figure 5.1: The setup used for testing DNA functionalized graphene/carbon nanotube FETs. Mass flow controllers (1) were used to control the flow rates of the lines. Chemicals were loaded into bubblers (2, and top right) or two-neck round-bottom flasks. The different streams were mixed (4) and flowed into the chamber (5, and bottom right) where a chip (bottom left) with 10-100 devices was electrically contacted. The bias was applied via an electrical feedthroughs (6,7) and the source-drain current was readout sequentially for each device. The lid was pushed down onto an o-ring seal using a trio of nuts (8). The gate voltage was applied to the base plate of the chamber via an alligator clip (9)

Devices were electrically contacted using feed-through connections into the chamber. Three generations of chamber lids and electronic measurement systems were used in the course of this work that allowed 10, 56 and 100 devices to be measured during a single run. A bias voltage (typically 100-300 mV) was applied to the devices and the devices were read out sequentially

during the same run using a picoammeter (Keithley 6485) and switching matrix. The first version of the setup used a 4x10 Keithley 7001 switching matrix with physical switches. This was upgraded to a solid state switching matrix (National Instruments PXI-2535 4x136 solid state switch matrix module, National Instruments PXI-1033 Chassis) for the second and third iterations of the setup, which allowed more devices to be switched with lower electrical noise and faster switching speeds. In a switching matrix, any row can be connected to any column. The source-drain bias, electrical ground and the ammeter were connected to the rows of the matrix, while the individual pins on the chip were connected to the columns of the matrix. This allowed the source and drain pins of a particular device to be connected to the bias voltage and ammeter respectively, while the other devices were grounded. The devices were cycled between with a typical sampling time of 50-500 milliseconds, depending on the number of devices, acceptable noise level and generation of the setup. In the final iteration, all 100 devices could be readout every 5 seconds. The gate voltage was applied using a Keithley 617 electrometer, which was connected to the base plate of the sensor chamber and electrically connected to the silicon substrate of the FET devices.

The setup was controlled by custom-written software. The first iteration of the setup was controlled by a LabView program written by Dr. Brett Goldsmith, the second and third using a program written by Dr. Eric Dattoli in C# in Microsoft Visual Studio. The interface of this program is shown in figure 5.2. It allows a set of devices (1-100) to be specified and, if desired, a gate voltage sweep range and gate voltage step size. Alternatively the gate voltage can be held fixed, as is the bias voltage. A recipe, written in Microsoft Excel, can be loaded to specify flow rates through the mass flow controllers as a function of time. This allows the setup to run for hours without user input.

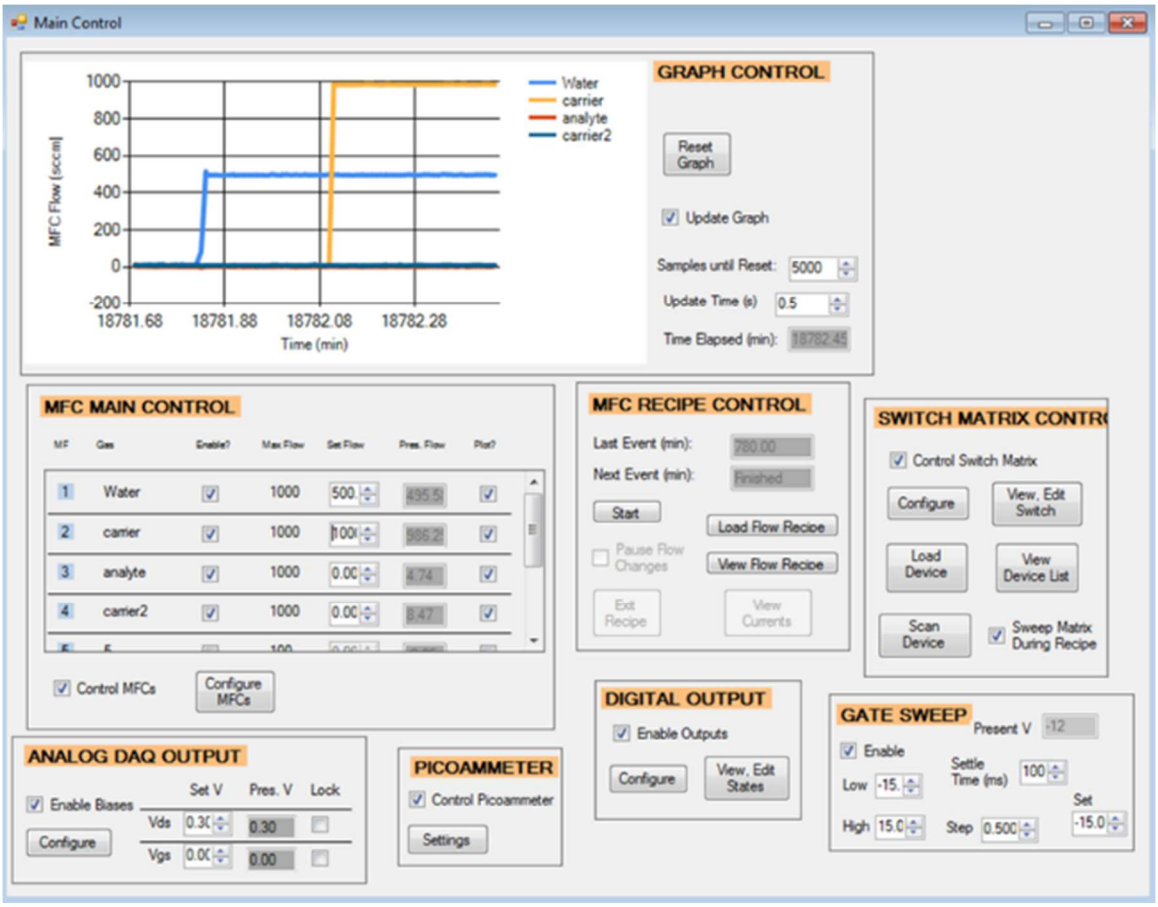

Figure 5.2: Front panel of the program used to control the vapor sensor setup. A flow rate recipe can be loaded and monitored. Simultaneously, a switching matrix is used to cycle through a desired set of up to 100 devices. The bias voltage and gate voltage – static or sweeping – that are applied to the devices can also be preset. The program can run for hours or overnight without the need for user input.

5.2 Differentiation of Complex Vapor Mixtures Using Versatile DNA-Carbon Nanotube Vapor Sensors

The results presented in this section have also appeared in the publication "Differentiation of Complex Vapor Mixtures Using Versatile DNA-Carbon Nanotube Vapor Sensors", N. J. Kybert, M. B. Lerner, J. S. Yodh, G. Preti, A. T. C. Johnson, *Nature Communications*, 2015, 6 (6128) doi:10.1038/ncomms7128

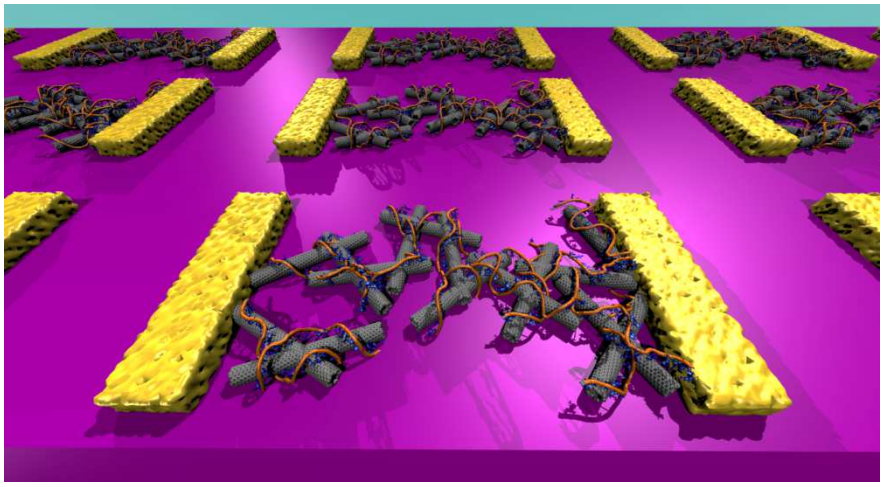

Figure 5.3: Schematic of a DNA/carbon nanotube FET array

Abstract

Vapor sensors based on functionalized carbon nanotubes (NTs) have shown great promise, with high sensitivity conferred by the reduced dimensionality and exceptional electronic properties of the NT. Critical challenges in the development of NT-based sensor arrays for chemical detection include the demonstration of reproducible fabrication methods and functionalization schemes that provide high chemical diversity to the resulting sensors.

Here, we outline a scalable approach to fabricating arrays of vapor sensors consisting of NT field effect transistors functionalized with single-stranded DNA (DNA-NT). DNA-NT sensors were highly reproducible, with responses that could be described through equilibrium thermodynamics. Target analytes were detected even in large backgrounds of volatile interferents. DNA-NT sensors were able to discriminate between highly similar molecules, including structural isomers and enantiomers. The sensors were also able to detect subtle variations in complex vapors, including mixtures of structural isomers and mixtures of many volatile organic compounds characteristic of humans.

Carbon nanotube (NT)-based sensors have been demonstrated for environmental, defense and medical sensing applications [1] using various device configurations, including mechanical resonators [2,3], optical [4] and capacitive [5, 6] sensors, and field effect transistors (FETs) [7, 8]. Chemical modification of the NT surface is a powerful method to influence the interaction strength between the NT and analyte molecules and thereby improve the device sensitivity and specificity. Surface functionalization has been accomplished in many ways, including polymer coatings,[9, 10] atomic doping,[11] decoration with metals[12, 13] or metal oxides,[14] and coating with single-stranded DNA (DNA) [8, 15]. The promise of DNA as a functionalizing agent is based on its complex but completely controlled chemistry, which provides affinity for a wide variety of analytes and enables control of sensor responses through choice of the DNA sequence. DNA is available commercially and is sufficiently cheap for use in scalable device fabrication processes. In previous work,[8, 15] DNA-NT transistors based on individual, CVD-grown nanotubes were used to detect single analytes at concentrations as low as a few ppb and to distinguish between highly similar compounds, including structural isomers and

enantiomers. Responses were fast (seconds), fully reversible, and depended on the identities of the analyte and DNA sequence. Scaling to large arrays was problematic because of the randomness of NT growth, which produces both semiconducting and metallic NTs in a 2:1 ratio, where only the former yield DNA-NT sensors with detectable responses to chemical vapors.[15]

The development of reproducible and scalable fabrication methods for large arrays of NT-based chemical sensors would mark a major step on the path to application of these technologies. Here we report the fabrication of NT FET arrays using commercially available solutions enriched in semiconducting NTs and NT-compatible photolithographic fabrication methods.[16] Arrays of NT FETs had very good device-to-device reproducibility and 90 % yield of useful devices. The arrays were then functionalized to give DNA-NT devices that were tested against compounds characteristically emitted by humans, including a reported volatile marker of skin cancer, as well as sets of molecules with similar chemical structures: *i.e.*, structural isomers and enantiomers. DNA-NT sensors demonstrated highly favorable sensing properties, very similar to those reported for sensors based on single NTs. [8, 15] They showed reproducible responses to single analytes that could be fit to predictions from equilibrium thermodynamics. These responses were almost identical when the target was presented in a background with a high concentration of compounds known to block human olfaction. DNA-NT sensors were found to provide differential responses to highly similar compounds, including enantiomers of limonene, and three distinct forms of pinene, a compound with two structural isomers, each with two enantiomeric forms. DNA-NT devices were also tested against vapor mixtures to provide a more realistic assessment of their potential for use in complex environments and medical diagnostics based on volatile biomarkers. The sensors were found to respond to complex mixtures of volatiles characteristically emitted by humans and to be sensitive to slight alterations of the mixture.

Results and Discussion

DNA-NT vapor sensors were fabricated using a scalable process based on commercial NT solutions, as described in the Methods section. The approach was adapted from earlier reports.[17, 18] Care was taken to develop a method that ensured the production of reproducible arrays of NT transistors where the channel consisted of a relatively sparse NT network (see Fig. 5.4a). To promote adhesion of NTs to the substrate, a reproducible, uniform monolayer of 3-aminopropyltriethoxysilane (APTES) was deposited using atomic layer deposition (Savannah 200, Cambridge Nanotech), with surface pretreatment by introduction of H_2O vapor to increase the concentration of hydroxyl groups. Optimum values of the concentration of the NT solution and the incubation time were found to be 10 mg/mL and 20 min, respectively. Atomic force microscopy (AFM) of a typical device before DNA deposition (Fig. 5.4a) showed a sparse network of NTs, typically 1-3 μm long and 0.5-1.5 nm in diameter, that provided multiple conducting pathways connecting the electrodes. The Raman spectrum of deposited NT films (Supplemental Figure 1 of the Supporting Information) showed a high ratio of the intensities of the G and D bands (G/D ~ 50), indicative of a very low defect density. Additionally, the G band was split into two sharp peaks (G- and G+), confirming the high percentage of semiconducting NTs in the sample.[19] As seen in Fig. 5.4b, current-gate voltage characteristics (I-Vg) of the devices were low-noise with good semiconducting behavior (95% functional device yield with 90% having an on/off ratio exceeding 20; see Fig. 5.4c). The measured distribution of threshold voltages across devices in a typical array (1.5 V ± 1.8 V) was indicative of low doping and high process reproducibility. A histogram of on-state resistances showed a peak in the range of 1 MΩ; 70% of devices had on-state resistances between 400 kΩ and 4 MΩ (Fig. 5.4d). These observations were consistent with

the expectation that a NT network with multiply connected pathways across the 10 µm channel length has minimal likelihood of a metallic pathway and provides reproducibility by averaging over variations in the NT and substrate properties.

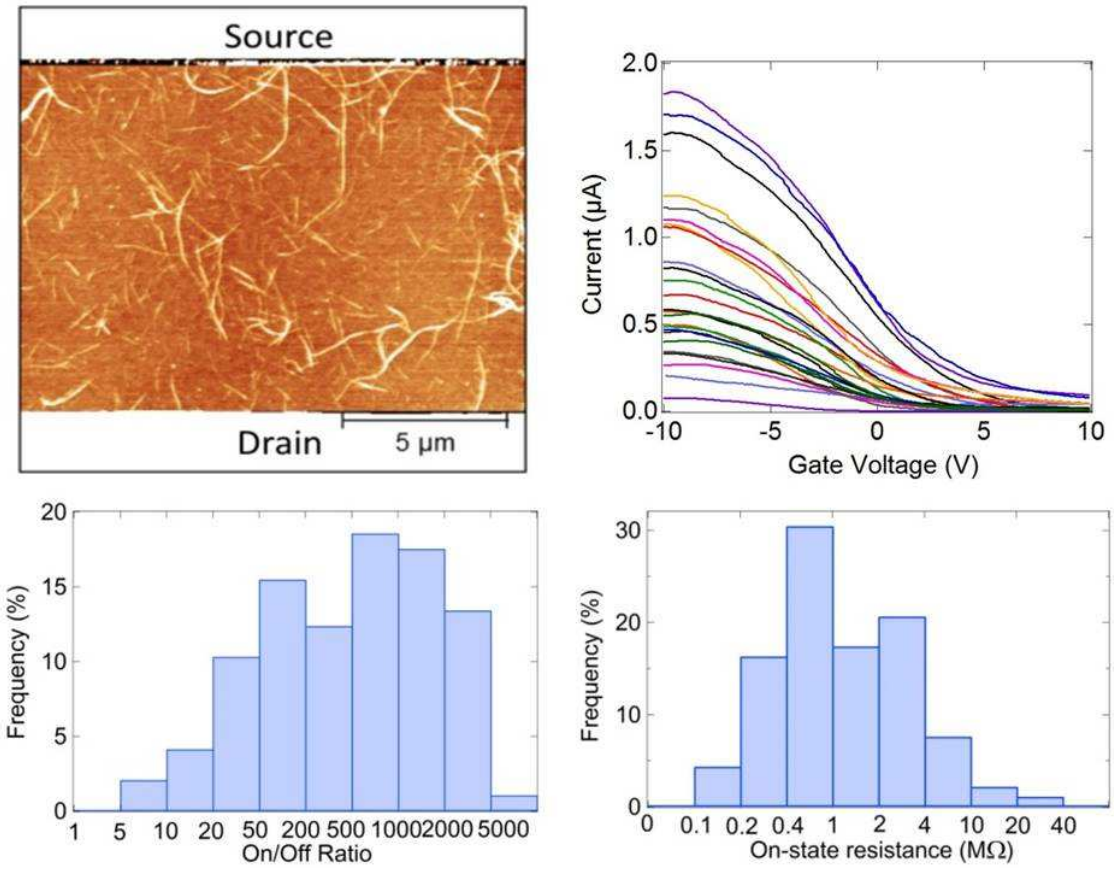

Figure 5.4 a) AFM image of a typical device showing a sparse nanotube network between electrodes. Z-scale is 4 nm. b) I(V_g) curves of a representative set of 25 devices, with V_{DS} = 100 mV. c) Histogram of on/off ratios shows consistent semiconducting behavior and large on/off ratios. d) On-state resistance histogram shows a tight spread, implying good reproducibility across devices.

Electrostatic "chemical gating" has been shown to be a primary mechanism in determining the electrical properties of chemically functionalized NT FETs.[20] It was therefore expected that the magnitude of the change in device current upon exposure to analytes would be

proportional to the transconductance of the device, which was typically proportional to the on-state current (Fig. 5.4b). This justified the use of the normalized change in current, $\Delta I/I_0$, as the sensor response parameter, as used previously for single-NT devices.[15, 21] Other detection mechanisms include changes in carrier scattering and capacitive effects due to adsorbed species. All-atom Molecular Dynamics simulations of DNA-NT indicate that DNA is strongly bound to the NT sidewall by attractive π-π stacking interactions,[22, 23] with a significant number of the bases being desorbed.[24] Our hypothesis is that that this results in a complex, sequence-specific set of binding pockets located within a few nanometers of the NT sidewall. Analyte molecules are solvated by the DNA hydration layer and then bound in the pockets, resulting in the observed DNA-NT signal.

Name	**DNA sequence**
Seq1	5’ GAG TCT GTG GAG GAG GTA GTC 3’
Seq2	5’ CTT CTG TCT TGA TGT TTG TCA AAC 3’
Seq3	5’ GCG CAT TGG GTA TCT CGC CCG GCT 3’
Seq4	5’ CCC GTT GGT ATG GGA GTT GAG TGC 3’

Table 5.1: DNA Oligomers used in this experiment

Four different DNA oligomers were used in this work (Table 5.1). To confirm the formation of a nanoscale DNA layer on the NTs, AFM images were taken of the same region of a NT film before and after DNA functionalization. The data showed a height increase of 0.56 ± 0.2 nm after application of DNA, similar to previous measurements of self-assembled DNA layers on graphene sheets[25] (see Supplemental Figure 2 of the Supporting Information). The substrate height and roughness remained unchanged, indicating DNA deposition was predominantly onto the NTs.

First experiments explored sensor responses to single compounds that are components of human body odors. Dimethylsulfone (DMSO2) is a compound found in human body fluids

including skin secretions and volatiles collected above human skin.[26, 27] It has no apparent odor and has been preliminarily identified as a volatile biomarker of basal cell carcinoma.[28] Isovaleric acid is a component of human sweat with an unpleasant odor;[28, 29] it is an unusual compound in that the limit of detection can differ by as much as a factor of 10,000 between individuals due to genetic variation.[30] Fig. 5.5a shows the responses of five DNA-NT devices based on DNA oligomer Seq2 to DMSO2 (red data) and the average response (black data) at concentrations ranging from 48 – 360 ppb. The device responses were rapid (seconds), reproducible in time and across devices, and they returned to baseline upon flushing with clean air without need for sensor refreshing. Average responses as a function of DMSO2 (isovaleric acid) concentration are plotted in Fig. 2b (Fig. 5.5c) for several DNA oligomers. In both cases the data are well fit by the prediction of a Langmuir-Hill model of analyte binding dynamics,[31]

$$\frac{\Delta I}{I_0} = A\frac{C^n}{{K_a}^n + C^n} + Z$$

Here, *C* is the analyte concentration, *A* is the magnitude of the response when all binding sites are occupied, K_a is the concentration at which half the maximum response is seen and *n* is the Hill coefficient describing cooperativity of binding. The best fit values for the offset parameter, *Z*, were very small, typically less than 0.1%. For the analytes tested, the best fit values for K_a were typically 0.5 to a few 10s of ppm, and the cooperativity parameter was close to 1 suggesting independent analyte binding. We drew the conclusion that DNA-NT devices were in thermal equilibrium with analyte vapors tested, consistent with the observation of rapid response and recovery (Fig. 5.5). Fit parameters for responses of DNA-NT based on the various DNA sequences to DMSO2 and isovaleric acid are summarized in Supplemental Table 1 of the Supporting Information. Additional numerical data quantifying sensor responses to these compounds are presented in Supplemental Table 2.

The sign and magnitude of DNA-NT sensor responses depended on both the DNA sequence used and the analyte. Isovaleric acid (pKa = 4.8) produced a positive signal (current increase), consistent with the expectation that it deprotonated and acquired a negative charge in the DNA hydration layer. DMSO2 was readily detected at the level of 10s of ppb. This species was expected to be uncharged in water, so the signal was ascribed to a dipolar interaction, similar to earlier reports.[20] Along with the results of additional experiments presented below, these data suggested that the DNA/NT sensor class has a high degree of chemical diversity, an important requirement for construction of a functional e-nose system.[32, 33]

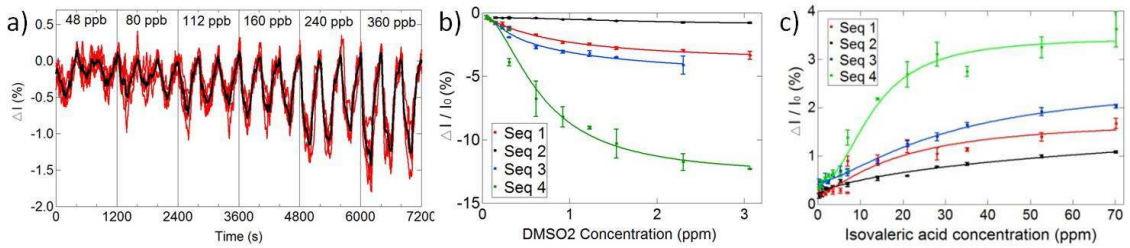

Figure 5.5: a) Responses of five DNA-NT devices based on Seq 4 to repeated pulses of DMSO2, with concentration in the range 48 – 360 ppb (red data). The average response is shown in black. b) Average responses of DNA-NT based on four different DNA oligomers to DMSO2 and the corresponding Langmuir-Hill fits. c) Similar data and fits for responses of DNA-NT based on four different DNA oligomers to isovaleric acid.

We next tested the ability of DNA-NT sensors to differentiate analytes with very similar molecular structure. Experiments were based on enantiomers of limonene and three isomers of pinene, a compound that has two structural isomers, each of which has a pair of enantiomers. The averaged responses of DNA-NT based on Seq1 to the enantiomers of limonene are shown in Fig. 5.6a; there is clear discrimination between these highly similar molecules. The standard Langmuir-Hill fit worked well for the data for D(+) limonene but poorly for L(-) limonene. Responses for L(-) limonene showed anomalous behavior with a positive response at low concentrations that crossed over to a negative response for concentrations exceeding ca. 40 ppm.

This behavior is consistent with the presence of two distinct types of binding sites for limonene, one that leads to a positive response for both enantiomers and one that leads to positive and negative responses for the D(+) and L(-) enantiomers, respectively. Given that our previous experiments, which employed DNA-NT based on Seq1 and single NTs grown by CVD, also showed positive responses for the D(+) enantiomer and negative responses for the L(-) form,[8] we suggest that the binding site that distinguished between enantiomers was associated with the DNA, while the other site corresponded to binding of the analyte to junctions between NTs in the network.

Isomers of pinene were also clearly distinguished by DNA-NT sensors (Fig. 5.6b); both the double bond location and the handedness of the pinene molecule affected the sensor responses, with DNA-NT based on Seq3 showing greater differentiation than those based on Seq1. As a further test of the differentiation power, DNA-NT devices based on Seq1 and Seq3 were tested against mixtures of the α(-) and β(-) structural isomers of pinene (Fig. 5.6c). The averaged responses of 5 devices based on Seq3 provided the ability to resolve composition changes of approximately 5-10% in a vapor where the total pinene concentration was held fixed at 130 ppm. Devices based on Seq1 showed less discrimination power for the mixtures of α(-) and β(-) pinene than those based on Seq 3, consistent with their respective responses to the neat analytes (Fig. 5.6b). Additional data quantifying the response of DNA/NT based on the four oligomers is found in Supplemental Table 2 of the Supporting Information. From these measurements it was concluded that the conformation of DNA bound to the NT sidewall was sufficiently complex to enable differential binding between these sets of highly similar molecules.

Stereo-specific sensing has been reported for other sensor modalities,[34-36] including DNA-NT sensors based on single CVD-grown NTs.[8] The chiral nature of DNA admits the

possibility of stereospecific interactions, which is of particular relevance in understanding the activity of DNA-binding drugs.[37] All-atom Molecular Dynamics simulations provide an approach to understanding the structure of DNA-NT hybrids[23, 24, 38] and should prove useful in unraveling the molecular mechanisms of enantiomer discrimination in this system.

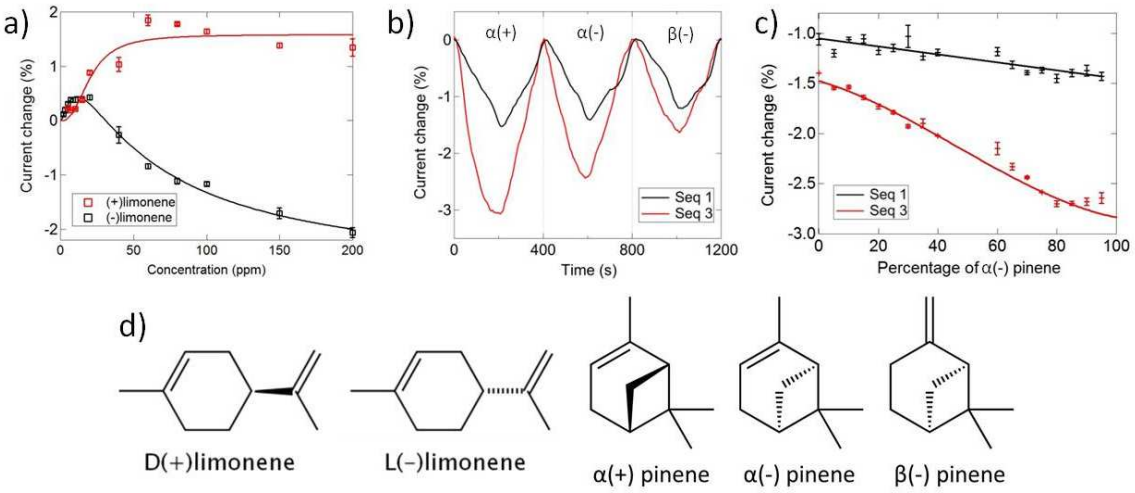

Figure 5.6: a) DNA-NT devices based on Seq1 clearly distinguish limonene enantiomers. The responses to D(+) limonene (red data) are well fit by a simple Langmuir-Hill equation, while responses to L(-) limonene (black data) require a two-component fit, suggesting the existence of two distinct binding sites. b) Responses of DNA-NT based on Seq 1 (black data) and Seq 3 (red data) to pulses of α(+),α(-) and β(-) pinene at a concentration of 130 ppm. The responses depend on both the location of the double bond and the handedness of the molecule. c) The responses of DNA-NT based on Seq1 and Seq3 decrease as the analyte is adjusted from pure α(-) pinene to an α(-)/β(-) mixture to pure β(-) pinene. d) Chemical structures of the limonene and pinene isomers used in the experiments.

DNA-NT sensor responses to isovaleric acid and its more pleasant-smelling ethyl ester (ethyl isovalerate) were examined to determine if the ester blocked the response of the DNA-NT to the acid. This experiment was based on previous studies, using *in vivo* olfaction, which demonstrated that ethyl esters of an organic acid responsible, in part, for human axillary odor[39] (*e.g.*, E-3-methyl-2-hexenoic acid), reduced the perception of this malodorous compound.[40] Strikingly, responses of DNA-NT sensors based on Seq3 to the target isovaleric acid at

concentrations of 7 – 53 ppm in clean air were almost identical to the responses in an interfering background of ethyl isovalerate at 3300 ppm (Fig. 5.7a).

In a second test, introduction of 460 ppm cis-3-hexen-1-ol left the responses of DNA-NT based on Seq3 to DMSO2 at 0.76 – 6.1 ppm essentially unchanged (Fig. 4b). This is significant because cis-3-hexen-1-ol is known to mask odors from human olfaction and is used in deodorant products by the fragrance industry.[41, 42] The lack of effective blocking of the response in these two cases presumably derives from the fact that the nature of DNA as a "receptor" for volatile compounds differs significantly from that of human olfactory receptor proteins (ORs). Thus, compounds that act to diminish the binding of specific volatiles to human ORs may have little or no effect on responses of DNA-NT devices.

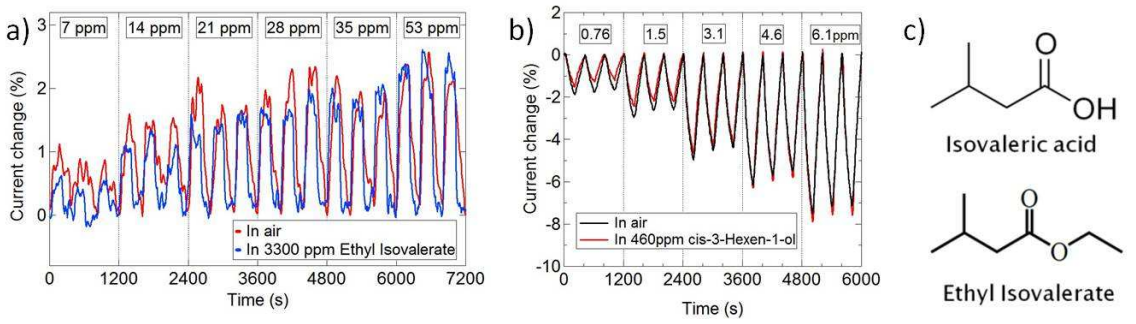

Figure 5.7: a) DNA-NT sensors based on Seq3 show near identical responses to 7-53 ppm isovaleric acid in clean air (red data) and in a background of 3300 ppm ethyl isovalerate (blue data). b) Average responses from four DNA-NT sensors based on Seq3 to 0.76 – 6.1 ppm DMSO2 in clean air (black data) and in a background of 460 ppm cis-3-hexen-1-ol (red data). c) Chemical structures of target analyte isovaleric acid and blocking compound ethyl isovalerate.

An essential characteristic of biological olfactory systems is the ability to differentiate between very similar *complex mixtures* of volatile compounds. Experiments to test the ability of DNA-NT devices in this domain were based on a mixture of 17 organic compounds, many of which are volatile and found in non-axillary skin sweat.[25] These were dissolved in physiological saline (see Table 5.2). DNA-NT devices were exposed to the headspace vapor of the original "parent"

mixture and also to that of “spiked” mixtures where one component was increased in concentration by a factor of 2-10. “Spiked” mixtures were based on compounds that were prevalent in the mixture (acetic acid) and those found in trace amounts (stearic acid and nonanal), with widely varying vapor pressures.

Compound	Concentration, mg/mL	Vapor Pressure, Torr (@ 20 C unless stated)
Acetic Acid	0.67	3.0
Lactic Acid	0.66	0.08
Glycerol	0.17	1 @ 125 C
Stearic Acid	0.03	1 @ 174 C
Acetoin	0.05	2.69
Propanoic Acid	0.09	2.9
Isobutyric Acid	0.01	1.5
Butyric Acid	0.45	0.43
Isovaleric Acid	0.01	0.38
2-Methylbutyric Acid	0.01	0.5
Isocaproic Acid	0.01	N/A
4-Methyl-phenol	0.05	1
Phenol	0.01	0.36
Dimethylsulfone	0.05	N/A
Nonanal	0.01	0.26
Indole	0.03	0.03
Squalene	0.20	2 @ 240 C

Table 5.2: Concentration and Vapor Pressure of Components of the Parent Complex Mixture Used in the Experiments

The concentrations of various components in the headspace of the mixtures were not measured. However, estimates were made using Raoult’s law, which assumes that the concentration of a mixture component is the product of the vapor pressure of the component and its molar fraction in the solution. For the parent mixture this yielded 793 ppb for acetic acid and 0.43 ppb for nonanal. Stearic acid is a solid at room temperature with a very low vapor pressure (see Table 5.2). Although no precise estimate could be formulated, the expected concentration in the headspace of the parent mixture would surely be well below 1 ppb. For a

spiked mixture, these concentrations were multiplied by the appropriate spiking factor (*i.e.*, 2x, 5x, or 10x).

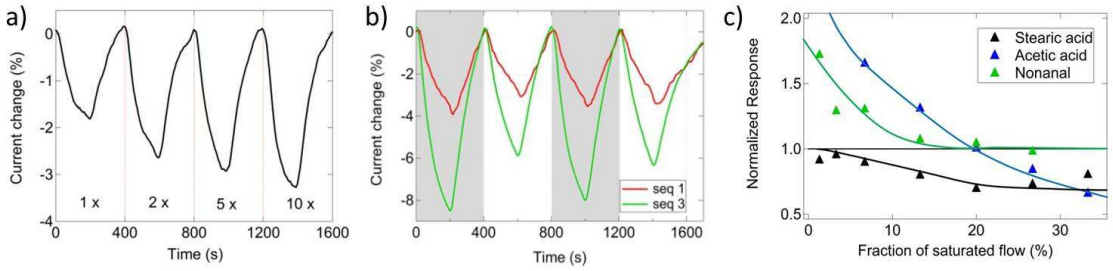

Figure 5.8: DNA-NT device based on Seq3 provides clear differential responses between the "parent" mixture and mixtures "spiked" with nonanal by factors of two, five and ten (2x, 5x, 10x, respectively). b) Responses of DNA-NT based on Seq1 (red data) and Seq3 (green data) to 33% saturated vapor of the "parent" mixture (gray background) and a "spiked" mixture with 10x increased concentration of stearic acid (white background). Devices based on Seq3 show a strong differential signal to the two mixtures while the differential signal for DNA-NT based on Seq1 is weak. c) Responses of DNA-NT based on Seq4 to diluted streams of headspace vapor of "spiked" mixtures, normalized to the response to the parent mixture. In each case, the named component is spiked by a factor 10x compared to its concentration in the parent solution. Markers are experimental data, and the solid lines are guides to the eye.

The spiked mixtures were exposed to DNA-NT devices concurrently with the standard mixture and the sensor responses ($\Delta I/I_0$) were recorded. DNA-NT devices were typically, but not always, found to provide strong differential responses between the parent mixture and spiked mixtures. Responses of DNA-NT based on Seq3 were very sensitive to the concentration of nonanal in the mixture (Fig. 5.8a). We note that the estimated concentration of nonanal in the vapor ranged from 0.43 – 4.3 ppb. Differential response of DNA-NT devices to the "parent" and "spiked" mixtures depended on the identity of the DNA oligomer. For example, responses of DNA-NT based on Seq1 to the "parent" mixture and a mixture "spiked" by 10x with stearic acid were nearly identical, while responses of DNA-NT based on Seq3 showed clear differentiation between these two mixtures (Fig. 5.8b, red and green data, respectively). The concentration of stearic acid in the vapor is not precisely known but is almost certainly at the level of a few ppb or lower. The implication is that stearic acid does not significantly bind to Seq1 in the presence of all the other

VOCs but that it does bind strongly to sequence 3. Furthermore, a very rich data set was obtained by considering DNA-NT differential responses to the headspace vapor of the "spiked" mixture at various dilutions with clean air. As seen in Fig. 5.8c, the dependence of the differential responses of DNA-NT based on Seq4 with dilution depends on the identity of the "spiked" component. Consequently, real world mixtures could potentially be identified by comparison to a standard mixture using DNA-NT sensors. By measuring response deviation as a function of dilution, it could be possible to identify exactly which compound in the mixture has been altered and by how much its concentration has changed.

Conclusions

In summary we have demonstrated a facile, potentially scalable method for fabricating DNA-NT vapor sensors that could enable their use in sensor arrays suitable for incorporation into an electronic nose system. We tested device responses against individual VOC analytes characteristic of humans and against complex mixtures that more closely resemble "real-world" samples. DNA-NT sensors showed excellent reproducibility, they responded within seconds to parts per billion concentrations, and their responses were in good agreement with predictions of equilibrium thermodynamics. Devices were able to differentiate between analytes with very similar molecular structure (*i.e.*, enantiomers and structural isomers), they were able to detect target analytes in a large background of an interfering VOC, and they could discriminate subtle changes in complex VOC mixtures. The use of DNA as the functionalizing agent holds the possibility that arrays of hundreds or thousands of individual sensors could be fabricated on a single chip and functionalized with a large number of different DNA oligomers. As each sequence has its own set of characteristic responses to a large number of various analytes, this approach

should allow analytes to be detected and distinguished at relevant concentrations across many applications, including deducing chemical composition in an unknown environment or disease diagnosis from VOCs.

Materials and Methods

Device Fabrication and Functionalization: Electrical contacts for FETs with channels 10 μm long and 25 μm wide were patterned by photolithography and metallized with Cr/Au *via* thermal evaporation. After O_2 plasma cleaning to remove residual photoresist, a 3-aminopropyltriethoxysilane (APTES) monolayer was deposited using atomic layer deposition (Savannah 200, Cambridge Nanotech), with surface pretreatment by introduction of H_2O vapor to increase the concentration of hydroxyl groups. Semiconducting NTs were deposited from solution (NanoIntegris, Isonanotubes-S 98%) by pipetting onto the surface of the chip and incubation in a humid atmosphere for 20 minutes. The NT-FET arrays were cleaned by immersion in isopropanol followed by immersion in a deionized (DI) water bath, followed annealing at 200°C for 1 hour to improve the electrical contacts. DNA solutions with a concentration of 100 μM were prepared by adding deionized (DI) water to as-received DNA (Invitrogen). Devices were functionalized by incubation in droplets of DNA solution in a humid atmosphere to suppress droplet evaporation. After 30 minutes, the DNA solution was blown off the wafer with compressed nitrogen, taking care not to cross-contaminate devices with other DNA sequences.

Preparation of Chemical Mixtures: A 5000 ppm solution of dimethylsulfone (DMSO2; Cambridge Isotope Laboratories, Inc.) in dipropylene glycol was prepared by heating and sonicating. The headspace concentration was measured by gas chromatography-mass spectrometry, as previously described,[8] and found to be 23 ppm. Other analytes used were purchased from Sigma

Aldrich and used as received. Mixtures of analytes were made by diluting in deionized water and shaking and sonicating as required to dissolve.

Acknowledgements

We acknowledge useful discussions with Dr. E. Dattoli. This research was supported by the Department of Defense US Air Force Research Laboratory and UES through Contract Nos. FA8650-09-D-5037 as well as support from the Army Research Office through grant #W911NF-11-1-0087. M.L. acknowledges the support of a SMART Fellowship. N.J.K. and J.S.Y. acknowledge the support of the Nano/Bio Interface Center through the National Science Foundation NSEC DMR08-32802. Use of the facilities of the Nano/Bio Interface Center is also acknowledged.

Supporting Information Available: Raman spectroscopy data for carbon nanotube films, indicating their low defect density and high content of semiconducting nanotubes. AFM data and associated histogram used to determine the distribution of diameters of the carbon nanotubes. Tables showing 1) details of the Langmuir-Hill fits for four different DNA sequences and two vapor analytes (DMSO2 and isovaleric acid); 2) response data for analyte-DNA oligomer combinations tested; and 3) response data for DNA-NT based on various DNA oligomers tested against the "parent" and "spiked" mixtures mentioned in the main text. This information is available free of charge *via* the Internet at http://pubs.acs.org.

5.3 Analysis of sweat simulant mixtures using multiplexed arrays of DNA-carbon nanotube vapor sensors

The results presented in this section have also appeared in the publication "Analysis of sweat simulant mixtures using multiplexed arrays of DNA-carbon nanotube vapor sensors", N. J. Kybert, L. Egan, R. Z. Waldman, X.-N. Zeng, M. Krein, G. Preti, J. A. Stuart, A. T. C. Johnson, *J. Forensic Sci. Criminol.*, 2014, 1(S102) doi: 10.15744/2348-9804.1.S102

Carbon nanotube (NT) based electronic vapor sensors were tested against synthetic sweat solutions, consisting of 13 volatile organic compounds (VOCs) in saline, in order to probe the device ability to analyze and differentiate vapors derived from complex biological samples. Arrays of up to 56 NT devices each were fabricated and functionalized with single stranded DNA to increase sensitivity and selectivity. DNA/NT devices were able to differentiate changes as small as 50% in a compound with estimated concentration in the vapor was at part-per-billion levels, in a complex vapor background that contained the thirteen VOCs. This sensor class has vapor response times on the order of ten seconds, and is reusable and self-refreshing. The fabrication process is scalable, and sensor arrays are compact compared to traditional analysis equipment such as gas chromatography/mass spectrometry (GC/MS). The detectable differences among the simulated sweat mixtures were on the same scale as person-to-person variations in VOCs reported by others previously, demonstrating that DNA/NT vapor sensors show great promise for odor-based chemical biometric applications.

INTRODUCTION

Humans emit a variety of volatile organic compounds (VOCs) in urine, sweat and other bodily fluids. A large body of literature now shows that an individual's emitted odors form a

unique chemical profile [43-45]. For example, studies have shown that VOC profiles possess characteristic components that depend on diet [46], gender [47], age [48] and ethnicity [45, 49, 50]. Sweat composition is also known to vary under stress, so much so that studies have shown that chemosignals of stress influence social judgments [51]. Olfactory evaluation can be an important part of clinical examination [52] and certain volatile compounds, emitted through the skin and other bodily fluids, have been shown to be possible biomarkers for a whole host of diseases and disorders [26, 53, 54]. However, this information, contained in the individual's volatile signature, remains essentially untapped. Techniques to quantitatively analyze VOC profiles in sweat and other bodily fluids could find applications in disease diagnostics, health and wellbeing monitoring and even for detection, identification or tracking of individuals.

Gas chromatography/mass spectrometry (GC/MS) and related techniques have been the most widely used methods of analyzing complex VOC profiles to date. These are "gold standard" techniques for researching unknowns, given the methods' ability to separate, identify and quantify compounds in complex mixtures of volatile compounds. However, there remains a need for technologies that can perform similar analysis quickly and efficiently on mixtures of known VOCs without the cost and bulk associated with current commercial techniques such as GC/MS, either desktop or smaller sized.

Vapor sensors based on low-dimensional carbon nanomaterials, such as graphene and carbon nanotubes (NTs), have been shown to have many of the required characteristics for such a task. These materials combine a favorable 'all-surface' geometry that maximizes the sensor's exposure to the vapor sample with highly sensitive electronic properties that are strongly affected by the local charge and molecular environment. Furthermore, their highly ordered surface structures allow for controlled chemical functionalization, including via covalent and π- π stacking

interactions. Surface modifications have included decoration with metals [12, 13] and metal oxides [14], polymer coatings [9], atomic doping [11] and functionalization with biomolecules [21], in particular single-stranded DNA [8, 25, 55, 56] . The advantages of DNA include its straightforward π- π stacking interaction with NTs and its complex yet controlled chemical structure, which causes self-assembled DNA layers on NTs to have binding sites for a wide array of volatile molecules. Conductance responses of the sensors upon exposure to analyte vapors are DNA-sequence dependent and an almost unlimited number of potential DNA sequences are available. DNA is also sufficiently inexpensive to be incorporated in large-scale device fabrication.

Previous studies on electronic vapor sensors based on DNA-functionalized carbon nanotubes have demonstrated the ability of these sensors to detect target analytes down to parts-per-billion level concentrations. These sensors can also discriminate between very similar molecules, such as homologous series of linear aldehydes and carboxylic acids, structural isomers and enantiomers [8, 55]. The device sensitivity is also maintained if the target is in a background of other, chemically similar, VOCs. Initial experiments on complex vapors from dilute mixtures of volatile compounds showed that sensors could distinguish changes in the mixtures [55].

In this work, we demonstrate that arrays of DNA/NT vapor sensors have sufficient detection and discrimination power to provide information on VOC contents of extremely similar synthetic axillary sweat mixtures. These synthetic sweat solutions are based on previous studies of Zeng et al. [47, 57] and consist of 13 of the characteristic odiferous compounds diluted to the average levels found in a group of males' axillary sweat. Headspace vapor from synthetic sweat solutions was pulsed into a chamber containing DNA/NT vapor sensors, and sensor responses to the VOCs were observed at the initial headspace concentration and when diluted by up to an order of magnitude with clean air. A series of very closely related solutions were synthesized by

changing the concentration of one of the components (either 9-decenoic acid or 3-methyl-2-hexenoic acid) to a value in the range 0-500% of the starting concentration. The differences in the solutions tested were smaller than variations in VOC profiles among individuals reported by other groups [43, 45]. The sensors demonstrated the ability to distinguish solutions between which the altered component's concentration differed by as little as 50%, while all other 12 components remained fixed. These differences are smaller than typical person-to-person variations in VOC profiles in sweat. Consequently, these results show that DNA/NT sensors could be appropriate for a variety of next-generation odor-based chemical biometrics tests with applications in determining the health, wellbeing or identity of individuals based on volatile signatures.

METHODS

DNA/NT array fabrication: The procedure was similar to previous experiments [55]. Many arrays of 56 devices each were fabricated in parallel on Al_2O_3 coated Si/SiO_2 wafers by first using photolithography/metallization to produce Cr/Au electrodes and then drop casting semiconducting-enriched (98%) nanotube solution (NanoIntegris Inc.) onto the chips. Careful washing, cleaning, and annealing steps were performed to remove surfactants and ensure good electrical contact between the NTs and gold electrodes [55].[25] Finally, DNA functionalization was performed by pipetting 100μM DNA solution onto the devices and allowing the DNA strands to diffuse to and bind onto the sidewalls of the NTs. The DNA strands bind via the π- π stacking interaction between the DNA bases and the NT surface [22, 23]. After 30 minutes the DNA solution was blown off the chip with compressed nitrogen gas, taking with it all unbound DNA, and the devices were ready to use. Four different randomly selected DNA sequences were used in this work, as shown in table 5.3.

Seq2	5’ CTT CTG TCT TGA TGT TTG TCA AAC 3’
Seq3	5’ GCG CAT TGG GTA TCT CGC CCG GCT 3’
Seq4	5’ CCC GTT GGT ATG GGA GTT GAG TGC 3’
Seq8	5’ AGT TCG GCA TGT GGA AAC TCC TTC 3’

Table 5.3: DNA sequences used in this work

Synthetic sweat: The composition of the sweat solutions was guided by previous studies [47, 57]. The male donors (N = 6) who were used to create the pooled, male axillary extracts analyzed by Zeng *et al*. also donated six separate axillary pads which were pooled by individual, extracted and analyzed separately. For each subject, the components constituting the characteristic axillary odorants were quantified using standard curves made from both commercially available and synthesized compounds (e.g., E-3-methyl-2-hexenoic acid). The amount of 3-hydroxy-3-methyl-hexanoic acid was estimated from the study of Natsch et al [58].

The mean amounts of each compound found in the six male donors were used to create the respective concentrations in the ‘standard’ sweat mixture used in this study; these are shown in table 5.4. The components were obtained commercially (Sigma Aldrich Co. unless otherwise stated) when possible. 3-Hydroxy-3-methyl-hexanoic acid (3H3MH), was obtained from PharmBlock, Inc. (Middleton, NY). Samples of E-3-methyl-2-hexenoic acid (3M2H) were obtained by synthesis [47]. The compounds were dissolved in deionized water by shaking and gentle heating. Finally 9g/L of sodium chloride was added to match physiological saline levels.

Compound	Concentration (mg/L)	Vapor Pressure (Torr)
Hexanoic acid	35	0.18
4-Ethylpentanoic acid	0.8	0.058
2-Ethylhexanoic acid	5	< 0.01
Heptanoic acid	16	0.011
3-Methyl-2-hexenoic acid	100	0.105 (est.)
Octanoic acid	42	0.02
7-Octenoic acid	11	0.0115
Nonanoic acid	55	1.7×10^{-3}
4-Ethyloctanoic acid	1	0.0018
8-Nonenoic acid	5	0.003 (est.)
Decanoic acid	61	3.7×10^{-4}
9-Decenoic acid	9	0.018
3-Hydroxy-3methyl-hexanoic acid	15	0.001

Table 5.4: Components of the standard sweat solution and their respective concentrations and vapor pressures.

Vapor delivery and sensor array readout: Vapors were delivered to the arrays of DNA/NT devices using a lab-built system, described previously [55]. A stream of clean, dry air was passed through a bubbler containing either a pure VOC or a sweat simulant and then diluted with streams of clean, dry air and clean, humidity-saturated air. By controlling the ratios of the three flows and mixing them before flowing through the sample chamber, the bubbler headspace vapor could be diluted as desired. The vapor samples were passed across the sensors for 2 minutes, after which the chamber was flushed with clean air for two minutes and a new measurement was taken in the same fashion. The humidity level of the sample chamber was held fixed at 50% unless otherwise noted, while the total flow rate through the sensing chamber was held fixed at 1000 sccm. A picoammeter (Keithley 6485) and multiplexing switching matrix (National Instruments PXI 1033) were used to read the current flow through the devices sequentially, measuring the whole array approximately every two seconds.

RESULTS AND DISCUSSION

After fabrication, devices were characterized by atomic force microscopy and electrical transport measurements, as shown for a typical device in fig. 5.9. Devices consisted of 1-3 µm long single-wall carbon nanotubes, joined together in sparse networks to span the 10 µm gap between the electrodes. The devices showed reproducible p-type electronic behavior, with ~ 95% of the devices exhibiting on-off ratios exceeding 20. As the sensor response mechanism for acids is typically chemical gating by positively charged deprotonated molecules, an increase in the device current upon exposure to the sweat stimulant vapor was expected. To compare devices with different on-state currents, the sensor response is reported as the percentage change in the current, $\Delta I/I_0$. The gate voltage was held fixed at -8 V for all vapor sensing measurements to maintain a high current level and transconductance, with the goal of maximizing the signal-to-noise ratio.

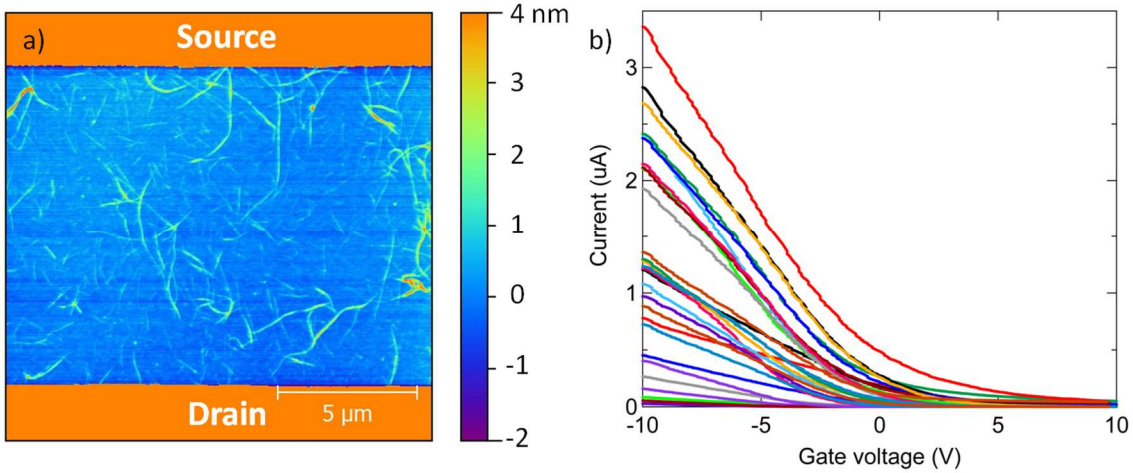

Figure 5.9: a) AFM image of a typical device showing a sparse nanotube network between electrodes. b) I(Vg) curves of a representative set of 28 devices from one of the sensor arrays, measured with V_{DS} = 100 mV.

As a first experiment, two compounds found in the sweat mixture, 9-decenoic acid and hexanoic acid, were tested separately in a background of clean air. As expected based on other

studies,[20] the sensors showed positive, albeit different, responses to both acids (Fig. 5.10a,b) with response times on the order of ten seconds (Fig. 5.10c). We hypothesize that the positive responses are due to deprotonation of the carboxylic acids within a nanoscale water layer bound to the DNA/NT. This is consistent with acid dissociation constants of 4.86 and 4.78 for hexenoic acid and 9-Decenoic acid respectively. For 9-Decenoic acid, the limit of detection is below 1.2ppm, the lowest concentration tested here.

Next, the standard sweat simulant, as defined in table 5.4, was tested. In fig. 5.10d, the dynamic responses of seq2 and seq8 functionalized devices to this mixture are shown. In this trial, the humidity was fixed at 100%, i.e. the headspace was diluted by fully humidified clean air. This approach allowed concentrations up to the pure simulant headspace to be analyzed without varying the humidity, ensuring that the sensors' responses could only be a result of the VOCs as everything else in the vapor transported into the sensor chamber was identical. All four sequences showed positive responses to the sweat mixture, as would be expected given that the components are various acids. The current change varied between 1% and 4% at the highest concentration, depending on the DNA sequence used.

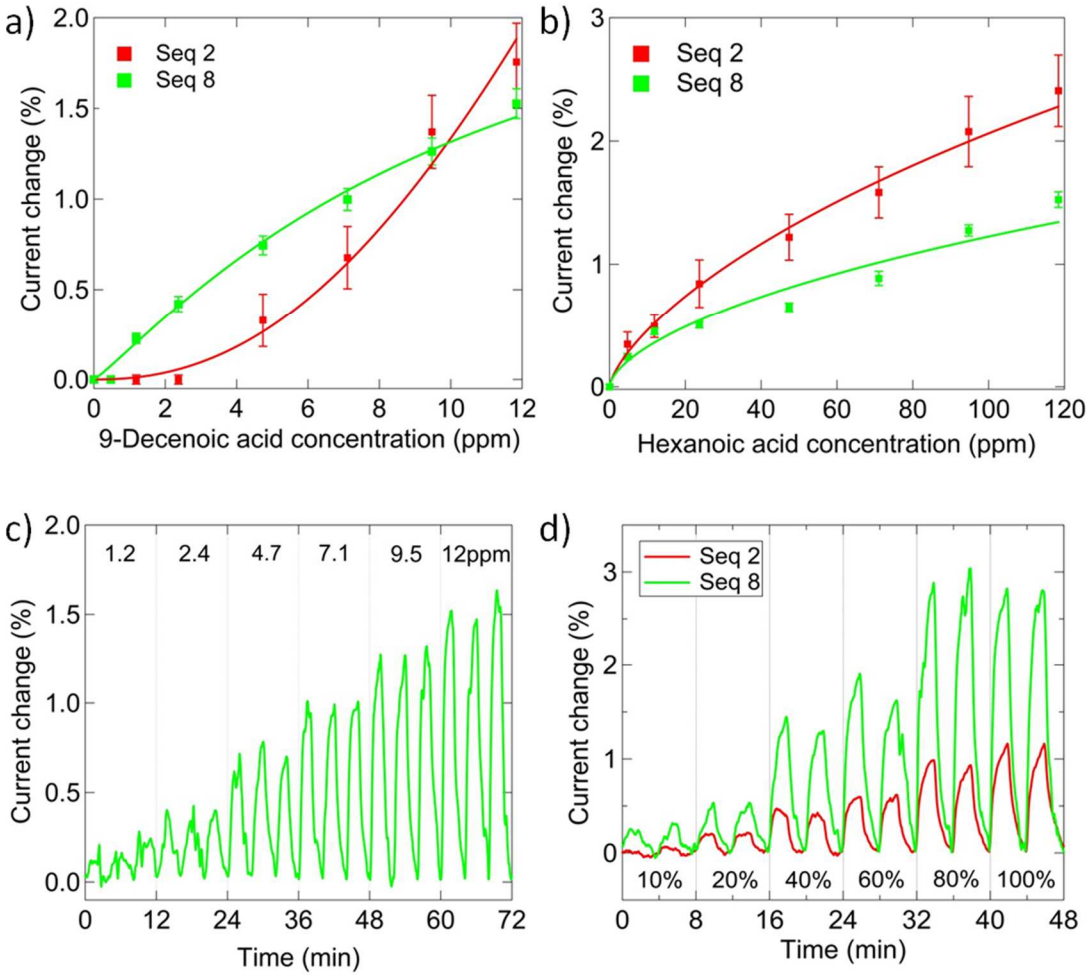

Figure 5.10 a) Current change as a function of 9-Decenoic acid concentration for 2 different DNA sequences. b) Current change as a function of hexanoic acid concentration for 2 different DNA sequences. c) Dynamic data, averaged across 16 devices, used to get seq8 trace in a. The humidity level in panels a)-c) was 50%. d) Responses for seq2 and seq8 functionalized devices to the synthetic sweat mixture at increasing concentrations. Humidity was fully saturated for this trial.

As a first step toward demonstrating and quantifying the ability of DNA-NT devices to detect changes in the composition of the simulant mixture, sensors based on seq3 were exposed to the standard mixture and a mixture where the compound 3H3MH was omitted. The sensors were able to distinguish the two mixtures, with smaller responses observed for the 3H3MH-free solution (Fig. 5.11a).

Next, a series of experiments was then carried out in which the concentration of a component in the mixture was varied between zero and 500% of the standard concentration. Two components were chosen for this, 3M2H and 9-Decenoic acid. 3M2H was chosen because it has been shown to be a principal contributor to human underarm odor [57] and suggested as a uniquely human odorant [59]. Furthermore, 3M2H concentrations, as well as other axillary odorants, have been shown to vary across ethnicities [45]; the standard mixture, detailed in table 5.4, contains a 3M2H concentration of 100 mg/L, a value chosen based on studies of Caucasian males' axillary sweat. Recent studies on a group of Japanese males found that the concentration of 3M2H in their axillary sweat is much lower, in the range 0-5 mg/L.[45] 9-Decenoic acid was chosen as a second component to vary due to its lower concentration in the simulated sweat solution (and headspace), which would make changes in its concentration more challenging to detect.

The concentrations of components in the headspace of the mixtures were not measured directly. However, estimates were made using Raoult's law, which assumes that the concentration of a mixture component is the product of the vapor pressure of the component and its molar fraction in the solution. For the standard solution, this yields a headspace concentration of 2 ppb for 3M2H and 0.02 ppb of 9-decenoic acid. Although it is known that real solution mixtures may show deviations from Raoult's law due to non-ideal mixing and chemical interactions between the constituents that change the components' effective vapor pressure, it is likely that the concentration of these VOCs in the headspace is extremely low (few ppb level or smaller). Moreover, the data presented below demonstrate that the DNA/NT sensor system is able to differentiate between mixtures where the amount of these compounds was changed by as little as 50% of the standard concentration. This implies that even this modest-sized DNA/NT array is

capable of detecting changes of just a few ppb in one component of a 13-component vapor mixture.

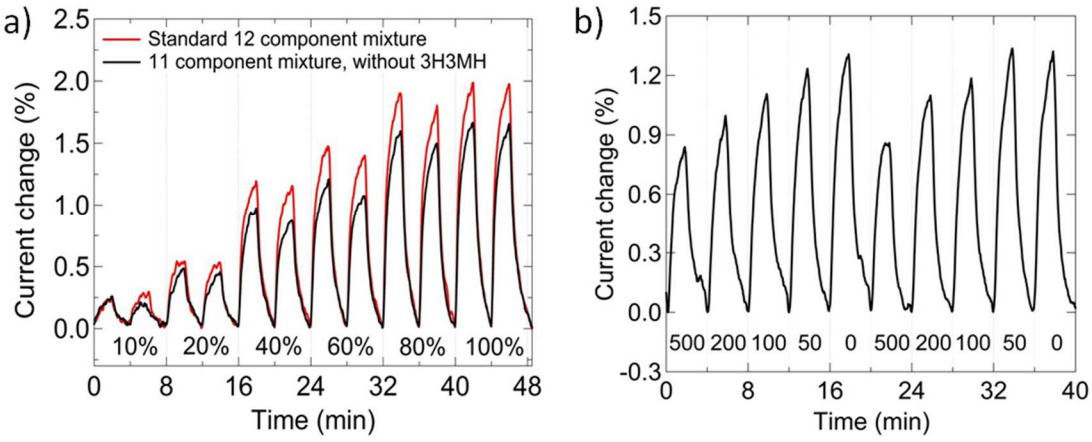

Figure 5.11: a) Dynamic responses from DNA/NT devices based on seq3 to vapors from sweat simulant mixtures differing only by the omission of one component, 3H3MH. Neither solution included 3M2H, which was obtained after this measurement was conducted. b) Dynamic responses from seq3 devices to 50% saturated vapor of 5 solutions of synthetic sweat with varying concentrations of 3M2H. Labels (0-500) refer to the percentage concentration of 3M2H in the solution responsible for each vapor pulse, referenced to the standard solution of Table 5.4. The set of measurements is repeated twice, and excellent reproducibility is observed.

Fig. 5.11b shows typical time-dependent data for this set of experiments, in this case the averaged signal from 12 identical prepared DNA/NT sensors in an array of devices. Solutions contained 0, 50, 100, 200 or 500% of the standard concentration of 9-decenoic acid or 3M2H, with the concentrations of all other components held fixed. The devices were exposed to the 5 solutions sequentially (in each case, a vapor sample was passed across the sensors for 2 minutes, after which the chamber was flushed with clean air for two minutes), and the series of measurements was repeated twice. Fig. 5.11b shows clear differentiation of the five solutions with varying 3M2H. Interestingly, the response magnitude decreases as the concentration of 3M2H is increased. While this may appear counterintuitive given that 3M2H is a carboxylic acid, it is possible that this occurs due to competitive binding between 3M2H and other molecules on

the sensor surface, so that the presence of additional 3M2H prevents the binding of other acids that generate larger responses.

As shown in fig. 5.12, opposite effects were observed for each of the four DNA sequences upon increasing either the concentration of 9-decenoic acid or 3M2H in the solutions: the sensor responses increased for all four DNA sequences as 9-decenoic acid (circles) was increased but decreased with increased relative concentration of 3M2H (squares). In each plot, the response magnitude for the standard solution is normalized to 1, allowing for easier comparison between sequences. The trends are similar across all sequences, with additional 3M2H leading to a decreased response and additional 9-Decenoic acid increasing the response for all sequences. However, the magnitude of the effect varies with DNA sequence: Seq2 and seq3 show the largest overall change in response magnitude, while seq4 is particularly sensitive to low concentrations of 9-Decenoic acid and most insensitive to 3M2H.

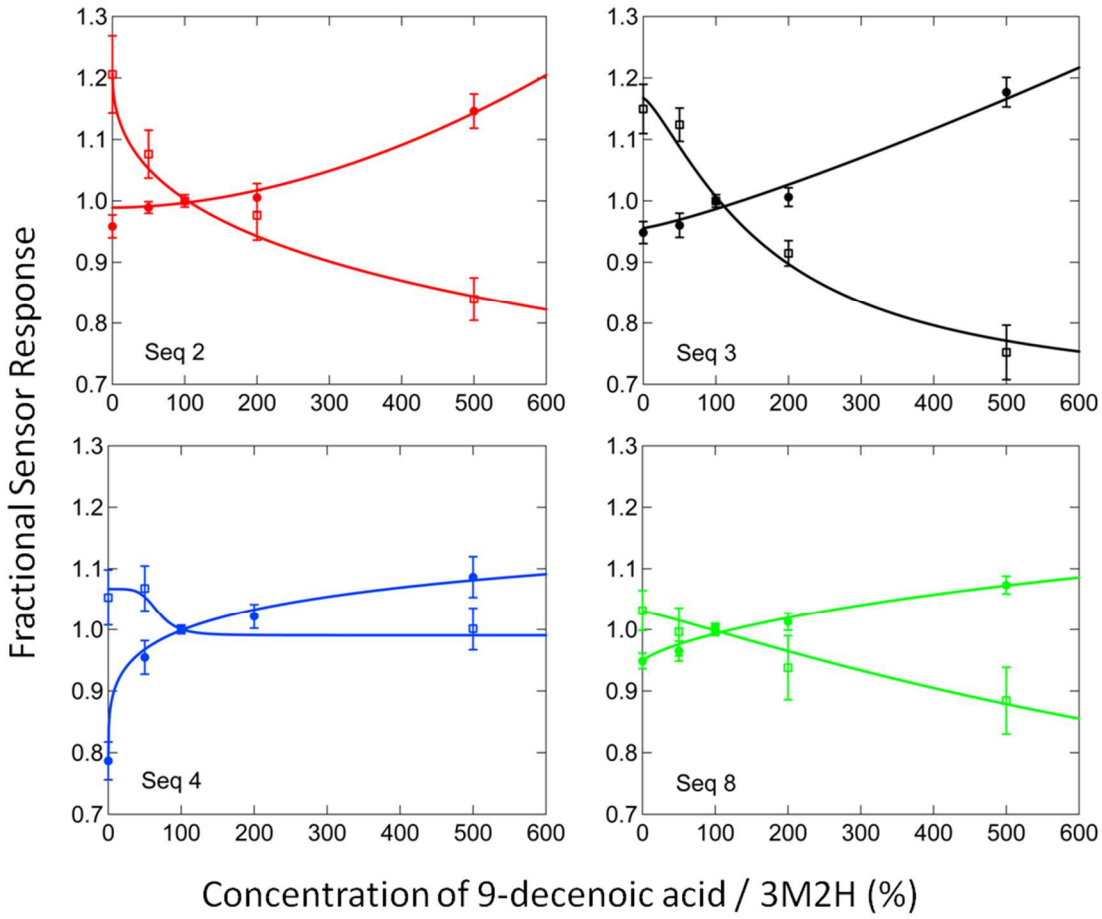

Figure 5.12: Normalized sensor responses for DNA/NT based on 4 different DNA sequences as the concentration of 9-Decenoic acid (filled circles) and 3M2H (open squares) are varied. The concentration of 9-Decenoic acid / 3M2H is varied between zero and 500% of the standard amount. The error bars reflect the spread of fractional sensor responses. Between 7 and 17 devices were used in each experiment.

We can claim that two solutions are distinguishable by an array of DNA/NT based on these four DNA sequences if the sensor response error bars do not overlap for at least one sequence. Using this definition, the set of 3M2H-varying solutions are all distinguishable from each other. The set of variable 9-decenoic acid solutions contains one pair (100% and 200% of the standard concentration) that is not significantly distinguishable based on the limited data set above. Also, if we consider the full set of 9 different solutions, another currently indistinguishable pair emerges (500% 9-decenoic and 0% 3M2H). However, we would expect that by increasing the number of

devices or the number of different DNA sequences used, full distinguishability should be obtainable. Furthermore, statistical techniques such as principal component analysis could be employed to determine the linear combinations of the raw data that best distinguish the solutions.

In conclusion, we have demonstrated a viable technology for fast, cheap, all-electronic analysis of known odor profiles based on DNA/NT vapor sensors. Synthetic solutions were chosen to allow controlled composition changes to be made, and a set of very similar solutions was distinguished using arrays based on 4 different DNA sequences. The techniques used here could be scaled up to include tens or hundreds of DNA sequences being read out simultaneously, while remaining small and cheap enough to be incorporated into a handheld device. The chemical diversity of DNA suggests that such a set of sensors would have great analytical power, allowing odor-based chemical biometrics to advance from a research topic to truly impactful health and forensic applications.

ACKNOWLEDGEMENTS

This work was supported by Lockheed Martin Advanced Technology Laboratories, as part of the NSF Accelerating Innovative Research Project AIR ENG-1312202. We acknowledge use of equipment associated with the Scanning Probe Facility of the Nano/Bio Interface Center, NSEC DMR08-32802.

5.4 Exploring Ovarian Cancer Screening using a Carbon Nanotube-DNA hybrids to Capture its Volatile Odor Signature

Introduction, Background and Motivation:

There were approximately 21,300 new cases of ovarian carcinoma are expected in the US in 2015, resulting in an estimated 14,200 deaths [60]. Diagnosis of ovarian cancer is complicated by the fact that cancers of the ovaries frequently cause no symptoms at all and when they do, the symptoms are diverse and non-specific. Complaints of bloating, pelvic pain, difficulty eating and urinary frequency are often misdiagnosed could be the result of gastrointestinal illnesses or other common ailments and consequently the rate of false diagnosis is very high [60].

Even more problematically, there is a complete lack of reliable screening strategies for accurate and early detection of ovarian cancer in women of average risk. Two proposed screening methods are transvaginal ultrasounds, which hope to image tumors of the ovaries and a blood test for a protein biomarker, CA-125. Unfortunately, transvaginal ultrasounds find many non-cancerous masses, unnecessary treatment of which causes significant risks for the patient. Similarly, while it is true that CA-125 levels are elevated in women with ovarian cancer, it has not proved useful as a screening test because there are other common conditions that cause high levels of CA-125. Consequently, a large scale annual screening trial, combining transvaginal ultrasound and CA-125 screening found that the combination “does not reduce disease-specific mortality in women at average risk for ovarian cancer” [61].

Since there are currently no reliable, early detection methods for ovarian cancer, only 15% of all ovarian cancers are diagnosed at a local stage (i.e., before metastasis) [62]. When diagnosed early, ovarian cancer has an excellent prognosis with a greater than 90% 5 year survival rate. However, the more common late stage of detection results in limited therapeutic strategies

with resulting high morbidity and mortality, with a survival rate of only 30% [62]. Consequently, any reliable technique that can accurately detect ovarian cancer in its early stage would yield better prognoses and have a great impact on overall patient survival.

Current diagnostics used by modern physicians rely heavily on our sense of sight (direct visualization, multiple imaging modalities), sound (auscultation, ultrasound) and touch (palpation). Olfaction once played a more significant role in diagnosis, but has been less prominent as imaging devices, genetic screening, and clinical laboratory tests have become more sensitive, specific, and sophisticated. In past centuries, physicians used body odors to aid in diagnosis and recognized that many body odors have evolved to convey messages about the individual to others. However, man's sense of smell is relatively inferior to most mammals and most physicians are not familiar with, or trained to work with odors; in addition, physicians are not familiar with techniques needed to collect and analyze volatile organic compounds (VOCs) which emanate from the body. Therefore, human body odors remain a relatively untapped source for information regarding cancer development and diagnosis.

The theoretical underpinning of a volatile signature of cancer is quite straightforward. As the tumor forms, the cancer cells multiply rapidly. Their metabolic rate is extremely high and the metabolic products, many of which could be volatile, will be different in identity and/or quantity for cancer cells than healthy cells. These VOCs will be present at the site of production, but also transported around the body via the blood stream and/or secreted in other bodily fluids. Recent literature suggests it should be possible to exploit the information contained in VOCs (odorants) emanating from human secretions and excretions to gain insight into the disease state of the individual. Evidence for smell, i.e. VOC patterns, as a diagnostic tool for disease came from anecdotal observations of dogs that changed their behavior when an owner became afflicted by

disease. Since then, clinical trials have demonstrated the validity of canine scent detection a wide variety of cancers including breast [63], bladder [64] and ovarian cancers [65], based on VOCs in breath, urine and blood samples respectively. Benchtop analytics, led by GC/MS and other gas chromatographic methods [66], have also shown VOC readout to be a valid disease detection mechanism, with specific VOCs having been identified for diseases including lung cancer [67], skin cancer [68] and breast cancer [69] amongst many others [66]. While both canine and CG/MS techniques appear viable, they suffer from drawbacks, including the cost of training and upkeep for dogs and the cost and readout complexity of GC/MS systems [70]. Consequently, there is a clear need for a compact technology that can perform the same readout quickly and inexpensively, ideally with sufficient simplicity to allow routine use in a doctor's office setting.

With this motivation in mind, we initiated a study of blood plasma samples from healthy women and women with malignant and benign ovarian tumors, with the goal of demonstrating a prototype VOC analysis technology for point-of-care diagnostics of ovarian cancer. The plasma samples were collected and processed by Dr. Janos Tanyi of the Ovarian Cancer Research Center at the Hospital of the University of Pennsylvania and distributed to three different research groups: a team of canine researchers at the Working Dog Center at the University of Pennsylvania led by Dr. Cynthia Otto training dogs to discriminate cancer samples from non-cancer ones, a team of olfaction experts at the Monell Chemical Senses Center led by Dr. George Preti studying the samples by GC/MS and our research team, studying the VOC content of the samples with the DNA/carbon nanotube technology introduced in sections 5.2 and 5.4 of this work. The results presented here will focus on the DNA/carbon nanotube data, but the long-term goal of the project is to incorporate insights and feedback from the other branches of the collaboration to inform the design and data analysis of the DNA/carbon nanotube sensor array.

Setup and Measurement of Pooled Samples

As an initial test, and to learn about how to work with plasma samples, we began our study using pooled plasma samples. The pooled samples were made up of blood plasma from 10 individuals each. The average ages of patients and controls used for the pools were as follows: benign group 58 ± 8 years; ovarian cancer group 61 ± 5 years; and control group 61 ± 5 years. Unique challenges arose in our vapor sensing of human plasma samples due to the low level of VOCs in plasma, and the small sample volumes (a few hundred µL). Since the concentrations of the volatile compounds in plasma as well as their volatility is quite low, simply using the bubbler techniques employed for the larger volume analytes or blowing carrier gas over the surface of a plasma sample did not result in sufficient evaporation of the VOCs in the sample to conduct detection measurements. After some optimization, we settled on the following procedure: 500 µL of pooled plasma from each group of patients and controls was loaded into a 25 mL two-neck round-bottom flask. 125 mg of NaCl was added to make the plasma less hospitable for volatiles. A millimeter-sized stir bar was added to each round-bottom and they were completely submerged together in a water bath which was heated to 50 °C and stirred vigorously, as shown in fig. 5.13. A false glass floor was used to ensure that the round-bottoms were all at exactly the same height and that they were not in direct contact with the hot plate, which had to be set to 85 °C in order for the bath to reach 50 °C. The inlet and outlet tubing was wrapped with small diameter coiled wire. Current from a 20 V power supply heated the tubing to prevent adsorption of VOCs on the tubing walls. A mass flow controller (MFC) was connected to the inlet of the round-bottom and a check-valve was connected to the outlet, keeping the headspace isolated until any carrier gas was pulsed through. The closed headspace was left to accumulate volatiles for 30 min, after which

nitrogen carrier gas was passed through the MFC, pushing a stream of VOCs from the plasma sample out of the round-bottom towards the sensor chamber. Along with the three plasma round-bottoms, a water bubbler was connected to the chamber inlet. Given that the plasma samples are mostly water it was important to use water vapor rather than dry nitrogen as the carrier gas, ensuring that the humidity reaching the chamber stayed approximately constant throughout the experiment.

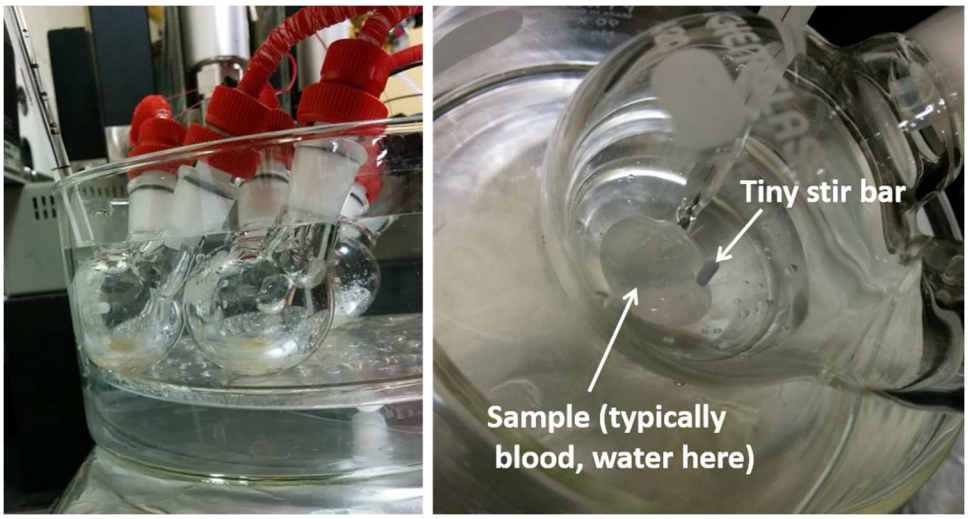

Figure 5.13: Loading blood serum in round bottom flasks. Salt and a stir bar were added to drive the VOCs into the headspace. The whole round bottom was submerged at 50 °C. The hot plate was set to 85 °C in order to reach this bath temperature. A false floor was used to ensure that the plasma round bottom was not in direct contact with the hotter bottom plate of the bath.

The experiment flow recipe began with a 30 minute period of just water vapor (1000 sccm) flowing into the chamber. This allowed time for the plasma sample VOCs to evaporate into the headspace and also allowed the baseline conductance of the nanotube FETs to be established. After thirty minutes, the flow through one of the round-bottoms was set to 200 sccm for two minutes, while the carrier flow was reduced to 800 sccm to keep the total flow constant. After sampling the plasma headspace for two minutes, the plasma flow was set to zero and the carrier flow was increased back to 200 sccm. Each plasma round-bottom was sampled in this

fashion three times with 12 minutes between repeated measurements of the same sample to allow the VOCs in vapor to build back up. This recipe is shown in fig. 5.14.

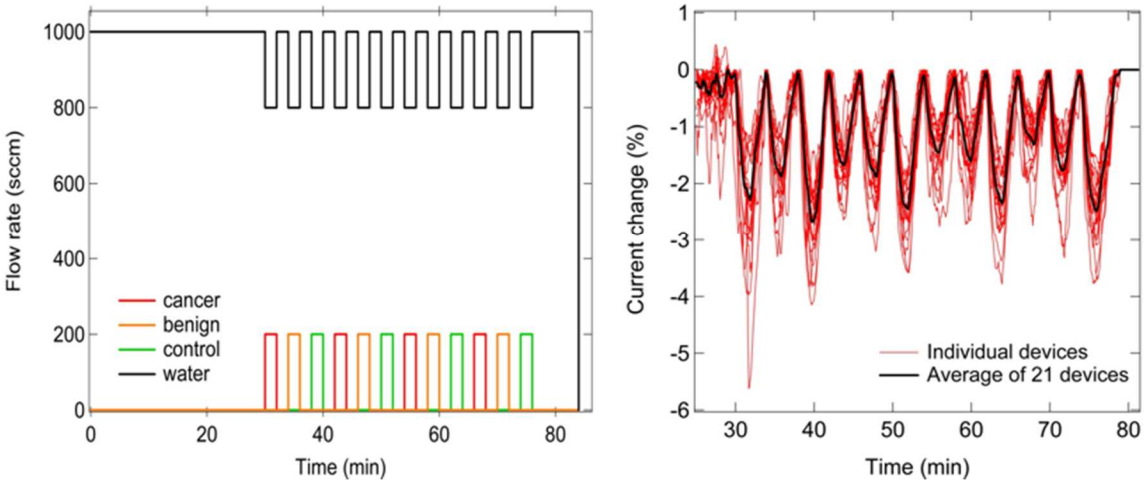

Figure 5.14: Flow recipe and raw data for a typical pooled plasma run.

Typical data for 21 seq 1 functionalized CNT devices responding to the sequential plasma sample VOCs is shown in figure 5.14. Over the four repetitions of "cancer-benign-control" a very clear trend emerges, in which the devices show largest responses to the pooled control plasma and smallest responses to the pooled cancer plasma. The very first measurement, at 30 minutes, induces an anomalously large response, a phenomena seen across many experimental runs. As a result, the first measurement of each plasma sample was ignored and the subsequent three were analyzed. The averaged trace of all seq1 devices (black) is plotted again in fig. 5.15 alongside the responses obtained from seq4 devices. A clear characteristic difference emerges. While the seq1 devices show responses of ~ -1.4 % to the cancer plasma VOCs, -1.7 % for benign and -2.4 % to the control samples, the seq4 samples show no ability to distinguish the plasma samples and produce responses of -0.9 % for all three plasma types. We note from fig. 5.15 a very small average decrease in the response magnitude of the devices between repetitions of the same measurement. We attribute this to a very slight reduction in the VOC levels that the plasma

samples are able to produce after they have already been sampled. While certainly a real effect, we believe that accounting for this by treating every sample the same way (4 2 minute pulses, 12 minutes apart) allows for fair comparison of the plasma samples.

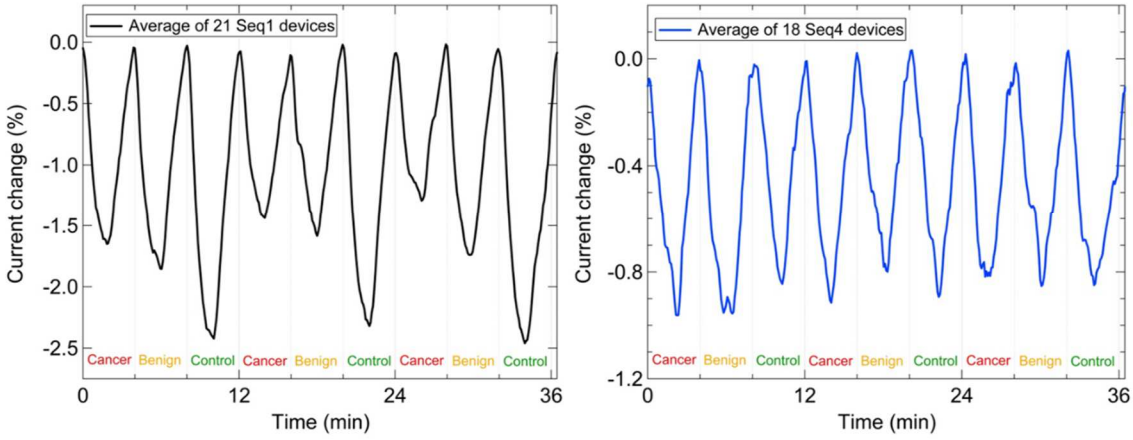

Figure 5.15: Average current change vs. time data for two different DNA sequences. While seq1 functionalized devices appear able to differentiate the three pooled plasma samples, seg4 devices show similar signals to all three samples.

A total of approximately 80 devices coated with 4 different DNA sequences were tested against the plasma samples. The maximum deviation for each device from the baseline current level was found and those numbers are averaged across to generate the data shown in fig. 5.16. Note that these numbers are slightly larger than the peak deviations shown above in fig. 5.15 as the maximum deviation for each device occurs at slightly different times. The cumulative data from the pooled samples shows an interesting pattern with significantly different magnitudes and patterns of responses across different sequences. Seq4 appeared completely unable to differentiate the three samples, while seq1 and seq5 are able to distinguish all three pooled samples at a statistically significant level. Seq2 appears to be able to differentiate the healthy pooled sample from the cancer and benign, which are not distinguished. All sequences show largest responses to the control plasma, but it is interesting to note the variability between

malignant and benign plasmas, which induce larger/smaller responses in seq1 and seq5. This data set reaffirmed the importance of the DNA sequences for sensor functionality and invoked optimism that significant trends would emerge when the pooled samples were replaced by plasma from individuals.

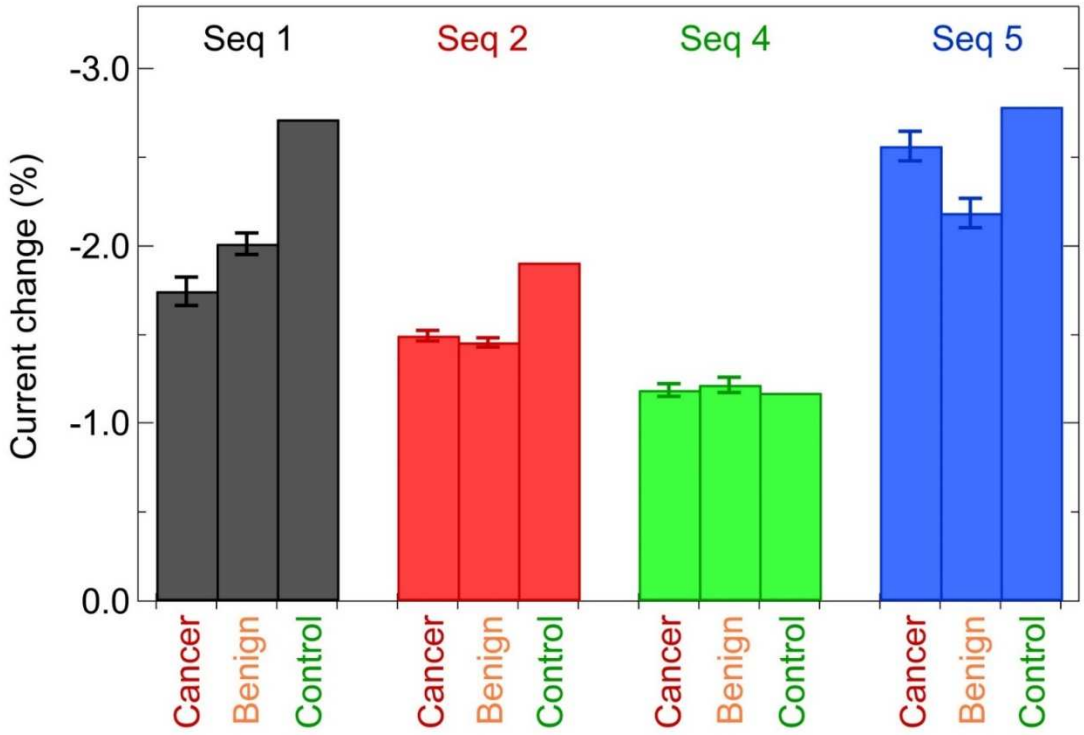

Figure 5.16: Responses of four different types of devices to the pooled serum samples. Each sequence provides a different set of responses that together yield a response pattern that is characteristic of the pooled sample. By using multiple sequences, the robustness with which the samples can be differentiated is greatly increased.

Measuring responses from individual blood plasma samples

Having established the ability to distinguish plasma samples based on their VOC content and observed promising trends in the pooled plasma data, we expanded the experiment by measuring 24 different plasma samples against a total of 142 different sensors. The sensors were spread across three chips, which were run consecutively against a set of five plasma samples

during one experiment. The sensor test setup was expanded for this experiment, as shown in fig. 5.17. The plasma samples were then replaced with five other ones and the three chips were cycled through again. This was repeated until the whole 142 x 24 data set had been collected.

DNA Sequences	
1	GAGTCTGTGGAGGAGGTAGTC
2	CTTCTGTCTTGATGTTTGTCAAAC
3	GCGCATTGGGTATCTCGCCCGGCT
4	CCCGTTGGTATGGGAGTTGAGTGC
5	GTACGGACTGTGAATGCGCGTTAG
6	GTATCTAGAGCGGGCGGGTACTCC
7	AAACAAATCTAATAATACTTCCCA
8	AGTTCGGCATGTGGAAACTCCTTC
9	CGCCTAGAGGTCAAGCGTGGTTGC
10	TGAAAGTGGGAAGCGACACGATGG

Table 5.5: The 10 DNA sequences used in the individual plasma sample experiments.

The plasma samples came from 10 women with late stage, malignant ovarian cancer, 5 women with benign ovarian tumors and 9 healthy controls. The 142 carbon nanotube FETs were each functionalized with one of 10 DNA sequences. Those sequences are shown in table 5.5. The updated setup and an example of data for a set of seq5 devices responding to 5 plasma samples is shown in fig. 5.17.

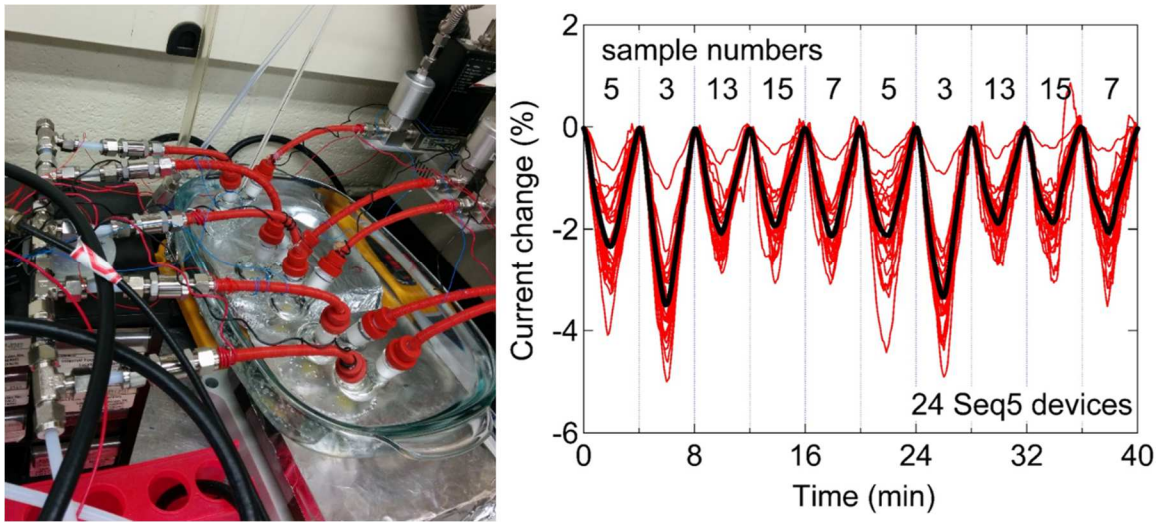

Figure 5.17 a) The setup was expanded in order to measure five plasma samples in a single run. b) Typical data from a run of 5 control plasma samples shows strong reproducibility between devices. While four of the plasma samples induce comparable responses, a fifth (#3) shows markedly larger responses for this DNA sequence.

While there is spread amongst the sensitivity of the devices, all the devices generally show very similar responses to four of the five plasma samples, with the fifth showing anomalously large responses. The average of all 24 seq5 devices shows very reproducible signals across two repetitions of all five samples. From this data, the average responses of samples 5, 7, 13 and 15 are all in the range -1.9 % to -2.24 %, while sample 3 has an average response of -3.44 %. The complete data set, with the average responses of all 10 sequences to the headspace vapor of all 24 plasma samples is shown in table 5.6. The data in the table is chronological (top to bottom) and color coded by plasma type (red for malignant, orange for benign, green for control).

Sample	Seq1	Seq2	Seq3	Seq4	Seq5	Seq6	Seq7	Seq8	Seq9	Seq10
49	-2.25	-1.54	-2.26	-3.33	-3.15	-2.62	-1.10	-4.61	-5.44	-3.87
46	-6.67	-2.16	-9.63	-7.15	-4.40	-3.97	-6.97	-7.54	-5.30	-7.83
52	-2.02	-0.95	-2.07	-2.14	-2.97	-2.33	-1.19	-2.83	-3.50	-3.00
57	-1.39	-0.72	-2.62	-1.88	-3.17	-0.31	-1.85	-2.16	-3.27	-1.74
50	-1.39	-0.74	-4.16	-1.89	-3.55	-1.04	-2.80	-2.56	-2.23	-2.26
5	-3.84	-0.60	-2.95	-1.79	-2.24	-2.17	-2.26	-4.31	-3.37	-4.45
3	-4.74	-1.71	-7.06	-3.21	-3.44	-3.39	-2.55	-6.60	-4.65	-5.13

13	-3.26	-0.90	-3.71	-1.82	-2.00	-2.03	-1.92	-4.06	-2.98	-3.61
15	-3.04	-0.95	-4.42	-1.90	-1.91	-1.45	-2.36	-4.45	-2.99	-3.19
7	-3.38	-0.72	-3.82	-1.84	-2.12	-2.03	-2.18	-4.91	-2.80	-4.05
54	-2.18	-1.57	-1.46	-1.09	-1.33	-1.24	-0.96	-2.72	-1.95	-2.00
53	-2.27	-1.80	-1.24	-1.18	-1.38	-1.27	-1.19	-2.70	-2.01	-2.21
58	-2.33	-1.91	-2.14	-1.27	-1.38	-1.32	-1.17	-2.94	-2.08	-2.06
64	-1.32	-1.21	-0.96	-0.50	-0.57	-0.42	-0.94	-1.09	-0.98	-1.02
56	-1.97	-1.64	-1.07	-0.96	-1.16	-0.93	-1.16	-2.36	-1.56	-1.79
48	-1.63	-1.60	-1.36	-1.15	-0.94	-0.89	-1.54	-1.84	-1.35	-1.48
45	-2.21	-2.39	-2.41	-1.59	-1.42	-1.75	-1.17	-2.98	-1.98	-1.80
66	-2.19	-1.56	-1.54	-1.14	-1.08	-1.16	-1.83	-2.25	-1.62	-1.69
68	-1.96	-1.29	-1.58	-1.07	-1.00	-1.03	-1.51	-2.14	-1.56	-1.54
65	-1.90	-2.11	-1.29	-0.96	-0.87	-0.78	-1.46	-2.14	-1.38	-1.46
14	-1.97	-1.12	-1.85	-0.88	-0.81	-0.85	-0.81	-1.84	-1.10	-1.29
9	-1.87	-1.26	-1.36	-0.79	-0.77	-0.75	-0.84	-1.84	-0.94	-1.24
18	-1.65	-1.11	-1.66	-0.81	-0.83	-0.67	-0.95	-1.89	-1.13	-1.32
17	-1.72	-1.08	-1.24	-0.75	-0.69	-0.58	-0.85	-1.66	-1.04	-1.20

Table 5.6: Unnormalized responses for all 10 sequences to the 24 individual plasma samples, color-coded by class.

Statistical Analysis of the Sensor Responses

The first processing step for the data was to slightly renormalized to adjust for a decrease in the sensitivity of the devices over the course of the experiments. This calibration was done by measuring the responses of all 142 devices to dimethyl methylphosphonate (DMMP), a stock chemical. Typical calibration values were in the range 0-30%, i.e. the final DMMP run after the last plasma experiment showed responses 30% lower than initial DMMP experiments. The recalibrated data is plotted in fig. 5.18. There appear to be characteristic differences in the responses that reflect sample class. For example, the control samples tend to produce larger responses for Seq1 functionalized devices than either benign or cancer plasma samples. However,

there is significant spread within each of the classes and there are outliers that seem to produce uniformly excessive or low responses, across many sequences.

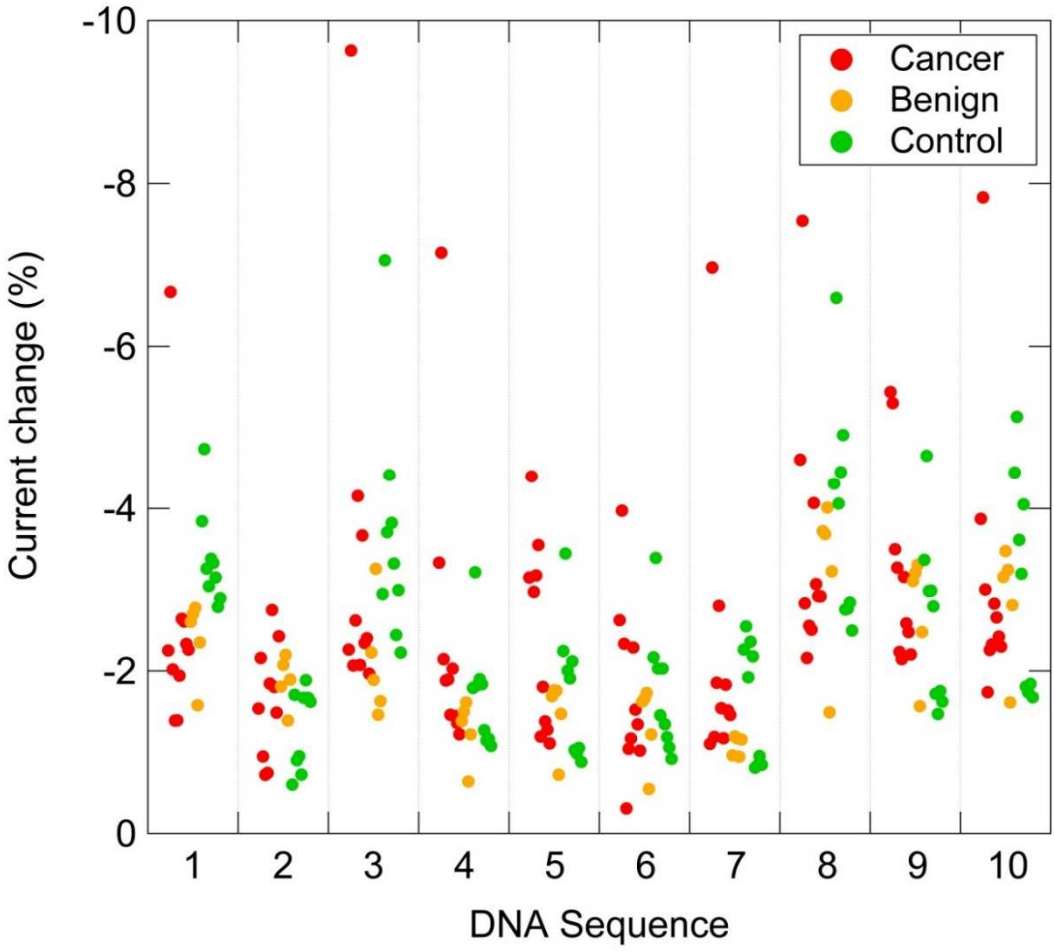

Figure 5.18: A visualization of the data. The y-axis value for a given point gives the response magnitude for that particular DNA sequence/plasma sample combination. The points are color-coded by class for clarity. The lateral separation of responses by a particular DNA sequence is not meaningful, but simply prevents overlapping points from becoming obscured.

Because of the small size of the data set, standard techniques like Linear Discriminant Analysis (LDA) and kernel discriminant analysis are not appropriate. Mapping to any nonlinear data type is not encouraged when there are more data types than patients in a given class. Thus, to continue the data analysis, we manipulated the raw data by using mild preprocessing. The following analysis bears resemblance to traditional LDA without defining or using a covariance

matrix [71]. Dr. Dan Lee, Department of Electrical and Systems Engineering, University of Pennsylvania, was consulted in devising this methodology. Care was taken to ensure that the method used was robust for small sample sizes.

Outliers inhibit natural clustering for small data sets. In order to improve clustering, we first normalized each of the patient response vectors (a row vector) by the sum over each given row. This type of normalization helps to separate out sample-to-sample "gain" differences, *e.g.,* a scaling constant which inflate or deflate current measurements. Generally, these types of normalizations are known as L_p normalizations. We used L_1 normalization given by

$$L_1 x_i = \frac{x_i}{\sum_{i=1}^{N} |x_i|}$$

where N is the number of patient samples within a class (e.g. for the Malignant class, $N = 10$) and x_i is the i^{th} element of a row vector. Applying L_1 normalization to the entire data set, we generated three new current response matrices for the three classes. This yields the following data (split into classes):

	Malignant									
	Seq1	**Seq2**	**Seq3**	**Seq4**	**Seq5**	**Seq6**	**Seq7**	**Seq8**	**Seq9**	**Seq10**
49	0.075	0.051	0.075	0.110	0.104	0.087	0.036	0.153	0.180	0.128
46	0.108	0.035	0.156	0.116	0.071	0.064	0.113	0.122	0.086	0.127
52	0.088	0.041	0.090	0.093	0.129	0.101	0.052	0.123	0.152	0.130
57	0.073	0.038	0.137	0.098	0.166	0.016	0.097	0.113	0.171	0.091
50	0.061	0.033	0.184	0.084	0.157	0.046	0.124	0.113	0.099	0.100
48	0.118	0.116	0.099	0.083	0.068	0.065	0.112	0.134	0.098	0.107
45	0.112	0.121	0.122	0.081	0.072	0.089	0.059	0.151	0.101	0.091
66	0.136	0.097	0.096	0.071	0.067	0.072	0.114	0.140	0.101	0.105
68	0.134	0.088	0.108	0.073	0.068	0.070	0.103	0.146	0.106	0.105

65	0.132	0.147	0.090	0.067	0.061	0.054	0.102	0.149	0.096	0.102
	Control:									
	Seq1	**Seq2**	**Seq3**	**Seq4**	**Seq5**	**Seq6**	**Seq7**	**Seq8**	**Seq9**	**Seq10**
5	0.137	0.021	0.105	0.064	0.080	0.078	0.081	0.154	0.120	0.159
3	0.112	0.040	0.166	0.076	0.081	0.080	0.060	0.155	0.109	0.121
13	0.124	0.034	0.141	0.069	0.076	0.077	0.073	0.154	0.113	0.137
15	0.114	0.036	0.166	0.071	0.072	0.054	0.089	0.167	0.112	0.120
7	0.121	0.026	0.137	0.066	0.076	0.073	0.078	0.176	0.101	0.145
14	0.157	0.089	0.148	0.070	0.065	0.068	0.065	0.147	0.088	0.103
9	0.160	0.108	0.117	0.068	0.066	0.064	0.072	0.158	0.081	0.106
18	0.137	0.092	0.138	0.067	0.069	0.056	0.079	0.157	0.094	0.110
17	0.159	0.100	0.115	0.069	0.064	0.054	0.079	0.154	0.096	0.111
	Benign:									
	Seq1	**Seq2**	**Seq3**	**Seq4**	**Seq5**	**Seq6**	**Seq7**	**Seq8**	**Seq9**	**Seq10**
54	0.132	0.095	0.088	0.066	0.081	0.075	0.058	0.165	0.118	0.121
53	0.132	0.104	0.072	0.068	0.080	0.074	0.069	0.157	0.117	0.128
58	0.125	0.103	0.115	0.068	0.074	0.071	0.063	0.158	0.112	0.111
64	0.147	0.134	0.107	0.055	0.063	0.047	0.104	0.121	0.109	0.113
56	0.135	0.112	0.073	0.066	0.079	0.064	0.079	0.162	0.107	0.123

Table 5.7: A complete table of responses to the plasma samples, after application of the L_1 norm.

Each of these matrices lives in a ten dimensional space, and each dimension is represented by an ssDNA sequence. We can define mean vectors $\mu_M, \mu_B,$ and μ_C which point from the origin of this ten dimensional space to the mean position of a given class (the subscript denotes the different classes). This vector is obtained by simply averaging down the columns of each of the class matrices and then transposing this row vector i.e.

$$\mu_i = \left(\frac{\sum_{j=1}^{N} x_j}{N}\right)^T$$

Here, the sum over *j* is a sum down each column. *N* is the number of patient samples (e.g. $N = 10$ for the Malignant class), and i denotes the i^{th} entry of mean vector. The mean vectors are defined for the three classes as follows,

$$\vec{\mu}_M = \begin{pmatrix} -0.10376 \\ -0.07677 \\ -0.11566 \\ -0.08763 \\ -0.09641 \\ -0.06649 \\ -0.09116 \\ -0.13440 \\ -0.11900 \\ -0.10874 \end{pmatrix}, \vec{\mu}_C = \begin{pmatrix} -0.13581 \\ -0.06080 \\ -0.13690 \\ -0.06889 \\ -0.07205 \\ -0.06705 \\ -0.07500 \\ -0.15807 \\ -0.10163 \\ -0.12360 \end{pmatrix}, \vec{\mu}_B = \begin{pmatrix} -0.13408 \\ -0.10976 \\ -0.09105 \\ -0.06480 \\ -0.07550 \\ -0.06601 \\ -0.07477 \\ -0.15241 \\ -0.11243 \\ -0.11918 \end{pmatrix}$$

We then define a mean difference vector $\vec{w}$. This is calculated by subtracting $\vec{\mu}_C$ from $\vec{\mu}_M$ component by component,

$$\vec{w} = \vec{\mu}_M - \vec{\mu}_C$$

We chose to take the mean difference vector between the malignant class and the healthy class because one might expect these data sets to be most dissimilar and because these data sets also were derived from the largest number of subjects, ensuring maximum robustness. This vector links the centers of the control and malignant clusters, and therefore denotes a 'direction' in the 10-dimensional space that best separates the two data sets. We can then take the projection of each individual vector (which, as a reminder, is made up of the normalized responses of the 10 different sequences to that particular plasma sample) in the w-direction and be confident that we are projecting the data set along the most optimized axis. Mathematically, this corresponds to taking the dot product of the normalized malignant/benign/control matrices and vector $\vec{w}$. This yields

$$\hat{M} \bullet \vec{w} = \begin{pmatrix} -0.00028 \\ -0.00384 \\ -0.00062 \\ +0.00172 \\ -0.00227 \\ -0.00211 \\ -0.0329 \\ -0.00323 \\ -0.00370 \\ -0.00285 \end{pmatrix}, \quad \hat{B} \bullet \vec{w} = \begin{pmatrix} -0.00416 \\ -0.00338 \\ -0.00422 \\ -0.00325 \\ -0.00348 \end{pmatrix}, \quad \hat{C} \bullet \vec{w} = \begin{pmatrix} -0.00582 \\ -0.00574 \\ -0.00589 \\ -0.00593 \\ -0.00668 \\ -0.00636 \\ -0.00580 \\ -0.00541 \\ -0.00548 \end{pmatrix}$$

We then visualize this data by plotting it, color-coded, along a number line. We can furthermore estimate Gaussian fits to the data, based on the mean and standard deviation of each list above.

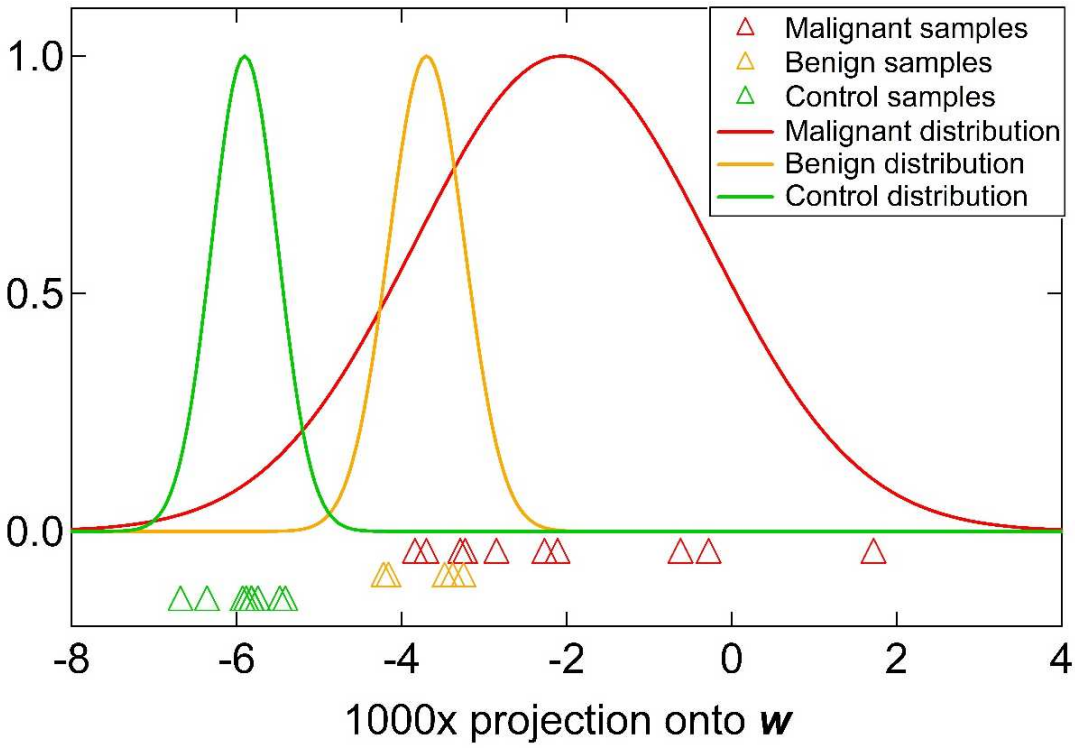

Figure 5.19: A visualization of the projections of each plasma sample along the difference vector $\vec{w}$. The triangular points along the x-axis of the plot are the projections for one plasma sample each. The different vertical offsets of the malignant, benign and control classes are to avoid obscuring any data. The control data is highly clustered and shows no overlap with the malignant and benign groups. The Gaussian curves above the data are estimated distributions of each group, based on the mean and standard deviation.

The control samples are all well clustered around an average projection of -0.006. They are very well distinguished from cancer and benign samples. The benign samples are also well clustered, while the spread amongst the malignant samples is much larger. The cancer and benign distributions appear to be quite different, but there remains some overlap. More samples would be needed to establish definitely whether the trends observed amongst the benign and malignant are robust.

Beyond descriptive proclamations, the final data format is now appropriate for a single Welch's t-test, which is a standard statistical test designed to compare two data sets and evaluate the probability of a null hypothesis, i.e. the chance that the mean values' for both sets would be equal given infinite sampling. To demonstrate the merit of the statistical analysis approach taken here, a series of t-tests between the different data sets have been conducted and their results are tabulated below.

1) p-values for the individual sensor types, without any normalization:

	Seq1	Seq2	Seq3	Seq4	Seq5	Seq6	Seq7	Seq8	Seq9	Seq10
Malignant-Control	0.226	0.027	0.413	0.152	0.130	0.466	0.212	0.313	0.263	0.422
Benign-Control	0.035	**0.003**	0.013	0.054	0.097	0.089	0.031	0.059	0.116	0.052
Malignant-Benign	0.260	0.299	0.047	0.035	0.016	0.089	0.046	0.135	0.038	0.112

Due to the presence of one sample with high responses for almost all sensor types, the variance amongst the malignant data was too high to meet a $p < 0.01$ threshold for any of the individual sequences' t-tests involving the malignant data set. Some of the tests met a lower standard of significance, $p < 0.05$. None of the sensor types alone is sufficient to differentiate all three classes, even at the $p < 0.05$ level.

2) p-values for the individual sensor types, using normalized data:

	Seq1	Seq2	Seq3	Seq4	Seq5	Seq6	Seq7	Seq8	Seq9	Seq10
Malignant-Control	**0.005**	0.193	0.061	**0.003**	0.045	0.474	0.069	**0.001**	0.084	0.041
Benign-Control	0.409	**0.002**	**0.002**	0.083	0.204	0.437	0.490	0.267	0.025	0.276
Malignant-Benign	**0.004**	0.024	0.050	**0.001**	0.071	0.480	0.110	0.048	0.286	0.044

The value of normalizing is shown by the fact that six of the sequences used now demonstrate $p < 0.05$ for at least one of the three pairs tested, and five of them can distinguish one pair of classes at a significance of $p < 0.01$. None of the individual sequences can distinguish all three plasma types with any meaningful significance.

3) p-values for the projections onto the multidimensional difference vector $\vec{w}$:

Malignant-Control	2.99×10^{-5}
Benign-Control	1.47×10^{-5}
Malignant-Benign	9.63×10^{-3}

A Welch's t-test on the malignant and control data above returns $p = 6 \times 10^{-5}$, making it extremely unlikely that the separation observed is simply an aberration that would disappear with increased sample size. Similarly, the benign and control samples are very robustly differentiated. These conclusions are in line with the visually separated data plotted above in figure 5.19.

The difference vector used in this analysis, $\vec{w}$, is optimized for differentiating the control and malignant data sets. Nevertheless, as shown in figure 5.19, a by-product was that the benign data became nicely clustered. It is statistically likely (99%) that the benign and malignant distributions are also differentiated by this analysis.

To verify the robustness of the data set, we performed a common technique for small data sets called "leave-one-out cross-validation" (LOOCV). LOOCV tests whether a "new" patient sample would fit into one of the classes found above. To perform LOOCV, we leave one of the malignant patient average current vectors, denoted $\vec{m}_i$, out of the analysis, find the new mean difference vector, $\vec{w}_i$, and dot each of the classes onto this vector. From this, we define new Gaussian distributions for each class. Finally, dot the malignant patient vector which was left out onto $\vec{w}_i$ and see whether its projection falls within the correct Gaussian distribution and find its distance from the new mean, denoted μ_i^M. The subscript i indicates which patient sample is removed from basic analysis and is mainly a book keeping device. This was iteratively completed with each of the ten malignant average current vectors left out one by one. Table 5.8 details which malignant plasma sample is left out and how far the sample strays from the mean of the malignant Gaussian distribution.

Sample Left Out (i)	**Mean of Malignant Distribution (μ_i^M)**	**Standard Deviation of Malignant Distribution (σ_i^M)**	$\vec{m}_i \cdot \vec{w}_i$	$Z_i^M = \frac{\mu_i^M - \vec{m}_i \cdot \vec{w}_i}{\sigma_i^M}$	$Z_i^C = \frac{\mu_i^H - \vec{m}_i \cdot \vec{w}_i}{\sigma_i^C}$
1	-0.002319	0.0015059	-0.00171	$-0.399\sigma_M$	$-7.823\sigma_H$
2	-0.001769	0.0018280	-0.00464	$+1.572\sigma_M$	$-2.992\sigma_H$
3	-0.002142	0.0015398	-0.00145	$-0.444\sigma_M$	$-7.781\sigma_H$
4	-0.002560	0.0010738	-0.00001	$-2.369\sigma_M$	$-11.72\sigma_H$
5	-0.001949	0.0016886	-0.00347	$+0.903\sigma_M$	$-4.204\sigma_H$
6	-0.001764	0.0023141	-0.00241	$+0.280\sigma_M$	$-8.067\sigma_H$
7	-0.001736	0.0021563	-0.00378	$-0.805\sigma_M$	$-4.954\sigma_H$
8	-0.001729	0.0021854	-0.00356	$+0.839\sigma_M$	$-5.942\sigma_H$
9	-0.001802	0.0020735	-0.00396	$+1.044\sigma_M$	$-5.367\sigma_H$
10	$\mathbf{-0.001690}$	$\mathbf{0.0023354}$	$\mathbf{-0.0037}$	$\mathbf{+0.875\sigma_M}$	$\mathbf{-4.470\sigma_H}$

Table 5.8: Results of the LOOCV protocol. Most importantly, in each case the 'left out' sample is a much closer fit with the rest of the malignant set than the control set, as reflected by the Z values.

The sample removed from the malignant data set is labeled $\overrightarrow{\mathbf{m}_\mathbf{i}}$, and the new mean difference vector between the malignant and control data set is labeled $\overrightarrow{\mathbf{w}_\mathbf{i}}$. The $\mathbf{Z}$ score is the distance $\overrightarrow{\mathbf{m}_\mathbf{i}} \cdot \overrightarrow{\mathbf{w}_\mathbf{i}}$ is from the mean in units of the standard deviation. In the fifth column, the $\mathbf{Z}$ score for the malignant class, denoted $\mathbf{Z_i^M}$ is listed. Each of the "new" samples dotted into the "new" mean difference vector is contained within 2.369 standard deviations of the malignant class from the new means of the malignant data set. For the malignant class, it occasionally falls in the left half the malignant Gaussian and occasionally falls in the right half the Gaussian, but often, it falls within a single $\boldsymbol{\sigma_i^M}$ of the mean of the malignant distribution. This indicates that, despite a small sample size, the data collected and the assignment of malignant is relatively robust. The final column in the table is the $\mathbf{Z}$ score with respect to the control samples, i.e., the distance $\overrightarrow{\mathbf{m}_\mathbf{i}} \cdot \overrightarrow{\mathbf{w}_\mathbf{i}}$ is from the mean of the healthy class, denoted $\boldsymbol{\mu_i^C}$, in units of the standard deviation, denoted $\boldsymbol{\sigma_i^C}$, of the healthy class. It is denoted $\mathbf{Z_i^C}$ for clarity. As expected, the $\mathbf{Z_i^C}$ scores are much larger in magnitude, because $\overrightarrow{\mathbf{m}_\mathbf{i}} \cdot \overrightarrow{\mathbf{w}_\mathbf{i}}$ is much farther from the mean of the control class. They are all negative because $\overrightarrow{\mathbf{m}_\mathbf{i}} \cdot \overrightarrow{\mathbf{w}_\mathbf{i}}$ always falls to the right of mean of the healthy class distribution.

In conclusion, we note that we have used simple statistical techniques to dramatically improve the clustering of the plasma response data. The resulting data sets appear very distinct, with no overlap at all between the responses obtained from plasma from malignant cancer patients and healthy controls. While the separation between the benign and malignant data sets is smaller, it is statistically likely that the true distributions are distinct. More data is necessary to strengthen that claim. Furthermore, while t-tests are used in this analysis as a simple, easy to understand quantification of differentiability, merely having different distributions across the different plasma types is insufficient for truly classifying individuals into malignant/benign/control

classes with low failure rates. More data is needed in order to understand the limits of this technology and whether these promising early results will translate into a true diagnostic tool with sufficiently low false positive and false negative rates. Extensions to these experiments, including some that incorporate the GC/MS findings of our collaborators at the Monell Chemical Senses Center, are discussed in outlook/future work in section 7.1xx.

5.5 Scalable Arrays of Chemical Vapor Sensors Based on DNA-Decorated Graphene

The results presented in this section have also appeared in the publication "Scalable Arrays of Chemical Vapor Sensors Based on DNA-Decorated Graphene", N. J. Kybert, G. H. Han, M. B. Lerner, E. N. Dattoli, A. Esfandiar, A. T. C. Johnson, *Nano Research.*, 2014, 7(1) pp 95-103.

Abstract

Arrays of chemical vapor sensors based on graphene field effect transistors functionalized with single-stranded DNA were demonstrated. Standard photolithographic processing was adapted for use on large-area graphene by including a metal protection layer, which protected the graphene from contamination and enabled fabrication of high quality field-effect transistors (GFETs). Processed graphene devices had hole mobilities of 1640 ± 250 cm^2/Vs and Dirac voltages of 15 ± 10 V under ambient conditions. Atomic Force Microscopy was used to verify that the graphene surface remained uncontaminated and therefore suitable for controlled chemical functionalization. Single-stranded DNA was chosen as the functionalization layer due to its affinity to a wide range of target molecules and π-π stacking interaction with graphene, which led to minimal degradation of device characteristics. The resulting sensor arrays showed analyte- and DNA sequence-dependent responses down to parts-per-billion concentrations. DNA/GFET sensors were able to differentiate among chemically similar analytes, including a series of carboxylic acids, and structural isomers of carboxylic acids and pinene. Evidence for the important role of electrostatic chemical gating was provided by the observation of understandable differences in the sensor response to two compounds that differed only by the

replacement of a (deprotonating) hydroxyl group by a neutral methyl group. Finally, target analytes were detected without loss of sensitivity in a large background of a chemically similar, volatile compound. These results motivate further development of the DNA-graphene sensor family for use in an electronic olfaction system.

In this work, we demonstrated a scalable photolithographic approach to graphene field effect transistor (GFET) fabrication that used a metal protection layer on the graphene to avoid photoresist contamination. The resulting arrays of back-gated GFETs fabricated on SiO2/Si substrates were highly reproducible with very clean surfaces, low doping levels, and average mobilities of 1640 ± 250 cm^2/Vs under ambient, comparable to results obtained using more complex modified-RCA cleaning procedures. The graphene transistor arrays were then functionalized with different single-stranded DNA sequences to detect and distinguish highly similar volatile organic compounds (VOCs), such as a sequence of homologous carboxylic acids and pinene isomers. Concentrations as small as 1 ppm elicited reproducible, fast responses with few-second time constants. The sensing responses were DNA-sequence dependent, and the current recovered to baseline without active refreshing. Aspects of the sensing mechanism were elucidated by comparing the responses to isobutyric acid and methyl isopropyl ketone (MIPK), whose chemical structure differs only in the substitution of a methyl group for a hydroxyl group. Finally, we demonstrated detection of isobutyric acid in a much larger background of MIPK without loss of sensitivity. These promising attributes were comparable to the results of our group's earlier experiments based on exfoliated graphene [25], and they show the potential of arrays of DNA-graphene hybrids for a host of vapor sensing applications.

Back-gated graphene transistor arrays were fabricated using two rounds of a photolithographic process that included a metal protection layer to shield the graphene from the

photoresist (see methods section). Resulting yields exceeded 90%. In vacuum, the devices demonstrated symmetric electron and hole conduction and Dirac voltages of 0-5 V (Fig. S-1 in the Electronic Supplementary Material (ESM)). In room air, the Dirac voltages of the devices were 15 ± 10 V, with the shift from 0 V attributed to modest doping by ambient air and humidity as well as the effect of silanol groups on the substrate [72]. The average hole mobility of the devices in air, calculated from the source-drain current-gate voltage characteristic (I_{sd}-V_g) and estimated back gate capacitance (ca. 12 nF/cm^2, calculated based on an oxide thickness of 300 nm and dielectric constant of 3.9) was found to be 940 ± 130 cm^2/Vs. This value was an underestimate of the intrinsic mobility of the GFET due to omission of the effects of gate field screening and contact resistance. The contact resistance was accounted for by fitting the I_{sd}-V_g curve with a series resistance model [73] that yielded a refined estimate of the channel mobility, the equilibrium carrier density, and contact resistance (Fig. S-2 in the ESM). Typical inferred values of the series resistance and equilibrium carrier density were 500-700 Ω and 5-7x10^{11} cm^{-2}, respectively. For the I_{sd}-V_g data shown in Fig. 5.20b, the model yielded values of 1640 cm^2/Vs and 890 cm^2/Vs for the hole and electron carrier mobilities, respectively, an impressive value but still somewhat lower than what was found in earlier experiments based on exfoliated graphene patterned using electron beam lithography [25]. Atomic force microscopy images showed surface profiles consistent with single layer graphene devices with low surface roughness, indicating that the graphene was very clean, with minimal contamination (Fig. S-3 in the ESM). The resulting ability to fabricate hundreds or thousands of high quality GFET devices in parallel with high yield using established processing techniques represented a vital step towards implementing graphene in numerous electronic applications.

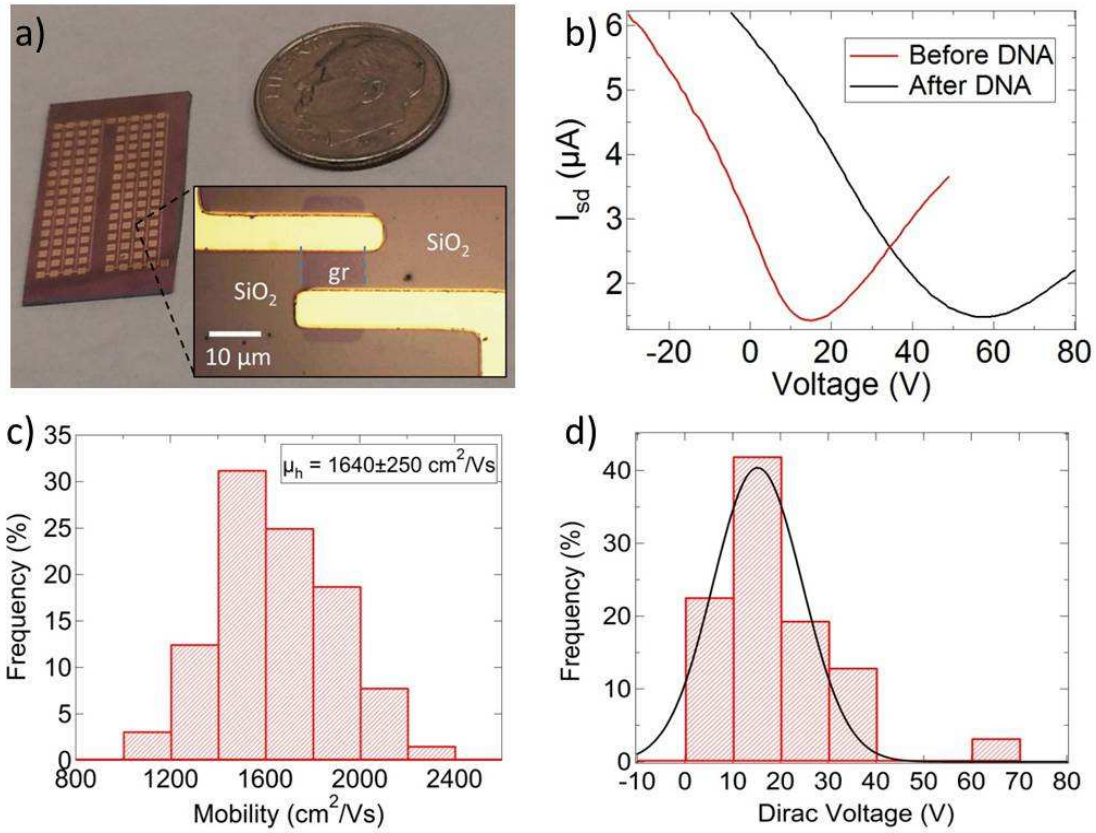

Figure 5.20: A dime-sized chips contained 112 devices with channel size 10 µm x15 µm. (b) Isd-Vg for a typical device with a hole mobility of 1640 cm²/Vs and Dirac voltage of 14 V. After DNA functionalization, the Dirac voltage is shifted to 58 V due to the negative charge on the DNA phosphate backbone. Histograms of (c) hole mobility (corrected for contact resistance) and (d) Dirac voltage, measured in ambient conditions, for typical arrays of 56 devices demonstrate the high quality transistor properties of the graphene devices. The black line is a Gaussian fit to the data.

One application of growing interest is the use of GFETs as electronic readout elements in large arrays of chemical vapor sensors, building on previous work based on exfoliated graphene [25]. Hybrid structures consisting of GFETs functionalized with single-stranded DNA were fabricated where the DNA provided chemical recognition for a variety of molecular analytes and the GFET provided all-electronic readout of molecular binding with very high sensitivity. DNA was expected to interact with the GFET through a non-covalent π-π stacking interaction, with minimal

effect on the carrier mobility of the GFET. GFETs were functionalized by incubation in droplets of DNA solution in a humid atmosphere that suppressed droplet evaporation. Two methods were used to confirm the self-assembly of a nanoscale layer of DNA. First, AFM showed a height increase of $\sim$ 0.65 nm after functionalization, consistent with the addition of a DNA monolayer and in agreement with previous measurements on exfoliated graphene [25]. Second, electronic measurements showed that DNA functionalization caused the Dirac point to shift toward positive back gate voltage (Fig. 5.20b). This was consistent with expectation since the DNA backbone has a high negative charge that provides a chemical gating effect similar to that observed for carbon nanotube FETs [20]. Vapor response experiments were carried out using four DNA oligomers:

Seq1: 5' GAG TCT GTG GAG GAG GTA GTC 3'

Seq2: 5' CTT CTG TCT TGA TGT TTG TCA AAC 3'

Seq3: 5' GCG CAT TGG GTA TCT CGC CCG GCT 3'

Seq4: 5' CCC GTT GGT ATG GGA GTT GAG TGC 3'

These sequences were selected for comparison with earlier experiments on DNA/graphene [25] (Seq 1 and 2) and DNA/carbon nanotube sensors [15, 55] (Seq 1-4). DNA/GFET devices were exposed to dilute vapors of propionic, butyric, hexanoic and octanoic acids, carboxylic acids that differ only in the length of the carbon chain (see Fig. S-4 in the ESM for the chemical structures of all analytes used for this work). As many as 10 devices were measured simultaneously while pulses of dilute analyte vapors at controlled concentrations were introduced into the sensing chamber, as described previously [55]. The duration of the analyte pulse was typically 200 sec, after which the flow was switched to clean air for 200 sec. The gas flow rate and relative humidity were held constant throughout the measurement, at 1500 sccm and 33%, respectively. The sensor response was reported as the normalized change in current, $\Delta I/I_0$, as in

previous work [25]. The response and recovery to baseline were reproducible in time and across devices, and they were well fit by double exponential functions with faster (dominant) time constants of less than five seconds (Fig. 5.21a and inset). The four carboxylic acids were clearly differentiated at all concentrations tested, as shown for DNA/GFET based on Seq1 in Fig. 5.21b. Responses of DNA/GFET were found to be much larger than those of bare GFETs and to be controlled by the identity of the DNA oligomer (Fig. 5.21c and Fig 5.21d). Taken together, these data suggested that the DNA/graphene system has the chemical diversity required for an electronic olfactory system. A table of responses for each carboxylic acid-DNA sequence combination tested is presented in table S-5 in the ESM.

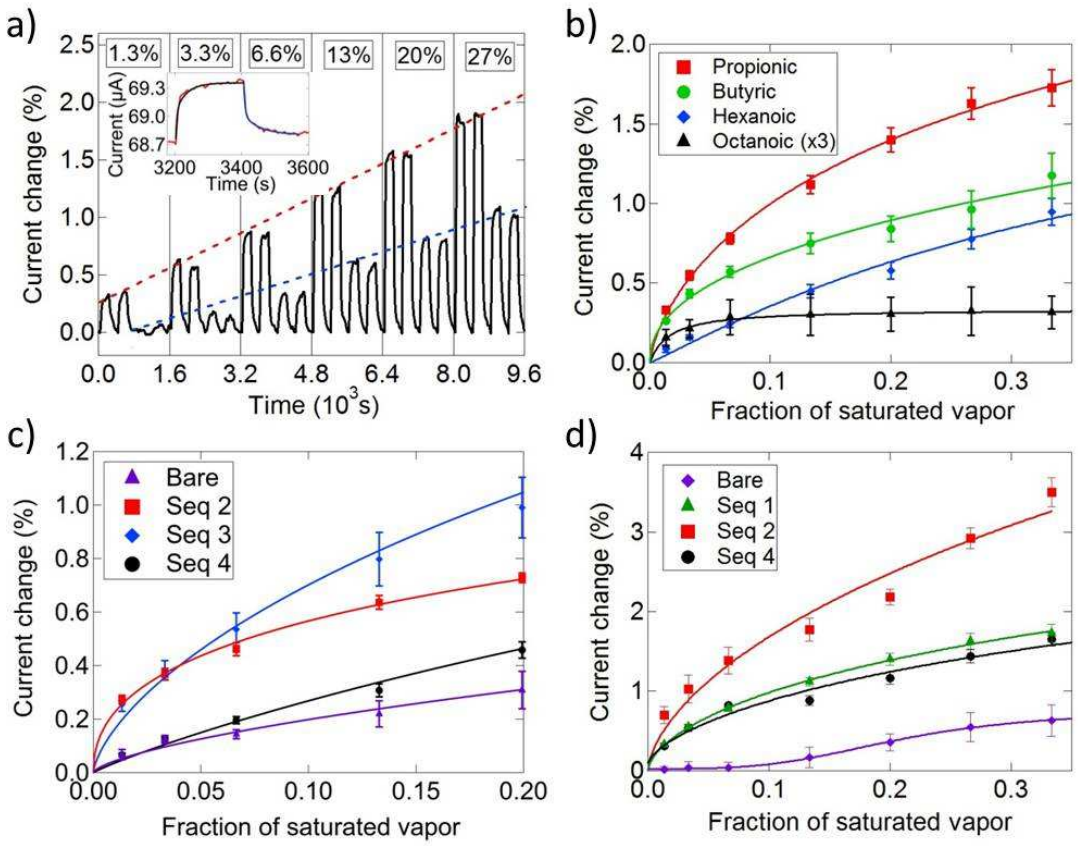

Figure 5.21: a) Normalized conductance changes for a DNA/GFET device based on Seq1 upon exposure to propionic acid and hexanoic acid vapor at concentrations in the range 1-27% saturated analyte vapor (50-1000 ppm for propionic acid and 3-63 pm for hexanoic acid). At each concentration, two pulse/flush cycles of propionic acid were followed by two pulse/flush cycles of hexanoic acid to show discrimination between analytes and response reproducibility. After each analyte pulse, the current returned to baseline during a flush with clean air. The red (blue) dotted line is a guide to the eye tracing out propionic (hexanoic) acid response magnitudes. Inset: Rise and fall in the current was fit by double exponential decays, with fast time constants of 3.5s (rise) and 4s (fall). Small background drift, ~ 0.5% over the entire run, has been subtracted from the raw data, which is shown in figure S-6. (b) Responses of DNA/GFET based on Seq1 as a function of concentration for each of the carboxylic acids tested show clear differentiation between analytes. Octanoic acid responses have been multiplied by a factor of 3 for clarity. Error bars reflect standard error of the mean of responses based on five devices and two tests of each device. (c) Sensor responses to butyric acid as a function of concentration for DNA/GFET based on 3 different DNA sequences. (d) Propionic acid responses for DNA/GFET based on different DNA oligomers.

Sensor responses as a function of analyte concentration were well described by a Langmuir-Hill model [31] of binding dynamics:

$$\frac{\Delta I}{I_0} = A\frac{C^n}{{K_a}^n + C^n} + Z$$

Here, C is the analyte concentration, A is the magnitude of the response when all binding sites are occupied, K_a is the concentration at which half the maximum response is seen, and n is the Hill coefficient describing cooperativity of binding. Typically, n was close to 1, indicating independent binding, while K_a ranged from less than 1 ppm (octanoic acid) to hundreds of ppm (propionic acid). For example, the best fit parameters for responses for DNA/GFET based on Seq2 to butyric acid were: A = 0.97 ± 0.25%, n = 0.80 ± 0.21, K_a = 0.06 ± 0.02, in units of fraction of saturated vapor, which corresponds to 34 ppm of butyric acid. Due to the large signal to noise, vapors were readily detected at small fractions of K_a, as shown in Fig. 5.21a, where propionic acid is easily detected at 1.3% of saturated flow while K_a = 70% of saturated flow. One would expect to be able to detect a vapor if the signal to noise level exceeded two. Based on the Langmuir-Hill fit parameters and the measured noise level ($\sim$ 0.01%), we estimate that propionic acid could be detected at an order of magnitude lower concentration, corresponding to ca. K_a/750. Similar performance would be expected for all the analytes tested for this work. The low noise level inherent to the graphene transduction element enables readout of analyte binding at concentrations far below the characteristic affinity of the DNA binding site.

DNA/GFET vapor sensors were found to discriminate between structural isomers of pinene that differ only in the location of a double bond. Fig. 5.22c shows the average response of five devices based on Seq2 to two pulses of α(-) and β(-) pinene at a concentration of $\sim$ 1000 ppm. Responses to β(-) pinene were approximately 40% larger than those to α(-) pinene. The plot of

response as a function of concentration, fig. 5.22d, showed that the response to α(-) pinene saturated at a lower value (A = 0.39 ± 0.04) than for β(-) pinene (A = 0.61 ± 0.07).

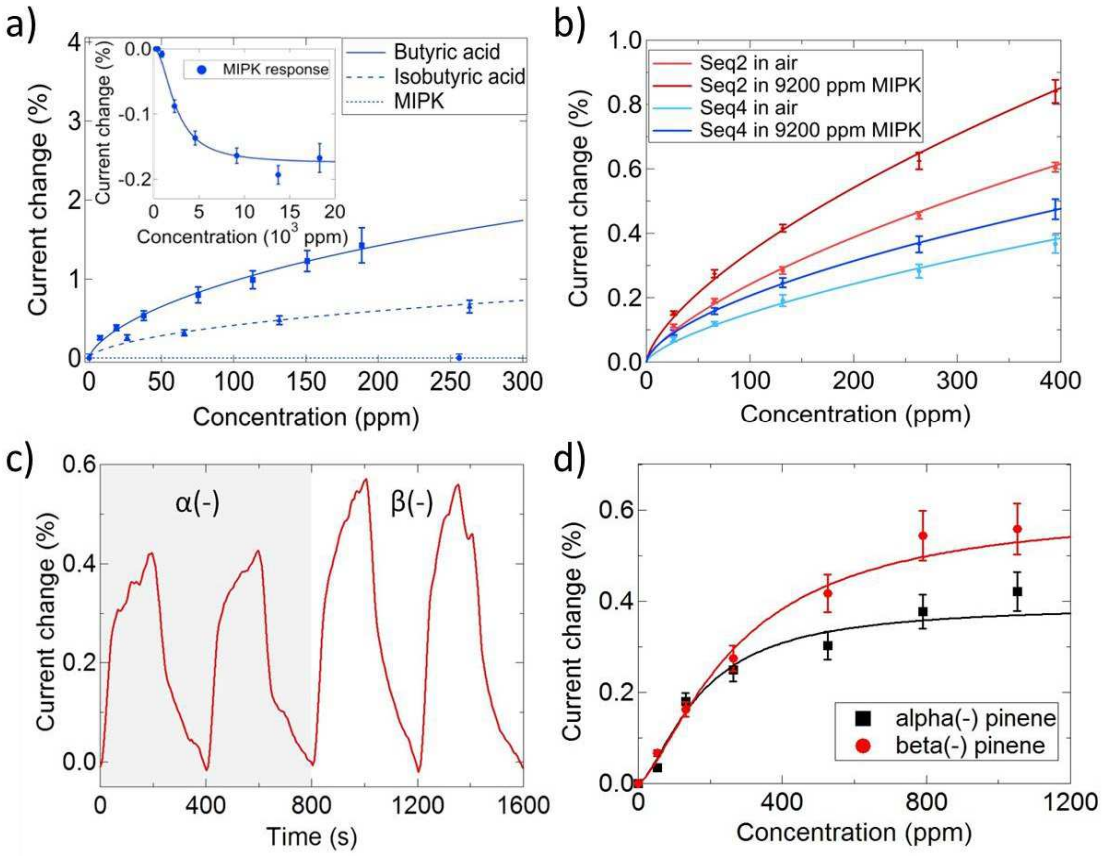

Figure 5.22: (a) Response as a function of concentration of butyric acid, isobutyric acid, and MIPK for DNA/GFET devices based on Seq3. The carboxylic acid isomers are clearly distinguished, while MIPK is detected only at larger concentrations (inset) and shows a response of opposite sign (b) Response vs concentration for DNA/GFET based on Seq2 and Seq4 responding to isobutyric acid in clean air and also in a constant background of 9200 ppm MIPK. Not only is isobutyric acid still detected, but the response magnitude is slightly enlarged, likely due to displacement of MIPK (the binding of which causes a negative response) from the sensor by bound butyric acid (c) Average response of 5 devices based on Seq2 to 1000 ppm of α(-) and β(-) pinene, repeated twice each. The response to β(-) pinene is reproducibly ~ 40% larger than the response to α (-) pinene. (d) Responses of DNA/GFET based on Seq2 as a function of concentration for α(-) and β(-) pinene, showing increasing divergence at higher concentrations. Langmuir-Hill fits saturate at 0.39±0.04 and 0.61±0.07 for α(-) and β(-) respectively.

DNA/GFET hybrids also differentiated between linear and branched carboxylic acids. Figure 5.22a shows the response as a function of concentration for butyric acid, the linear isomer, and isobutyric acid, the branched isomer for DNA/GFET sensors based on Seq3. All four sequences tested were able to distinguish the isomers, with butyric acid eliciting a stronger response at a given concentration. These responses were compared to responses to methyl isopropyl ketone (MIPK), a molecule whose chemical structure differs from that of isobutyric acid only by replacement of a hydroxyl group by a methyl group (Fig. 5.22a). Despite the very low noise level in the devices, responses to MIPK were not resolvable for concentrations below 300 ppm, in contrast the carboxylic acid species, which were readily detected at this level. As MIPK has a much larger vapor pressure than isobutyric acid, high vapor concentrations were also tested. In this regime, MIPK showed negative responses that saturated at approximately -0.2% for concentrations exceeding 10 ppt (Figure 5.22a inset). Responses to isobutyric acid were much larger than those to MIPK at equal concentrations, whether expressed in absolute units or as a fraction of a saturated vapor.

The observation of drastically different responses to isobutyric acid and MIPK helped elucidate the sensing mechanism for carboxylic acids, and, more generally, the mechanism for analytes that are subject to protonation or deprotonation in the nanoscale water layer adsorbed on the DNA, assumed to be near pH = 7. We propose that carboxylic acid molecules are absorbed by a nanoscale water layer that is bound by the (hydrophilic) DNA. The molecules deprotonate in the water and become negatively charged species that couple to binding sites associated with the DNA. This results in a net negative charge that is localized near the GFET channel and a shift of the I_{sd}-V_g curve to positive gate voltage, as a more positive gate voltage is required to achieve the same local electrostatic environment. Since the measurement is conducted with zero gate

voltage, where the carriers are holes (Fig. 5.20b), the response to the carboxylic acid vapor is a current increase.

This proposed mechanism is consistent with the observation of a very small response to MIPK, where the hydroxyl group is replaced by a methyl group that is not subject to deprotonation. The response to MIPK was also of the opposite sign (inset to Fig. 5.22a). A possible explanation for the negative response in the absence of a net molecular charge is that a molecular dipole effect dominates. MIPK has a dipole moment of 2.79 in Debye units [74] due to the highly electronegative oxygen. If binding sites associated with the DNA preferentially orient this dipole with respect to the graphene, it could present a net positive charge to the GFET, resulting in an electrostatic gating which would reduce the current through the device. Finally, sensors were exposed to concentrations of isobutyric acid in the range 20-400 ppm in a large, constant background of MIPK (9200 ppm; Figure 5.22b); in this case, the "refresh" pulse consisted of flowing air and MIPK at 9200 ppm. The presence of isobutyric acid was detected at concentrations as low as 20 ppm. Interestingly, the magnitude of the sensor response was increased compared to the measurement of isobutyric in a background of clean air with a "refresh" pulse of clean air. For DNA/GFET based on Seq4, exposed to isobutyric acid at concentrations above 100 ppm, the difference in sensing response in the presence of MIPK as opposed to clean air was saturated at $\sim$ 0.1 %, very close to the response measured for the same devices to MIPK at that concentration (Fig. 5.22a, inset). This data set was rationalized by assuming it involved competitive binding of MIPK and isobutyric acid, with the isobutyric acid having the larger affinity. This would lead to the isobutyric acid completely displacing the MIPK, so the expected sensing response would be the sum of a contribution due to desorption of MIPK (+ 0.10%) and adsorption of isobutyric acid (+ 0.38%), in agreement with the observed value of 0.48%.

In conclusion, we demonstrated a photolithographic processing technique for wafer scale, CVD-grown graphene that retained its high quality electronic properties and atomically clean surface, enabling their use as DNA-functionalized chemical vapor sensors. The devices had very favorable sensor attributes including fast response, low electronic noise, limits of detection below 1 ppm for some analytes, and the ability to differentiate between extremely similar analytes, specifically structural isomers. The sign and magnitude of these responses were explained by considering the charge distributions formed in the neighborhood of the sensor due to the presence of the nanoscale, hydrated DNA layer. It was found that devices based on different DNA oligomers had uncorrelated analyte response profiles, implying that DNA/graphene hybrids have the chemical diversity required for a variety of electronic nose-type applications. Photolithography-based processing not only enhances the feasibility of graphene based vapor sensor technology, but also represents an important advance on the pathway towards numerous other applications that require large-scale processing of graphene.

Methods:

Graphene Transistor Fabrication: Graphene was grown by low pressure chemical vapor deposition on 99.8% purity copper foil (4" diameter tube furnace; 1020 °C; flow rates of 80 sccm H_2, 50 sccm CH_4, pressure of 1 Torr; 60 minute growth time; 7.5 cm x 15 cm substrate) and transferred to 300 nm SiO2/Si substrates by the 'bubbling' transfer method [75]. After a 1 hour acetone bath, a 20 nm layer of gold was deposited to protect the graphene from subsequent processing. A first round of bi-layer (PMGI/S1813) photolithography [16] was used to define the channel region, exposing the surrounding gold and graphene. The exposed gold was removed by wet etching (1:9 Gold etchant TFA (iodine/potassium iodide complex): deionized water) and the now-exposed graphene was removed using oxygen plasma (300 mTorr, 50W, 1 min). After liftoff

of the resist on top of the channel, a second round of photolithography was used to contact the channel region with Ti/Pd contacts. Finally, gold on top of the channel was removed by wet etching with TFA as described above, leaving pristine graphene with Au/Ti/Pd contacts, connected to large Ti/Pd features. This method ensured that the graphene channel was free of photoresist residue contamination. Any gold etchant or PMMA residue on the graphene was removed by first annealing at atmospheric pressure at 190 °C for 1 hour in an Ar/H2 environment and then soaking the sample in acetone for 5 hours.

DNA functionalization: Crystals of single-stranded DNA of the desired base sequence (Invitrogen) were dissolved in deionized water and diluted to a concentration of 100 μM. Droplets of DNA solution were applied to graphene samples using a pipette, and the sample was incubated in a humid atmosphere to suppress droplet evaporation. After 30 minutes, the droplet was blown off the wafer with pressurized nitrogen, taking care to avoid cross-contamination devices incorporating different DNA sequences.

Measurement of Device Responses to Analyte Vapors: Vapors were delivered into a home-built 6 cm x 2.5 cm x 1 cm chamber via computer-controlled system of mass flow controllers, as described in section 5.1. Clean air (Praxair UN1002) was flowed through a bubbler containing the liquid analyte to create a stream of saturated vapor (flow rate of 1 – 500 sccm). Another stream was flowed through a bubbler containing water to create a stream of saturated water vapor (500 sccm). These two streams were mixed with a stream of clean air whose flow rate was adjusted such that the total flow rate was maintained at 1500 sccm, at 33% relative humidity. Devices were electrically contacted using feed-through connections into the chamber. A 100 mV bias was applied to the devices and currents from up to 10 devices were read out sequentially during the same run using a switching matrix (Keithley 7001) and picoammeter (Keithley 6485). The data

were smoothed to reduce electrical noise and baseline drift, as discussed further in the ESM. Between 5 and 20 devices were measured for each DNA-analyte combination and the sensing response was defined as the normalized change in the conductance, averaged across multiple devices and measurements.

Acknowledgements

This research was supported by the Nano/Bio Interface Center through the National Science Foundation NSEC DMR08-32802, and the work involved use of its facilities. Support from Lockheed Martin is also gratefully acknowledged. M.L. acknowledges the support of a SMART Fellowship.

5.6 DNA-Decorated Graphene Nanomesh for Detection of Chemical Vapors

The results presented in this section have also appeared in the publication "DNA-Decorated Graphene Nanomesh for Detection of Chemical Vapors", A. Esfandiar, N. J. Kybert, E. N. Dattoli, G. H. Han, M. B. Lerner, O. Akhavan, A. Irajizan, A. T. C. Johnson, *Appl. Phys. Lett.*, 2013, 103(183110).

Abstract

Chemically functionalized graphene field effect transistors (GFETs) are promising candidates for detection of vapor and bioorganic materials. It is therefore of interest to explore different functionalization schemes as well as strategies to enhance device sensitivity through sample geometry. To this end we explored the vapor sensor properties of graphene nanomesh (GNM) sensors functionalized with single stranded DNA. The sensor fabrication method was scalable and the devices were capable of detecting different classes of volatile compounds, including carboxylic acids, aldehydes, organophosphates, and explosives. GNM devices had larger vapor responses than standard GFET devices, suggesting the presence of more binding sites for analyte molecules at oxidized edges and lattice defects. DNA-GNM devices were able to discriminate between homologous species with detection limits in the few ppm range, and demonstrated fast response and recovery times at room temperature. Their responses were controlled by the base sequence of the DNA, making the sensor class an intriguing candidate for use in an electronic nose system.

Graphene is a two-dimensional carbon nanomaterial with zero band gap and extraordinary electronic properties that has been intensely investigated for chemical and biomolecular sensors [76, 77]. Pristine graphene is a relatively inert material that shows little

response to many targets of interest [78], so it is desirable to develop tunable and robust methods for functionalization and targeted sensitization of graphene devices. Attachment of suitable chemical components, addition of catalyst nanoparticles, chemical doping by plasma, patterning and making defects at the edges [79-81] are common methods for functionalization of graphene. The method of functionalization directly determines the sensitivity and selectivity of the resulting graphene sensor. "Electronic nose" systems, composed of large sensor arrays coupled to suitable signal processing electronics and pattern recognition algorithms, seek to mimic biological olfaction by combining data from many independent, uncorrelated sensing elements and differentiating analytes using a unique set, or "fingerprint", of sensor responses. This allows an array containing a given number of different types of sensors to identify and classify a much larger number of analytes [82].

We have explored the potential of patterned CVD graphene sensors for this application. A nanomesh structure was patterned from large area graphene using plasma etching around hexagonally close packed polystyrene (PS) beads. In comparison with sensors based on micro-scale graphene devices, we observed that the graphene nanomesh (GNM) had improved sensitivity and enhanced selectivity when functionalized by single-stranded DNA. The method for device functionalization was robust and reproducible, and it yielded sensors with sequence-dependent responses, making this system of interest for development for electronic nose-type applications.

Low pressure chemical vapor deposition (LPCVD) was used to grow monolayer graphene on copper foil (99.8% purity, Alfa Aesar). The system temperature was 980 $^{\circ}$ C, the pressure was 700 mTorr, and the process gas flows were 40 sccm of methane and 50 sccm of hydrogen. We transferred the graphene onto a 300 nm SiO_2/Si substrate using the "bubble" transfer

method [75]. This process was done in an aqueous solution of 0.1 M NaOH with 20 V potential difference between the cathode (platinum plate) and anode (graphene/copper foil). We then formed a self-assembled monolayer of polystyrene (PS) beads (350 nm diameter) at the interface of ethanol/water on a glass slide [83]. This monolayer was gently lowered into a beaker of distilled water, so that it kept its structure on the water surface. A graphene-Si/SiO_2 substrate was pulled up through the layer of PS beads to form close packed domains of beads on the graphene surface. The sample was dried in air, and a gentle plasma etch process (plasma power of 25 W, 10 – 100 sec) was used to remove the unprotected graphene. After plasma etching, PS beads were removed from the graphene by immersion in n-methyl pyrrolidinone (NMP) for 1 hour and then washing with acetone and isopropanol. Using this method, samples of graphene nanomesh (GNM) were produced at centimeter scales with high uniformity.

AFM images of several nanomesh samples with different etching times are shown in Fig. 5.23a. The images show well-ordered graphene domains, connected by narrow graphene nano-ribbons, with considerably more edge than pristine graphene. The ribbon width and electrical properties of the nanomesh were tuned by controlling the etching time. The structural order and extent of chemical doping of graphene samples with different plasma etching times were investigated by Raman spectroscopy (Fig 5.23b). After the etch step, the high intensity of the D peak (1345 cm^{-1}) relative to the G peak (ca. 1580 cm^{-1}; intensity ratio $I_D/I_G \geq 1.5$), the presence of the D'- peak (1620 cm^{-1}), and the reduction in the I_{2D}/I_G ratio all indicate the presence of significant lattice disorder and defects in GNM compared with pristine graphene [84]. It is known that defects and dangling bonds are created at the edges during the plasma etching process [83]. These structural defects can serve as reactive sites for chemical doping and ssDNA adsorption, favoring stronger interaction between the graphene nanomesh and adsorbed chemical species. The

observed shift of the G peak from 1580 cm^{-1} to 1590 cm^{-1} (Fig 5.23b, inset) were assigned to hole doping (~ 3.8×10^{12} cm^{-2}) of the GNM due to defect sites and oxidized dangling bonds at the edges [85, 86]. _ENREF_10

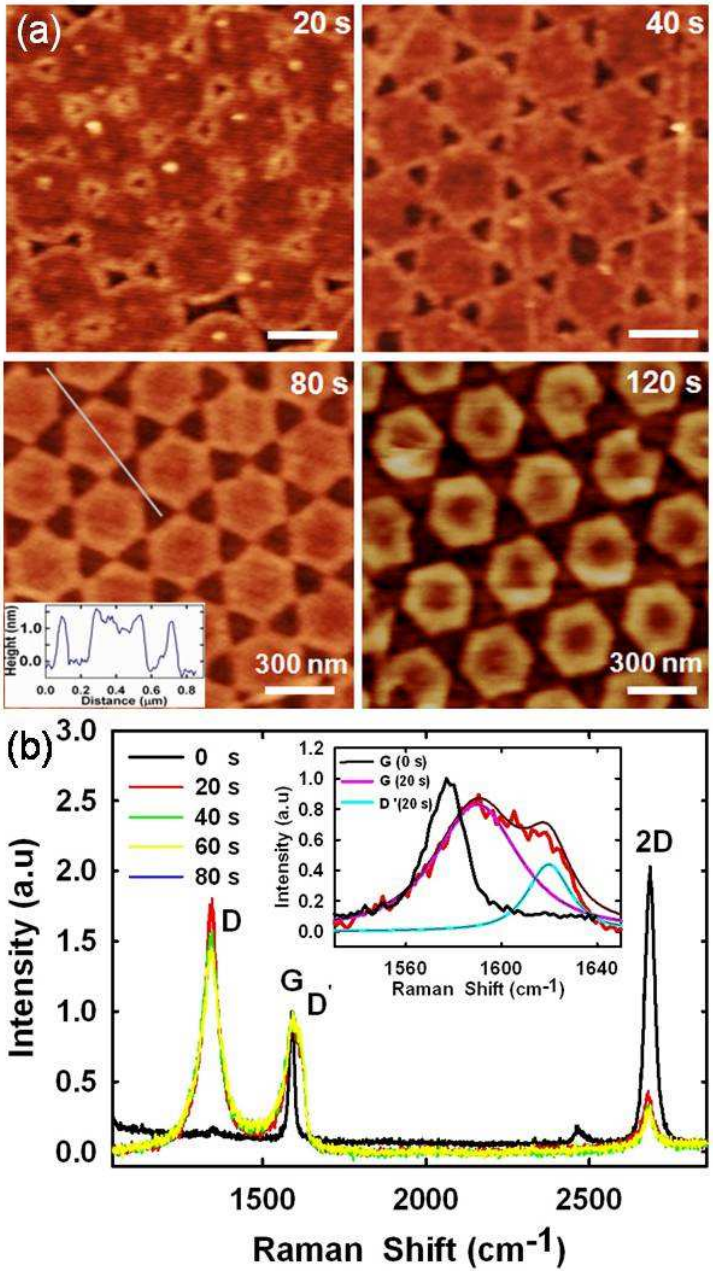

Figure 5.23: (a) AFM images and (b) Raman spectra from GNM structures fabricated using different plasma etching times. Inset: The G peak for graphene with 0 s etch time is a sharp single peak. In contrast, after 20 s etching, the G peak is significantly broadened, with two major components.

After the GNM was defined, contact electrodes were patterned using a photolithographic process that incorporated a gold buffer layer to protect the graphene from contamination by photoresist residues [56]. The electrodes were metalized with 5 nm Ti/50 nm Pd to yield GNM field effect transistors (FETs) with 3 μm channel length and 15 μm channel width, where the bulk silicon substrate served as a global back gate. For comparison, standard (uneteched) graphene FETs were prepared using an identical photolithographic process. Devices were cleaned by annealing at 200° C in a H_2/Ar atmosphere and then functionalized with DNA as done previously for devices based on carbon nanotubes [15] and mechanically exfoliated graphene [25]. Experiments were based on two DNA sequences:

Seq1: 5′ GAG TCT GTG GAGGAG GTA GTC 3′

Seq2: 5′ CCC GTT GGT ATGGGA GTT GAG TGC 3′

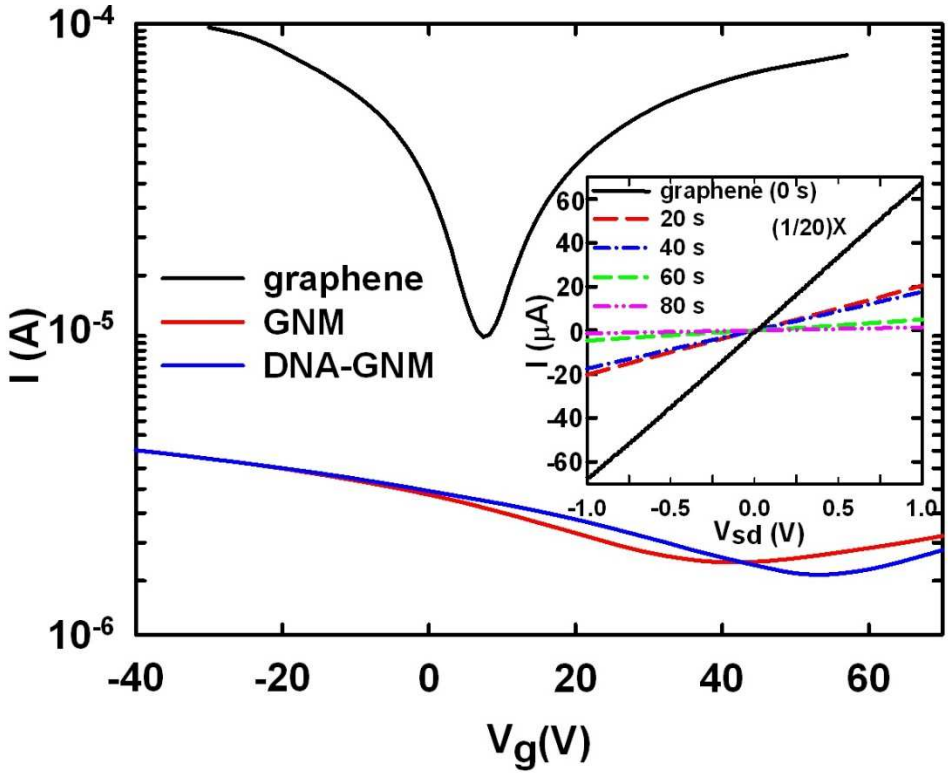

Figure 5.24: Current-gate voltage characteristics of different samples with 100 mV source-drain voltage (V_{sd}). Inset: I-V_{sd} for GNM and graphene devices at zero gate voltage.

DNA was expected to bind to the GNM via π-π stacking interactions between bases of the DNA and bulk graphene and possibly also via electrostatic/hydrogen bonding interactions between the primary amines of the bases and oxygen-containing groups at the edges of GNM [87]. Therefore, AFM images and corresponding height profiles were collected on GNM samples before and after DNA functionalization. They showed an apparent height increase for the GNM of 0.5 - 1.0 nm after adsorption of DNA, consistent with previous measurements of DNA absorption onto exfoliated graphene [25].

Graphene and GNM devices were characterized electronically by measuring the source-drain current as a function of the backgate voltage (I-V_g), with representative data shown in Fig. 5.24. Using an analysis that corrected for the contact resistance [88], it was found that graphene

devices had high carrier mobility (> 800 cm^2/Vs), low doped carrier level (Dirac voltages of a few volts; doped carrier density ca. 6 x $10^{11}/cm^2$), and contact resistances of 260 ± 10 Ω.

In comparison, GNM devices showed an order of magnitude reduction in the on-state current, a shift of the I-V_g of ca. +30 V, and a dramatic reduction of the carrier mobility to approximately 10 cm^2/V-s, all consistent with the presence of structural defects and p-type (hole) doping induced by plasma etching [89]. The reduction in mobility was ascribed to strong charge carrier scattering due to roughness and ill-defined chemical bonding at etched edges of the GNM [90, 91], and interior defects formed during the etch process. Longer etching time caused the electrical resistance to increase from several kΩ to MΩ (Fig. 5.24, inset), consistent with the expected decrease in the width of graphene channels and increased carrier scattering from edge defects. Vapor sensing experiments were mainly conducted with GNM samples fabricated with a plasma etch time of 20 sec since these were found to exhibit a desirable combination of relatively high conductivity and low current noise.

It was observed that application of DNA to the GNM device caused the Dirac point to shift once more by approximately + 20 V (Fig. 5.24); this was attributed to chemical gating of the device by the negatively charged backbone of DNA [20, 25]. ENREF 19 The shift of the Dirac point was used to estimate the doped charge carrier density of the as-fabricated GNM and the DNA-functionalized GNM, leading to values of 3.45×10^{12} cm^{-2} and 4.20×10^{12} cm^{-2} respectively. These values agreed to within 10% with estimates derived from the measured shift of the G band in the Raman spectra [86].

Vapor response experiments were performed under controlled humidity (33%) and at constant total flow rate (1500 sccm). To achieve these conditions, lines of dry clean air were bubbled though the various analytes and water to create saturated vapor streams. To collect

vapor response data, the flows through an analyte line and the humidity line were mixed with a flow of pure carrier gas to create a vapor with controlled relative humidity and analyte concentration (estimated using tabulated vapor pressure values). The device current was monitored with a bias voltage of 1.0 V and zero gate voltage. In order to compare responses from sensors with different resistance values, the data are presented as change in current normalized to the current measured in flowing clean air.

Fig. 5.25 presents responses to several analytes for devices based on as-fabricated graphene, GNM, DNA-GNM based on oligomer Seq1, and DNA-GNM based on Seq2. Fig. 5.25a shows dynamic responses of each device type to increasing concentrations of dimethyl methylphosphonate (DMMP), a nerve gas simulant. Two repetitions of each concentration (200 sec, followed by purging with clean air for 200 sec) were used to demonstrate the reproducibility of the responses. The devices demonstrated fast response times (~ seconds) and recovery to baseline upon flushing with clean air. Negative responses were seen for DMMP, as expected since it is known to be an electron donor, which should lead to reduced conduction in p-type devices [92]. It was observed that as-fabricated graphene devices responded to DMMP at the tested concentrations (50-300 ppm) and that the response was essentially saturated at 50 ppm, in contrast to our earlier reports of null response for devices based on exfoliated graphene [25]. This was ascribed to the presence of a low concentration of defects in CVD graphene that provided binding sites for DMMP. The GNM response to DMMP was roughly the same as that of CVD graphene for concentrations below 100 ppm (~ -2%), but the magnitude of the response increased to ~ -8% at 300 ppm. This is consistent with enhanced interaction between DMMP and binding sites formed by the plasma etching at the edge of the GNM, where dangling bonds, hydroxyl and carboxyl groups and lattice defects are expected to be prevalent. After DNA functionalization,

GNM devices showed a sequence-dependent response that reflected differences in the attraction between DMMP and the two DNA sequences [15, 25, 55]. DNA-GNM devices based on Seq1 showed a smaller vapor response magnitude than unfunctionalized GNM, which was attributed to suppression of DMMP binding at the GNM edge sites due to the presence of DNA, while DNA in the bulk region did not provide sufficient affinity for DMMP binding to compensate. In contrast, the responses to DMMP of DNA-GNM devices based on Seq2 were enhanced at all concentrations tested, indicating high affinity between this oligomer and DMMP.

Additional experiments were conducted with hexanoic acid and propionic acid (Fig. 5.25b,c). As-fabricated graphene devices showed very small positive responses to both compounds, consistent with our earlier reports that concluded that one sensor response mechanism is chemical gating of holes due to deprotonation of carboxyl groups in ambient water [20, 25, 78], which was presumably present in only small amounts on clean CVD graphene. GNM devices showed much larger, positive responses to both hexanoic acid and propionic acid (the former at concentration as low as 1 ppm), consistent with the presence of additional water on the sample due to edge defects induced by the etching process. DNA functionalization led to a significant, sequence-dependent increase in the response for all concentrations tested. Fig. 5.25d shows the response as a function of concentration of hexanoic and propionic acid, for as prepared GNM and DNA-GNM based on Seq1 and Seq2; error bars reflect the standard error of the mean for a set of eight measured devices of each type and multiple tests of each device-analyte pair. Interestingly, DNA-GNM devices based on Seq1 had the strongest response to hexanoic acid at all concentrations, while DNA-GNM devices based on Seq2 responded more strongly at low concentrations of propionic acid and less strongly at high concentrations. The data in fig. 5.25d were well fit by Langmuir- Hill isotherms of the form

$$\frac{\Delta I}{I_0} = A\frac{C^n}{K_d^n + C^n} + Z$$

Here *C* is the analyte concentration, *A* is the magnitude of the saturated response, K_d is the concentration at which half the maximum response is seen and *n* is the Hill coefficient describing cooperativity of binding [93]. The best-fit values for the offset parameter, *Z*, were always found to be statistically consistent with zero. For example, for GNM functionalized with Seq2, the best-fit parameters were: $A = 6.4 \pm 2.1\%$, $n = 0.70 \pm 0.24$, $K_d = 450 \pm 200$ ppm, and $Z = -0.5 \pm 0.5\%$.

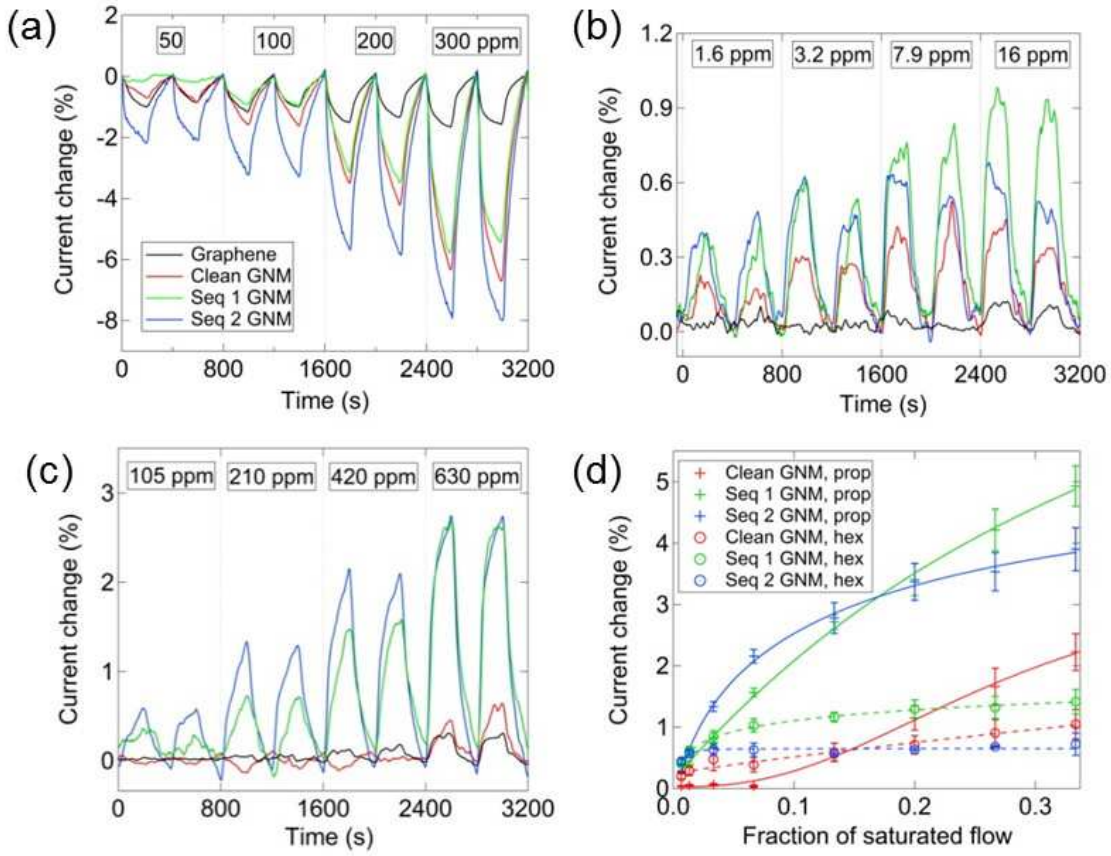

Figure 5.25: (a-c) Responses of devices based on graphene, graphene nanomesh (GNM), DNA-GNM based on Seq1, and DNA-GNM based on Seq2 to: a) DMMP b) hexanoic acid, and c) propionic acid. d) Average response as a function of concentration for GNM, DNA-GNM based on Seq1, and DNA-GNM based on Seq2. Fits are derived from Langmuir-Hill isotherms.

Analyte VOC	Est. Conc. (ppm)	Graphene (%)	GNM (%)	GNM/seq 1 (%)	GNM/seq2 (%)
DMMP	200	-1.3 ±0.2	-3.8 ±0.3	-3.5 ±0.3	**-5.8 ±0.5**
DNT	90	-0.6 ±0.1	-2.7 ±0.4	-1.6 ±0.2	**-7.1 ±0.3**
Propionic acid	210	<0.1	<0.1	0.7 ±0.1	**1.3 ±0.1**
Hexanoic acid	8	<0.1	0.5 ±0.2	0.8 ±0.1	**0.6 ±0.1**
Nonanal	11	-0.2 ± 0.1	-1.3 ±0.2	-0.3 ±0.1	**-2.7 ±0.2**
Decanal	**13**	**-0.7 (±0.1)**	**-0.8 (±0.2)**	**-0.2 (±0.1)**	**-2.2 (±0.3)**

Table 5.9: Responses of bare graphene, GNM and DNA-GNM to a variety of volatile analytes at ppm concentrations.

As seen from Table 5.9, GNM devices consistently showed greater responses to analyte vapors than graphene devices, which was attributed to the presence of more reactive sites at the GNM edges due to etching. It was observed that DNA-GNM devices exhibited responses that were controlled by the sequence of the DNA, as observed earlier for devices based on carbon nanotubes [15] and on exfoliated graphene [25]. These attributes make DNA-functionalized GNM-based sensors potentially useful for the detection and classification of vapors consisting of many different compounds over a wide range of concentrations and chemical families. The sequence dependent behaviors in the sensing data may reflect more complex mechanisms beyond simple electrostatic interactions. More detailed experiments are needed to determine the operational mechanism of these types of DNA-functionalized sensors. In future experiments, GNM could potentially be functionalized by other chemical groups and biomaterials for targeted sensing and electronic nose-type applications in either gas or liquid environments.

References

1. Kauffman, D.R. and A. Star, *Carbon nanotube gas and vapor sensors.* Angewandte Chemie-International Edition, 2008. **47**(35): p. 6550-6570.
2. Zuniga, C., et al., *Nanoenabled microelectromechanical sensor for volatile organic chemical detection.* Applied Physics Letters, 2009. **94**: p. 223122.
3. Penza, M., et al., *Alcohol detection using carbon nanotubes acoustic and optical sensors.* Applied Physics Letters, 2004. **85**(12): p. 2379-2381.
4. Barone, P.W., et al., *Near-infrared optical sensors based on single-walled carbon nanotubes.* Nature Materials, 2005. **4**(1): p. 86-92.
5. Snow, E.S., et al., *Chemical detection with a single-walled carbon nanotube capacitor.* Science, 2005. **307**(5717): p. 1942-1945.
6. Varghese, O.K., et al., *Gas sensing characteristics of multi-wall carbon nanotubes.* Sensors and Actuators B-Chemical, 2001. **81**(1): p. 32-41.
7. Star, A., et al., *Electronic detection of specific protein binding using nanotube FET devices.* Nano Letters, 2003. **3**(4): p. 459-463.
8. Khamis, S.M., et al., *DNA-decorated carbon nanotube-based FETs as ultrasensitive chemical sensors: Discrimination of homologues, structural isomers, and optical isomers.* Aip Advances, 2012. **2**(2).
9. Pengfei, Q.F., et al., *Toward large arrays of multiplex functionalized carbon nanotube sensors for highly sensitive and selective molecular detection.* Nano Letters, 2003. **3**(3): p. 347-351.
10. Star, A., et al., *Nanoelectronic carbon dioxide sensors.* Advanced Materials, 2004. **16**(22): p. 2049-2052.
11. Zhang, Y.M., D.J. Zhang, and C.B. Liu, *Novel chemical sensor for cyanides: Boron-doped carbon nanotubes.* Journal of Physical Chemistry B, 2006. **110**(10): p. 4671-4674.
12. Star, A., et al., *Gas sensor array based on metal-decorated carbon nanotubes.* Journal of Physical Chemistry B, 2006. **110**(42): p. 21014-21020.
13. Kauffman, D.R., et al., *Understanding the Sensor Response of Metal-Decorated Carbon Nanotubes.* Nano Letters, 2010. **10**(3): p. 958-963.
14. Liang, Y.X., Y.J. Chen, and T.H. Wang, *Low-resistance gas sensors fabricated from multiwalled carbon nanotubes coated with a thin tin oxide layer.* Applied Physics Letters, 2004. **85**(4): p. 666-668.
15. Staii, C., et al., *DNA-decorated carbon nanotubes for chemical sensing.* Nano Letters, 2005. **5**(9): p. 1774-1778.
16. Khamis, S.M., R.A. Jones, and A.T.C. Johnson, *Optimized photolithographic fabrication process for carbon nanotube devices.* AIP Advances, 2011. **1**(2): p. 022106.
17. Wang, C., et al., *Wafer-Scale Fabrication of Separated Carbon Nanotube Thin-Film Transistors for Display Applications.* Nano Letters, 2009. **9**(12): p. 4285-4291.
18. Choi, S.-J., et al., *Comparative study of solution-porcessed carbon nanotube network transistors.* Applied Physics Letters, 2012. **101**: p. 112104.
19. Dresselhaus, M.S., et al., *Raman spectroscopy on isolated single wall carbon nanotubes.* Carbon, 2002. **40**(12): p. 2043-2061.

20. Lerner, M.B., et al., *Toward Quantifying the Electrostatic Transduction Mechanism in Carbon Nanotube Molecular Sensors.* Journal of the American Chemical Society, 2012. **134**(35): p. 14318-14321.
21. Goldsmith, B.R., et al., *Biomimetic Chemical Sensors Using Nanoelectronic Readout of Olfactory Receptor Proteins.* Acs Nano, 2011. **5**(7): p. 5408-5416.
22. Johnson, R.R., A.T. Johnson, and M.L. Klein, *Probing the structure of DNA-carbon nanotube hybrids with molecular dynamics.* Nano Lett, 2008. **8**(1): p. 69-75.
23. Johnson, R.R., A.T. Johnson, and M.L. Klein, *The nature of DNA-base-carbon-nanotube interactions.* Small, 2010. **6**(1): p. 31-4.
24. Johnson, R.R., et al., *Free Energy Landscape of a DNA-Carbon Nanotube Hybrid Using Replica Exchange Molecular Dynamics.* Nano Letters, 2009. **9**(2): p. 537-541.
25. Lu, Y., et al., *DNA-decorated graphene chemical sensors.* Applied Physics Letters, 2010. **97**(8): p. 083107.
26. Gallagher, M., et al., *Analyses of volatile organic compounds from human skin.* British Journal of Dermatology, 2008. **159**(4): p. 780-791.
27. Zeng, X.-N., et al., *Analysis of the characteristic human female axillary odors: qualitative comparison to males.* Journal of Chemical Ecology, 1996. **22**: p. 237-257.
28. Preti, G., et al., *Odors and disease: Volatile biomarkers from human skin cancer.* Chemical Senses, 2008. **33**: p. S138-S139.
29. Kanda, F., et al., *Elucidation of chemical compounds responsible for foot malodour.* British Journal of Dermatology, 1990. **122**: p. 1771-1776.
30. Menashe, I., et al., *Genetic elucidation of huyman hypersomia to isovaleric acid.* PLoS Biology, 2007. **5**: p. e:284.
31. Hill, A.V., *The possible effects of the aggregation of the molecules of huemoglobin on its dissociation curves.* Journal of Physiology, 1910. **40**: p. 4-7.
32. Bondavalli, P., P. Legagneux, and D. Pribat, *Carbon nanotube based transistors as gas sensors: State of the art and critical review.* Sensors and Actuators B-Chemical, 2009. **140**: p. 304-318.
33. Wilson, A.D. and M. Baietto, *Applications and advances in electronic-nose technologies.* Sensors, 2009. **9**: p. 5099-5148.
34. Xu, C., S.C. Ng, and H.S. Chan, *Self-assembly of perfunctionalized beta-cyclodextrins on a quartz crystal microbalance for real-time chiral recognition.* Langmuir, 2008. **24**(16): p. 9118-9124.
35. Kurzawski, P., V. Schurig, and A. Hierlemann, *Chiral sensing using a complementary metal-oxide semiconductor-integrated three-transducer microsensor system.* Anal Chem, 2009. **81**(22): p. 9353-9364.
36. Torsi, L., et al., *A sensitivity-enhanced field-effect chiral sensor.* Nature Materials, 2008. **7**: p. 412-417.
37. Corradini, R., et al., *Chirality as a tool in nucleic acid recognition: principles and relevance in biotechnology and in medicinal chemistry.* Chirality, 2007. **19**(4): p. 269-94.
38. Johnson, R.R., A.T.C. Johnson, and M.L. Klein, *Probing the Structure of DNA-Carbon Nanotube Hybrids with Molecular Dynamics.* Nano Letters, 2008. **8**: p. 69-75.
39. Zeng, X.-N., et al., *An investigation of human apocrine gland secretion for axillary odor precursors.* Journal of Chemical Ecology, 1992. **18**: p. 1039-1055.

40. Pierce, J., J.D., et al., *Cross-adaptation of sweaty-smelling 3-methyl-2-hexenoic acid by its ethyl esters is determined by structural similarity.* Journal of the Society of Cosmetic Chemists, 1996. **47**: p. 363-375.
41. Serra, S., C. Fuganti, and E. Brenna, *Biocatalytic preparation of natural flavours and fragrances.* Trends in Biotechnology, 2005. **23**(4): p. 193-198.
42. Wysocki, C.J., et al., *Cross-adaptation fo a model human stress-related odor with fragrance chemicals and ethyl esters of axillary odorants: Gender-specific effects.* Journal of Flavour Fragrance, 2009. **24**: p. 209-218.
43. Natsch, A., et al., *A broad diversity of volatile carboxylic acids, released by a bacterial aminoacylase from axilla secretions, as candidate molecules for the determination of human-body odor type.* Chemistry & Biodiversity, 2006. **3**(1): p. 1-20.
44. Hasegawa, Y., M. Yabuki, and M. Matsukane, *Identification of new odoriferous compounds in human axillary sweat.* Chemistry & Biodiversity, 2004. **1**(12): p. 2042-2050.
45. Akutsu, T., et al., *Individual comparisons of the levels of (E)-3-methyl-2-hexenoic acid, an axillary odor-related compound, in Japanese.* Chemical Senses, 2006. **31**(6): p. 557-563.
46. Czarnowski, D., et al., *Effect of a Low Carbohydrate-Diet on Plasma and Sweat Ammonia Concentrations during Prolonged Nonexhausting Exercise.* European Journal of Applied Physiology and Occupational Physiology, 1995. **70**(1): p. 70-74.
47. Zeng, X.N., et al., *Analysis of characteristic human female axillary odors: Qualitative comparison to males.* Journal of Chemical Ecology, 1996. **22**(2): p. 237-257.
48. Haze, S., et al., *2-Nonenal newly found in human body odor tends to increase with aging.* Journal of Investigative Dermatology, 2001. **116**(4): p. 520-524.
49. Martin, A., et al., *A Functional ABCC11 Allele Is Essential in the Biochemical Formation of Human Axillary Odor.* Journal of Investigative Dermatology, 2010. **130**(2): p. 529-540.
50. Prokop-Prigge, K.A., et al., *Identification of volatile organic compounds in human cerumen.* J Chromatogr B Analyt Technol Biomed Life Sci, 2014. **953-954**: p. 48-52.
51. Dalton, P., et al., *Chemosignals of Stress Influence Social Judgments.* Plos One, 2013. **8**(10).
52. Senol, M. and P. Fireman, *Body odor in dermatologic diagnosis.* Cutis, 1999. **63**(2): p. 107-111.
53. Shirasu, M. and K. Touhara, *The scent of disease: volatile organic compounds of the human body related to disease and disorder.* Journal of Biochemistry, 2011. **150**(3): p. 257-266.
54. Shirasu, M., et al., *Dimethyl Trisulfide as a Characteristic Odor Associated with Fungating Cancer Wounds.* Bioscience Biotechnology and Biochemistry, 2009. **73**(9): p. 2117-2120.
55. Kybert, N.J., et al., *Differentiation of Complex Vapor Mixtures Using Versatile DNA-Carbon Nanotube Chemical Sensor Arrays.* Acs Nano, 2013. **7**(3): p. 2800-2807.
56. Kybert, N.J., et al., *Scalable arrays of chemical vapor sensors based on DNA-decorated graphene.* Nano Research, 2013. **7**(1): p. 95-103.
57. Zeng, X.N., et al., *Analysis of Characteristic Odors from Human Male Axillae.* Journal of Chemical Ecology, 1991. **17**(7): p. 1469-1492.
58. Natsch, A., et al., *A specific bacterial aminoacylase cleaves odorant precursors secreted in the human axilla.* Journal of Biological Chemistry, 2003. **278**(8): p. 5718-5727.
59. Sawano, K., K. Ishida, and A. Shimada, *Perfume composition*, in *United States Patent*. 1992: USA.

60. *American Cancer Society, Cancer Facts and Figures 2015*. 2015.
61. Buys, S.S., et al., *Effect of screening on ovarian cancer mortality: The prostate, lung, colorectal and ovarian (plco) cancer screening randomized controlled trial.* JAMA, 2011. **305**(22): p. 2295-2303.
62. Petricoin Iii, E.F., et al., *Use of proteomic patterns in serum to identify ovarian cancer.* The Lancet, 2002. **359**(9306): p. 572-577.
63. McCulloch, M., et al., *Diagnostic accuracy of canine scent detection in early- and late-stage lung and breast cancers.* Integrative Cancer Therapies, 2006. **5**(1): p. 30-39.
64. Willis, C.M., et al., *Olfactory detection of human bladder cancer by dogs: proof of principle study.* British Medical Journal, 2004. **329**(7468): p. 712-714A.
65. Horvath, G., H. Andersson, and S. Nemes, *Cancer odor in the blood of ovarian cancer patients: a retrospective study of detection by dogs during treatment, 3 and 6 months afterward.* Bmc Cancer, 2013. **13**.
66. Kouremenos, K.A., M. Johansson, and P.J. Marriott, *Advances in Gas Chromatographic Methods for the Identification of Biomarkers in Cancer.* Journal of Cancer, 2012. **3**: p. 404-420.
67. Bajtarevic, A., et al., *Noninvasive detection of lung cancer by analysis of exhaled breath.* Bmc Cancer, 2009. **9**.
68. Preti, G., et al., *Odors and Disease: Volatile Biomarkers from Human Skin Cancer.* Chemical Senses, 2008. **33**(8): p. S138-S139.
69. Woo, H.M., et al., *Mass spectrometry based metabolomic approaches in urinary biomarker study of women's cancers.* Clinica Chimica Acta, 2009. **400**(1-2): p. 63-69.
70. Krone, N., et al., *Gas chromatography/mass spectrometry (GC/MS) remains a pre-eminent discovery tool in clinical steroid investigations even in the era of fast liquid chromatography tandem mass spectrometry (LC/MS/MS).* Journal of Steroid Biochemistry and Molecular Biology, 2010. **121**(3-5): p. 496-504.
71. Balakrishnama, S. and A. Ganapathiraju, *Linear discriminant analysis-a brief tutorial.* Institute for Signal and information Processing, 1998.
72. Nagashio, K., et al., *Electrical transport properties of graphene on SiO2 with specific surface structures.* Journal of Applied Physics, 2011. **110**(2): p. 024513.
73. Liao, L., et al., *High-κ oxide nanoribbons as gate dielectrics for high mobility top-gated graphene transistors.* Proceedings of the National Academy of Sciences, 2010. **107**(15): p. 6711-6715.
74. Abboud, J.L.M. and R. Notari, *Critical compilation of scales of solvent parameters. Part I. Pure, non-hydrogen bond donor solvents*, in *Pure and Applied Chemistry*. 1999. p. 645.
75. Gao, L., et al., *Repeated growth and bubbling transfer of graphene with millimetre-size single-crystal grains using platinum.* Nat Commun, 2012. **3**: p. 699.
76. Ratinac, K.R., et al., *Toward ubiquitous environmental gas sensors - Capitalizing on the promise of Graphene.* Environmental Science and Technology, 2010. **44**: p. 1167-1176.
77. Stine, R., et al., *Fabrication, optimization, and use of graphene field effect sensors.* Analytical Chemistry, 2013. **85**: p. 509-521.
78. Dan, Y., et al., *Intrinsic response of graphene vapor sensors.* Nano Lett, 2009. **9**(4): p. 1472-5.
79. Georgakilas, V., et al., *Functionaliztion of graphene: Covalent and non-covalent approaches, derivatives, and applications.* Chemical Reviews, 2013. **112**: p. 6156-6214.

80. Lin, Y.-C., C.-Y. Lin, and P.-W. Chiu, *Controllable graphene N-doping iwth ammonia plasma.* Applied Physics Letters, 2010. **96**: p. 133110.
81. Tan, X., et al., *Control and enhancement of graphene sensitivity by engineering edge defects.* IEEE Sensors Journal, 2012: p. 978-1-4577.
82. Hopfield, J.J., *Odor space and olfactory processing: collective algorithms and neural implementation.* Proceedings of the National Academy of Sciences of the United States of America, 1999. **96**: p. 12506-12511.
83. Dai, Z.H., et al., *Phase diagram, deisgn of monolayer binary colloidal crystals, and their fabrication based on ethanol-asssited self-assembly at the air/water interface.* ACS Nano, 2012. **6**: p. 6706-6716.
84. Wang, M., et al., *CVD Growth of Large Area Smooth-edged Graphene Nanomesh by Nanosphere Lithography.* Scientific Reports, 2013. **3**.
85. Yan, J., et al., *Electric field effect tuning of electron-phonon coupling in graphene.* Physical Review Letters, 2007. **98**: p. 166802.
86. Das, A., et al., *Monitoring dopants by Raman scattering in an electrochemically top-gated graphene transistor.* Nature Nanotechnology, 2008. **3**(4): p. 210-215.
87. Premkumar, T. and K.E. Geckeler, *Graphene-DNA hybrid materials: Assembly, applications, and prospects.* Progress in Polymer Science, 2012. **37**: p. 515-529.
88. Liao, L., et al., *High-kappa oxide nanoribbons as gate dielectrics for high mobility top-gated graphene transistors.* Proceedings of the National Academy of Sciences of the United States of America, 2010. **107**: p. 6711-6715.
89. Kim, M., et al., *Electronic transport and raman scattering in size-controlled nanoperforated graphene.* ACS Nano, 2012. **6**: p. 9846-9854.
90. Betti, A., G. Flori, and G. Iannaccone, *Investigation of low-field mobility in graphene nanoribbons.* IEEE Transactions on Electron Devices, 2011. **58**: p. 2824-2830.
91. Liang, X.M., et al., *Electrostatic force assisted exfoliation of prepatterned few-layer graphenes into device sites.* Nano Letters, 2009. **9**: p. 467-472.
92. Novak, J.P., et al., *Nerve agent detection using networks of single-walled carbon nanotubes.* Applied Physics Letters, 2003. **83**(19): p. 4026-4028.
93. Lehninger, A.L., D.L. Nelson, and M.M. Cox, *Lehninger Principles of Biochemistry*. 5th ed. 2008, New York: W.H. Freeman.

CHAPTER 6: Detection of Specific Molecular Targets in Solution

Chapter 6 is focused on the development of biosensors for molecular targets in solution. The method used to attack this type of detection challenge is to design chemistries to attach specific receptors for the target biomolecules to the nanomaterial FET surface. In section 6.1, carbon nanotube FETs are non-covalently functionalized with pyrene-boronic acid. Pyrene π-π stacks onto graphitic surfaces, while the boronic acid groups are known to react with glucose to form a negatively charged boronate anion. By inducing this reaction on the surface of the carbon nanotube, we are able to read out the binding event as a concentration-dependent shift in the carbon nanotube I-V_g curve, allowing glucose detection down to a limit of detection of 1 μM, making this a promising technology for glucose detection in saliva and potentially demonstrating a route towards bloodless glucose monitoring.

In chapter 6.2, a re-engineered cell membrane protein called the μ-opiod receptor is tethered to monolayer MoS_2 by coordinately-covalently linking a nickel ion to the surface sulfur atoms in the MoS_2 and binding that nickel ion to a histidine tag on the protein. Evidence for binding of the protein to the MoS_2 surface includes AFM studies of the MoS_2 surfaces, as well as electronic shifts after protein attachment. The resulting hybrid FETs are used to read out the concentration of enkephalin, an opiod peptide. Again, we demonstrate a concentration-dependent response in the I-V_g curve and we measure an affinity of the FET for enkephalin in the 10s nM range, in agreement with other affinity measurements for this protein. We envision this as the first set of experiments that could lead towards an MoS_2 based solid-state platform with electronic readout for the monitoring of peptide-protein, opiod-protein and protein-protein interactions.

6.1 Scalable, Non-Invasive Glucose Sensor Based on Boronic Acid Functionalized Carbon Nanotube Transistors

Abstract

We developed a scalable, label-free all-electronic sensor for D-glucose based on a carbon nanotube transistor functionalized with pyrene-1-boronic acid. This sensor responds to glucose in the range 1μM – 100 mM, which includes typical glucose concentrations in human blood and saliva. Control experiments establish that functionalization with the boronic acid provides high sensitivity and selectivity for glucose. The devices show better sensitivity than commercial blood glucose meters and could represent a general strategy to bloodless glucose monitoring by detecting low concentrations of glucose in saliva.

Carbon nanotube field effect transistors (NT FETs) provide a unique platform for biosensing applications [1, 2]. Since every atom is on the surface, carbon nanotubes are highly sensitive to small changes in their immediate surroundings, making them ideal readout elements for chemical sensors. Ease of fabrication, well-understood carbon chemistry, and fast electronic readout (≤1 ms) make functionalized CNTFETs desirable as chemical sensors for biomolecular detection [3-5].

Diabetes mellitus affects nearly 300 million people worldwide and its incidence is expected to increase rapidly in the coming decades[6]. Continuous and accurate monitoring of patient blood glucose levels is critical for diagnosis and management of the disease. One approach for detecting glucose in fluid is complexation by boronic acid moieties [7]. This method is superior to the more common enzymatic detection strategies because it is not affected by factors that affect mass transport of the analyte and enzyme activity [8]. Commercially available glucose

sensors consume the analyte, must prevent protein denaturation over a long time period, and require mediators to transport electrons into the conduction channel [9, 10]. In contrast, boronic acid-mediated detection is based on equilibrium thermodynamics and does not require special treatment of the sensor to maintain structural integrity [10]. Complexation of boronic acid with a monosaccharide results in a boronate anion, which can affect the local electrostatic environment surrounding the nanotube [11, 12]. Nanotube-based glucose sensors have been demonstrated using a variety of techniques [13, 14]; however, the sensitivity of nanotube FETs to the local charge environment suggests that this modality could potentially attain the lowest detection limits [15, 16]. The prevalence of boronate anions created from bound glucose molecules is expected to modulate the electronic transport properties of the FET in a concentration-dependent manner. Carbon nanotube-based sensors with sensitivity equal to or greater than commercially available enzyme-based immunoassays would then potentially be useful for glucose monitoring in bodily fluids other than blood, such as saliva, eliminating the need for daily, uncomfortable finger pricking.

Biosensors that combine chemical elements for analyte recognition with an all-electronic, nano-enabled readout element would be ideal for medical diagnosis if they could be made cost effective. The use of solutions enriched in semiconducting nanotubes [17, 18] for wafer-scale fabrication of thin-film transistors has been reported [19], and this approach was recently extended in a demonstration of the production of large arrays of reproducible vapor sensors based on DNA-functionalized NT transistors [20]. A similar process was used to create the devices used in these experiments, offering the prospect that they could be produced with high yield.

Experiments were performed using solutions of carbon nanotubes comprised of 98% semiconducting NTs (NanoIntegris, Inc.), with a concentration of 10 mg/L. Transistor arrays were

fabricated on oxidized silicon wafers (oxide thickness 500 nm). Atomic layer deposition (ALD) was used to create a monolayer of 3-aminopropyltriethoxysilane (APTES) to promote adhesion of the carbon nanotubes [21, 22], which can also improve the performance of nanotube-based sensors [23]. Drops of NT solution were pipetted onto the APTES-coated wafer and incubated in a humid environment for 20 minutes. The wafer was then washed in 2 successive isopropanol baths for 5 minutes each, followed by a deionized water bath for 10 minutes, and the wafer was then dried using compressed nitrogen gas. Source and drain electrodes were composed of 50 nm of titanium, defined via a photolithographic process optimized for NT devices [24] and metallized in an electron beam evaporator. Titanium was chosen purposefully as the electrode material because it forms a self-passivating oxide layer under ambient, thus ensuring that any sensing response is due to the interactions between the analyte and the NTs rather than the metal contacts [25]. This completed the three-terminal field effect transistor (FET) geometry with the silicon backplane acting as a global backgate.

The efficacy of functionalization of NT transistors with pyrene compounds, including pyrene-1-boronic acid, has been documented previously by us via atomic force microscopy, X-ray photoelectron spectroscopy, and electronic measurements [15]. FET devices were submerged in 5 μM pyrene-1-boronic acid in acetonitrile for 2 hours, then transferred to baths of acetonitrile, isopropanol, and DI water for 5 minutes each and dried with compressed nitrogen. The sample was then baked on a hot plate at 120°C for 2 hours in order to drive off any remaining solvents.

Saccharide solutions (glucose, lactose) were prepared by dissolving a known mass of sugar in DI water to achieve the desired concentrations. To start a sensing experiment, two 500 nL droplets of pure DI water were pipetted onto the channel region to allow the sensor to equilibrate to liquid temperature, pH, ionic strength, etc. Glucose/lactose solutions of increasing

concentrations were then added to the existing water droplets in 500 nL increments with the resulting equilibrium concentrations used in measuring sensor responses. Each glucose/lactose concentration was measured on 6-8 different devices to ensure reproducibility. The principle of operation is illustrated in Figure 6.1.

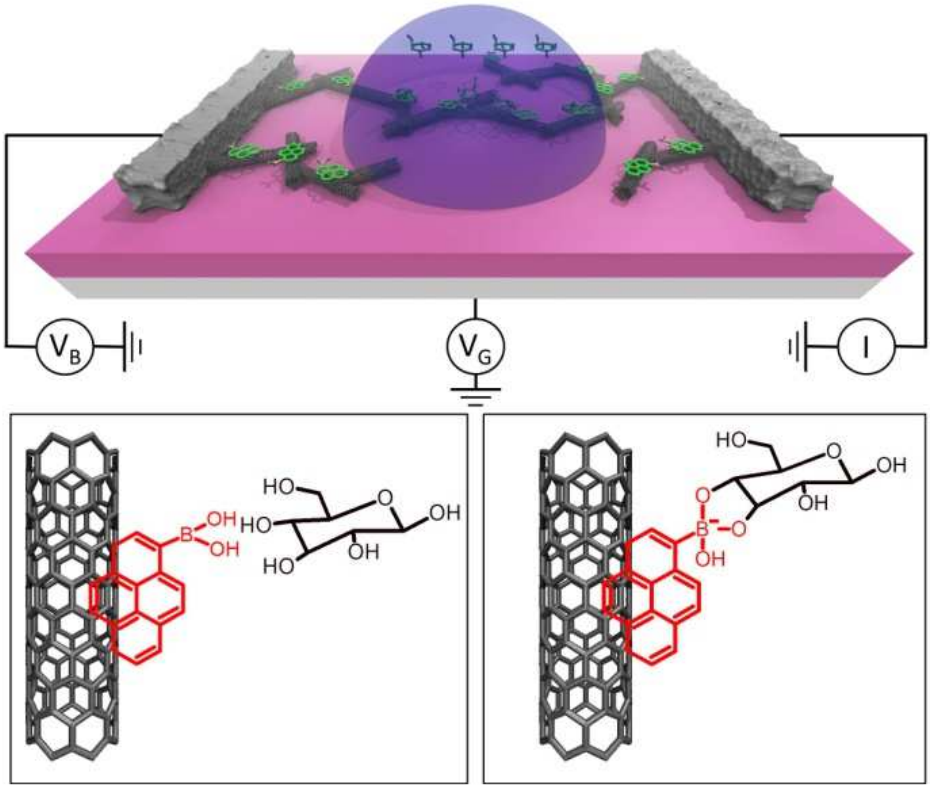

Figure 6.1: a) Schematic of the experimental geometry. B) Illustration of glucose binding to a nanotube functionalized with pyrene-1-boronic acid. c) Bound glucose forms a boronate anion complex that has electrostatic effects on the nanotube FET.

Figure 6.2 shows current-gate voltage (I-V_g) characteristics from the as-fabricated NT FET, after functionalization with pyrene-1-boronic acid, and after exposure to glucose solution. Following incubation in pyrene-1-boronic acid, devices showed an increase of ~ 2-3V in threshold voltage V_{TH}, defined as the voltage required to deplete carriers in the channel. The threshold voltage was calculated by fitting the I-V_g curve with a tangent line at the point of maximum

transconductance and determining the intercept of this line with the gate voltage axis[26]. This increase in V_{TH} can be ascribed to electrostatic "chemical gating" of the device by negatively charged boronic acid moieties in the presence of a thin water layer that accumulates on the hydrophilic substrate [15].

Functional groups on the substrate surface can change the local pH in this thin water layer by as much as two pH units [27]. The proton-accepting, amine-terminated functional groups in the APTES monolayer would be expected to raise the pH in the interfacial water layer, making it slightly basic. Under these conditions, the pyrene-1-boronic acid with a pK_a of 8.8 [28] would be significantly deprotonated (13.6% deprotonated for pH 8 and 31.9% for pH 8.5), so each molecule acts as a negatively charged local electrostatic gate. In order to compensate for the effect of this local gate, the field supplied by the global backgate would have to be more positive, hence the shift to the right in the threshold voltage on the I-V_g characteristic. Upon introduction of glucose, the threshold voltage increased slightly (1-2 V depending on glucose concentration) and the ON state current (current at V_g = -10V) decreased by a factor that varied systematically with glucose concentration (see supporting information).

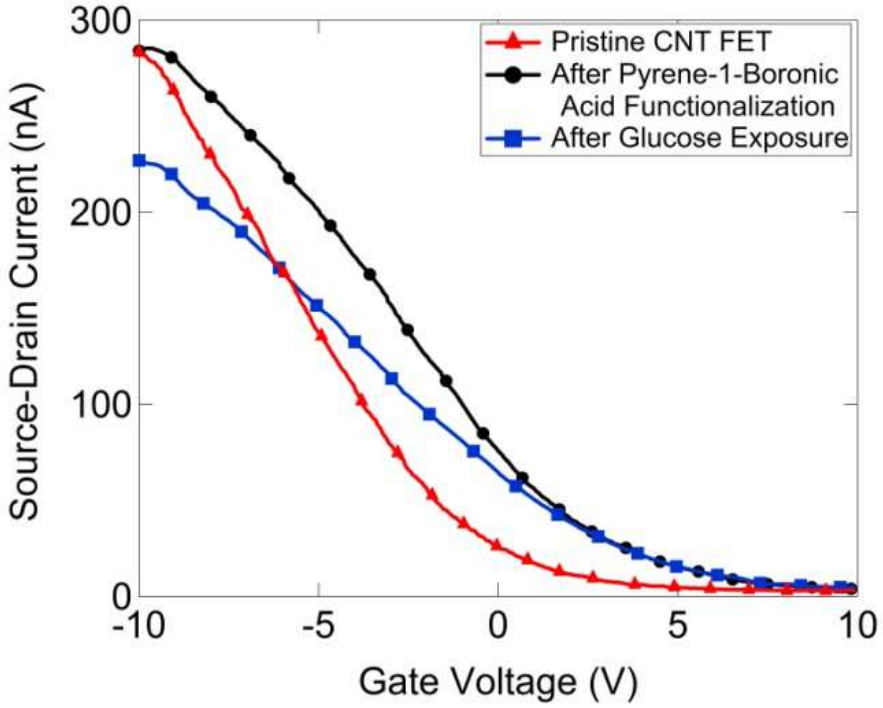

Figure 6.2: Current-gate voltage characteristic from a nanotube FET after each step in the experiment. Data from the as-fabricated nanotube FET is shown in red with triangular markers. The measured curve after functionalization with pyrene-1-boronic acid is shown in black with circle markers. The measured curve after exposure to a 1mM glucose solution is shown in blue with square markers. Bias voltage is 100 mV.

Measurements of sensor response as a function of glucose concentration were taken with the back gate voltage set to -5V, which was a region of maximum transconductance for all samples used. To account for differences in device resistance, the sensor response was recorded as the fractional change in DC current at constant bias voltage ($\Delta I/I$). Device resistance was monitored as successive drops of glucose solution were added to the channel region in order to progressively increase the overall glucose concentration. It was observed that the fractional decrease in device current grew monotonically as the concentration of glucose was increased. Moreover, this fractional decrease in current was found to depend only on the glucose concentration and was independent of the sequence of glucose concentrations delivered to the sensor and the time between droplet deliveries (Fig. 6.3). Expected response times were informed by a calculation of

the diffusion limits for glucose molecules in water. The diffusion length is given by $L = \sqrt{Dt}$ [29], where *D* is the diffusion constant (6.7 x 10^{-6} cm^2/s for glucose in water [30]) and *t* is the diffusion time. Analyte droplets were observed to spread over the hydrophilic SiO_2/APTES substrate such that droplet height did not exceed ca. 60 µm. From the diffusion equation, this corresponds to a diffusion time of 1.3 sec, which is the estimated upper bound for the equilibration time for sensor within the drop.

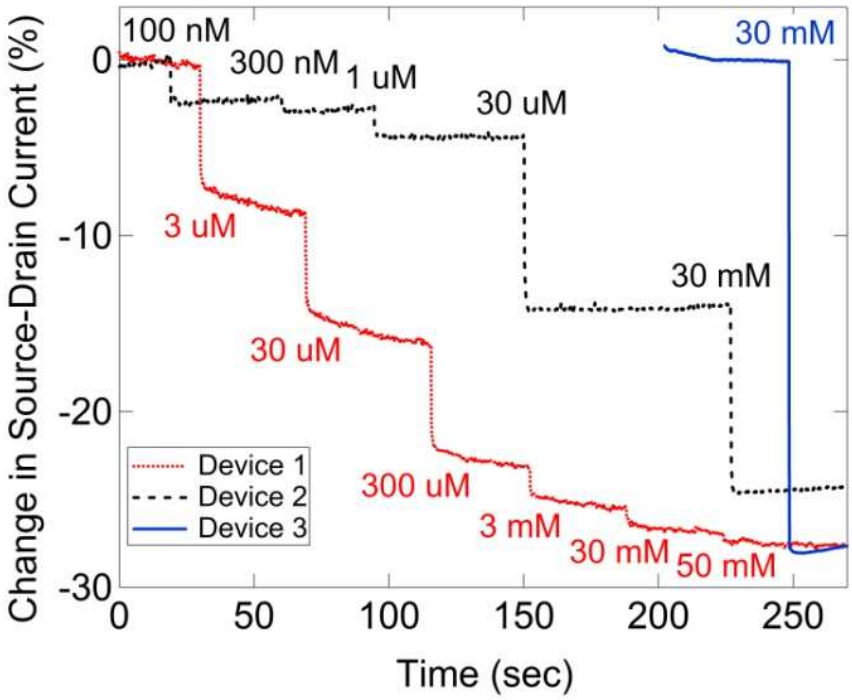

Figure 6.3: Normalized reduction in source-drain current for three devices. Regardless of the sequence of droplets added to the sensor, a glucose concentration of 30 mM produces a response of approximately 26% ± 2%.

From a collection of time traces similar to those in Fig. 6.3, the sensor response as a function of glucose concentration was calculated. Each concentration was tested on 6-8 devices to ensure reproducibility. The sensor responses agree with a model based on the Hill-Langmuir equation for equilibrium ligand-receptor binding (Fig. 6.4)[31, 32]:

$$\Delta V_{TH} = A\frac{(c/K_d)^n}{1+(c/K_d)^n} + Z$$

Here *c* is the glucose concentration, *A* is the sensor response at saturation when all glucose binding sites are occupied, *Z* is an offset that accounts for the response to pure water, K_d is the dissociation constant describing the concentration at which half of available binding sites are occupied, and *n* is the Hill coefficient describing cooperativity of binding.

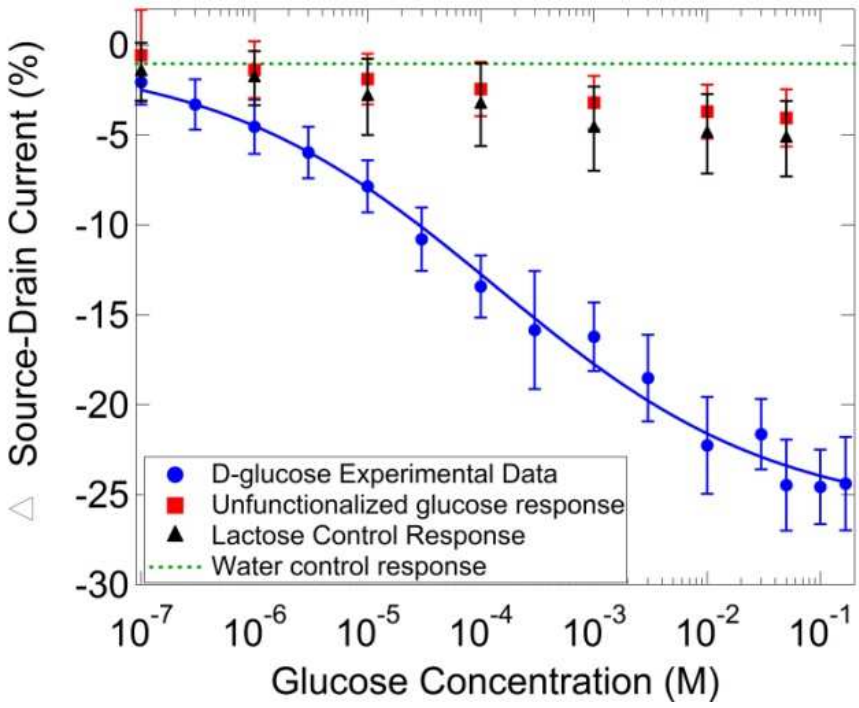

Figure 6.4: Sensor response as a function of glucose concentration (blue circles) with the corresponding Hill-Langmuir fit (blue line). Also included are data from three control measurements. In the first, un-functionalized devices show minimal response to glucose exposure (red squares). In the second, devices functionalized with pyrene-1-boronic acid show minimal response upon exposure to lactose solution, used as a negative control (black triangles). Functionalized devices show a null response upon exposure to DI water (green dashed line).

The best fit to the glucose data yielded a saturated response *A* = -25.3% ± 0.7%, offset parameter *Z* = -0.80% ± 0.74%, dissociation constant K_d = 122 µM ±27 µM, and *n* = 0.36 ± 0.08. The best fit value of the offset parameter Z =- 0.80% ± 0.74% was statistically indistinguishable from the experimentally measured responses of seven devices to DI water as a negative control (ΔI=-0.50% ± 0.54%). The value of the dissociation constant determined from the fit (122 µM ±27

μM) describes the concentration of glucose at which half the receptors are occupied; this regime coincides with glucose levels of diagnostic significance. For example, Jurysta et al. found a statistically significant difference between salivary glucose concentrations for diabetic and non-diabetic patients within the operational range of this sensor [33].

The best fit value of the cooperativity parameter, n = 0.36 ± 0.08, indicates negatively cooperative binding of glucose to the boronic acid receptor in the context of the NT FET biosensor. The interpretation is that binding of a two glucose molecules by adjacent boronic acids is suppressed, possibly because the boronate anion formed when the first glucose molecule binds to a boronic acid creates an electrostatic radius within which additional bound anions are unstable. The data presented in Fig. 6.4 show that the measured responses from a collection of 6-8 devices could be used to discriminate between pure water (ΔI/I=-0.50% ± 0.54%) and water containing glucose at a concentration of 300 nM (ΔI/I=-3.31% ± 1.40%).

The observed reduction in source-drain current is consistent with increased carrier scattering due to the presence of boronate anions formed by bound glucose in the local electrostatic environment of the carbon nanotube. As described in the Supplemental Information, a single device exposed to increasing concentrations of glucose solution showed a monotonic decrease in transistor mobility, consistent with carrier scattering being responsible for the decrease in device conduction.

As a control experiment, boronic acid-functionalized sensors were exposed to a solution of lactose in the same manner as glucose exposure. Lactose, a 1→4 oligosaccharide, is known to have a low binding affinity for boronic acid moieties [34, 35]. Figure 6.4 shows the sensor response to several concentrations of lactose. Exposure to lactose at concentrations below 1 mM is not distinguishable from the response to pure water, and the signal saturates at a low level of

approximately -6%. This small decrease in current is likely due to non-specifically bound molecules increasing carrier scattering at these high sugar concentrations. In a second control experiment, unfunctionalized devices were exposed to glucose solutions. The average responses, calculated using 8 devices, were below 5% even for glucose concentrations as high as 10 mM. We thus concluded that the sensing response from boronic acid-functionalized carbon nanotube transistors is specific for glucose, and that the pyrene chemistry is required to effectively bind glucose with high density along the nanotube sidewall.

To summarize, we developed a robust and reproducible fabrication method for carbon nanotube-based glucose sensors that exhibited excellent sensitivity and selectivity. Device responses were shown to vary systematically with glucose concentration in a clinically relevant range, with a minimum detection limit of 300 nM. Control experiments were used to confirm the effectiveness of the functionalization chemistry and the selectivity of the sensor for glucose over another sugar. Potential applications include glucose sensors for diabetics based on either blood or salivary glucose levels where the pyrene boronic acid functionalized nanotube FET provides chemical specificity and all-electronic readout. The incorporation of solution phase nanotubes makes such devices promising candidates for scalable, point-of-care diagnostic tools. Such devices would potentially eliminate the need for frequent, uncomfortable finger pricking for blood glucose measurements and would greatly improve diabetic peoples' quality of life while still maintaining a high level of diagnostic accuracy.

Acknowledgements: This work was supported by the Nano/Bio Interface Center through the National Science Foundation NSEC DMR08-32802. Use of the facilities of the Nano/Bio Interface

Center is also acknowledged. Mitchell Lerner acknowledges the support of a SMART Fellowship, and Manuel Lopez was supported by NSF REU site grant DMR-1062638.

6.2 A Molybdenum Disulfide-μ Opioid Receptor Hybrid Sensor and Opioid Testing Platform

Nanomaterials such as carbon nanotubes, graphene and molybdenum disulfide have shown great promise for biosensing applications due to their environmentally sensitive electronic properties and all-surface geometries that result in enhanced sensitivity. In particular, nanomaterial-protein hybrid devices have been shown to be sensitive to conformational changes of a single protein [36] and to detect cancer biomarker proteins [37], endogenous peptides [38] and live bacteria [5] down to femtomolar concentrations [37-39].

Proteins are coupled to nanomaterials by linker chemistries that target particular exposed residues in the protein. For example, the ubiquity of amine sites on proteins has motivated the development of linker chemistries for amine residues to carbon nanotubes or graphene that can be utilized for almost any protein of interest [40-42]. However, in order to increase device-to-device reproducibility and lower detection thresholds, controlling protein orientation can be beneficial. In particular, poly-histidine tags (histags) that are routinely used to extract proteins during their expression, have been targeted for this purpose [4, 43, 44].

In this work, we demonstrate the first protein sensor arrays based on CVD grown molybdenum disulfide. We also introduce a novel nickel ion mediated surface functionalization scheme for protein attachment via the histag directly to the sulfur surface, without the need for deposition of a top dielectric. This linker chemistry is extremely short, ensuring that the binding events to be monitored are occurring as close as possible to the MoS_2, a factor that is critically important for real-world applications where ionic solutions result in sufficiently short Deby lengths to screen binding events occurring further from the device. We apply this linker chemistry

to attach a re-engineered μ opioid receptor (MUR), a g-protein coupled receptor (GPCR) native to the human cell membrane. The resulting devices are used to readout the binding of enkephalin, an endogenous opioid, with an affinity that agree with measurements using traditional techniques. Given the scalability of these arrays, the quick and accurate binding readout enabled by the MoS_2 transistor sensitivity and the fact that 40% of modern pharmaceuticals target GPCRs [45], we speculate on the possibility of developing this work into a solid-state drug testing platform that would allow for rapid readout of the interactions between novel drugs and their intended protein target in a solid-state test bed.

Recently, monolayer molybdenum disulfide (MoS_2) has emerged as a two-dimensional material that can be exfoliated from bulk samples [46, 47] and grown by scalable methods such as chemical vapor deposition [48-50]. Typically, sulfur sublimated from a solid is introduced into the furnace along with a molybdenum source such as molybdenum oxide [51, 52] or ammonia heptamolybdate [50] and growth of triangular monolayer flakes is nucleated directly on an insulating substrate. The mobility of MoS_2, typically in the range 0.1-200 cm^2/Vs [50, 53, 54] depending on the sample quality and preparation method as well as the substrate and presence of an encapsulating dielectric, cannot compete with that of graphene. However, the presence of a 1.8 eV direct bandgap for the monolayer [47] means that MoS_2 devices demonstrate on/off ratios up to 10^6 [50, 53], can be gated completely off and exhibit photoluminescence [55, 56]. These properties make MoS_2 extremely promising for photonic/electronic applications including sensors [57, 58], solar cells [59, 60], optical modulators [61, 62] and valleytronics [63].

MoS_2 samples for this experiment were grown via a CVD process in a 1” Thermo Schientific “Lindberg Blue” tube furnace. Microliter droplets of saturated ammonia heptamolybdate solution were dried onto the corners of a Si/SiO_2 growth substrate that had

previously been coated with a layer of sodium cholate. The sodium cholate is applied by spin coating a 1 % solution at 4000 rpm for 60 seconds. The sodium cholate is a known growth promoter, acting to increase diffusion of the molybdenum source by increasing the surface adhesive energy relative to the adatom cohesive energy. The growth substrate was placed in the center of the furnace and heated to 800 °C. A 25 mg sulfur pellet was placed on a piece of silicon and positioned upstream in the furnace such that its temperature was approximately 150 °C, sufficient for the pellet to melt and evaporate slowly. A flow of 500 sccm N_2 carried the sulfur vapor into the furnace during a 30 minute growth period. After growth, the sample was rapidly cooled by cracking open the furnace and sliding it downstream with respect to the 1" quart tube. The growth setup is shown schematically in fig. 6.5a.

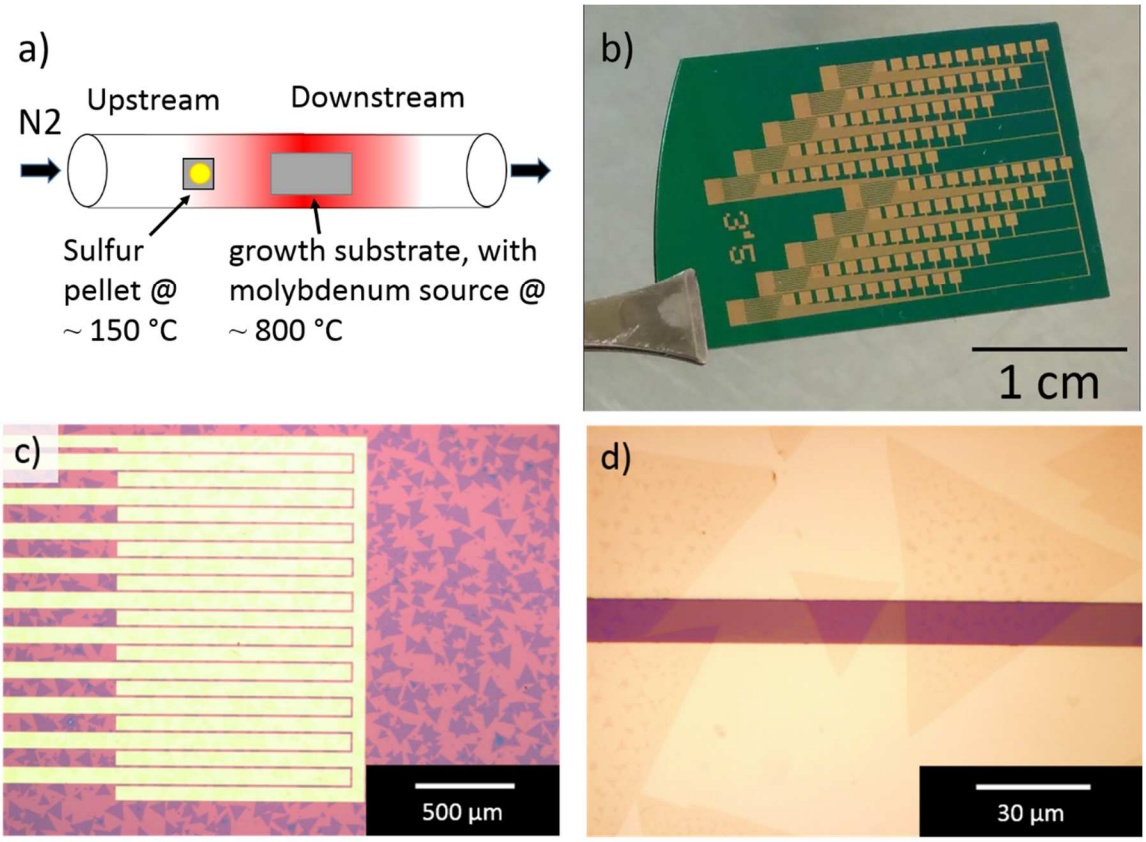

Figure 6.5: MoS_2 growth and devices. a) Schematic of the CVD growth setup. b) Picture of the device layout onto which the MoS_2 is transferred. Each of ten columns of contact pads leads to a cluster of interdigitated electrodes, one of which is shown in c). d) Many triangular, crystalline monolayer MoS_2 flakes span the electrodes.

After growth, the Si/SiO2 surface was decorated with triangular crystals of monolayer MoS_2. In order to fabricate arrays of devices while minimizing the need for lithography and etching steps that can contaminate and degrade the samples, we transferred the randomly grown MoS_2 onto prefabricated electrodes by releasing the samples from the growth substrate onto a polymer support [48]. This was accomplished by spinning a layer of PMMA onto the sample and floating it on a bath of 0.1 M KOH, which released the PMMA and MoS_2 flakes from the SiO_2 substrate by slowly etching the very top SiO_2 atoms. The floating PMMA layer was then transferred into successive water baths in order to wash off residual KOH and finally scooped onto a target substrate that had prefabricated arrays of metal contacts, defined using photolithography (fig.

6.5b). After drying the transferred MoS_2 and polymer support, the PMMA was removed by spraying acetone at the surface for 5 minutes. Without drying, the sample was then placed in an acetone bath for a minimum of 5 hours to remove residual PMMA contamination. Panels 6.5c,d show the resulting devices, with many individual MoS_2 flakes spanning each pair of electrodes.

The electrode design used individual source fingers, interdigitated with a common drain. The separation between the fingers was 10 μm and each pair of contacts had an effective device area of 10 μm x 2 mm, which ensured that many MoS_2 flakes would be spanning the electrodes and the yield of functional devices would be high. Furthermore, we expect that by measuring the electrical response from many flakes we will obtain much greater device-to-device reproducibility of the electrical responses in biosensing experiments than if the channel of each device was a single MoS_2 flake. One hundred devices on a single chip were arranged into ten clusters of ten devices that could later be biochemically functionalized by cluster. One such cluster is shown in fig. 6.5c.

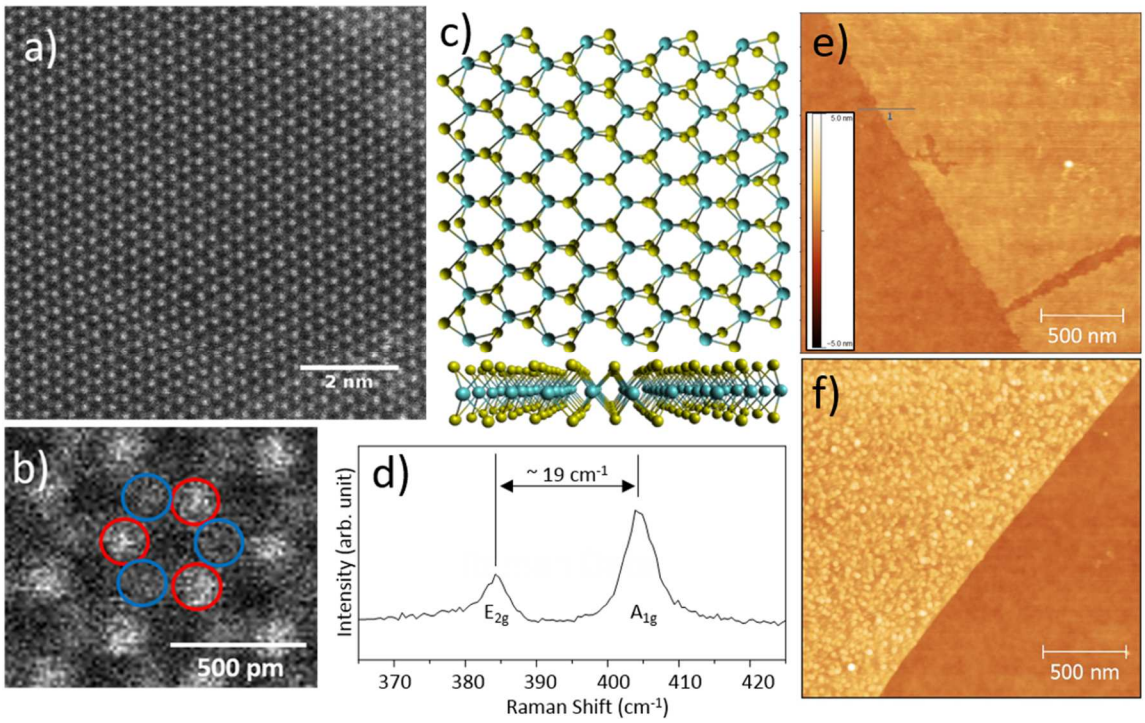

Figure 6.6: MoS_2 Characterization. ACTEM showed the expected hexagonal lattice (a,c) with brightness differences for the Mo and S sites (b), with extremely high crystallinity across the field of view. The positions and separation of the E_{2g} and A_{1g} Raman peaks (d) are also consistent with monolayer MoS_2. AFM showed a pristine surface with a height of 0.8 nm (e) before functionalization, and dense coverage with 2-3 nm high features after functionalization, consistent with coverage of proteins bound with the Ni^{2+}-histidine linker.

The material was characterized after transfer by AFM, aberration corrected TEM (ACTEM) and Raman spectroscopy. AFM height images (fig. 6.6e) showed that the material was ~ 0.8 nm thick, consistent with monolayer MoS_2 [64]. The absence of obvious contamination and low surface roughness indicate that the material is clean and uniform. HRTEM shows the expected hexagonal lattice, with different brightness for the heavier molybdenum and lighter sulfur sites (fig. 6.6a,b). Finally, Raman spectroscopy shows the expected E_{2g} and A_{1g} MoS_2 intraband vibrational modes with a separation of 19 cm^{-1} (fig. 6.6d) [64, 65], the expected spacing for single layer MoS_2. Together, this data confirms the MoS_2 samples are highly crystalline and uniformly monolayer.

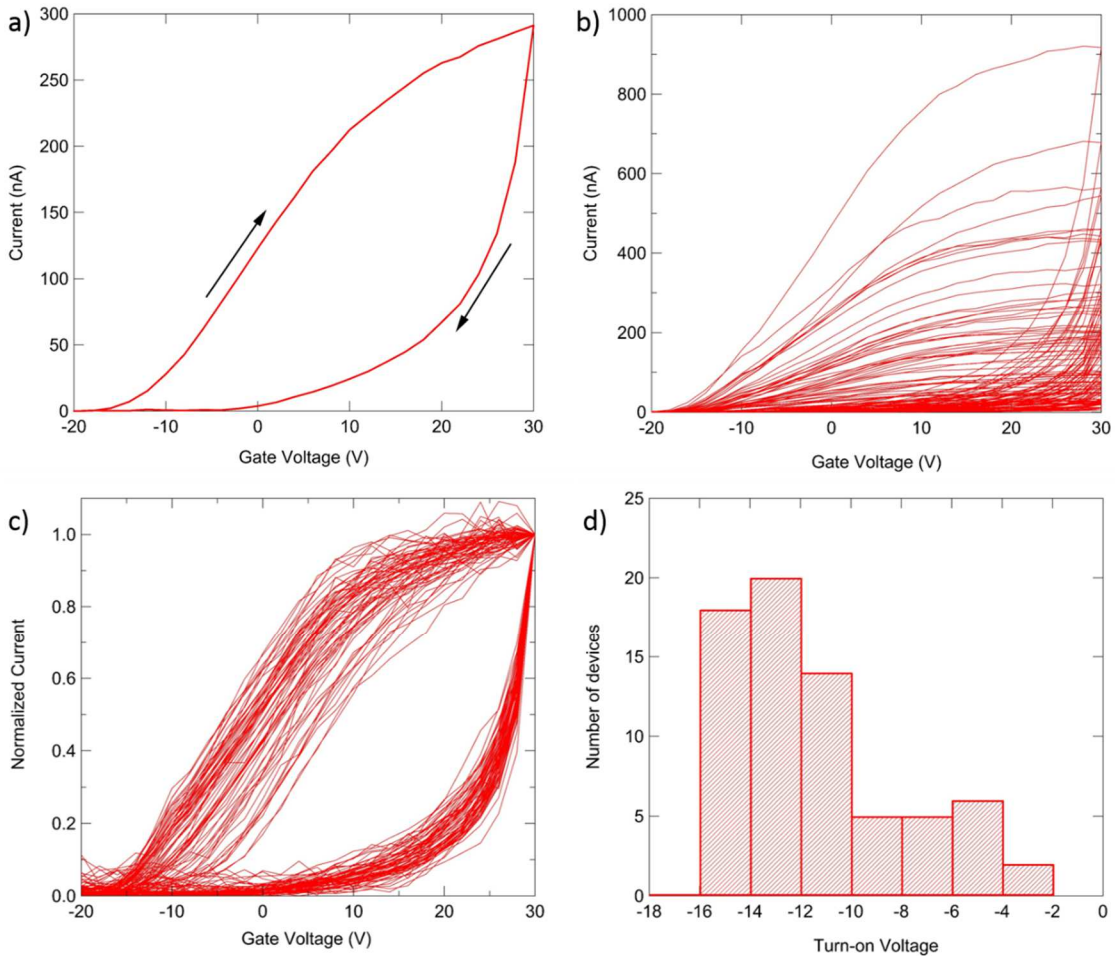

Figure 6.7: Electrical characteristics of the MoS2 devices. a) Devices turn on around -10 V and show hysteresis on the return sweep. 70 devices all exhibit similar shape of the transistor curve (c) with significant spread in on-state current (b). A histogram of turn-on voltages shows that most devices turn on in a reasonably tight window of -16 V to -10 V (d).

$I(V_g)$ sweeps of the devices were taken in ambient air using the global back gate. The devices showed the expected n-type behavior of MoS_2, with hysteresis due to atmospheric adsorbates such as moisture [66] and substrate charge traps [67]. Fig. 6.7a shows the $I(V_g)$ of a single device comprised of multiple MoS2 crystals, such as the ones shown in fig. 6.5. The contact resistance and atmospheric adsorbates are limiting the transconductance of the device [57]. Having contacts on top of the material would likely reduce the contact resistance and increase the device mobility, but at the expense of additional surface contamination that can impact

surface chemistry. Fig 6.7b shows I(V_g) curves for 70 devices from seven clusters on a single chip. The yield is over 95 % (2 failed devices) and the devices demonstrate very similar curves with different on-state currents. The spread in on-state currents primarily reflects the variability in the number of MoS_2 flakes spanning the electrodes. This is shown clearly in fig. 6.7c, where the curves are normalized by the on-state current. A histogram of threshold voltages shows a tight distribution, with roughly ¾ of devices having a turn-on voltage in the range -16 to -10 V.

Previous studies [39, 68] monitoring the binding of proteins using MoS_2 transistors have utilized a top dielectric which has a known surface chemistry to attach proteins. One downside of that approach is that the binding event is now quite far from the transistor channel. In this work, we demonstrate direct functionalization of the MoS_2, using nickel ions to attach to the histag of the protein. A similar surface functionalization approach using nickel has previously been applied to attach ligands to MoS_2 nanoparticles in order to alter their solubility [69]. We expose the MoS_2 to a 5 mM $NiCl_2$ solution and the Ni^{2+} ions are able to form coordinate covalent bonds with a trio of sulfur atoms in the top layer of MoS_2. These ions are then available to bind to nickel chelating agents, such as histidine [4, 44], nitrilotriacetic acid [4], ethylene diamines [70] and nickel porphyrins [71]. As we are using a reengineered membrane protein, the histidine tag is available and is an ideal anchor site, with the advantage of orientational control of the protein. The resulting MoS_2-protein hybrid structure is shown in fig. 6.8b,c. The histag has been used as an anchor site in other biosensor designs, including carbon nanotube [4] and graphene [44] FETs. Those functionalization schemes typically use a diazonium salt to make an sp^3 defect in the nanotube sidewall, which acts as an anchor for the subsequent chemistry steps. The final chemical linker, ending with a nickel ion bound to a protein histidine tag is depicted in fig. 6.8a. Advantage of our MoS_2 functionalization scheme include that the simple one-step surface chemistry reduces

the complexity of the functionalization procedure and results in an extremely short linker. This ensures strong coupling of the MoS_2 to the protein interactions and should render the devices robust against screening that occurs in samples with significant salt concentrations. This chemistry could also be generalized to an arbitrary protein by incorporating additional functionalization steps. For example, nitrilotriacetic acid is a known chelating agent for Ni^{2+} that would leave carboxylic acid groups exposed, a known anchor for established crosslinking chemistries to amine residues [41].

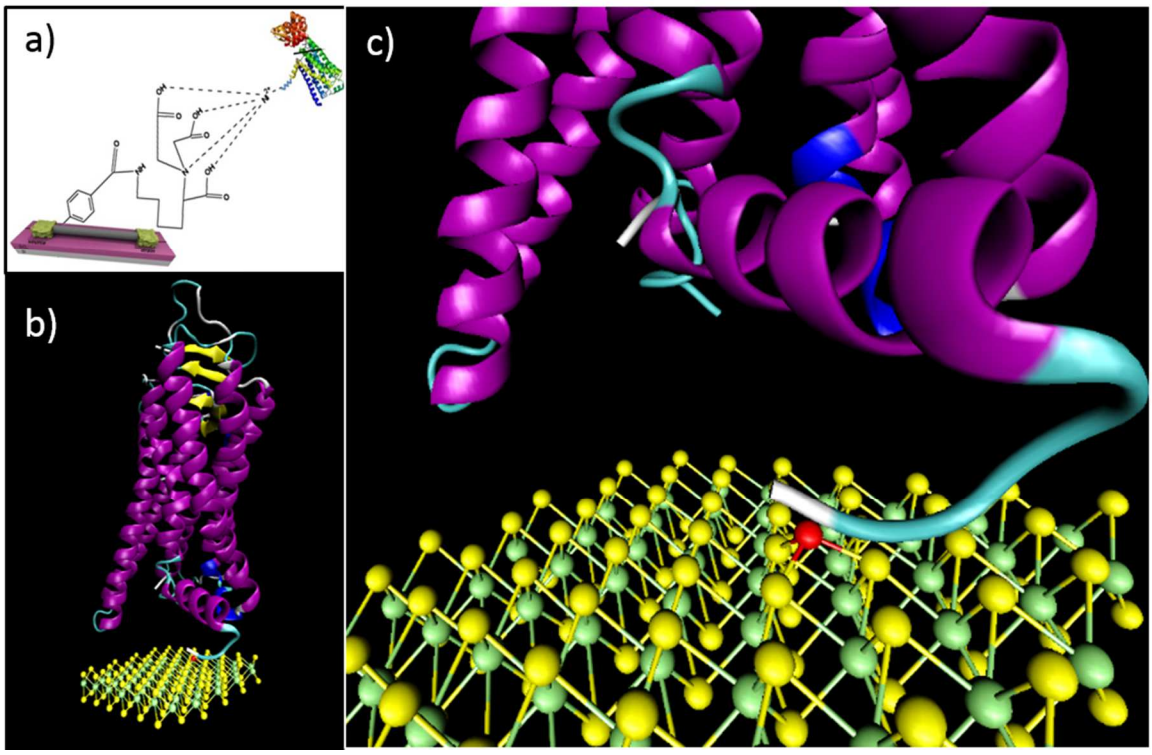

Figure 6.8: MoS2 structure and functionalization schematic. Sulfur atoms are shown in yellow, molybdenum in green. The nickel ion used as a protein linker is shown in red. The MUR protein is made of seven connected α-helices, and C-terminus and N-terminus tails that contribute to the protein function. Nanotube histag chemistry for comparison is shown in (a).

The protein chosen for these experiments is a redesigned, water-soluble variant of the μ-opioid receptor (MUR) [72]. The MUR belongs to a class of proteins called GPCRs that are

responsible for binding target ligands ranging from small molecules to large proteins. GPCRs are native to the hydrophobic cell membrane, and are not typically stable in water or buffer conditions. The exterior amino acids in the transmembrane portion of the protein are overwhelmingly hydrophobic, which impedes protein expression and causes the protein to denature and aggregate in buffer solutions, leading to loss of functionality. However, a computationally informed redesign of the exterior amino acids sequences can make the protein more hydrophilic, and thus stable outside the membrane [72]. The redesigned variant of the MUR used in this experiment was expressed in E. coli and purified using standard techniques, without the need for a membrane, membrane surrogate or nanodisk arrangement [72].

Physiologically, the MUR is involved in pain and reward recognition pathways. More specifically, the MUR has a high affinity for both endogenous and exogenous opioids such as heroin, morphine, β-endorphin and β-FNA. Painkillers such as morphine are agonists that derive their function by binding to MUR and activating a biological response, while other exogenous compounds such as β-FNA are antagonists that bind but inhibit function. The reengineered MUR has also been previouosly used in a graphene biosensor device. In this configuration, protein function was retained, as defined based on the affinity for a target molecule, naltrexone, which is a MUR antagonist [38, 72]. In this experiment, the target molecule is enkephalin is an endogenous opioid peptide that acts as a neuromodulator, inhibiting the neurotransmitters in the pathway for pain in the brain and spinal cord. Enkephalin expression by the body thus reduces both the physical and emotional impact of pain.

Atomic force microscopy was used to examine the surface morphology before and after protein attachment. A MUR concentration of 10 μM in solution was found to give high density attachment. Fig. 6.6f shows an MoS_2 flake after chemistry, from the same substrate as the image

in fig. 6.6e, which was taken before protein attachment. The MoS_2 surface is now covered in a uniform layer of 3 nm high features, consistent with a 46 kDa protein. The SiO_2 surface remains very smooth and featureless, indicating that the proteins are not simple adsorbing randomly on the surface but instead are preferentially bound to the Ni ions on the MoS_2. This indicates that the protein attachment is both highly dense and very specific.

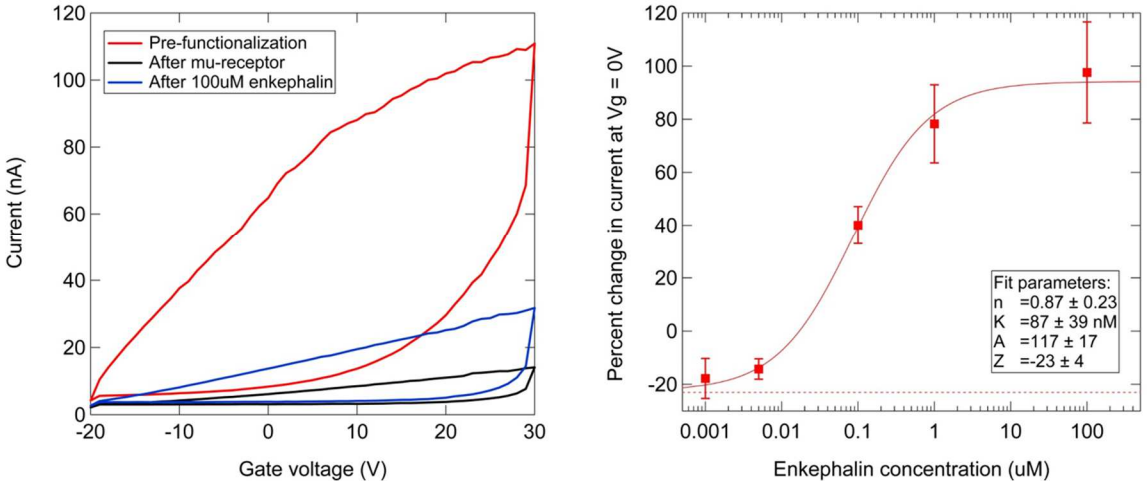

Figure 6.9: Electrical signatures of protein and target binding. The conductivity of the device drops considerably after protein attachment and then increases upon exposure to enkephalin. The data is well described by a Langmui-Hill isotherm

After MUR attachment, the conductance of the devices dropped by approximately 70 %. This is attributed to the use of electrons in the binding, as well as increased scattering of the charge carriers due to the presence of the Ni^{2+} ions. The devices were then exposed to a target opioid, Met-enkephalin. At high concentrations of enkephalin, the device conductance was found to recover, increasing by up to 100%. A response vs. concentration curve, plotting the percentage conduction increase as a function of the enkephalin concentration, showed a sigmoidal trend that is well fit by a Langmuir-Hill binding model for equilibrium ligand-receptor binding, i.e.

$$\frac{\Delta I}{I_0} = A\frac{C^n}{{K_a}^n + C^n} + Z$$

where C is the enkephalin concentration, A is the magnitude of response when all binding sites are occupied, K_a is the concentration at which half the maximum response is seen and n is the Hill coefficient describing the cooperativity of binding. For this data set, $A = 117 \pm 17\ \%$, $K_a = 87 \pm 39\ nM$ and $n = 0.87 \pm 0.23$. An affinity of approximately $n = 1$ is reasonable as it implies that the binding of enkephalin to one MUR does not impact the binding affinity of the other receptors on the MoS_2 surface. From other measurements, enkephalin is known to bind to the MUR with an affinity in the range of 10s of nanomoles, plausible based on broad agreement with previous measurements of MUR-antagonist affinity [38, 72]. Consequently, this data demonstrates that we have retained the functionality of the reengineered membrane protein and are able to rapidly read out the concentration of targets with high sensitivity using the MoS_2 FETs.

References

1. Chen, R.J., Choi, H.C., Bangsaruntip, S., Yenilmez, E., et al., *An investigation of the mechanisms of electronic sensing of protein adsorption on carbon nanotube devices.* Journal of the American Chemical Society, 2004. **126**(5): p. 1563-1568.
2. Allen, B.L., Kichambare, P.D., and Star, A., *Carbon nanotube field-effect-transistor-based biosensors.* Advanced Materials, 2007. **19**(11): p. 1439-1451.
3. Star, A., Gabriel, J.C.P., Bradley, K., and Gruner, G., *Electronic detection of specific protein binding using nanotube FET devices.* Nano Letters, 2003. **3**(4): p. 459-463.
4. Goldsmith, B.R., Mitala, J.J., Josue, J., Castro, A., et al., *Biomimetic Chemical Sensors Using Nanoelectronic Readout of Olfactory Receptor Proteins.* Acs Nano, 2011. **5**(7): p. 5408-5416.
5. Lerner, M.B., Goldsmith, B.R., McMillon, R., Dailey, J., et al., *A carbon nanotube immunosensor for Salmonella.* AIP Advances, 2011. **1**(4): p. 042127.
6. Melmed, S., Polonsky, K.S., Larsen, P.R., and Kronenberg, H.M., *Williams Textbook of Endocrinology*. 12 ed. 2011: Saunders. 1371–1435.
7. James, T.D., Sandanayake, K.R.A.S., and Shinkai, S., *Saccharide sensing with molecular receptors based on boronic acid.* Angewandte Chemie-International Edition, 1996. **35**(17): p. 1910-1922.
8. James, T.D., Sandanayake, K.R.A.S., and Shinkai, S., *Chiral Discrimination of Monosaccharides Using a Fluorescent Molecular Sensor.* Nature, 1995. **374**(6520): p. 345-347.
9. Takahashi, S. and Anzai, J., *Phenylboronic acid monolayer-modified electrodes sensitive to sugars.* Langmuir, 2005. **21**(11): p. 5102-5107.
10. Shoji, E. and Freund, M.S., *Potentiometric saccharide detection based on the pKa changes of poly(aniline boronic acid).* Journal of the American Chemical Society, 2002. **124**(42): p. 12486-12493.
11. Ori, A. and Shinkai, S., *Electrochemical Detection of Saccharides by the Redox Cycle of a Chiral Ferrocenylboronic Acid-Derivative - a Novel Method for Sugar Sensing.* Journal of the Chemical Society-Chemical Communications, 1995(17): p. 1771-1772.
12. Cordes, D.B., Gamsey, S., and Singaram, B., *Fluorescent quantum dots with boronic acid substituted viologens to sense glucose in aqueous solution.* Angewandte Chemie-International Edition, 2006. **45**(23): p. 3829-3832.
13. Yum, K., Ahn, J.H., McNicholas, T.P., Barone, P.W., et al., *Boronic Acid Library for Selective, Reversible Near-Infrared Fluorescence Quenching of Surfactant Suspended Single-Walled Carbon Nanotubes in Response to Glucose.* Acs Nano, 2012. **6**(1): p. 819-830.
14. Lin, Y.H., Lu, F., Tu, Y., and Ren, Z.F., *Glucose biosensors based on carbon nanotube nanoelectrode ensembles.* Nano Letters, 2004. **4**(2): p. 191-195.
15. Lerner, M.B., Resczenski, J.M., Amin, A., Johnson, R.R., et al., *Toward Quantifying the Electrostatic Transduction Mechanism in Carbon Nanotube Molecular Sensors.* Journal of the American Chemical Society, 2012. **134**(35): p. 14318-14321.
16. Lerner, M.B., D'Souza, J., Pazina, T., Dailey, J., et al., *Hybrids of a Genetically Engineered Antibody and a Carbon Nanotube Transistor for Detection of Prostate Cancer Biomarkers.* Acs Nano, 2012. **6**(6): p. 5143-5149.

17. Arnold, M.S., Stupp, S.I., and Hersam, M.C., *Enrichment of Single-Walled Carbon Nanotubes by Diameter in Density Gradients.* Nano Letters, 2005. **5**(4): p. 713-718.
18. Arnold, M.S., Green, A.A., Hulvat, J.F., Stupp, S.I., et al., *Sorting carbon nanotubes by electronic structure using density differentiation.* Nat Nano, 2006. **1**(1): p. 60-65.
19. Wang, C., Zhang, J.L., Ryu, K.M., Badmaev, A., et al., *Wafer-Scale Fabrication of Separated Carbon Nanotube Thin-Film Transistors for Display Applications.* Nano Letters, 2009. **9**(12): p. 4285-4291.
20. Kybert, N.J., Lerner, M.B., Yodh, J.S., Preti, G., et al., *Differentiation of complex vapor mixtures using versatile DNA-carbon nanotube chemical sensor arrays.* ACS Nano, 2013. **7**(3): p. 2800-7.
21. LeMieux, M.C., Roberts, M., Barman, S., Jin, Y.W., et al., *Self-sorted, aligned nanotube networks for thin-film transistors.* Science, 2008. **321**(5885): p. 101-104.
22. Liu, J., Casavant, M.J., Cox, M., Walters, D.A., et al., *Controlled deposition of individual single-walled carbon nanotubes on chemically functionalized templates.* Chemical Physics Letters, 1999. **303**(1-2): p. 125-129.
23. Auvray, S., Derycke, V., Goffman, M., Filoramo, A., et al., *Chemical optimization of self-assembled carbon nanotube transistors.* Nano Letters, 2005. **5**(3): p. 451-455.
24. Khamis, S.M., Jones, R.A., and Johnson, A.T.C., *Optimized photolithographic fabrication process for carbon nanotube devices.* AIP Advances, 2011. **1**(2): p. 022106.
25. Heller, I., Kong, J., Heering, H.A., Williams, K.A., et al., *Individual single-walled carbon nanotubes as nanoelectrodes for electrochemistry.* Nano Letters, 2005. **5**(1): p. 137-142.
26. Dürkop, T., Getty, S.A., Cobas, E., and Fuhrer, M.S., *Extraordinary Mobility in Semiconducting Carbon Nanotubes.* Nano Letters, 2004. **4**(1): p. 35-39.
27. O'Reilly, J.P., Butts, C.P., l'Anson, I.A., and Shaw, A.M., *Interfacial pH at an isolated silica-water surface.* Journal of the American Chemical Society, 2005. **127**(6): p. 1632-3.
28. Hall, D.G., *Boronic acids : preparation and applications in organic synthesis, medicine and materials*. 2nd completely rev. ed. 2011, Weinheim: Wiley-VCH.
29. Bird, G.A., *Molecular gas dynamics*. Oxford engineering science series. 1976, Oxford: Clarendon Press. xvi, 238 p.
30. Longsworth, L.G., *Diffusion Measurements, at 25-Degrees, of Aqueous Solutions of Amino Acids, Peptides and Sugars.* Journal of the American Chemical Society, 1953. **75**(22): p. 5705-5709.
31. Lehninger, A.L., Nelson, D.L., and Cox, M.M., *Lehninger Principles of Biochemistry*. 5th ed. 2008, New York: W.H. Freeman.
32. Hill, A.V., *The Possible Effects of the Aggregation of the Molecules of Hemoglobin on Its Oxygen Dissociation Curve.* Journal of Physiology, 1910(40): p. 4-7.
33. Jurysta, C., Bulur, N., Oguzhan, B., Satman, I., et al., *Salivary glucose concentration and excretion in normal and diabetic subjects.* J Biomed Biotechnol, 2009. **2009**: p. 430426.
34. Nagai, Y., Kobayashi, K., Toi, H., and Aoyama, Y., *Stabilization of Sugar-Boronic Esters of Indolylboronic Acid in Water Via Sugar Indole Interaction - a Notable Selectivity in Oligosaccharides.* Bulletin of the Chemical Society of Japan, 1993. **66**(10): p. 2965-2971.
35. Stones, D., Manku, S., Lu, X.S., and Hall, D.G., *Modular solid-phase synthetic approach to optimize structural and electronic properties of oligoboronic acid receptors and sensors for the aqueous recognition of oligosaccharides.* Chemistry-a European Journal, 2004. **10**(1): p. 92-100.

36. Choi, Y., Moody, I.S., Sims, P.C., Hunt, S.R., et al., *Single-Molecule Lysozyme Dynamics Monitored by an Electronic Circuit.* Science, 2012. **335**(6066): p. 319-324.
37. Lerner, M.B., D'Souza, J., Pazina, T., Dailey, J., et al., *Hybrids of a Genetically Engineered Antibody and a Carbon Nanotube Transistor for Detection of Prostate Cancer Biomarkers.* ACS Nano, 2012. **6**(6): p. 5143-5149.
38. Lerner, M.B., Matsunaga, F., Han, G.H., Hong, S.J., et al., *Scalable Production of Highly Sensitive Nanosensors Based on Graphene Functionalized with a Designed G Protein-Coupled Receptor.* Nano Letters, 2014. **14**(5): p. 2709-2714.
39. Sarkar, D., Liu, W., Xie, X., Anselmo, A.C., et al., *MoS2 Field-Effect Transistor for Next-Generation Label-Free Biosensors.* ACS Nano, 2014. **8**(4): p. 3992-4003.
40. Lerner, M.B., Dailey, J., Goldsmith, B.R., Brisson, D., et al., *Detecting Lyme disease using antibody-functionalized single-walled carbon nanotube transistors.* Biosensors and Bioelectronics, 2013. **45**(0): p. 163-167.
41. Jiang, K., Schadler, L.S., Siegel, R.W., Zhang, X., et al., *Protein immobilization on carbon nanotubes via a two-step process of diimide-activated amidation.* Journal of Materials Chemistry, 2004. **14**(1): p. 37-39.
42. Kodali, V.K., Scrimgeour, J., Kim, S., Hankinson, J.H., et al., *Nonperturbative Chemical Modification of Graphene for Protein Micropatterning.* Langmuir, 2011. **27**(3): p. 863-865.
43. Wang, L., Wei, L., Chen, Y., and Jiang, R., *Specific and reversible immobilization of NADH oxidase on functionalized carbon nanotubes.* Journal of Biotechnology, 2010. **150**(1): p. 57-63.
44. Lu, Y., Lerner, M.B., John Qi, Z., Mitala, J.J., et al., *Graphene-protein bioelectronic devices with wavelength-dependent photoresponse.* Applied Physics Letters, 2012. **100**(3): p. 033110.
45. Overington, J.P., Al-Lazikani, B., and Hopkins, A.L., *How many drug targets are there?* Nat Rev Drug Discov, 2006. **5**(12): p. 993-996.
46. Li, H., Wu, J., Yin, Z., and Zhang, H., *Preparation and Applications of Mechanically Exfoliated Single-Layer and Multilayer MoS2 and WSe2 Nanosheets.* Accounts of Chemical Research, 2014. **47**(4): p. 1067-1075.
47. Mak, K.F., Lee, C., Hone, J., Shan, J., et al., *Atomically thin MoS(2): a new direct-gap semiconductor.* Phys Rev Lett, 2010. **105**(13): p. 136805.
48. Zhan, Y., Liu, Z., Najmaei, S., Ajayan, P.M., et al., *Large-Area Vapor-Phase Growth and Characterization of MoS2 Atomic Layers on a SiO2 Substrate.* Small, 2012. **8**(7): p. 966-971.
49. Schmidt, H., Wang, S., Chu, L., Toh, M., et al., *Transport Properties of Monolayer MoS2 Grown by Chemical Vapor Deposition.* Nano Letters, 2014. **14**(4): p. 1909-1913.
50. Han, G.H., Kybert, N.J., Naylor, C.H., Lee, B.S., et al., *Seeded growth of highly crystalline molybdenum disulphide monolayers at controlled locations.* Nat Commun, 2015. **6**.
51. van der Zande, A.M., Huang, P.Y., Chenet, D.A., Berkelbach, T.C., et al., *Grains and grain boundaries in highly crystalline monolayer molybdenum disulphide.* Nat Mater, 2013. **12**(6): p. 554-561.
52. Lee, Y.-H., Zhang, X.-Q., Zhang, W., Chang, M.-T., et al., *Synthesis of Large-Area MoS2 Atomic Layers with Chemical Vapor Deposition.* Advanced Materials, 2012. **24**(17): p. 2320-2325.

53. Radisavljevic, B., Radenovic, A., Brivio, J., Giacometti, V., et al., *Single-layer MoS2 transistors.* Nat Nanotechnol, 2011. **6**(3): p. 147-50.
54. Novoselov, K.S., Jiang, D., Schedin, F., Booth, T.J., et al., *Two-dimensional atomic crystals.* Proceedings of the National Academy of Sciences of the United States of America, 2005. **102**(30): p. 10451-10453.
55. Splendiani, A., Sun, L., Zhang, Y., Li, T., et al., *Emerging Photoluminescence in Monolayer MoS2.* Nano Letters, 2010. **10**(4): p. 1271-1275.
56. Mouri, S., Miyauchi, Y., and Matsuda, K., *Tunable Photoluminescence of Monolayer MoS2 via Chemical Doping.* Nano Letters, 2013. **13**(12): p. 5944-5948.
57. Liu, B., Chen, L., Liu, G., Abbas, A.N., et al., *High-Performance Chemical Sensing Using Schottky-Contacted Chemical Vapor Deposition Grown Monolayer MoS2 Transistors.* ACS Nano, 2014. **8**(5): p. 5304-5314.
58. Perkins, F.K., Friedman, A.L., Cobas, E., Campbell, P.M., et al., *Chemical Vapor Sensing with Monolayer MoS2.* Nano Letters, 2013. **13**(2): p. 668-673.
59. Tsai, M.-L., Su, S.-H., Chang, J.-K., Tsai, D.-S., et al., *Monolayer MoS2 Heterojunction Solar Cells.* ACS Nano, 2014. **8**(8): p. 8317-8322.
60. Bernardi, M., Palummo, M., and Grossman, J.C., *Extraordinary Sunlight Absorption and One Nanometer Thick Photovoltaics Using Two-Dimensional Monolayer Materials.* Nano Letters, 2013. **13**(8): p. 3664-3670.
61. Zhang, W., Huang, J.-K., Chen, C.-H., Chang, Y.-H., et al., *High-Gain Phototransistors Based on a CVD MoS2 Monolayer.* Advanced Materials, 2013. **25**(25): p. 3456-3461.
62. Roy, K., Padmanabhan, M., Goswami, S., Sai, T.P., et al., *Graphene-MoS2 hybrid structures for multifunctional photoresponsive memory devices.* Nat Nano, 2013. **8**(11): p. 826-830.
63. Mak, K.F., McGill, K.L., Park, J., and McEuen, P.L., *The valley Hall effect in MoS2 transistors.* Science, 2014. **344**(6191): p. 1489-1492.
64. Lee, C., Yan, H., Brus, L.E., Heinz, T.F., et al., *Anomalous Lattice Vibrations of Single- and Few-Layer MoS2.* ACS Nano, 2010. **4**(5): p. 2695-2700.
65. Li, H., Zhang, Q., Yap, C.C.R., Tay, B.K., et al., *From Bulk to Monolayer MoS2: Evolution of Raman Scattering.* Advanced Functional Materials, 2012. **22**(7): p. 1385-1390.
66. Late, D.J., Liu, B., Matte, H.S.S.R., Dravid, V.P., et al., *Hysteresis in Single-Layer MoS2 Field Effect Transistors.* ACS Nano, 2012. **6**(6): p. 5635-5641.
67. Bertolazzi, S., Krasnozhon, D., and Kis, A., *Nonvolatile Memory Cells Based on MoS2/Graphene Heterostructures.* ACS Nano, 2013. **7**(4): p. 3246-3252.
68. Wang, L., Wang, Y., Wong, J.I., Palacios, T., et al., *Functionalized MoS2 Nanosheet-Based Field-Effect Biosensor for Label-Free Sensitive Detection of Cancer Marker Proteins in Solution.* Small, 2014. **10**(6): p. 1101-1105.
69. Tahir, M.N., Zink, N., Eberhardt, M., Therese, H.A., et al., *Overcoming the Insolubility of Molybdenum Disulfide Nanoparticles through a High Degree of Sidewall Functionalization Using Polymeric Chelating Ligands.* Angewandte Chemie International Edition, 2006. **45**(29): p. 4809-4815.
70. McCarthy, P.J., Hovey, R.J., Ueno, K., and Martell, A.E., *Inner Complex Chelates. I. Analogs of Bisacetylacetoneethylenediimine and its Metal Chelates1,2*. Journal of the American Chemical Society, 1955. **77**(22): p. 5820-5824.
71. A. Shelnutt, J., Song, X.-Z., Ma, J.-G., Jia, S.-L., et al., *Nonplanar porphyrins and their significance in proteins.* Chemical Society Reviews, 1998. **27**(1): p. 31-42.

72. Perez-Aguilar, J.M., Xi, J., Matsunaga, F., Cui, X., et al., *A computationally designed water-soluble variant of a G-protein-coupled receptor: the human mu opioid receptor.* PloS one, 2013. **8**(6): p. e66009.

CHAPTER 7: Conclusions, Outlook and Future Work

Nanomaterial-based devices have the potential to generate a new wave of technologies, with applications spanning from comparatively mundane applications such as composite materials and touchscreens, through major technological needs such as energy harvesting, digital electronics and radio frequency communications, all the way to futuristic possibilities such as quantum computing. In this thesis, I first presented results that push the state-of-the-art in CVD growth and device fabrication for nanomaterials including graphene, carbon nanotubes and monolayer molybdenum disulfide (chapter 4). These scalable techniques yield arrays of FET devices based on crystalline, low-dimensional material with excellent electronic performance (conductivity, mobility, on-off ratio). I then applied these devices to bio/chemical sensing applications in vapor (chapter 5) to detect chemical traces, distinguish complex vapor mixtures and finally detect ovarian cancer based on a volatile odor signature. The same nanomaterial device platforms were used to detect biomarkers in solution, including glucose and enkephalin, an opiod peptide (chapter 6). In this chapter I summarize and discuss future possibilities for each of these sensing fields in turn.

7.1 Summary, Conclusions and Future Prospects for Vapor Sensing Experiments

Based on the results presented in chapter 5, we can conclude that carbon nanotube and graphene FETs functionalized with biomolecules such as single-stranded DNA demonstrate a wide variety of desirable performance characteristics for vapor sensing applications. These include fast readout of target chemicals down to part-per-billion concentrations, the ability to distinguish isomers and other closely related compounds and distinguish chemical mixtures that differ in subtle but controlled ways. Furthermore, we noted that changing the DNA sequence led to a different set of sensor binding sites, different vapor responses and ultimately a different set of information. Consequently, this technology is suitable for electronic nose-type applications, where arrays of sensors provide independent information for increased analytical power. A first real-world application in this direction is demonstrated in section 5.4 where serum samples from patients with ovarian cancer and benign ovarian growths are distinguished from samples from healthy women using DNA/carbon nanotube hybrid sensor arrays with ten different sensor types. Below I examine remaining hurdles towards implementing these kinds of applications and propose directions for future research.

7.1.1 Scalable surface functionalization

The human nose has approximately 400 different olfactory proteins that are responsible for binding volatile targets, and many copies of each, encoded by approximately 400 different genes [1]. The patterns of responses of this biological sensor array allow humans to distinguish an enormous number of odorous compounds, despite the fact that humans can only name a few of them. An early lower bound of 6500 different odors was estimated in 1927 [2]. This was rounded

up to 10,000, the number which was routinely quoted in the scientific literature until and a recent study that, on the basis of test subjects' abilities to distinguish odor mixtures, estimates the number of distinguishable odors to be closer to 1 trillion [3]. Dogs, rates and mice, all mammals with heightened senses of smell in comparison to humans, each have over a thousand different genes encoding for olfactory proteins [1]. It thus stands to reason that an electronic nose system might need to monitor hundreds or thousands of independent receptors in order to achieve the analytical power of mammalian olfaction.

As we scale from one hundred nanomaterial devices to potentially thousands on a single chip, and from ten different DNA sequences to hundreds, the current methods of functionalizing the transistors will no longer be viable. Currently, DNA is pipetted by hand onto the clustered channels of the devices, which are arranged in such a fashion that the droplets of DNA solution can be blown off the surface of the sample without cross-contaminating. A more sophisticated approach is necessary moving forward.

One potential advance in this direction would be to functionalize the devices using removable microfluidic channels, as shown in fig. 7.1. We have experimented with PDMS molds for this purpose, which would allow solutions containing different chemicals/DNA strands/targets to be flowed across different devices. By using a photolithographically defined array of microfluidic channels that are compatible with the chip architecture, we could functionalize regions of the chip tens or perhaps hundreds of different ways. The biggest hurdle in incorporating this technique into our device fabrication scheme is the delicate balance required when curing and binding the PDMS mold onto the silicon chip. If the PDMS is insufficiently stuck to the chip, solutions can leak out of their channels and merge. If the adhesion of the mold is too strong, removing the mold without damaging the nanomaterial circuitry is not possible. A further concern

is the potential leakage of hydrophobic PDMS monomers from the walls of the mold, into the solution and onto the nanomaterial surfaces. If this happens, it can disrupt functionalization schemes and ruin device performance.

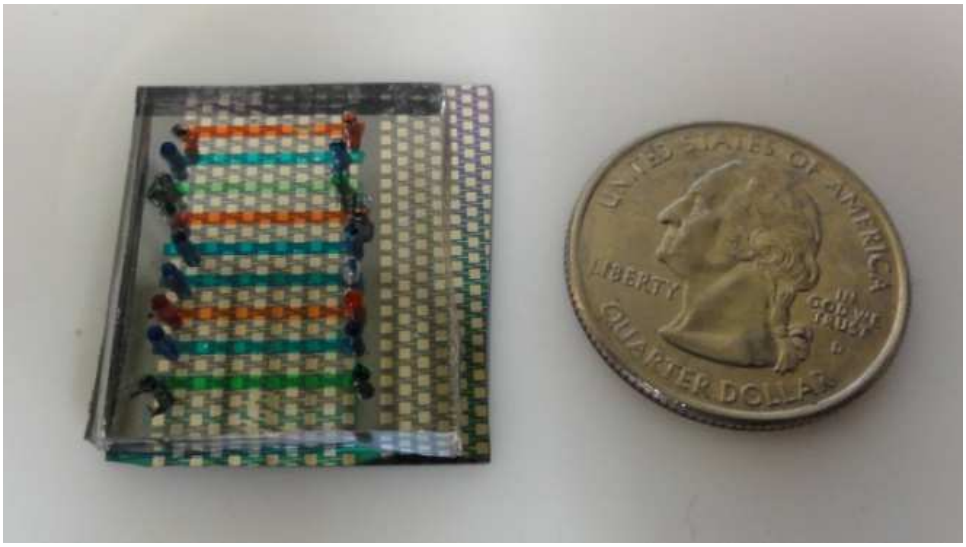

Figure 7.1: A PDMS mold with 9 independent fluid channels adhered to an FET array. Dyed water is used to visualize the channels, which confine the fluid well.

7.1.2 Portable Readout Electronics

In order to move beyond expensive benchtop vapor response testing systems and progress towards a portable, compact system appropriate for point-of-care diagnostics, the electronics need to be miniaturized. In collaboration with David Isele and Camillo J. Taylor of the Computer and Information Science Department at the University of Pennsylvania, we designed and tested prototype electronic boards that perform the same functions as the tabletop switching matrix, picoammeter and source meter used throughout this thesis. A picture of the two boards is shown in fig. 7.2.

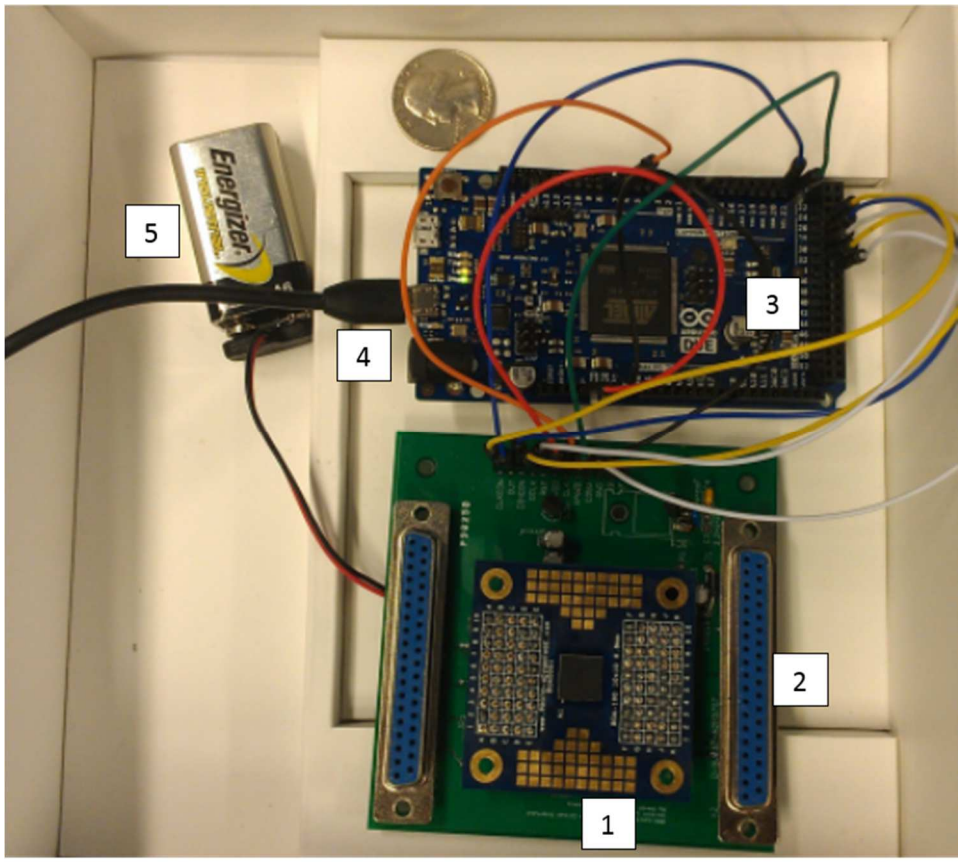

Figure 7.2: Compact electronic circuits for monitoring the sensor array. A commercial microcontroller board (top) is used in combination with a prototype board (bottom) that features a 64 channel current-input ADC.

The signals of interest are fluctuations around currents at the scale of 10^{-7}A, hence our circuit requires sensitivity at/below the nanoamp scale. To capture these small signals we use the DDC264 (1), a current-input analog-to-digital converter made by Texas Instruments. The DDC264 has 64 input channels that can be used to measure small currents on the scale of nanoamps. It can be configured to provide either 16 or 20 bits of precision for each measurement. Two large 37-pin D-subminiature connectors (2) are currently used to ensure compatibility with the sensor chamber on the desktop setup, but could be replaced by a more compact connector in future when interfacing with packaged chips.

We use an Arduino Due micro-controller (3, the whole board) to communicate with the current reader (DDC264). The Arduino micro-controller is also used to provide a 5V power supply (acquired from USB) which powers the other circuit components. The Arduino interfaces to the DDC264 sensor and sends the resulting digital current readings to a laptop via a USB connection (4). To provide a variable bias voltage on the scale of 100 milliamps, a resistor in series with a zener diode is used as a voltage regulator for a 9 V battery (5). Since we are working with small currents with even smaller changes in current, this solution is stable and draws less power than a standard voltage regulator.

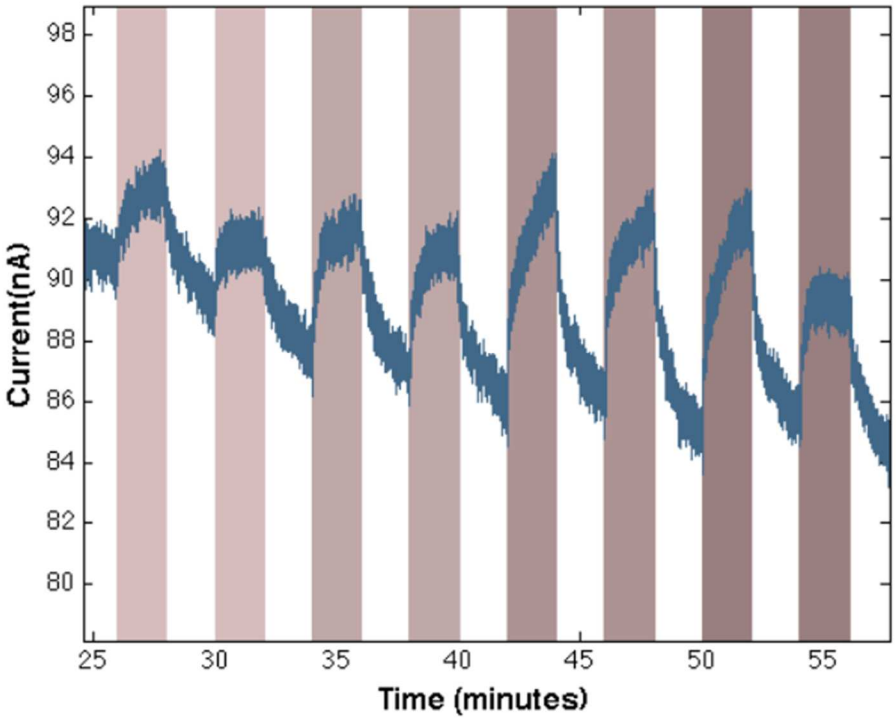

Figure 7.3: Current vs time data from a single channel using the compact electronics. From left to right, the concentration of VOCs from a synthetic mixture of acids is increasing, reflected in increasing responses when the flow is directed over the devices (grey).

Figure 7.3 shows data from a single channel of the sensor array, read out using the portable electronics connected to a sensor chamber very similar to the one shown in figure 5.1.

The DNA-coated carbon nanotube device is responding to pulses of VOCs from the synthetic sweat solution used in section 5.3 and the responses agree with the trends observed in section 5.3. This demonstrates the functionality of the low-footprint electronics, a necessary step in transitioning this technology off the lab bench and into a portable system.

7.1.3 Supplementing DNA-coated sensors with specific receptors to increase analytical power

In the results presented in section 5.4, DNA-coated carbon nanotubes were used to distinguish the volatile content of blood plasma samples, with characteristic trends in a data set of 24 samples that reflect whether the sample came from a patient with ovarian cancer, a benign ovarian tumor or a healthy control donor. As part of this interdisciplinary study, Dr. George Preti and Dr. Katherine Prokop-Prigge analyzed the same plasma samples using gas chromatography/mass spectrometry (GC/MS) to identify the volatile organic compounds that vary in concentration between the three groups. These results could be used in future to inform the design of the sensor array, with versatile non-specific DNA receptors complimented by specific receptors for particular VOC targets. Average quantities of selected VOCs in the different plasma types are shown in fig. 7.4. These are just two of approximately two dozen VOCs that appear to characteristically differ amongst the different groups of plasma samples.

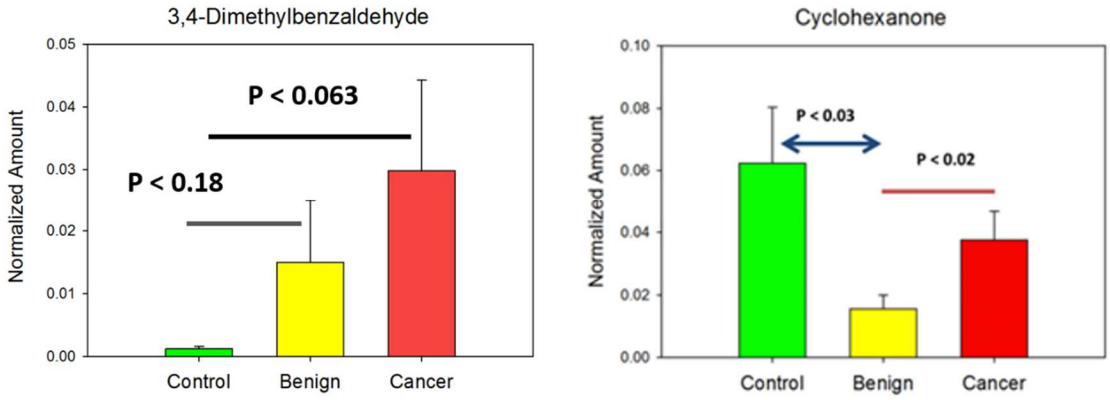

Figure 7.4: Concentrations of 3,4-dimethylbenzaldehyde and cyclohexanone in malignant, benign and control samples, as determined by GC/MS. 3,4-dimethylbenzaldehyde concentration is highly elevated in plasma samples from many cancer patients. The concentration of cyclohexanone, along with many other VOCs, appears to suppressed in individuals with ovarian tumors.

An example of a more specific receptor that would bind benzaldehydes could be phenol hydroxylamine. The phenol group ensures adhesion of the receptor to the sp^2 carbon nanomaterial via π-π stacking. Hydroxylamines and aldehydes are known to react to form an oxime. If the sensor were exposed to 3,4-dimethylbenzaldehyde, the result would be 3,4-dimethylbenzaldehyde oxime, which would remain tethered to the phenol anchor. We would expect the nitrogen to acquire a positive charge. Due to the binding of an additional molecule and the generation of a charge species on the nanomaterial surface, we would expect a substantial effect on the nanomaterial FET properties. This sensitive and more specific receptor would complement the DNA coated FETs already demonstrated throughout this work.

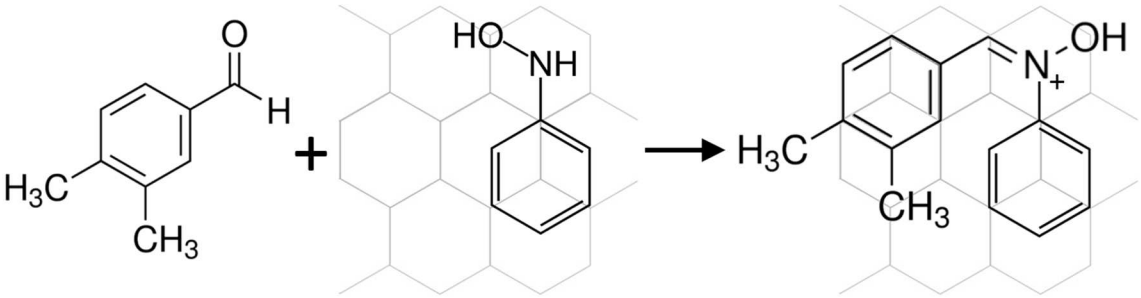

Figure 7.5: Schematic of the binding of 3,4-dimethylbenzaldehyde to phenol hydroxylamine, a proposed receptor compatible with sp^2 carbon surfaces.

7.2 Summary, Conclusions and Future Prospects for Solution Biomarker Detection

We have shown that MoS_2 FETs are able to read out protein-target interactions. Exposure of the re-engineered mu-opiod receptor to enkephalin at varying concentrations was monitored using the MoS_2 $I(V_g)$ and the binding affinity measured in this way was in agreement with what should be expected for this interaction. We also showed that carbon nanotubes functionalized with pyrene boronic acid are able to detect glucose down to micromolar concentrations, which could be the basis of a technology to detect glucose at concentrations found in saliva.

There are many steps that needs to be demonstrated in order for these technologies to mature into useful products. The next step would be to detect the targets not in pure buffer, but in a more complicated mixture of proteins and lipids that more closely resembles a real sample. Sensor array functionality will be dramatically increased if it is possible to show that differently functionalized sensors on the same chip are able to detect the concentrations of individual biomarkers in a mixture with a significant background concentrations of potential interferents.

Provided the sensitivities to small molecule, peptide and protein targets can be replicated in that more complex environment, techniques will then need to be developed to work with real samples such as blood or saliva. One concern is that salt from the solutions can screen the protein from the nanomaterial. In both experiments presented in chapter 6, we have mitigated this concern by using extremely short linker chemistries. Another concern is that other components in real samples will non-specifically adsorb onto the nanomaterial surfaces and thus give spurious signals that will overwhelm the specific response from the actual target molecules. One approach to this problem might be to purify the original sample and remove as much of the background material as possible before exposing the sensors to it, but this will have to be done in such a way

as to not dilute down the target molecules. Research in sample purification is already underway in biochemistry labs across the world and it's a critical piece to the puzzle for many diagnostic technologies, not just the nanomaterial FETs discussed here. If all of these steps can be accomplished, nanomaterial-based biomarker detection and disease diagnostics will be well on their way to making a commercial and clinical impact.

References

1. Ache, B.W. and J.M. Young, *Olfaction: Diverse Species, Conserved Principles.* Neuron, 2005. **48**(3): p. 417-430.
2. Crocker, E. and L. Henderson, *Analysis and classification of odors.* American Perfumer and Essential Oil Review, 1927. **22**(325-327): p. 116.
3. Bushdid, C., et al., *Humans Can Discriminate More than 1 Trillion Olfactory Stimuli.* Science, 2014. **343**(6177): p. 1370-1372.

APPENDIX

Appendix A: CVD growth of Carbon Nanotubes

1. Weigh out 10 mg of 99.999+% pure Iron Nitrate Nonahydrate (from Sigma Aldrich).
    a. Crystals should be small, ~ 2 mg in weight, and nearly translucent. Yellowed crystals are oxidized and require higher concentrations to produce the same nanotube density.
    b. Precise measurements are important. Changes in the final concentration of as little as 5% can result in a different nanotube growth density.
2. Wash the Iron Nitrate crystals into a 50 mL Falcon tube with isopropanol. Make sure to wash out all crystals.
    a. Use of stronger solvents, such as acetone, can break the shell structure that forms around the catalyst nanoparticles which would disturb the tight diameter distribution.
3. At this point, the catalyst concentration is 10 mg Iron Nitrate /50 mL Isopropanol = 200 mg/L. Dilute this stock solution with isopropanol to a final concentration of 1.5-10 mg/L, depending on the desired nanotube density. 1.5mg/L gives isolated single nanotubes, 10mg/L gives a low density network of carbon nanotubes.
    a. Catalyst solutions oxidize quickly. A given solution can be used the day it was prepared, but cannot be stored for future use.
4. Place a 100 mm diameter oxide Si/SiO_2 wafer in the spinner. Pipet 4 mL of /L catalyst solution onto the wafer surface, covered it completely.
5. Spin the wafer at 3000 rpm until the catalyst dries, about 20 seconds.

a. Newton's rings, an interference pattern of concentric circles will be visible for a few seconds.

6. Cleave the wafer (if necessary) to fit into the tube furnace being used.
7. Slide the wafer pieces into the furnace.
    a. It is possible to grow multiple wafers simultaneously if you put one in upside down, under the other wafer pieces, with the catalyst-coated side facing the quartz tube.
8. Make sure both tube ends and all connections are sealed tight. Ensure proper negative pressure on the outlet of the tube furnace.
    a. Any oxygen leak, even from the adjacent furnace on the same tanks being open to ambient, will prevent nanotubes from being grown at all.
9. For Johnson lab 2" furnace, flow 600 sccm argon, 320 sccm hydrogen, 2500 sccm methane for 10 mintues to flush out the tube of oxygen. After 10 min, turn off the methane. Flow just Ar and H_2 5 more minutes.
    a. Any residual methane in the furnace while it heats will blacken the quartz tube with carbon soot.
10. Begin heating the furnace to 900°C. In the Johnson Lab 2" furnace, this takes about an hour.
11. As soon as the temperature gauge reaches 900°C, begin flowing the methane again at 2500 sccm with argon and hydrogen still flowing. Let the methane flow for 2 minutes.
    a. Most of the nanotube growth occurs over the first 20 sec or so. The remaining time is just a precaution.

12. After growth, turn off the methane flow and close the valve. Turn off the heater power to begin cooling.
13. At 400°C, open the furnace lid to promote cooling.
    a. Do not open the furnace above 400°C. Rapid cooling at high temperatures can cause the ceramic insulators to crack.
14. At 100°C, turn off argon and hydrogen flow. Open the tube endcap and remove samples. Make sure gas tanks are closed for safety purposes.

Appendix B: Low pressure CVD graphene growth recipe

- **Copper Foil Preparation**

  1. Cut a pieces of 99.9% Copper foil such that it fits onto the quartz holder.
  2. Roll the copper foil up and slide into a 50 mL falcon tube. Fill the falcon tube with acetone Sonicate for 10 minutes.
  3. Pour out acetone and immediately refill with isopropanol. Shake briefly, then pour out isopropanol and refill once more.
  4. Take out the foil and blow dry with N2.
  5. Place inner side of the foil (side NOT touching falcon tube) face down on the quartz holder. This bottom face of the copper (side of the sheet in contact with the quartz holder) will have the highest-quality graphene growth.

- **Furnace Setup**

  1. Open the entry port on the right side of the tube furnace.
  2. Ensure that the furnace is situated on the right-half side of the quartz process tube. Align the black arrows at the bottom of the furnace. You may move the furnace by simply pushing it gently along its rails.
  3. Open the clam-shell furnace.
  4. Clean the quartz tube, the quartz thermal blocks, and the quartz sample holder gently. To clean the tube, use towels wetted with IPA to scrub the inside of the tube. To clean the quartz blocks and the quartz sample holder, use towels wetted with IPA to gently rub off the copper deposition.

5. Place one of the quartz thermal blocks at the left (upstream) end of the furnace. The block should be aligned with the left edge of the insulation. Use the metal rod/hook to move the block.
6. Put your copper foil on top of the quartz holder and slide into the center of the right zone of the two-zone tube furnace. Use the long metal rod to push the holder into position.
7. Place the other quartz thermal block at the right (downstream) end of the furnace.
8. Inspect and make sure that the o-ring on the endmost face of the righthand flange is free of dirt or dust. Remove any dirt with clean gloves.
9. Apply vacuum grease to the right hand flange o-ring and secure the hexagonal stainless steel end plate by screwing in all three machine screws by hand (they should not be tight and should leave some space for the end plate to pop out in case of over pressure).
10. The furnace should look be in the state pictured in figure 4.6. Close the clam shell furnace.

- **Process Start**

1. Turn on water chiller. Make sure both pump and chiller are on.
2. Make sure valve connecting quartz tube outlet to vacuum pump at the right end of the furnace is closed. Turn on the vacuum pump.
3. **Slowly** open vacuum valve to avoid moving the thermal blocks or quartz holder.
4. Wait for the system to pump down to below 1 Torr. Pressure should reach to ~60 mTorr range with a couple minutes;
5. Open the Hydrogen and Methane tanks, regulators and valves on the wall.
6. Set the H2 MFC to 80 sccm. The pressure should increase to ~615 mTorr
7. Set the CH4 MFC to 45 sccm. The pressure should increase to ~925 mTorr.
8. Flow 80 sccm of H2 and 45 sccm of CH4 for 5 min in order to flush the lines.

9. Set the CH4 flow to 0 sccm.

- **Process**

1. Begin ramp up of furnace temperature. Wait for ~ 70 minutes for the furnace to reach 1020 °C
2. Anneal the copper foil for 40 minutes at 1020 C.
3. Set the CH4 MFC to 45 sccm.
4. Wait for 60 minutes for the graphene to growth.
5. Turn off the furnace heater and crack the clamshell furnace open approximately an inch.

- **Furnace Cooling**

1. Wait until the oven reaches 900 C, then slide the furnace left on its rails, exposing the region of the quartz tube containing the foil.
2. Wait until the furnace reaches 500 C. Then switch the CH4 MFC to **OFF** and fully open the clam shell furnace.
3. Wait until the furnace reaches below 80 C, switch the H2 MFC to **OFF**.
4. Wait until the pressure reaches a value ~55 mTorr.
5. Close the vacuum valve completely and turn off the pump, pressure should remain stable at ~55 mTorr.
6. Open nitrogen tank. Backfill the quartz tube with nitrogen by setting nitrogen MFC to 5000 sccm flow.
7. Once pressure reaches atmosphere, open the downstream endcap and remove the thermal blocks and quartz holder.
8. Turn off the water chiller and close all tanks and valves.
9. Clean the quartz tube, thermal blocks and quartz holder with isopropanol.

Appendix C: CVD Growth of Boron Nitride

- **Copper Foil Preparation**

1. Cut high purity copper foil (99.8%) into a rectangular piece of dimensions 3 inch x 1.5 inch. These dimensions ensure maximum growth area with uniform coverage area in a 1" CVD furnace.
2. Take a clean centrifuge tube and fill with acetic acid. Immerse the copper foil completely in the acid and close the lid.
3. Sonicate the copper foil for 10 minutes. This process cleans the surface of the copper foil to avoid any ambiguous growth sites during the growth process.
4. After sonication, take clean tweezers and move the copper foil into a clean bath of DI water. This is to remove the acetic acid residue off the surface of the copper foil. Wait for 10 minutes. After 10 minutes spray DI water on both sides of the copper foil to ensures near complete removal of acetic acid residue.
5. Place the foil flat on a clean surface and gently blow dry using compressed nitrogen. Make sure you do not cause any deformations on the surface of the copper while blowing dry.

- **Growth Process**

1. Using clean tweezers place a pellet of ammonia borane in the center of the glass tube on the precursor holder.
2. Place a cleaned quartz tube into the CVD furnace and insert the source holder into the upstream end of the quartz tube. Tighten the upstream endcap.
3. Move the furnace to the right such that the right edge of the insulation of the furnace is 17 cm from the upstream quartz tube endcap.
4. Move the precursor holder all the way to this endcap, as far from the furnace as possible.

5. Once the furnace is in position, insert the cleaned copper foil into the downstream end of the quartz tube. Use a metallic rod to push the copper foil through the tube such that the center of the foil is adjacent to the furnace thermocouple. This is to ensure symmetrical temperature distribution across the surface area of the foil.
6. Close the downstream endcap of the quartz tube tightly.
7. Close the furnace lid. Open the valves of the argon gas tank and hydrogen gas tank. Set their flow rates to 500 sccm Ar and 50 sccm H_2
8. Switch the furnace on and set the temperature of the furnace to 1057 ^{o}C.
9. Wait for 30 minutes. After approximately 20 minutes, the furnce will have reached 1057 ^{o}C. Leave the foil annealing at high temperature for 10 more minutes.
10. After 30 minutes of ramp up/annealing, move the source pellet to 8 cm away from the furnace. Simultaneously reduce the flow rate of the H_2 to 20 sccm and wait for 15 minutes
11. After 15 minutes move the source back to the upstream end of the quartz tube using the magnet and simultaneously switch off the furnace heater.
12. Move the furnace downstream (left) until the foil is just protruding outside the furnace insulation.
13. Crack open the furnace using a metallic block of thickness 1".
14. When the temperature of the furnace is at 700 ^{o}C use a metallic block of greater height (about 3") inches to open the furnace (this allows faster cooling of the furnace)
15. When the temperature of the furnace is at 500^{o}C, use a metallic block of height (about 6 inches) to keep open the furnace.
16. Once the furnace has cooled below 100 ^{o}C, set the flow of the H_2 gas to 0 sccm and then close all the valves of the H_2 gas line.

17. After closing the H_2 gas tank, remove the sample from the downstream end of the quartz tube using a metallic rod while still allowing the Argon gas to flow at 500 sccm.
18. After removing the sample, set the flow of argon gas to 0 sccm and close all valves of the Argon gas flow and then finally close the argon gas tank.
19. Remove the source from the upstream end of the quartz tube. Pull it out from the tube using a magnet and tweezers.

BIBLIOGRAPHY

A. Shelnutt, J., Song, X.-Z., Ma, J.-G., Jia, S.-L., et al., *Nonplanar porphyrins and their significance in proteins.* Chemical Society Reviews, 1998. **27**(1): p. 31-42.

Abboud, J.L.M. and R. Notari, *Critical compilation of scales of solvent parameters. Part I. Pure, non-hydrogen bond donor solvents*, in *Pure and Applied Chemistry*. 1999. p. 645.

Ache, B.W. and J.M. Young, *Olfaction: Diverse Species, Conserved Principles.* Neuron, 2005. **48**(3): p. 417-430.

Ajayan, P. and O. Zhou, *Applications of Carbon Nanotubes*, in *Carbon Nanotubes*, M. Dresselhaus, G. Dresselhaus, and P. Avouris, Editors. 2001, Springer Berlin Heidelberg. p. 391-425.

Akutsu, T., et al., *Individual comparisons of the levels of (E)-3-methyl-2-hexenoic acid, an axillary odor-related compound, in Japanese.* Chemical Senses, 2006. **31**(6): p. 557-563.

Allen, B.L., Kichambare, P.D., and Star, A., *Carbon nanotube field-effect-transistor-based biosensors.* Advanced Materials, 2007. **19**(11): p. 1439-1451.

American Cancer Society, Cancer Facts and Figures 2015. 2015.

Amit, C., *Interconnects for nanoscale MOSFET technology: a review.* Journal of Semiconductors, 2013. **34**(6): p. 066001.

Ando, T., *Screening Effect and Impurity Scattering in Monolayer Graphene.* Journal of the Physical Society of Japan, 2006. **75**(7): p. 074716.

Arnold, M.S., Green, A.A., Hulvat, J.F., Stupp, S.I., et al., *Sorting carbon nanotubes by electronic structure using density differentiation.* Nat Nano, 2006. **1**(1): p. 60-65.

Arnold, M.S., Stupp, S.I., and Hersam, M.C., *Enrichment of Single-Walled Carbon Nanotubes by Diameter in Density Gradients.* Nano Letters, 2005. **5**(4): p. 713-718.

Auvray, S., Derycke, V., Goffman, M., Filoramo, A., et al., *Chemical optimization of self-assembled carbon nanotube transistors.* Nano Letters, 2005. **5**(3): p. 451-455.

Bajtarevic, A., et al., *Noninvasive detection of lung cancer by analysis of exhaled breath.* Bmc Cancer, 2009. **9**.

Balakrishnama, S. and A. Ganapathiraju, *Linear discriminant analysis-a brief tutorial.* Institute for Signal and information Processing, 1998.

Balandin, A.A., et al., *Superior Thermal Conductivity of Single-Layer Graphene.* Nano Letters, 2008. **8**(3): p. 902-907.

Balandin, A.A., *Thermal properties of graphene and nanostructured carbon materials.* Nat Mater, 2011. **10**(8): p. 569-581.

Bao, W.Z., et al., *High mobility ambipolar MoS2 field-effect transistors: Substrate and dielectric effects.* Applied Physics Letters, 2013. **102**: p. 042104.

Barone, P.W., et al., *Near-infrared optical sensors based on single-walled carbon nanotubes.* Nature Materials, 2005. **4**(1): p. 86-92.

Barreiro, A., et al., *Graphene at High Bias: Cracking, Layer by Layer Sublimation, and Fusing.* Nano Letters, 2012. **12**(4): p. 1873-1878.

Basiuk, E.V., et al., *Interaction of Oxidized Single-Walled Carbon Nanotubes with Vaporous Aliphatic Amines.* The Journal of Physical Chemistry B, 2002. **106**(7): p. 1588-1597.

Baughman, R.H., A.A. Zakhidov, and W.A. de Heer, *Carbon Nanotubes--the Route Toward Applications.* Science, 2002. **297**(5582): p. 787-792.

Behnam, A., et al., *Transport in Nanoribbon Interconnects Obtained from Graphene Grown by Chemical Vapor Deposition.* Nano Letters, 2012. **12**(9): p. 4424-4430.

Bernardi, M., Palummo, M., and Grossman, J.C., *Extraordinary Sunlight Absorption and One Nanometer Thick Photovoltaics Using Two-Dimensional Monolayer Materials.* Nano Letters, 2013. **13**(8): p. 3664-3670.

Bertolazzi, S., Krasnozhon, D., and Kis, A., *Nonvolatile Memory Cells Based on MoS2/Graphene Heterostructures.* ACS Nano, 2013. **7**(4): p. 3246-3252.

Betti, A., G. Flori, and G. Iannaccone, *Investigation of low-field mobility in graphene nanoribbons.* IEEE Transactions on Electron Devices, 2011. **58**: p. 2824-2830.

Biercuk, M., S. Ilani, C. Marcus, and P. McEuen, *Electrical Transport in Single-Wall Carbon Nanotubes*, in *Carbon Nanotubes*, A. Jorio, G. Dresselhaus, and M. Dresselhaus, Editors. 2008, Springer Berlin Heidelberg. p. 455-493.

Binnig, G., C.F. Quate, and C. Gerber, *Atomic Force Microscope.* Physical Review Letters, 1986. **56**(9): p. 930-933.

Bird, G.A., *Molecular gas dynamics*. Oxford engineering science series. 1976, Oxford: Clarendon Press. xvi, 238 p.

Bolotin, K.I., et al., *Ultrahigh electron mobility in suspended graphene.* Solid State Communications, 2008. **146**(9–10): p. 351-355.

Bolotin, K.I., K.J. Sikes, J. Hone, H.L. Stormer, et al., *Temperature-dependent transport in suspended graphene.* Phys Rev Lett, 2008. **101**(9): p. 096802.

Bondavalli, P., P. Legagneux, and D. Pribat, *Carbon nanotube based transistors as gas sensors: State of the art and critical review.* Sensors and Actuators B-Chemical, 2009. **140**: p. 304-318.

Bresnehan, M.S., et al., *Integration of hexagonal boron nitride with quasi-freestanding epitaxial graphene: toward wafer-scale, high-performance devices.* ACS nano, 2012. **6**(6): p. 5234-5241.

Britnell, L., et al., *Electron Tunneling through Ultrathin Boron Nitride Crystalline Barriers.* Nano Letters, 2012. **12**(3): p. 1707-1710.

Brivio, J., D.T.L. Alexander, and A. Kis, *Ripples and layers in ultrathin MoS2 membranes.* Nano Letters, 2011. **11**: p. 5148-5153.

Brown, S.D.M., A. Jorio, P. Corio, M.S. Dresselhaus, et al., *Origin of the Breit-Wigner-Fano lineshape of the tangential \textit{G} -band feature of metallic carbon nanotubes.* Physical Review B, 2001. **63**(15): p. 155414.

Burg, B.R. and D. Poulikakos, *Large-scale integration of single-walled carbon nanotubes and graphene into sensors and devices using dielectrophoresis: A review.* Journal of Materials Research, 2011. **26**(13): p. 1561-1571.

Bushdid, C., et al., *Humans Can Discriminate More than 1 Trillion Olfactory Stimuli.* Science, 2014. **343**(6177): p. 1370-1372.

Buys, S.S., et al., *Effect of screening on ovarian cancer mortality: The prostate, lung, colorectal and ovarian (plco) cancer screening randomized controlled trial.* JAMA, 2011. **305**(22): p. 2295-2303.

Chang, H.Y., et al., *High-performance, highly bendable MoS2 transistors with high-k dielectrics for flexible low-power systems.* ACS Nano, 2013. **7**(6): p. 5446-52.

Chen, J.-H., C. Jang, S. Xiao, M. Ishigami, et al., *Intrinsic and extrinsic performance limits of graphene devices on SiO2.* Nat Nano, 2008. **3**(4): p. 206-209.

Chen, R.J., Choi, H.C., Bangsaruntip, S., Yenilmez, E., et al., *An investigation of the mechanisms of electronic sensing of protein adsorption on carbon nanotube devices.* Journal of the American Chemical Society, 2004. **126**(5): p. 1563-1568.

Chhowalla, M., H.S. Shin, G. Eda, L.-J. Li, et al., *The chemistry of two-dimensional layered transition metal dichalcogenide nanosheets.* Nat Chem, 2013. **5**(4): p. 263-275.

Choi, S.-J., et al., *Comparative study of solution-porcessed carbon nanotube network transistors.* Applied Physics Letters, 2012. **101**: p. 112104.

Choi, Y., Moody, I.S., Sims, P.C., Hunt, S.R., et al., *Single-Molecule Lysozyme Dynamics Monitored by an Electronic Circuit.* Science, 2012. **335**(6066): p. 319-324.

Ci, L., et al., *Atomic layers of hybridized boron nitride and graphene domains.* Nat Mater, 2010. **9**(5): p. 430-435.

Coleman, J.N., U. Khan, W.J. Blau, and Y.K. Gun'ko, *Small but strong: A review of the mechanical properties of carbon nanotube–polymer composites.* Carbon, 2006. **44**(9): p. 1624-1652.

Cordes, D.B., Gamsey, S., and Singaram, B., *Fluorescent quantum dots with boronic acid substituted viologens to sense glucose in aqueous solution.* Angewandte Chemie-International Edition, 2006. **45**(23): p. 3829-3832.

Corradini, R., et al., *Chirality as a tool in nucleic acid recognition: principles and relevance in biotechnology and in medicinal chemistry.* Chirality, 2007. **19**(4): p. 269-94.

Crocker, E. and L. Henderson, *Analysis and classification of odors.* American Perfumer and Essential Oil Review, 1927. **22**(325-327): p. 116.

Cubillas, P. and M.W. Anderson, *Atomic Force Microscopy*, in *Multi Length-Scale Characterisation*. 2014, John Wiley & Sons, Ltd. p. 121-193.

Czarnowski, D., et al., *Effect of a Low Carbohydrate-Diet on Plasma and Sweat Ammonia Concentrations during Prolonged Nonexhausting Exercise.* European Journal of Applied Physiology and Occupational Physiology, 1995. **70**(1): p. 70-74.

Dai, Z.H., et al., *Phase diagram, deisgn of monolayer binary colloidal crystals, and their fabrication based on ethanol-asssited self-assembly at the air/water interface.* ACS Nano, 2012. **6**: p. 6706-6716.

Dalton, P., et al., *Chemosignals of Stress Influence Social Judgments.* Plos One, 2013. **8**(10).

Dan, Y., Y. Lu, N.J. Kybert, Z. Luo, et al., *Intrinsic response of graphene vapor sensors.* Nano Lett, 2009. **9**(4): p. 1472-5.

Das, A., et al., *Monitoring dopants by Raman scattering in an electrochemically top-gated graphene transistor.* Nature Nanotechnology, 2008. **3**(4): p. 210-215.

Dean, C.R., A.F. Young, MericI, LeeC, et al., *Boron nitride substrates for high-quality graphene electronics.* Nat Nano, 2010. **5**(10): p. 722-726.

Dean, C.R., A.F. Young, P. Cadden-Zimansky, L. Wang, et al., *Multicomponent fractional quantum Hall effect in graphene.* Nat Phys, 2011. **7**(9): p. 693-696.

Dresselhaus, M.S., A. Jorio, M. Hofmann, G. Dresselhaus, et al., *Perspectives on Carbon Nanotubes and Graphene Raman Spectroscopy.* Nano Letters, 2010. **10**(3): p. 751-758.

Dresselhaus, M.S., G. Dresselhaus, A. Jorio, A.G. Souza Filho, et al., *Raman spectroscopy on isolated single wall carbon nanotubes.* Carbon, 2002. **40**(12): p. 2043-2061.

Dresselhaus, M.S., G. Dresselhaus, and P. Avouris, *Carbon nanotubes : synthesis, structure, properties, and applications*. Topics in applied physics. 2001, Berlin ; New York: Springer. xv, 447 p.

Du, X., I. Skachko, A. Barker, and E.Y. Andrei, *Approaching ballistic transport in suspended graphene.* Nat Nano, 2008. **3**(8): p. 491-495.

Dürkop, T., Getty, S.A., Cobas, E., and Fuhrer, M.S., *Extraordinary Mobility in Semiconducting Carbon Nanotubes.* Nano Letters, 2004. **4**(1): p. 35-39.

Erickson, K.J., et al., *Longitudinal Splitting of Boron Nitride Nanotubes for the Facile Synthesis of High Quality Boron Nitride Nanoribbons.* Nano Letters, 2011. **11**(8): p. 3221-3226.

Fan, X., et al., *Band gap opening of graphene by doping small boron nitride domains.* Nanoscale, 2012. **4**(6): p. 2157-2165.

Fan, Y., B.R. Goldsmith, and P.G. Collins, *Identifying and counting point defects in carbon nanotubes.* Nat Mater, 2005. **4**(12): p. 906-911.

Ferrari, A.C., J.C. Meyer, V. Scardaci, C. Casiraghi, et al., *Raman Spectrum of Graphene and Graphene Layers.* Physical Review Letters, 2006. **97**(18): p. 187401.

Ferrari, A.C., *Raman spectroscopy of graphene and graphite: Disorder, electron–phonon coupling, doping and nonadiabatic effects.* Solid State Communications, 2007. **143**(1–2): p. 47-57.

Fiori, G., et al., *Lateral Graphene–hBCN Heterostructures as a Platform for Fully Two-Dimensional Transistors.* ACS Nano, 2012. **6**(3): p. 2642-2648.

Fogler, M.M., F. Guinea, and M.I. Katsnelson, *Pseudomagnetic Fields and Ballistic Transport in a Suspended Graphene Sheet.* Physical Review Letters, 2008. **101**(22): p. 226804.

Frank, O., M. Mohr, J. Maultzsch, C. Thomsen, et al., *Raman 2D-Band Splitting in Graphene: Theory and Experiment.* ACS Nano, 2011. **5**(3): p. 2231-2239.

Fratini, S. and F. Guinea, *Substrate-limited electron dynamics in graphene.* Physical Review B, 2008. **77**(19): p. 195415.

Fujita, M., et al., *Peculiar Localized State at Zigzag Graphite Edge.* Journal of the Physical Society of Japan, 1996. **65**(7): p. 1920-1923.

Gallagher, M., et al., *Analyses of volatile organic compounds from human skin.* British Journal of Dermatology, 2008. **159**(4): p. 780-791.

Gan, L. and Z. Luo, *Turning off Hydrogen To Realize Seeded Growth of Subcentimeter Single-Crystal Graphene Grains on Copper.* ACS Nano, 2013. **7**(10): p. 9480-9488.

Gannett, W., W. Regan, K. Watanabe, T. Taniguchi, et al., *Boron nitride substrates for high mobility chemical vapor deposited graphene.* Applied Physics Letters, 2011. **98**(24): p. 242105.

Gao, L., et al., *Repeated growth and bubbling transfer of graphene with millimetre-size single-crystal grains using platinum.* Nat Commun, 2012. **3**: p. 699.

Gao, Y., et al., *Toward Single-Layer Uniform Hexagonal Boron Nitride–Graphene Patchworks with Zigzag Linking Edges.* Nano Letters, 2013. **13**(7): p. 3439-3443.

Garcia, A.G.F., et al., *Effective Cleaning of Hexagonal Boron Nitride for Graphene Devices.* Nano Letters, 2012. **12**(9): p. 4449-4454.

Georgakilas, V., et al., *Functionaliztion of graphene: Covalent and non-covalent approaches, derivatives, and applications.* Chemical Reviews, 2013. **112**: p. 6156-6214.

George, A.S., Z. Mutlu, R. Ionescu, R.J. Wu, et al., *Wafer Scale Synthesis and High Resolution Structural Characterization of Atomically Thin MoS2 Layers.* Advanced Functional Materials, 2014. **24**(47): p. 7461-7466.

Ghosh, S., X. An, R. Shah, D. Rawat, et al., *Effect of 1- Pyrene Carboxylic-Acid Functionalization of Graphene on Its Capacitive Energy Storage.* The Journal of Physical Chemistry C, 2012. **116**(39): p. 20688-20693.

Goldsmith, B.R., Mitala, J.J., Josue, J., Castro, A., et al., *Biomimetic Chemical Sensors Using Nanoelectronic Readout of Olfactory Receptor Proteins.* Acs Nano, 2011. **5**(7): p. 5408-5416.

Gong, C., et al., *Metal Contacts on Physical Vapor Deposited Monolayer MoS2.* ACS Nano, 2013. **7**(12): p. 11350-11357.

Goossens, A.M., et al., *Mechanical cleaning of graphene.* Applied Physics Letters, 2012. **100**(7): p. 073110.

Gorbachev, R.V., et al., *Hunting for Monolayer Boron Nitride: Optical and Raman Signatures.* Small, 2011. **7**(4): p. 465-468.

Hähnlein, B., et al., *Side-gate graphene field-effect transistors with high transconductance.* Applied Physics Letters, 2012. **101**(9): p. 093504.

Haider, M., H. Rose, S. Uhlemann, E. Schwan, et al., *A spherical-aberration-corrected 200 kV transmission electron microscope.* Ultramicroscopy, 1998. **75**(1): p. 53-60.

Hall, D.G., *Boronic acids : preparation and applications in organic synthesis, medicine and materials*. 2nd completely rev. ed. 2011, Weinheim: Wiley-VCH.

Han, G.H., et al., *Influence of Copper Morphology in Forming Nucleation Seeds for Graphene Growth.* Nano Letters, 2011. **11**(10): p. 4144-4148.

Han, G.H., J.A. Rodriguez-Manzo, C.W. Lee, N.J. Kybert, et al., *Continuous growth of hexagonal graphene and boron nitride in-plane heterostructures by atmospheric pressure chemical vapor deposition.* ACS Nano, 2013. **7**(11): p. 10129-38.

Han, G.H., Kybert, N.J., Naylor, C.H., Lee, B.S., et al., *Seeded growth of highly crystalline molybdenum disulphide monolayers at controlled locations.* Nat Commun, 2015. **6**.

Hanafi, Z.M., M.A. Khilla, and A.M. H., *The thermal decomposition of ammonium heptamolybdate.* Thermochimica Acta, 1981. **45**: p. 221-232.

Hao, Y., et al., *The Role of Surface Oxygen in the Growth of Large Single-Crystal Graphene on Copper.* Science, 2013. **342**(6159): p. 720-723.

Hasegawa, Y., M. Yabuki, and M. Matsukane, *Identification of new odoriferous compounds in human axillary sweat.* Chemistry & Biodiversity, 2004. **1**(12): p. 2042-2050.

Haze, S., et al., *2-Nonenal newly found in human body odor tends to increase with aging.* Journal of Investigative Dermatology, 2001. **116**(4): p. 520-524.

He, K., et al., *Experimental demonstration of continuous electronic structure tuning via strain in atomically thin MoS2.* Nano Lett, 2013. **13**(6): p. 2931-6.

Heller, I., A.M. Janssens, J. Männik, E.D. Minot, et al., *Identifying the Mechanism of Biosensing with Carbon Nanotube Transistors.* Nano Letters, 2008. **8**(2): p. 591-595.

Heller, I., Kong, J., Heering, H.A., Williams, K.A., et al., *Individual single-walled carbon nanotubes as nanoelectrodes for electrochemistry.* Nano Letters, 2005. **5**(1): p. 137-142.

Hill, A.V., *The Possible Effects of the Aggregation of the Molecules of Hemoglobin on Its Oxygen Dissociation Curve.* Journal of Physiology, 1910(40): p. 4-7.

Hodge, S.A., M.K. Bayazit, K.S. Coleman, and M.S. Shaffer, *Unweaving the rainbow: a review of the relationship between single-walled carbon nanotube molecular structures and their chemical reactivity.* Chem Soc Rev, 2012. **41**(12): p. 4409-29.

Hoffman, D.M., G.L. Doll, and P.C. Eklund, *Optical properties of pyrolytic boron nitride in the energy range 0.05\char22{}10 eV.* Physical Review B, 1984. **30**(10): p. 6051-6056.

Hopfield, J.J., *Odor space and olfactory processing: collective algorithms and neural implementation.* Proceedings of the National Academy of Sciences of the United States of America, 1999. **96**: p. 12506-12511.

Horvath, G., H. Andersson, and S. Nemes, *Cancer odor in the blood of ovarian cancer patients: a retrospective study of detection by dogs during treatment, 3 and 6 months afterward.* Bmc Cancer, 2013. **13**.

Hwang, E.H., S. Adam, and S.D. Sarma, *Carrier Transport in Two-Dimensional Graphene Layers.* Physical Review Letters, 2007. **98**(18): p. 186806.

Iijima, S., *Helical microtubules of graphitic carbon.* Nature, 1991. **354**(6348): p. 56-58.

Iqbal, M.W., et al., *Superior characteristics of graphene field effect transistor enclosed by chemical-vapor-deposition-grown hexagonal boron nitride.* Journal of Materials Chemistry C, 2014. **2**(37): p. 7776-7784.

Ishigami, M., et al., *Atomic Structure of Graphene on SiO2.* Nano Letters, 2007. **7**(6): p. 1643-1648.

Ishigami, M., J.H. Chen, W.G. Cullen, M.S. Fuhrer, et al., *Atomic Structure of Graphene on SiO2.* Nano Letters, 2007. **7**(6): p. 1643-1648.

Jain, N., et al., *Graphene interconnects fully encapsulated in layered insulator hexagonal boron nitride.* Nanotechnology, 2013. **24**(35): p. 355202.

James, T.D., Sandanayake, K.R.A.S., and Shinkai, S., *Chiral Discrimination of Monosaccharides Using a Fluorescent Molecular Sensor.* Nature, 1995. **374**(6520): p. 345-347.

James, T.D., Sandanayake, K.R.A.S., and Shinkai, S., *Saccharide sensing with molecular receptors based on boronic acid.* Angewandte Chemie-International Edition, 1996. **35**(17): p. 1910-1922.

Jariwala, D., et al., *Emerging device applications for semiconducting two-dimensional transition metal dichalcogenides.* ACS Nano, 2014. **8**(2): p. 1102-20.

Jariwala, D., et al., *Gate-tunable carbon nanotube-MoS2 heterojunction p-n diode.* Proc Natl Acad Sci U S A, 2013. **110**(45): p. 18076-80.

Jiang, K., Schadler, L.S., Siegel, R.W., Zhang, X., et al., *Protein immobilization on carbon nanotubes via a two-step process of diimide-activated amidation.* Journal of Materials Chemistry, 2004. **14**(1): p. 37-39.

Jo, I., et al., *Thermal conductivity and phonon transport in suspended few-layer hexagonal boron nitride.* Nano letters, 2013. **13**(2): p. 550-554.

Johnson, R.R. *Rolling up a Graphene Sheet into a Carbon Nanotube*. 2015 [cited 2015; Available from: http://www.physics.upenn.edu/~robertjo/gallery/.

Johnson, R.R., A.T. Johnson, and M.L. Klein, *The nature of DNA-base-carbon-nanotube interactions.* Small, 2010. **6**(1): p. 31-4.

Johnson, R.R., A.T.C. Johnson, and M.L. Klein, *Probing the Structure of DNA-Carbon Nanotube Hybrids with Molecular Dynamics.* Nano Letters, 2008. **8**: p. 69-75.

Johnson, R.R., et al., *Free Energy Landscape of a DNA-Carbon Nanotube Hybrid Using Replica Exchange Molecular Dynamics.* Nano Letters, 2009. **9**(2): p. 537-541.

Jurysta, C., Bulur, N., Oguzhan, B., Satman, I., et al., *Salivary glucose concentration and excretion in normal and diabetic subjects.* J Biomed Biotechnol, 2009. **2009**: p. 430426.

Kanda, F., et al., *Elucidation of chemical compounds responsible for foot malodour.* British Journal of Dermatology, 1990. **122**: p. 1771-1776.

Katsnelson, M. and A. Geim, *Electron scattering on microscopic corrugations in graphene.* Philosophical Transactions of the Royal Society A: Mathematical, Physical and Engineering Sciences, 2008. **366**(1863): p. 195-204.

Kauffman, D.R. and A. Star, *Carbon nanotube gas and vapor sensors.* Angewandte Chemie-International Edition, 2008. **47**(35): p. 6550-6570.

Kauffman, D.R., et al., *Understanding the Sensor Response of Metal-Decorated Carbon Nanotubes.* Nano Letters, 2010. **10**(3): p. 958-963.

Khamis, S.M., et al., *DNA-decorated carbon nanotube-based FETs as ultrasensitive chemical sensors: Discrimination of homologues, structural isomers, and optical isomers.* Aip Advances, 2012. **2**(2).

Khamis, S.M., Jones, R.A., and Johnson, A.T.C., *Optimized photolithographic fabrication process for carbon nanotube devices.* AIP Advances, 2011. **1**(2): p. 022106.

Kim, K.K., et al., *Synthesis of Monolayer Hexagonal Boron Nitride on Cu Foil Using Chemical Vapor Deposition.* Nano Letters, 2012. **12**(1): p. 161-166.

Kim, K.S., et al., *Large-scale pattern growth of graphene films for stretchable transparent electrodes.* Nature, 2009. **457**(7230): p. 706-710.

Kim, M., et al., *Electronic transport and raman scattering in size-controlled nanoperforated graphene.* ACS Nano, 2012. **6**: p. 9846-9854.

Kim, S.M., et al., *Synthesis of Patched or Stacked Graphene and hBN Flakes: A Route to Hybrid Structure Discovery.* Nano Letters, 2013. **13**(3): p. 933-941.

Kobayashi, Y., T. Akasaka, and T. Makimoto, *Hexagonal boron nitride grown by MOVPE.* Journal of Crystal Growth, 2008. **310**(23): p. 5048-5052.

Kodali, V.K., Scrimgeour, J., Kim, S., Hankinson, J.H., et al., *Nonperturbative Chemical Modification of Graphene for Protein Micropatterning.* Langmuir, 2011. **27**(3): p. 863-865.

Kouremenos, K.A., M. Johansson, and P.J. Marriott, *Advances in Gas Chromatographic Methods for the Identification of Biomarkers in Cancer.* Journal of Cancer, 2012. **3**: p. 404-420.

Kretinin, A.V., Y. Cao, J.S. Tu, G.L. Yu, et al., *Electronic properties of graphene encapsulated with different two-dimensional atomic crystals.* Nano Lett, 2014. **14**(6): p. 3270-6.

Krone, N., et al., *Gas chromatography/mass spectrometry (GC/MS) remains a pre-eminent discovery tool in clinical steroid investigations even in the era of fast liquid chromatography tandem mass spectrometry (LC/MS/MS).* Journal of Steroid Biochemistry and Molecular Biology, 2010. **121**(3-5): p. 496-504.

Kumar, S., et al., *Reliable processing of graphene using metal etchmasks.* Nanoscale Research Letters, 2011. **6**(1): p. 390.

Kurzawski, P., V. Schurig, and A. Hierlemann, *Chiral sensing using a complementary metal-oxide semiconductor-integrated three-transducer microsensor system.* Anal Chem, 2009. **81**(22): p. 9353-9364.

Kybert, N.J., et al., *Scalable arrays of chemical vapor sensors based on DNA-decorated graphene.* Nano Research, 2013. **7**(1): p. 95-103.

Kybert, N.J., Lerner, M.B., Yodh, J.S., Preti, G., et al., *Differentiation of complex vapor mixtures using versatile DNA-carbon nanotube chemical sensor arrays.* ACS Nano, 2013. **7**(3): p. 2800-7.

Late, D.J., Liu, B., Matte, H.S.S.R., Dravid, V.P., et al., *Hysteresis in Single-Layer MoS2 Field Effect Transistors.* ACS Nano, 2012. **6**(6): p. 5635-5641.

Lauritsen, J.V., et al., *Size-dependent structure of MoS2 nanocrystals.* Nature nanotechnology, 2007. **2**(1): p. 53-58.

Lee, C., Yan, H., Brus, L.E., Heinz, T.F., et al., *Anomalous Lattice Vibrations of Single- and Few-Layer MoS2.* ACS Nano, 2010. **4**(5): p. 2695-2700.

Lee, J.-H., et al., *Wafer-scale growth of single-crystal monolayer graphene on reusable hydrogen-terminated germanium.* Science, 2014. **344**(6181): p. 286-289.

Lee, K.H., et al., *Large-Scale Synthesis of High-Quality Hexagonal Boron Nitride Nanosheets for Large-Area Graphene Electronics.* Nano Letters, 2012. **12**(2): p. 714-718.

Lee, Y.H., et al., *Synthesis and transfer of single-layer transition metal disulfides on diverse surfaces.* Nano Lett, 2013. **13**(4): p. 1852-7.

Lee, Y.H., et al., *Synthesis of large-area MoS2 atomic layers with chemical vapor deposition.* Adv Mater, 2012. **24**(17): p. 2320-5.

Lee, Y.-H., Zhang, X.-Q., Zhang, W., Chang, M.-T., et al., *Synthesis of Large-Area MoS2 Atomic Layers with Chemical Vapor Deposition.* Advanced Materials, 2012. **24**(17): p. 2320-2325.

Lehninger, A.L., D.L. Nelson, and M.M. Cox, *Lehninger Principles of Biochemistry*. 5th ed. 2008, New York: W.H. Freeman.

Lehninger, A.L., Nelson, D.L., and Cox, M.M., *Lehninger Principles of Biochemistry*. 5th ed. 2008, New York: W.H. Freeman.

LeMieux, M.C., Roberts, M., Barman, S., Jin, Y.W., et al., *Self-sorted, aligned nanotube networks for thin-film transistors.* Science, 2008. **321**(5885): p. 101-104.

Lerner, M.B., Dailey, J., Goldsmith, B.R., Brisson, D., et al., *Detecting Lyme disease using antibody-functionalized single-walled carbon nanotube transistors.* Biosensors and Bioelectronics, 2013. **45**(0): p. 163-167.
Lerner, M.B., D'Souza, J., Pazina, T., Dailey, J., et al., *Hybrids of a Genetically Engineered Antibody and a Carbon Nanotube Transistor for Detection of Prostate Cancer Biomarkers.* Acs Nano, 2012. **6**(6): p. 5143-5149.

Lerner, M.B., Goldsmith, B.R., McMillon, R., Dailey, J., et al., *A carbon nanotube immunosensor for Salmonella.* AIP Advances, 2011. **1**(4): p. 042127.

Lerner, M.B., Matsunaga, F., Han, G.H., Hong, S.J., et al., *Scalable Production of Highly Sensitive Nanosensors Based on Graphene Functionalized with a Designed G Protein-Coupled Receptor.* Nano Letters, 2014. **14**(5): p. 2709-2714.

Lerner, M.B., Resczenski, J.M., Amin, A., Johnson, R.R., et al., *Toward Quantifying the Electrostatic Transduction Mechanism in Carbon Nanotube Molecular Sensors.* Journal of the American Chemical Society, 2012. **134**(35): p. 14318-14321.

Levendorf, M.P., et al., *Graphene and boron nitride lateral heterostructures for atomically thin circuitry.* Nature, 2012. **488**(7413): p. 627-632.

Li, H., et al., *Controlled synthesis of topological insulator nanoplate arrays on mica.* Journal of the American Chemical Society, 2012. **134**: p. 6132-6135.

Li, H., Wu, J., Yin, Z., and Zhang, H., *Preparation and Applications of Mechanically Exfoliated Single-Layer and Multilayer MoS2 and WSe2 Nanosheets.* Accounts of Chemical Research, 2014. **47**(4): p. 1067-1075.

Li, H., Zhang, Q., Yap, C.C.R., Tay, B.K., et al., *From Bulk to Monolayer MoS2: Evolution of Raman Scattering.* Advanced Functional Materials, 2012. **22**(7): p. 1385-1390.

Li, L., et al., *High-Quality Boron Nitride Nanoribbons: Unzipping during Nanotube Synthesis.* Angewandte Chemie, 2013. **125**(15): p. 4306-4310.

Li, X., et al., *Evolution of Graphene Growth on Ni and Cu by Carbon Isotope Labeling.* Nano Letters, 2009. **9**(12): p. 4268-4272.

Li, X., et al., *Large-Area Graphene Single Crystals Grown by Low-Pressure Chemical Vapor Deposition of Methane on Copper.* Journal of the American Chemical Society, 2011. **133**(9): p. 2816-2819.

Li, X., et al., *Large-Area Synthesis of High-Quality and Uniform Graphene Films on Copper Foils.* Science, 2009. **324**(5932): p. 1312-1314.

Li, X., X. Wang, L. Zhang, S. Lee, et al., *Chemically Derived, Ultrasmooth Graphene Nanoribbon Semiconductors.* Science, 2008. **319**(5867): p. 1229-1232.

Liang, X., et al., *Toward Clean and Crackless Transfer of Graphene.* ACS Nano, 2011. **5**(11): p. 9144-9153.

Liang, X.M., et al., *Electrostatic force assisted exfoliation of prepatterned few-layer graphenes into device sites.* Nano Letters, 2009. **9**: p. 467-472.

Liang, Y.X., Y.J. Chen, and T.H. Wang, *Low-resistance gas sensors fabricated from multiwalled carbon nanotubes coated with a thin tin oxide layer.* Applied Physics Letters, 2004. **85**(4): p. 666-668.

Liao, A., et al., *Thermal dissipation and variability in electrical breakdown of carbon nanotube devices.* Physical Review B, 2010. **82**(20): p. 205406.

Liao, A.D., et al., *Thermally Limited Current Carrying Ability of Graphene Nanoribbons.* Physical Review Letters, 2011. **106**(25): p. 256801.

Liao, L., et al., *High-κ oxide nanoribbons as gate dielectrics for high mobility top-gated graphene transistors.* Proceedings of the National Academy of Sciences, 2010. **107**(15): p. 6711-6715.

Lin, Y.-C., C.-Y. Lin, and P.-W. Chiu, *Controllable graphene N-doping iwth ammonia plasma.* Applied Physics Letters, 2010. **96**: p. 133110.

Lin, Y.H., Lu, F., Tu, Y., and Ren, Z.F., *Glucose biosensors based on carbon nanotube nanoelectrode ensembles.* Nano Letters, 2004. **4**(2): p. 191-195.

Lin, Y.-M., et al., *Operation of Graphene Transistors at Gigahertz Frequencies.* Nano Letters, 2009. **9**(1): p. 422-426.

Lin, Y.-M., et al., *Wafer-scale graphene integrated circuit.* Science, 2011. **332**(6035): p. 1294-1297.

Ling, X., et al., *Role of the Seeding Promoter in MoS2 Growth by Chemical Vapor Deposition.* Nano Letters, 2014. **14**(2): p. 464-472.

Liu, B., Chen, L., Liu, G., Abbas, A.N., et al., *High-Performance Chemical Sensing Using Schottky-Contacted Chemical Vapor Deposition Grown Monolayer MoS2 Transistors.* ACS Nano, 2014. **8**(5): p. 5304-5314.

Liu, G., et al., *Epitaxial graphene nanoribbon array fabrication using BCP-assisted nanolithography.* ACS nano, 2012. **6**(8): p. 6786-6792.

Liu, J., Casavant, M.J., Cox, M., Walters, D.A., et al., *Controlled deposition of individual single-walled carbon nanotubes on chemically functionalized templates.* Chemical Physics Letters, 1999. **303**(1-2): p. 125-129.

Liu, K.-K., et al., *Growth of Large-Area and Highly Crystalline MoS2 Thin Layers on Insulating Substrates.* Nano Letters, 2012. **12**(3): p. 1538-1544.

Liu, L., et al., *Graphene Oxidation: Thickness-Dependent Etching and Strong Chemical Doping.* Nano Letters, 2008. **8**(7): p. 1965-1970.

Liu, W., C. Hierold, and M. Haluska, *Electrical contacts to individual SWCNTs: A review.* Beilstein J Nanotechnol, 2014. **5**: p. 2202-15.

Liu, Y., A. Dobrinsky, and B.I. Yakobson, *Graphene Edge from Armchair to Zigzag: The Origins of Nanotube Chirality?* Physical Review Letters, 2010. **105**(23): p. 235502.

Liu, Y., et al., *Half-Metallicity in Hybrid Graphene/Boron Nitride Nanoribbons with Dihydrogenated Edges.* The Journal of Physical Chemistry C, 2011. **115**(19): p. 9442-9450.

Liu, Z., et al., *In-plane heterostructures of graphene and hexagonal boron nitride with controlled domain sizes.* Nat Nano, 2013. **8**(2): p. 119-124.

Longsworth, L.G., *Diffusion Measurements, at 25-Degrees, of Aqueous Solutions of Amino Acids, Peptides and Sugars.* Journal of the American Chemical Society, 1953. **75**(22): p. 5705-5709.

Lu, J., et al., *Why semiconducting single-walled carbon nanotubes are separated from their metallic counterparts.* Small, 2007. **3**(9): p. 1566-76.

Lu, Y., et al., *DNA-decorated graphene chemical sensors.* Applied Physics Letters, 2010. **97**(8): p. 083107.

Lu, Y., et al., *In Situ Electronic Characterization of Graphene Nanoconstrictions Fabricated in a Transmission Electron Microscope.* Nano Letters, 2011. **11**(12): p. 5184-5188.

Lu, Y., Lerner, M.B., John Qi, Z., Mitala, J.J., et al., *Graphene-protein bioelectronic devices with wavelength-dependent photoresponse.* Applied Physics Letters, 2012. **100**(3): p. 033110.

Luo, Z., et al., *Effect of Substrate Roughness and Feedstock Concentration on Growth of Wafer-Scale Graphene at Atmospheric Pressure.* Chemistry of Materials, 2011. **23**(6): p. 1441-1447.

Luo, Z., et al., *Growth Mechanism of Hexagonal-Shape Graphene Flakes with Zigzag Edges.* ACS Nano, 2011. **5**(11): p. 9154-9160.

Mak, K.F., Lee, C., Hone, J., Shan, J., et al., Atomically thin MoS(2): a new direct-gap semiconductor. Phys Rev Lett, 2010. 105(13): p. 136805.

Mak, K.F., McGill, K.L., Park, J., and McEuen, P.L., The valley Hall effect in MoS2 transistors. Science, 2014. 344(6191): p. 1489-1492.

Malard, L.M., M.A. Pimenta, G. Dresselhaus, and M.S. Dresselhaus, Raman spectroscopy in graphene. Physics Reports, 2009. 473(5–6): p. 51-87.

Martin, A., et al., A Functional ABCC11 Allele Is Essential in the Biochemical Formation of Human Axillary Odor. Journal of Investigative Dermatology, 2010. 130(2): p. 529-540.

McCarthy, P.J., Hovey, R.J., Ueno, K., and Martell, A.E., Inner Complex Chelates. I. Analogs of Bisacetylacetoneethylenediimine and its Metal Chelates1,2. Journal of the American Chemical Society, 1955. 77(22): p. 5820-5824.

McCulloch, M., et al., Diagnostic accuracy of canine scent detection in early- and late-stage lung and breast cancers. Integrative Cancer Therapies, 2006. 5(1): p. 30-39.

Melmed, S., Polonsky, K.S., Larsen, P.R., and Kronenberg, H.M., Williams Textbook of Endocrinology. 12 ed. 2011: Saunders. 1371–1435.

Menashe, I., et al., Genetic elucidation of huyman hypersomia to isovaleric acid. PLoS Biology, 2007. 5: p. e:284.

Meyer, E., Atomic force microscopy. Progress in Surface Science, 1992. 41(1): p. 3-49.

Mintmire, J.W. and C.T. White, Electronic and structural properties of carbon nanotubes. Carbon, 1995. 33(7): p. 893-902.

Mintmire, J.W. and C.T. White, Universal Density of States for Carbon Nanotubes. Physical Review Letters, 1998. 81(12): p. 2506-2509.

Molitor, F., et al., Local gating of a graphene Hall bar by graphene side gates. Physical Review B, 2007. 76(24): p. 245426.

Monkhorst, H.J. and J.D. Pack, Special points for Brillouin-zone integrations. Physical Review B, 1976. 13(12): p. 5188-5192.

Moser, J., A. Barreiro, and A. Bachtold, Current-induced cleaning of graphene. Applied Physics Letters, 2007. 91(16): p. 163513.

Mouri, S., Miyauchi, Y., and Matsuda, K., Tunable Photoluminescence of Monolayer MoS2 via Chemical Doping. Nano Letters, 2013. 13(12): p. 5944-5948.

Murali, R., et al., Breakdown current density of graphene nanoribbons. Applied Physics Letters, 2009. 94: p. 243114.

Nagai, Y., Kobayashi, K., Toi, H., and Aoyama, Y., Stabilization of Sugar-Boronic Esters of Indolylboronic Acid in Water Via Sugar Indole Interaction - a Notable Selectivity in Oligosaccharides. Bulletin of the Chemical Society of Japan, 1993. 66(10): p. 2965-2971.

Nagashio, K., et al., Electrical transport properties of graphene on SiO2 with specific surface structures. Journal of Applied Physics, 2011. 110(2): p. 024513.

Najmaei, S., et al., Vapour phase growth and grain boundary structure of molybdenum disulphide atomic layers. Nat Mater, 2013. 12(8): p. 754-759.

Nakada, K., et al., Edge state in graphene ribbons: Nanometer size effect and edge shape dependence. Physical Review B, 1996. 54(24): p. 17954-17961.

Nam, H., et al., MoS2 Transistors Fabricated via Plasma-Assisted Nanoprinting of Few-Layer MoS2 Flakes into Large-Area Arrays. ACS Nano, 2013. 7: p. 5870-5881.

Natsch, A., et al., A broad diversity of volatile carboxylic acids, released by a bacterial aminoacylase from axilla secretions, as candidate molecules for the determination of human-body odor type. Chemistry & Biodiversity, 2006. 3(1): p. 1-20.

Natsch, A., et al., A specific bacterial aminoacylase cleaves odorant precursors secreted in the human axilla. Journal of Biological Chemistry, 2003. 278(8): p. 5718-5727.

Nish, A., J.-Y. Hwang, J. Doig, and R.J. Nicholas, Highly selective dispersion of single-walled carbon nanotubes using aromatic polymers. Nat Nano, 2007. 2(10): p. 640-646.

Nomura, K. and A.H. MacDonald, Quantum Transport of Massless Dirac Fermions. Physical Review Letters, 2007. 98(7): p. 076602.

Novak, J.P., et al., Nerve agent detection using networks of single-walled carbon nanotubes. Applied Physics Letters, 2003. 83(19): p. 4026-4028.

Novoselov, K.S., A.K. Geim, S.V. Morozov, D. Jiang, et al., Electric field effect in atomically thin carbon films. Science, 2004. 306(5696): p. 666-9.

Novoselov, K.S., A.K. Geim, S.V. Morozov, D. Jiang, et al., Two-dimensional gas of massless Dirac fermions in graphene. Nature, 2005. 438(7065): p. 197-200.

Novoselov, K.S., Jiang, D., Schedin, F., Booth, T.J., et al., Two-dimensional atomic crystals. Proceedings of the National Academy of Sciences of the United States of America, 2005. 102(30): p. 10451-10453.

Novoselov, K.S., Z. Jiang, Y. Zhang, S.V. Morozov, et al., Room-Temperature Quantum Hall Effect in Graphene. Science, 2007. 315(5817): p. 1379.

Ohno, Y., K. Maehashi, and K. Matsumoto, Label-Free Biosensors Based on Aptamer-Modified Graphene Field-Effect Transistors. Journal of the American Chemical Society, 2010. 132(51): p. 18012-18013.

Opatkiewicz, J.P., M.C. LeMieux, and Z. Bao, Influence of Electrostatic Interactions on Spin-Assembled Single-Walled Carbon Nanotube Networks on Amine-Functionalized Surfaces. ACS Nano, 2010. 4(2): p. 1167-1177.

O'Reilly, J.P., Butts, C.P., l'Anson, I.A., and Shaw, A.M., Interfacial pH at an isolated silica-water surface. Journal of the American Chemical Society, 2005. 127(6): p. 1632-3.

Ori, A. and Shinkai, S., Electrochemical Detection of Saccharides by the Redox Cycle of a Chiral Ferrocenylboronic Acid-Derivative - a Novel Method for Sugar Sensing. Journal of the Chemical Society-Chemical Communications, 1995(17): p. 1771-1772.

Overington, J.P., Al-Lazikani, B., and Hopkins, A.L., How many drug targets are there? Nat Rev Drug Discov, 2006. 5(12): p. 993-996.

Paolo, G., et al., QUANTUM ESPRESSO: a modular and open-source software project for quantum simulations of materials. Journal of Physics: Condensed Matter, 2009. 21(39): p. 395502.

Park, S.J., O.S. Kwon, S.H. Lee, H.S. Song, et al., Ultrasensitive flexible graphene based field-effect transistor (FET)-type bioelectronic nose. Nano Lett, 2012. 12(10): p. 5082-90.

Park, W., et al., Photoelectron Spectroscopic Imaging and Device Applications of Large-Area Patternable Single-Layer MoS2 Synthesized by Chemical Vapor Deposition. ACS Nano, 2014. 8: p. 4961-4968.

Pengfei, L., et al., High-Yield Fabrication of Graphene Chemiresistors With Dielectrophoresis. Nanotechnology, IEEE Transactions on, 2012. 11(4): p. 751-759.

Pengfei, Q.F., et al., Toward large arrays of multiplex functionalized carbon nanotube sensors for highly sensitive and selective molecular detection. Nano Letters, 2003. 3(3): p. 347-351.

Penza, M., et al., Alcohol detection using carbon nanotubes acoustic and optical sensors. Applied Physics Letters, 2004. 85(12): p. 2379-2381.

Perdew, J.P., K. Burke, and M. Ernzerhof, Generalized Gradient Approximation Made Simple. Physical Review Letters, 1996. 77(18): p. 3865-3868.

Perez-Aguilar, J.M., Xi, J., Matsunaga, F., Cui, X., et al., A computationally designed water-soluble variant of a G-protein-coupled receptor: the human mu opioid receptor. PloS one, 2013. 8(6): p. e66009.

Perkins, F.K., Friedman, A.L., Cobas, E., Campbell, P.M., et al., Chemical Vapor Sensing with Monolayer MoS2. Nano Letters, 2013. 13(2): p. 668-673.

Petricoin Iii, E.F., et al., Use of proteomic patterns in serum to identify ovarian cancer. The Lancet, 2002. 359(9306): p. 572-577.

Pierce, J., J.D., et al., Cross-adaptation of sweaty-smelling 3-methyl-2-hexenoic acid by its ethyl esters is determined by structural similarity. Journal of the Society of Cosmetic Chemists, 1996. 47: p. 363-375.

Ping, J. and M.S. Fuhrer, Layer number and stacking sequence imaging by transmission electron microscopy. Nano Letters, 2012. 12: p. 4635-4641.

Pirkle, A., et al., The effect of chemical residues on the physical and electrical properties of chemical vapor deposited graphene transferred to SiO2. Applied Physics Letters, 2011. 99(12): p. 122108.

Premkumar, T. and K.E. Geckeler, Graphene-DNA hybrid materials: Assembly, applications, and prospects. Progress in Polymer Science, 2012. 37: p. 515-529.

Preti, G., et al., Odors and Disease: Volatile Biomarkers from Human Skin Cancer. Chemical Senses, 2008. 33(8): p. S138-S139.

Prokop-Prigge, K.A., et al., Identification of volatile organic compounds in human cerumen. J Chromatogr B Analyt Technol Biomed Life Sci, 2014. 953-954: p. 48-52.

Qi, Z.J., et al., Correlating Atomic Structure and Transport in Suspended Graphene Nanoribbons. Nano Letters, 2014. 14(8): p. 4238-4244.

Quhe, R., et al., Tunable and sizable band gap of single-layer graphene sandwiched between hexagonal boron nitride. NPG Asia Mater, 2012. 4: p. e6.

Radisavljevic, B., M.B. Whitwick, and A. Kis, Integrated circuits and logic operations based on single-layer MoS2. ACS Nano, 2011. 5(12): p. 9934-8.

Radisavljevic, B., Radenovic, A., Brivio, J., Giacometti, V., et al., Single-layer MoS2 transistors. Nat Nanotechnol, 2011. 6(3): p. 147-50.

Ramer, N.J. and A.M. Rappe, Designed nonlocal pseudopotentials for enhanced transferability. Physical Review B, 1999. 59(19): p. 12471-12478.

Rappe, A.M., et al., Optimized pseudopotentials. Physical Review B, 1990. 41(2): p. 1227-1230.

Ratinac, K.R., et al., Toward ubiquitous environmental gas sensors - Capitalizing on the promise of Graphene. Environmental Science and Technology, 2010. 44: p. 1167-1176.

Reich, S., J. Maultzsch, C. Thomsen, and P. Ordejón, Tight-binding description of graphene. Physical Review B, 2002. 66(3): p. 035412.

Ritter, K.A. and J.W. Lyding, The influence of edge structure on the electronic properties of graphene quantum dots and nanoribbons. Nat Mater, 2009. 8(3): p. 235-242.

Rose, H.H., Historical aspects of aberration correction. Journal of Electron Microscopy, 2009. 58(3): p. 77-85.

Roy, K., Padmanabhan, M., Goswami, S., Sai, T.P., et al., Graphene-MoS2 hybrid structures for multifunctional photoresponsive memory devices. Nat Nano, 2013. 8(11): p. 826-830.

Ryo, N., S. Tatsuya, and T. Katsumi, Determination of Carrier Type Doped from Metal Contacts to Graphene by Channel-Length-Dependent Shift of Charge Neutrality Points. Applied Physics Express, 2011. 4(3): p. 035101.

Safron, N.S., et al., Barrier-Guided Growth of Micro- and Nano-Structured Graphene. Advanced Materials, 2012. 24(8): p. 1041-1045.

Salvatore, G.A., et al., Fabrication and transfer of flexible few-layers MoS2 thin film transistors to any arbitrary substrate. ACS Nano, 2013. 7(10): p. 8809-15.

Sarkar, D., Liu, W., Xie, X., Anselmo, A.C., et al., MoS2 Field-Effect Transistor for Next-Generation Label-Free Biosensors. ACS Nano, 2014. 8(4): p. 3992-4003.

Sawano, K., K. Ishida, and A. Shimada, Perfume composition, in United States Patent. 1992: USA.

Schmidt, H., Wang, S., Chu, L., Toh, M., et al., Transport Properties of Monolayer MoS2 Grown by Chemical Vapor Deposition. Nano Letters, 2014. 14(4): p. 1909-1913.

Schwierz, F., Graphene transistors. Nat Nano, 2010. 5(7): p. 487-496.

Senol, M. and P. Fireman, Body odor in dermatologic diagnosis. Cutis, 1999. 63(2): p. 107-111.

Serra, S., C. Fuganti, and E. Brenna, Biocatalytic preparation of natural flavours and fragrances. Trends in Biotechnology, 2005. 23(4): p. 193-198.

Shi, H., et al., Exciton dynamics in suspended monolayer and few-layer MoS(2) 2D crystals. ACS Nano, 2013. 7(2): p. 1072-80.

Shi, Y., et al., Synthesis of Few-Layer Hexagonal Boron Nitride Thin Film by Chemical Vapor Deposition. Nano Letters, 2010. 10(10): p. 4134-4139.

Shirasu, M. and K. Touhara, The scent of disease: volatile organic compounds of the human body related to disease and disorder. Journal of Biochemistry, 2011. 150(3): p. 257-266.

Shirasu, M., et al., Dimethyl Trisulfide as a Characteristic Odor Associated with Fungating Cancer Wounds. Bioscience Biotechnology and Biochemistry, 2009. 73(9): p. 2117-2120.

Shoji, E. and Freund, M.S., Potentiometric saccharide detection based on the pKa changes of poly(aniline boronic acid). Journal of the American Chemical Society, 2002. 124(42): p. 12486-12493.

Snow, E.S., et al., Chemical detection with a single-walled carbon nanotube capacitor. Science, 2005. 307(5717): p. 1942-1945.

Song, L., et al., Large Scale Growth and Characterization of Atomic Hexagonal Boron Nitride Layers. Nano Letters, 2010. 10(8): p. 3209-3215.

Splendiani, A., Sun, L., Zhang, Y., Li, T., et al., Emerging Photoluminescence in Monolayer MoS2. Nano Letters, 2010. 10(4): p. 1271-1275.

Sreeprasad, T.S., P. Nguyen, N. Kim, and V. Berry, Controlled, Defect-Guided, Metal-Nanoparticle Incorporation onto MoS2 via Chemical and Microwave Routes: Electrical, Thermal, and Structural Properties. Nano Letters, 2013. 13(9): p. 4434-4441.

Staii, C., et al., DNA-decorated carbon nanotubes for chemical sensing. Nano Letters, 2005. 5(9): p. 1774-1778.

Star, A., et al., Gas sensor array based on metal-decorated carbon nanotubes. Journal of Physical Chemistry B, 2006. 110(42): p. 21014-21020.

Star, A., et al., Nanoelectronic carbon dioxide sensors. Advanced Materials, 2004. 16(22): p. 2049-2052.

Star, A., Gabriel, J.C.P., Bradley, K., and Gruner, G., Electronic detection of specific protein binding using nanotube FET devices. Nano Letters, 2003. 3(4): p. 459-463.

Stine, R., et al., Fabrication, optimization, and use of graphene field effect sensors. Analytical Chemistry, 2013. 85: p. 509-521.

Stones, D., Manku, S., Lu, X.S., and Hall, D.G., Modular solid-phase synthetic approach to optimize structural and electronic properties of oligoboronic acid receptors and sensors for the aqueous recognition of oligosaccharides. Chemistry-a European Journal, 2004. 10(1): p. 92-100.

Sun, Z., et al., Growth of graphene from solid carbon sources. Nature, 2010. 468(7323): p. 549-552.

Sundaram, R.S., et al., Electroluminescence in single layer MoS2. Nano Lett, 2013. 13(4): p. 1416-21.

Sutter, P., et al., Interface Formation in Monolayer Graphene-Boron Nitride Heterostructures. Nano Letters, 2012. 12(9): p. 4869-4874.

Tahir, M.N., Zink, N., Eberhardt, M., Therese, H.A., et al., Overcoming the Insolubility of Molybdenum Disulfide Nanoparticles through a High Degree of Sidewall Functionalization Using Polymeric Chelating Ligands. Angewandte Chemie International Edition, 2006. 45(29): p. 4809-4815.

Takahashi, S. and Anzai, J., Phenylboronic acid monolayer-modified electrodes sensitive to sugars. Langmuir, 2005. 21(11): p. 5102-5107.

Tan, X., et al., Control and enhancement of graphene sensitivity by engineering edge defects. IEEE Sensors Journal, 2012: p. 978-1-4577.

Thess, A., et al., Crystalline Ropes of Metallic Carbon Nanotubes. Science, 1996. 273(5274): p. 483-487.

Tian, J.F., et al., Ambipolar graphene field effect transistors by local metal side gates. Applied Physics Letters, 2010. 96(26): p. 263110.

Torsi, L., et al., A sensitivity-enhanced field-effect chiral sensor. Nature Materials, 2008. 7: p. 412-417.

Tsai, M.-L., Su, S.-H., Chang, J.-K., Tsai, D.-S., et al., Monolayer MoS2 Heterojunction Solar Cells. ACS Nano, 2014. 8(8): p. 8317-8322.

Tu, X., S. Manohar, A. Jagota, and M. Zheng, DNA sequence motifs for structure-specific recognition and separation of carbon nanotubes. Nature, 2009. 460(7252): p. 250-3.

van der Zande, A.M., Huang, P.Y., Chenet, D.A., Berkelbach, T.C., et al., Grains and grain boundaries in highly crystalline monolayer molybdenum disulphide. Nat Mater, 2013. 12(6): p. 554-561.

Varghese, O.K., et al., Gas sensing characteristics of multi-wall carbon nanotubes. Sensors and Actuators B-Chemical, 2001. 81(1): p. 32-41.

Vlassiouk, I., et al., Role of Hydrogen in Chemical Vapor Deposition Growth of Large Single-Crystal Graphene. ACS Nano, 2011. 5(7): p. 6069-6076.

Wallace, P.R., The Band Theory of Graphite. Physical Review, 1947. 71(7): p. 476.

Wang, C., Zhang, J.L., Ryu, K.M., Badmaev, A., et al., Wafer-Scale Fabrication of Separated Carbon Nanotube Thin-Film Transistors for Display Applications. Nano Letters, 2009. 9(12): p. 4285-4291.

Wang, L., et al., One-Dimensional Electrical Contact to a Two-Dimensional Material. Science, 2013. 342(6158): p. 614-617.

Wang, L., Wang, Y., Wong, J.I., Palacios, T., et al., Functionalized MoS2 Nanosheet-Based Field-Effect Biosensor for Label-Free Sensitive Detection of Cancer Marker Proteins in Solution. Small, 2014. 10(6): p. 1101-1105.

Wang, L., Wei, L., Chen, Y., and Jiang, R., Specific and reversible immobilization of NADH oxidase on functionalized carbon nanotubes. Journal of Biotechnology, 2010. 150(1): p. 57-63.

Wang, M., et al., A Platform for Large-Scale Graphene Electronics – CVD Growth of Single-Layer Graphene on CVD-Grown Hexagonal Boron Nitride. Advanced Materials, 2013. 25(19): p. 2746-2752.

Wang, M., et al., CVD Growth of Large Area Smooth-edged Graphene Nanomesh by Nanosphere Lithography. Scientific Reports, 2013. 3.

Wang, Q.H., Z. Jin, K.K. Kim, A.J. Hilmer, et al., Understanding and controlling the substrate effect on graphene electron-transfer chemistry via reactivity imprint lithography. Nat Chem, 2012. 4(9): p. 724-732.

Wang, X., L. Zhi, and K. Müllen, Transparent, Conductive Graphene Electrodes for Dye-Sensitized Solar Cells. Nano Letters, 2008. 8(1): p. 323-327.

Warner, J.H., M. Mukai, and A.I. Kirkland, Atomic structure of ABC rhombohedral stacked trilayer graphene. ACS Nano, 2012. 6(6): p. 5680-6.

Westenfelder, B., et al., Transformations of carbon adsorbates on graphene substrates under extreme heat. Nano letters, 2011. 11(12): p. 5123-5127.

Wienold, J., R.E. Jentoft, and T. Ressler, Structural investigation of the thermal decomposition of ammonium heptamolybdate by in situ XAFS and XRD. European Journal of Inorganic Chemistry, 2003(6): p. 1058-1071.

Wilder, J.W.G., L.C. Venema, A.G. Rinzler, R.E. Smalley, et al., Electronic structure of atomically resolved carbon nanotubes. Nature, 1998. 391(6662): p. 59-62.

Willis, C.M., et al., Olfactory detection of human bladder cancer by dogs: proof of principle study. British Medical Journal, 2004. 329(7468): p. 712-714A.

Wilson, A.D. and M. Baietto, Applications and advances in electronic-nose technologies. Sensors, 2009. 9: p. 5099-5148.

Woo, H.M., et al., Mass spectrometry based metabolomic approaches in urinary biomarker study of women's cancers. Clinica Chimica Acta, 2009. 400(1-2): p. 63-69.

Wu, B., et al., Equiangular Hexagon-Shape-Controlled Synthesis of Graphene on Copper Surface. Advanced Materials, 2011. 23(31): p. 3522-3525.

Wu, W., D. De, S.-C. Chang, Y. Wang, et al., High mobility and high on/off ratio field-effect transistors based on chemical vapor deposited single-crystal MoS2 grains. Applied Physics Letters, 2013. 102(14): p. 142106.

Wu, W., et al., Growth of Single Crystal Graphene Arrays by Locally Controlling Nucleation on Polycrystalline Cu Using Chemical Vapor Deposition. Advanced Materials, 2011. 23(42): p. 4898-4903.

Wysocki, C.J., et al., Cross-adaptation fo a model human stress-related odor with fragrance chemicals and ethyl esters of axillary odorants: Gender-specific effects. Journal of Flavour Fragrance, 2009. 24: p. 209-218.

Xia, F., et al., The origins and limits of metal-graphene junction resistance. Nature nanotechnology, 2011. 6(3): p. 179-184.

Xu, C., S.C. Ng, and H.S. Chan, Self-assembly of perfunctionalized beta-cyclodextrins on a quartz crystal microbalance for real-time chiral recognition. Langmuir, 2008. 24(16): p. 9118-9124.

Yan, J., et al., Electric field effect tuning of electron-phonon coupling in graphene. Physical Review Letters, 2007. 98: p. 166802.

Yu, Q., et al., Control and characterization of individual grains and grain boundaries in graphene grown by chemical vapour deposition. Nat Mater, 2011. 10(6): p. 443-449.

Yu, W.J., et al., Highly efficient gate-tunable photocurrent generation in vertical heterostructures of layered materials. Nat Nanotechnol, 2013. 8(12): p. 952-8.

Yu, W.J., et al., Vertically stacked multi-heterostructures of layered materials for logic transistors and complementary inverters. Nat Mater, 2013. 12(3): p. 246-52.

Yum, K., Ahn, J.H., McNicholas, T.P., Barone, P.W., et al., Boronic Acid Library for Selective, Reversible Near-Infrared Fluorescence Quenching of Surfactant Suspended Single-Walled Carbon Nanotubes in Response to Glucose. Acs Nano, 2012. 6(1): p. 819-830.

Zeng, H., et al., “White Graphenes”: Boron Nitride Nanoribbons via Boron Nitride Nanotube Unwrapping. Nano Letters, 2010. 10(12): p. 5049-5055.

Zeng, X.-N., et al., An investigation of human apocrine gland secretion for axillary odor precursors. Journal of Chemical Ecology, 1992. 18: p. 1039-1055.

Zeng, X.N., et al., Analysis of Characteristic Odors from Human Male Axillae. Journal of Chemical Ecology, 1991. 17(7): p. 1469-1492.

Zeng, X.-N., et al., Analysis of the characteristic human female axillary odors: qualitative comparison to males. Journal of Chemical Ecology, 1996. 22: p. 237-257.

Zhan, Y., et al., Large-Area Vapor-Phase Growth and Characterization of MoS2 Atomic Layers on a SiO2 Substrate. Small, 2012. 8(7): p. 966-971.

Zhan, Y., Liu, Z., Najmaei, S., Ajayan, P.M., et al., Large-Area Vapor-Phase Growth and Characterization of MoS2 Atomic Layers on a SiO2 Substrate. Small, 2012. 8(7): p. 966-971.

Zhang, A., et al., Band gap engineering in graphene and hexagonal BN antidot lattices: A first principles study. Applied Physics Letters, 2011. 98(2): p. 023105.

Zhang, R., Y. Zhang, Q. Zhang, H. Xie, et al., Growth of half-meter long carbon nanotubes based on Schulz-Flory distribution. ACS Nano, 2013. 7(7): p. 6156-61.

Zhang, W., Huang, J.-K., Chen, C.-H., Chang, Y.-H., et al., High-Gain Phototransistors Based on a CVD MoS2 Monolayer. Advanced Materials, 2013. 25(25): p. 3456-3461.

Zhang, Y.M., D.J. Zhang, and C.B. Liu, Novel chemical sensor for cyanides: Boron-doped carbon nanotubes. Journal of Physical Chemistry B, 2006. 110(10): p. 4671-4674.

Zhao, X., Y. Li, J. Wang, Z. Ouyang, et al., Interactive Oxidation–Reduction Reaction for the in Situ Synthesis of Graphene–Phenol Formaldehyde Composites with Enhanced Properties. ACS Applied Materials & Interfaces, 2014. 6(6): p. 4254-4263.

Zheng, M., A. Jagota, E.D. Semke, B.A. Diner, et al., DNA-assisted dispersion and separation of carbon nanotubes. Nat Mater, 2003. 2(5): p. 338-42.

Zuniga, C., et al., Nanoenabled microelectromechanical sensor for volatile organic chemical detection. Applied Physics Letters, 2009. 94: p. 223122.